

# Tunnelling into InAs Quantum Dots

by Richard John Allan Hill M.Sci.

Thesis submitted to the University of Nottingham for  
the degree of Doctor of Philosophy, September 2002

To Anna

# Contents

<b>Abstract</b>	<b>vii</b>
<b>Acknowledgements</b>	<b>viii</b>
<b>Publications</b>	<b>ix</b>
<b>1 Basics</b>	<b>1</b>
1.1 Introduction . . . . .	1
1.1.1 Resonant tunnelling in solid state devices . . . . .	2
1.1.2 Quantum dots . . . . .	3
1.1.3 Resonant tunnelling via quantum dot states . . . . .	4
1.1.4 Thesis overview . . . . .	5
1.1.5 Note about axes convention . . . . .	6
1.2 Basic concepts . . . . .	6
1.2.1 One electron model . . . . .	6
1.2.2 Semiconductors . . . . .	7
Doping . . . . .	7
Heterostructures . . . . .	8
1.2.3 Effective mass approximation . . . . .	8
1.3 Properties of GaAs, (AlGa)As and InAs crystals . . . . .	10
1.3.1 GaAs . . . . .	10
1.3.2 AlAs . . . . .	12
1.3.3 (AlGa)As . . . . .	12

---

1.3.4	InAs . . . . .	13
1.3.5	Band alignment at a heterojunction . . . . .	14
1.4	Two dimensional electron system . . . . .	14
1.4.1	Two dimensional system in a magnetic field . . . . .	16
	Landau levels . . . . .	17
1.4.2	Scattering effects . . . . .	20
	Landau levels in the presence of scattering . . . . .	22
1.5	Zero dimensional electron system . . . . .	22
1.5.1	InAs quantum dot . . . . .	22
1.6	Electron $g$ factor . . . . .	23
1.6.1	Effective $g$ factor in a crystal . . . . .	24
1.7	Tunnelling . . . . .	25
1.7.1	Resonant tunnelling . . . . .	28
1.7.2	Analytic expressions for the Bardeen transfer matrix	32
	Tunnelling between a 3D and a 2D system . . . . .	33
	Tunnelling between a 2D and a 0D system . . . . .	33
<b>2</b>	<b>Apparatus, experimental techniques and samples</b>	<b>36</b>
2.1	Oxford Instruments 0.3 K He <sup>3</sup> cryostat . . . . .	36
2.2	High pressure apparatus . . . . .	38
2.2.1	Unipress high pressure liquid clamp cell . . . . .	38
2.2.2	Cryogenics 4 K cryostat . . . . .	39
2.3	$I(V)$ measurement techniques . . . . .	39
2.3.1	Basic $I(V)$ measurement circuit . . . . .	39
2.3.2	Computer assisted automation . . . . .	41
2.3.3	Sources of noise and noise reduction techniques . . . . .	42
	Electrical equipment . . . . .	43
	Cables and connections . . . . .	43
	Fundamental noise limits . . . . .	44

---

2.3.4	Applying bias to Schottky gates . . . . .	46
2.4	Samples . . . . .	47
2.4.1	Wafer growth . . . . .	47
	Growth of self-assembled quantum dots . . . . .	48
2.4.2	Wafer <i>NU1403</i> . . . . .	49
	Device fabrication . . . . .	52
2.4.3	Wafer <i>NU1673</i> . . . . .	52
	Device fabrication . . . . .	55
<b>3</b>	<b>Resonant tunnelling through a single quantum dot</b>	<b>63</b>
3.1	Introduction . . . . .	63
3.2	Devices . . . . .	65
3.3	Low temperature $I(V)$ characteristics . . . . .	65
3.4	Evidence for tunnelling via quantum dot states . . . . .	69
	3.4.1 Coulomb blockade . . . . .	71
	3.4.2 Isolated resonant features at low voltage . . . . .	73
3.5	A model for the resonant tunnel current . . . . .	73
	3.5.1 Emitter state wave function . . . . .	76
	3.5.2 Quantum dot state wave function . . . . .	76
	3.5.3 Current flow between the emitter and quantum dot state	77
	Transfer matrix element . . . . .	77
	Resonant current as measure of the local density of states in the emitter . . . . .	78
	3.5.4 Forward bias tunnel current . . . . .	79
	3.5.5 Variation in the resonant current with voltage . . . . .	80
	Leverage factor . . . . .	80
	Change in the energy of a QD state with voltage . . . . .	80
	Occupancy of states in the emitter . . . . .	81
	3.5.6 Result . . . . .	81

---

3.6	Low temperature $I(V)$ characteristics of isolated resonant features . . . . .	82
3.7	$I(V)$ characteristic of feature $d$ . . . . .	85
3.7.1	Thermal activation of the onset and measurement of the leverage factor . . . . .	86
3.7.2	Estimate of the Fermi energy of the 2DES from the voltage width of the feature . . . . .	88
3.8	$I(V)$ characteristics at high pressure . . . . .	88
3.9	Summary . . . . .	93
<b>4</b>	<b>Quantum dot as a spectroscopic probe of Landau levels</b>	<b>94</b>
4.1	Introduction . . . . .	94
4.2	Spectroscopic probe of Landau levels . . . . .	95
4.2.1	Low temperature $I(V)$ traces in magnetic field . . . . .	95
4.2.2	Colour-scale $I(B, V)$ plot of the data . . . . .	98
4.2.3	Expected voltage positions of the Landau levels . . . . .	99
4.2.4	Fermi energy in magnetic field . . . . .	99
	Obtaining the electron density from oscillations in $E_F$ . . . . .	99
	Diamagnetic shift of quantum dot state . . . . .	100
4.3	Quasiparticle lifetime . . . . .	101
4.4	Data from devices $a$ and $b$ . . . . .	105
4.5	Summary . . . . .	106
<b>5</b>	<b>High magnetic field spectroscopy of a 2DES</b>	<b>111</b>
5.1	Introduction . . . . .	111
5.2	Low temperature $I(V)$ in high magnetic field . . . . .	113
5.3	Change in the Fermi energy at filling factor 2 . . . . .	117
5.4	Plot of current versus filling factor and voltage . . . . .	120
5.4.1	Change in filling factor with voltage . . . . .	121
5.4.2	Measurements of electron density . . . . .	123
5.4.3	Result . . . . .	125

---

5.5	Measuring the $g$ factor in the 2DES . . . . .	126
5.5.1	The 2DES $g$ -factor between $\nu = 2$ and $\nu = 1$ . . . . .	129
	Spin splitting of QD state . . . . .	129
	Result . . . . .	130
5.5.2	The 2DES $g$ -factor at $\nu = 1$ . . . . .	131
5.5.3	Discussion of results . . . . .	132
5.5.4	Conclusion . . . . .	134
5.6	Multiple peak structure at $\nu = 1, 2, 4$ . . . . .	135
<b>6</b>	<b>Tunnelling through quantum dots in a gated device</b>	<b>141</b>
6.1	Introduction . . . . .	141
6.2	Device . . . . .	142
6.2.1	Low temperatures $I(V)$ characteristics . . . . .	145
	Adjustment for ‘hidden’ resistance . . . . .	148
6.2.2	Applying voltage to the gate electrodes . . . . .	150
6.3	Magneto-tunnelling spectroscopy . . . . .	158
6.3.1	A model for the resonant tunnel current . . . . .	160
	Emitter states . . . . .	160
	Quantum dot states . . . . .	161
	Current flow between emitter and a single QD state . . . . .	164
	Dependence of $\mathcal{T}$ on $B$ . . . . .	167
6.3.2	Results: $G(B)$ dependence . . . . .	169
6.4	Magneto-tunnelling spectroscopy on an individual QD . . . . .	170
6.4.1	Fits to analytic wave functions . . . . .	178
6.4.2	Estimate of the size of the QD wave functions in real space . . . . .	181
6.4.3	Comparisons with results from other QDs . . . . .	183
6.5	Conclusions and future prospects . . . . .	185

# Abstract

This thesis describes an experimental study of the electronic properties of semiconductor heterostructure tunnel devices. InAs self-assembled quantum dots (QDs) are incorporated into the barrier layer of a GaAs/AlAs/GaAs tunnel diode. When a voltage,  $V$ , is applied across the device, we observe resonant features in the tunnel current,  $I$ , whenever an electron state in one of the QDs comes into resonance with an occupied electron state in the emitter. We employ an electron state of a single QD as a spectroscopic probe of a two-dimensional electron system (2DES), from the Fermi energy to the subband edge [1]. For magnetic field  $\mathbf{B}$  applied parallel to the current, we observe peaks in the  $I(V)$  characteristics corresponding to the formation of Landau levels in the 2DES. We obtain quantitative information about the energy dependence of the quasiparticle lifetime,  $\tau_{\text{qp}}$ , of the 2DES. We find that  $\tau_{\text{qp}} \sim 2.5\hbar/(E_{\text{F}} - E)$ , in contrast with the expectation for a normal Fermi liquid, but in agreement with predictions for a Fermi liquid state of a disordered 2DES. Close to filling factor  $\nu = 1$  we observe directly the exchange enhancement of the  $g$  factor.

This thesis also describes the design, realisation and measurement of a tunnel diode incorporating InAs QDs and a series of 4 planar electrostatic gates. By applying a bias to the gates, it is possible to selectively inject current into a particular QD. We use magneto-tunnelling spectroscopy to determine the energy levels of the ground and excited state of a single QD, and to map the spatial form of the wave functions of these states [2].

The effect of pressure on the resonant tunnelling of the QDs is also described.

[1] P. C. Main *et al.*, Phys. Rev. Lett. **84**, 729 (2000)

[2] R. J. A. Hill *et al.*, Appl. Phys. Lett. **79**, 3275 (2001)

# Acknowledgements

I would like to express my sincere thanks to a number of people:

I am grateful to the Engineering and Physical Sciences Research Council for a maintenance grant.

I am indebted to my supervisors, Prof. Peter Main and Prof. Laurence Eaves, for their invaluable tuition and patient guidance.

I would like to thank Drs. Simon Stoddart, Guy Austing, Igor Itskevich and Amalia Patanè for the time and energy they spent ‘teaching me the ropes’ with circuits, cryostats, processing and pressure cells. I particularly thank Guy for his friendship and for helping me to find my way during my time in Japan, kanpai! Many thanks also to Dr. Mohammed Henini for growing the samples used in this thesis.

Many thanks to John Dennis for the provision of liquid helium, and to Malcom Carter, John Middleton and all the support staff for (often last-minute) finely skilled technical work on the equipment.

Thanks to my friends in Nottingham, particularly Stan, Charlie, Nic, Fergal, Helen, Volker, Andy, Laurie, Philip, Ingrid, Boel, Amalia, Oleg, Andreas, Kevin, Sam, Simon, Lou, Kev and Dave. Cheers guys. Particular thanks to Boel for welcome assistance with the experimental work presented in chapter 6. And thanks to the Autumn-Winter ’99 Soubudai gang for some fantastic memories, Roch, Franklin, Brian, Frederic, Sebastian, Hashisan and Kawaharazuka-san.

Thanks to Mum, Dad and Rach for their continuing love and support, and finally a big thanks to my fiancée Anna, for, well, everything.

# Publications

## **Probing the quantum states of self-assembled InAs dots by magnetotunnelling spectroscopy**

Physical Review B, vol.65, no.16, pp.165308-20, 15 April 2002.

Patanè A, Hill R J A, Eaves L, Main P C, Henini M, Zambrano M L, Levin A, Mori N, Hamaguchi C, Dubrovskii Yu V, Vdovin E E, Austing D G, Tarucha S and Hill G.

## **Controlling the electron tunnelling through InAs self-assembled dots**

Journal of Applied Physics, vol.91, no.5, pp.3474-76, 1 March 2002.

Hill R J A, Patanè A, Main P C, Henini M, Eaves L, Tarucha S and Austing D G.

## **Measuring the energy levels and wave functions in a single quantum dot**

Physica E, vol.13, no.1-4, pp.634-37, February 2002.

Hill R J A, Patanè A, Main P C, Eaves L, Gustafson B, Henini M, Tarucha S and Austing D G.

## **Mapping the wave functions in quantum dots**

Physica E, vol.12, no.1-4, pp.794-801, January 2002.

Main P C, Patanè A, Hill R J A, Levin A, Eaves L, Henini M, Austing D G, Tarucha S, Dubrovskii Yu V and Vdovin E E.

## **Magnetotunnelling spectroscopy of an individual quantum dot in a gated tunnel diode**

Applied Physics Letters, vol.79, no.20, pp.3275-712, November 2001.

Hill R J A, Patanè A, Main P C, Eaves L, Gustafson B, Henini M, Tarucha S and Austing D G.

**High pressure as a tool to study electron localization**

Physica Status Solidi B, vol.223, no.2, pp.555-98, January 2001.

Hill R J A, Itskevich I E, Stoddart S T, Murphy H M, Thornton A S G, Main P C, Eaves L, Henini M, Maude D K and Portal J-C.

**Phase coherence and size effects in double quantum well mesoscopic wires**

Physica E, vol.6, no.1-4, pp.672-5, February 2000.

Stoddart S T, Hill R J A, Neumann A C, Main P C, Nogaret A, Eaves L, Henini M and Beaumont S P.

**Energy dependence of the quasiparticle lifetime in a 2DES**

Physica E, vol.6, no.1-4, pp.327-30, February 2000.

Hill R J A, Stoddart S T, Main P C, Eaves L, Benedict K A and Henini M.

**Landau-level spectroscopy of a two-dimensional electron system by tunnelling through a quantum dot**

Physical Review Letters, vol.84, no.4, pp.729-32, 24 January 2000.

Main P C, Thornton A S G, Hill R J A, Stoddart S T, Ihn T, Eaves L, Benedict K A and Henini M.

**Marge:** *Homer? Where are you?*

**Homer:** (from beyond) *Uh, I'm somewhere where I don't know where I am.*

**Marge:** *Do you see towels? If you see towels, you're probably in the linen closet again.*

**Homer:** (from beyond) *Just a second. No, it's a place I've never seen before.*

**Selma:** *Ah, the shower!*

... **Lisa:** *Well, where's my Dad?*

**Prof. Frink:** *Well, it should be obvious to even the most dim-witted individual who holds an advanced degree in hyperbolic topology, that Homer Simpson has stumbled into...the third dimension. Here is an ordinary square... (draws on blackboard)*

**Chief Wiggum:** *Whoa, whoa. Slow down, egghead!*

**Prof. Frink:** *...but suppose we extend the square beyond the two dimensions of our universe along the hypothetical 'Z' axis, there. (draws a wireframe cube on the blackboard...everyone gasps)*

**Prof. Frink:** *This forms a three-dimensional object known as a 'cube', or a 'Frinkahedron' in honour of its discoverer.*

**Homer:** (from beyond) *Help me! Are you helping me, or are you going on and on?*

**Prof. Frink:** *Oh, right. And, of course, within, we find the, er, doomed individual.*

—The Simpsons in “Homer<sup>3</sup>”.

# Chapter 1

## Basics

### 1.1 Introduction

When a classically-behaving object encounters a potential barrier it cannot pass the barrier unless it has energy greater than the potential height of the barrier.

An object that behaves quantum mechanically, on the other hand, such as the electron, will always have some probability to pass the barrier, even when its energy is less than the barrier height. When an electron of energy  $E$  passes a barrier of potential height  $V > E$  the electron is said to *tunnel* through the barrier. The probability that tunnelling occurs decreases exponentially with decreasing electron energy, and with increasing barrier height and thickness.

If another potential barrier is added, so that a potential well is formed between the two barriers, an electron can reside in one of the *quasi-bound* states of the well for a time before it tunnels out of the well via one of the barriers. The probability for tunnelling through this double barrier system increases significantly if the energy of the incident electron matches that of one of the quasi-bound states in the well. This phenomenon is known as *resonant tunnelling*.

### 1.1.1 Resonant tunnelling in solid state devices

The study of tunnelling phenomena in solid state physics has a long history in well-known systems such as the Si/SiO<sub>2</sub> structures that currently dominate the field of commercially produced integrated circuits, and in the metal/metal-oxide structures used, for example, in the superconducting Josephson tunnel junction.

However, research into solid state *resonant* tunnelling structures has been dominated to date by the III-V semiconductors. Primarily this is because there exist groups of III-V materials that have almost exactly the same lattice constant; examples are the GaAs and (AlGa)As semiconductors (lattice constant at room temperature,  $a = 5.65 \text{ \AA}$ ), In<sub>*x*</sub>Ga<sub>1-*x*</sub>As and In<sub>*x*</sub>Al<sub>1-*x*</sub>As ( $a = 5.65 + 0.40x \text{ \AA}$ ), and InAs and AlSb ( $a = 6.05 \text{ \AA}$  and  $6.14 \text{ \AA}$  respectively). This allows very thin epitaxial films of, for example, GaAs and (AlGa)As to be grown on top of one another by a modern growth technique such as molecular beam epitaxy (MBE) or metal-organic chemical vapour deposition (MOCVD), with minimal disturbance to the continuity of the crystal lattice. High purity, reproducible layers can be grown this way, with precisely controlled thicknesses (approaching the atomic scale) and sharp interfaces between the layers. Because the band gap is different in the different material layers there is a change in the energy of the conduction band at the interface, presenting a potential step for the electrons.

To observe resonant tunnelling in a real device the de Broglie wavelength of the electrons striking the barriers should be of the order of, or greater than, the size of the quantum well. This is equivalent to saying that the range of the incident electrons' energies should be less than the energy level separation of the quasi-bound states in the well. Semiconductors are therefore ideally suited to producing resonant tunnelling devices, since the electron carrier concentrations are relatively low (compared to metals) and are controllable by the addition of dopants to the semiconductor. The best results are usually achieved at low temperatures,  $T \sim 4 \text{ K}$ . At higher temperatures, phonons scatter the electrons inelastically causing decoherence of the electron wave function in and around the well.

The first observation of resonant tunnelling in a solid state structure was

made by Chang, Esaki and Tsu (1974). They observed resonant tunnelling in a double barrier structure made by sandwiching a thin planar layer of GaAs between two layers of (AlGa)As, grown by MBE. The thickness of the (AlGa)As barrier layers and the width of the GaAs well were of the order of a few tens of angstroms. By applying a voltage across the structure they were able to vary the energy of the quasi-bound states relative to the energy of the electrons incident on the barriers. They observed peaks in the tunnelling current whenever the voltage was such that the energy of the electrons striking the barrier coincided with that of a quasi-bound state in the well.

### 1.1.2 Quantum dots

Since 1974, advances in growth and fabrication techniques have allowed the creation of structures that confine the electrons in more than one dimension, to two or all three dimensions (Kelly 1995). For example, by chemically or physically etching a planar double barrier structure, *quantum wires* and *quantum dots* can be fabricated in which the electrons are confined to one (1D) and zero (0D) dimensions respectively [see, for example Reed *et al.* (1988), Dellow *et al.* (1992), Sivan *et al.* (1994), Wang *et al.* (1994) and Austing *et al.* (1995, 1997b)].

The semiconductor quantum dot (QD) is often regarded as an ‘artificial atom’ in the sense that the bound electron states of the QD take the form of a set of discrete atom-like orbitals. Unlike atoms however, the confining potential of a QD takes the form of a three-dimensional box, rather than the central nuclear potential of the atom. In addition, electrons in a QD are subject to scattering by phonons in the crystal lattice.

Modern lithographic techniques have made possible the fabrication of QDs with sizes as small as 50-100 nanometres (Meirav and Foxman 1996). Resonant tunnelling has been used as a tool to reveal a variety of properties of the QDs, such as the spectrum of single electron orbitals (Reed *et al.* 1988, Sivan *et al.* 1994, Smoliner *et al.* 1994, Schmidt *et al.* 1995), single electron charging (Meirav and Foxman 1996) and atomic-like rules for the filling of the QD

orbitals (Tarucha *et al.* 1996, Austing *et al.* 1997b, Tarucha 1998).

One problem with the etching process used to define such QDs is that it introduces defects into the crystal lattice. Recently, an alternative way of producing nanometer-sized QDs has been developed based on crystal growth techniques (Nötzel 1992). This method relies on there being a *lattice mismatch* between two semiconductors. When one is grown upon the other, by either of the modern growth techniques (MBE or MOCVD), some material combinations result in three-dimensional island growth rather than layer-by-layer growth. Examples are (InGa)As/GaAs, InP/InGaP and Ge/Si (see the review by Bimberg *et al.* (1998) and references therein).

This thesis is concerned specifically with the InAs/(AlGa)As combination. As InAs is deposited on (AlGa)As, the lattice mismatch between the two materials causes a build up of strain in the crystal lattice. As more InAs is deposited, it eventually becomes energetically more favourable for the InAs to continue to grow in the form of three-dimensional ‘islands’ rather than as a uniform film. This is known as *Stranski-Krastanow* growth. When the InAs islands are capped with a second layer of (AlGa)As, the islands form isolated potential wells in which the electrons are confined in all three dimensions. Transmission electron microscopy studies have shown that defect-free QDs can be grown consistently this way (Nötzel 1992). These QDs typically have base sizes of the order of 10 nm, comparable heights, and a surface density typically of the order of  $10^{14}$  to  $10^{15}$  QDs per square metre (Itskevich *et al.* 1996, Bimberg *et al.* 1998).

Although most research on such ‘self-assembled’ QDs has focussed on their optical properties, reflecting their promising applications in the field of semiconductor lasers (Bimberg *et al.* 1998), there have been a number of experiments to study resonant tunnelling through them.

### 1.1.3 Resonant tunnelling via quantum dot states

Resonant tunnelling via the zero-dimensional states associated with impurities within a potential barrier has been studied for many years in metal-oxide devices; see, for example, Lambe and Jaklevic (1968), Koch and Hart-

stein (1985) and Bending and Beasley (1985) and more recently in GaAs/(AlGa)As systems, Dellow *et al.* (1992), Sakai *et al.* (1993), Geim *et al.* (1994a, 1994b), Deshpande *et al.* (1996), Schmidt *et al.* (1996b, 1997), Itskevich *et al.* (1998), Vitusevich *et al.* (2000), Holder *et al.* (2000), Deshpande *et al.* (2000) and Main *et al.* (2000b).

The first experiments on resonant tunnelling through self-assembled QDs were performed by Itskevich *et al.* (1996), Narihiro *et al.* (1997) and Suzuki *et al.* (1997), who studied single tunnel barrier devices incorporating InAs QDs grown in the centre plane of an (AlGa)As or AlAs barrier layer. All groups observed oscillations in the current-voltage characteristics of their devices which they attributed to resonant tunnelling via QD states. Remarkably, given the large number of QDs in each device (of the order of a million), they observed a number of isolated features at low-voltage which they could attribute to *tunnelling via single states of individual* QDs, rather than an ensemble average.

#### 1.1.4 Thesis overview

Following work by Itskevich *et al.* (Itskevich *et al.* 1996, Thornton 1998b), chapters 3, 4 and 5 present experiments in which a single zero-dimensional state of an individual self-assembled QD is used as a spectroscopic probe of the local density of states of a two dimensional electron system (2DES). When a magnetic field is applied perpendicular to the barrier layer, Landau levels are directly observed and it is shown how this observation may be used to obtain quantitative information on the lifetime of quasi-holes deep below the Fermi energy. In addition, an enhancement of the electron  $g$  factor is observed in the 2DES at high magnetic fields and complex temperature dependent features are observed in the current-voltage characteristic.

Chapter 6 demonstrates the use of a new type of device, incorporating a novel lateral gating technology (Austing *et al.* 1997a, Austing *et al.* 1999), to address a particular InAs QD from an ensemble consisting of many hundreds of QDs. A recently developed magneto-tunnelling technique (Sakai *et al.* 1993, Mori *et al.* 1995, Narihiro *et al.* 1997, Vdovin *et al.* 2000) is used to

image the  $k$ -space wave functions of a single QD.

The remainder of this chapter discusses in more detail the relevant material properties of GaAs, (AlGa)As and InAs, moving onto a more rigorous treatment of the resonant tunnelling process and the features of low-dimensional electron systems. Chapter 2 covers the design of the samples and discusses the techniques used to fabricate them and measure their properties.

### 1.1.5 Note about axes convention

Since this thesis deals with structures grown in layers, it is convenient to define an axes convention such that the  $z$  axis lies perpendicular to the growth plane, while the  $x$  and  $y$  axes lie parallel to the growth plane. This convention will be used throughout the thesis.

## 1.2 Basic concepts

This section gives a brief review of the basic concepts upon which this thesis is built. More thorough introductions can be found in the books by Ashcroft and Mermin (1976), Kittel (1996), or Davies (1998).

### 1.2.1 One electron model

The basis for the discussion of most of the results in this thesis is the *one electron model*. In this approximation it is assumed that we can treat an electron in a crystal as an independent particle, moving in the potential due to the fixed ions and the *average* potential produced by all the other electrons; no attempt is made to consider the interactions between *individual* electrons. In the simplest variation of this approximation, the Hartree approximation, the wave function of the electron system  $\Psi(\mathbf{r}_1, \mathbf{r}_2, \dots, \mathbf{r}_n)$  is written as a simple product of one-electron wave functions,  $\psi_i(\mathbf{r})$  (Davies 1998). Each one-electron wave function obeys a one-electron Schrödinger equation,

(Davies 1998, Ashcroft and Mermin 1976)

$$\hat{\mathcal{H}}\psi_i = \left( \frac{\hat{\mathbf{p}}^2}{2m} + U(\mathbf{r}) \right) \psi_i(\mathbf{r}) = \epsilon\psi_i(\mathbf{r}), \quad (1.1)$$

where  $\hat{\mathbf{p}}$  is the momentum operator,  $m$  is the free-electron mass and  $U(\mathbf{r})$  includes the potentials due to the crystal ions and the time-averaged potential due to the other electrons.

Because  $U(\mathbf{r})$  is periodic in a crystal, the stationary solutions to the one-electron Hamiltonian for a perfect crystal are Bloch functions, (Ashcroft and Mermin 1976)

$$\psi_{n\mathbf{k}}(\mathbf{r}) = u_{n\mathbf{k}}(\mathbf{r})e^{i\mathbf{k}\cdot\mathbf{r}}, \quad (1.2)$$

with energies

$$\hat{\mathcal{H}}\psi_{n\mathbf{k}} = \epsilon_{n\mathbf{k}}\psi_{n\mathbf{k}}, \quad (1.3)$$

where  $u_{n\mathbf{k}}(\mathbf{r})$  has the periodicity of the crystal lattice. The band structure,  $\epsilon_{n\mathbf{k}}$ , and other properties of the relevant materials are reviewed in the next section.

## 1.2.2 Semiconductors

The devices presented in this thesis are made from alternating layers of the semiconductors GaAs, (AlGa)As and InAs, grown by MBE.

The characteristic feature of a semiconductor is the gap in the allowed one-electron energy levels,  $\epsilon_{n\mathbf{k}}$ , at the Fermi energy. The states below the gap form the valence bands and are fully occupied by electrons at  $T = 0$  K, while the states above form the conduction bands and are completely unoccupied at  $T = 0$  K.

### Doping

In order to produce carriers, impurities called dopants can be added to the semiconductor crystal. In MBE and MOCVD these dopants are added during growth. The dopants introduce states into the gap close to the valence band

in the case of ‘p-type’ impurities, or the conduction band in the case of ‘n-type’ impurities. The impurity states are then easily ionised to produce free carriers in the neighbouring band. With very high impurity concentrations, the wavefunctions of neighbouring impurity states may overlap sufficiently to produce an impurity band of de-localised states which allows conduction at  $T = 0$  K (metallic behaviour). This regime will not be considered here, however.

In this thesis, only n-type doping is considered. For the GaAs/(AlGa)As system, the n-type dopant is usually silicon.

MBE or MOCVD growth techniques allow the doping of individual crystal layers to be highly selective. This means that the carrier densities and conductivity of the layers can be precisely controlled. Such a facility is important for the devices presented in this thesis.

Several minima or ‘valleys’ occur in the energy of the lowest conduction band as a function of the Bloch wave vector,  $\mathbf{k}$ . By n-type doping, the valley states can be populated with electrons, with the lowest energy valleys populated first.

## Heterostructures

A *heterostructure* is a material made from a combination of two or more semiconductor crystals; for example, a layer of (AlGa)As grown upon a layer of GaAs. At the interface, or *heterojunction*, between the two semiconductors there is a discontinuous change in the band gap. This means that there is a step change in the energies of the conduction band and valence band across the junction.

### 1.2.3 Effective mass approximation

The presence of impurities in a semiconductor crystal spoils the periodicity of the crystal lattice so that the stationary solutions to the one-electron Hamiltonian (equation 1.1) are no longer Bloch functions. An interface between two semiconductors in a heterostructure, or an externally applied

electric field has the same effect.

Instead of trying to find exact solutions for the stationary states in such a system, it is often possible, and more illuminating, to work within the *effective mass approximation*. In this approximation, solutions are found to a simplified Schrödinger equation, in which the periodic crystal potential is ignored, provided that we use a modified mass for the electrons.

We write the stationary solutions to the system as a linear combination of Bloch functions. In one-dimension, (Davies 1998)

$$\psi(x) = \sum_n \int_{-\pi/a}^{\pi/a} \tilde{\chi}(k) u_{nk}(x) e^{ikx} \frac{dk}{2\pi}. \quad (1.4)$$

For conduction electrons in a ‘simple’ band such as the non-degenerate valley centred on  $\mathbf{k} = 0$  in GaAs ( $\Gamma$  valley),  $\psi(x)$  can be approximated as a Bloch function multiplied by an envelope function, (Davies 1998)

$$\psi(x) \approx u_{n0} \chi(x). \quad (1.5)$$

In the above equation,  $u_{n0}$  is the periodic part of the  $\mathbf{k} = 0$  Bloch function, and the envelope function,  $\chi(x)$ , is the Fourier transform of  $\tilde{\chi}(k)$ . The above approximation relies on the perturbation to the periodic crystal potential being small compared to the band gap, so that only one band—the conduction band—contributes significantly to the sum in equation 1.4, and that  $\chi(x)$  varies slowly on the scale of the lattice constant. With this approximation, the original Schrödinger equation for  $\psi(x)$  can now be re-written as an eigenvalue equation involving  $\chi(x)$  alone. In particular, for states with energies within a few meV of the  $\Gamma$  valley minimum, where the dispersion relation is approximately parabolic, the eigenvalue equation for the envelope function,  $\chi(x)$ , can be written in the form of a Schrödinger equation,

$$\left( \frac{-\hbar^2}{2m^*} \nabla^2 + U(\mathbf{r}) + E_\Gamma \right) \chi(\mathbf{r}, t) = i\hbar \frac{\partial}{\partial t} \chi(\mathbf{r}, t) = \epsilon \chi(\mathbf{r}, t), \quad (1.6)$$

where  $m^*$  is the *effective mass* and  $E_\Gamma$  is the energy of the bottom of the  $\Gamma$  band. This is the effective mass approximation and will be used as the basis for discussion of the results in this thesis. The envelope function,  $\chi(x)$ , will

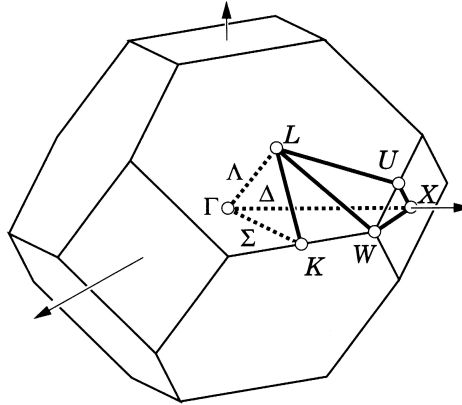


Figure 1.1: Brillouin zone of the face-centre cubic crystal, labelling the points of high symmetry. From Davies (1998).

usually be referred to simply as ‘the wave function’ and often written as  $\psi$  with the understanding that the effective mass approximation is being used.

## 1.3 Properties of GaAs, (AlGa)As and InAs crystals

This section gives a short review of the crystal properties of GaAs, (AlGa)As and InAs that are most relevant to the experiments in this thesis. Many of the material parameters given in this section are under constant revision as new measurements are made. The data given here are taken from a recent review of III-V band parameters by Vurgaftman *et al.* (2001).

### 1.3.1 GaAs

The GaAs crystal is a zinc blende structure. It may be viewed as consisting of two interpenetrating face-centre cubic (FCC) sub-lattices, each with lattice constant  $a$  (Ashcroft and Mermin 1976). The two sub-lattices are displaced from one another by  $(\frac{1}{4}, \frac{1}{4}, \frac{1}{4})a$ . The Ga atoms occupy the sites on one of the sub-lattices, and As occupies the sites on the other.

The lattice constant is  $a = 0.565325 + 3.88 \times 10^{-6}(T - 300 \text{ K}) \text{ nm}$ , where

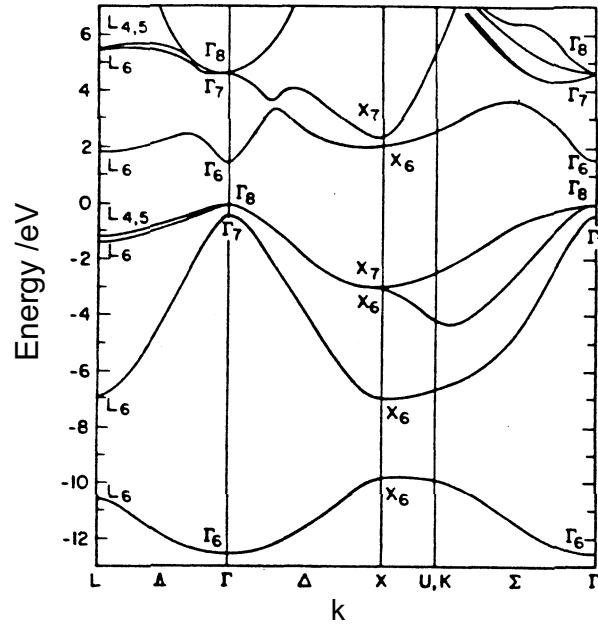


Figure 1.2: Calculated band structure of GaAs. From Chelikowsky and Cohen (1976).

$T$  is the temperature in Kelvin. The bond length is  $\frac{\sqrt{3}}{4}a \approx 0.24$  nm. The reciprocal lattice is body-centred cubic with a conventional unit cell of size  $b = 4\pi/a$ . The first Brillion zone is a truncated octahedron as depicted in figure 1.1. The band structure for GaAs is shown in figure 1.2. It can be seen from this figure that the lowest point of the conduction band occurs at the  $\Gamma$  point,  $\mathbf{k} = 0$ . Therefore, in n-type doped GaAs, the conduction electrons lie in the  $\Gamma$  valley. The dispersion relation,  $E(\mathbf{k})$ , is approximately parabolic and isotropic for states within a few meV of the conduction band minimum,

$$E(\mathbf{k}) \approx E(0) + \frac{\hbar^2 k^2}{2m^*}, \quad (1.7)$$

where the effective mass  $m^* \approx 0.067m_e$  for the  $\Gamma$  point at low temperature, and  $m_e$  is the free electron mass. At higher energies, the effective mass becomes dependent on the magnitude and direction of  $\mathbf{k}$ .

Satellite  $X$  and  $L$  valleys lie about 480 and 290 meV above the bottom of the  $\Gamma$  valley respectively and remain unpopulated for the doping concentrations considered in this thesis. The band gap between the bottom of the conduction band and the top of the valence band is 1.42 eV at room temperature, increasing to 1.52 eV below about 40 K.

### 1.3.2 AlAs

The AlAs lattice is also a zinc-blende structure with a lattice constant of  $a = 0.56611 + 2.90 \times 10^{-6}(T - 300 \text{ K}) \text{ nm}$ . The lowest energy in the conduction band occurs close to the  $X$  points rather than at the  $\Gamma$  point as in GaAs. There are six equivalent  $X$ -valleys centred on  $\mathbf{k} = (\pm 0.903, 0, 0)b$ ,  $(0, \pm 0.903, 0)b$  and  $(0, 0, \pm 0.903)b$ . As in the case of the  $\Gamma$  valley, a parabolic dispersion relation similar to equation 1.7 can be used, except that the effective mass is now dependent on the direction of the crystal momentum. For example, for the valley centred on the point  $\mathbf{k} = (0, 0, 0.903)b$ ,

$$E(\mathbf{k}) \approx E([0, 0, 0.903]b) + \frac{\hbar^2(k_x^2 + k_y^2)}{2m_{\Gamma}^*} + \frac{\hbar^2(k_z - 0.903b)^2}{2m_{\text{L}}^*}, \quad (1.8)$$

where  $m_{\text{L}}^* = 0.97m_e$  and  $m_{\Gamma}^* = 0.22m_e$  at low temperature. The effective mass at the  $\Gamma$  point is  $0.15m_e$  at low temperature.

The highest energy in the valence band lies at the  $\Gamma$  point, so the band gap in AlAs is indirect. The indirect  $\Gamma$ - $X$  band gap is 2.24 eV at low temperature. The  $\Gamma$ - $\Gamma$  energy gap is 3.10 eV at low temperature.

### 1.3.3 (AlGa)As

The alloy (AlGa)As has the same crystal structure as that of GaAs, except that a fraction  $x$  of Ga atoms have been replaced by Al atoms. Bloch's theorem cannot be applied directly to (AlGa)As since the translational symmetry is broken by the random substitution of the Al atoms. Instead, the crystal is usually modelled by treating it as a perfect 'virtual' crystal whose properties lie somewhere between that of GaAs and AlAs, plus some imperfections which can be treated with perturbation theory. The properties of the virtual crystal are determined by interpolating between those of GaAs and AlAs. The lattice constant,  $a$ , of  $\text{Al}_x\text{Ga}_{1-x}\text{As}$  is given, to a first approximation, by linearly interpolating the lattice constants of AlAs and GaAs. This gives the lattice constant as a function of the aluminium fraction  $x$ ,

$$a(x) = (0.56533 + 0.00078x) \text{ nm} \quad (1.9)$$

at room temperature. The difference in the lattice constant,  $a$ , between  $x = 0$  and  $x = 1$  (i.e. between the GaAs and AlAs crystals) is less than  $0.01a$ . Hence the interfaces between GaAs and (AlGa)As can be made extremely smooth, with few defects.

For high values of  $x$ , the lowest energy states in the conduction band lie at the  $X$  points as in AlAs. As the aluminium content is reduced, the  $X$  valley states move up in energy relative to the  $\Gamma$  valley states. For  $x < 0.45$ , the  $X$  states lie above the  $\Gamma$  states as is the case in GaAs. For all values of  $x$ , the highest energy states in the valence band lie at the  $\Gamma$  point.

The band gap as a function of  $x$  is assumed to follow the form

$$E_g = (1 - x)E_g^{\text{GaAs}} + xE_g^{\text{AlAs}} - x(1 - x)C. \quad (1.10)$$

The first two terms represent a simple linear interpolation between the band gaps of AlAs and GaAs. The last term allows for some deviation from a linear interpolation, known as *bowing*. For the  $\Gamma$  conduction band, the bowing parameter  $C$  is,

$$C = -0.127 + 1.310x \text{ eV}, \quad (1.11)$$

and is assumed to be independent of temperature. For the  $X$  band,  $C = 0.055$ .

The effective mass of electrons in the  $\Gamma$  conduction band of (AlGa)As may be approximated by a linear interpolation of the AlAs and GaAs effective masses. This gives

$$m^*(x) = (0.067 + 0.083x)m_e \quad (1.12)$$

for  $\text{Al}_x\text{Ga}_{1-x}\text{As}$  at low temperature.

### 1.3.4 InAs

InAs has the same crystal structure as GaAs and AlAs and has a lattice constant of  $0.60583 + 2.74 \times 10^{-6}(T - 300 \text{ K}) \text{ nm}$ . The band gap is between the  $\Gamma$  points of the conduction band and the valence band and is 0.354 eV

at room temperature, increasing to 0.420 eV at low temperature. The bulk InAs effective mass is  $m^* = 0.026m_e$  at low temperature.

### 1.3.5 Band alignment at a heterojunction

Whilst the band gaps of the above materials are well known, it is more difficult to establish the exact alignment of the bands at a heterojunction. The band offsets given below have been derived from recommended values at low temperature, given by Vurgaftman *et al.* (2001). Note that the energies are given *relative to the bottom of the  $\Gamma$  conduction band in GaAs*.

The energy of the conduction band at the  $\Gamma$  point in  $\text{Al}_x\text{Ga}_{1-x}\text{As}$ , as a function of the fractional aluminium content,  $x$ , is

$$\Delta E_{\Gamma}(\text{eV}) = 1.18x - 1.44x^2 + 1.31x^3. \quad (1.13)$$

The conduction band energy at the  $X$  point in  $\text{Al}_x\text{Ga}_{1-x}\text{As}$  is

$$\Delta E_X(\text{eV}) = 0.46 - 0.33x + 0.06x^2. \quad (1.14)$$

The energy of the bottom of the  $\Gamma$  conduction band in bulk InAs is  $\Delta E_{\Gamma} = 0.89$  eV.

The band offsets between GaAs, AlAs and InAs are shown schematically in figure 1.3.

## 1.4 Two dimensional electron system

A quantum well in the conduction band is formed at an interface between undoped GaAs and n-type (AlGa)As (Davies 1998). Electrons liberated from the donor ions in the (AlGa)As cascade over the potential step at the junction until the chemical potentials on either side of the junction align at equilibrium (figure 1.4). This produces a separation of charge, with the electrons becoming trapped in a roughly triangular-shaped potential well at the junction. This type of potential well is formed in the devices that are

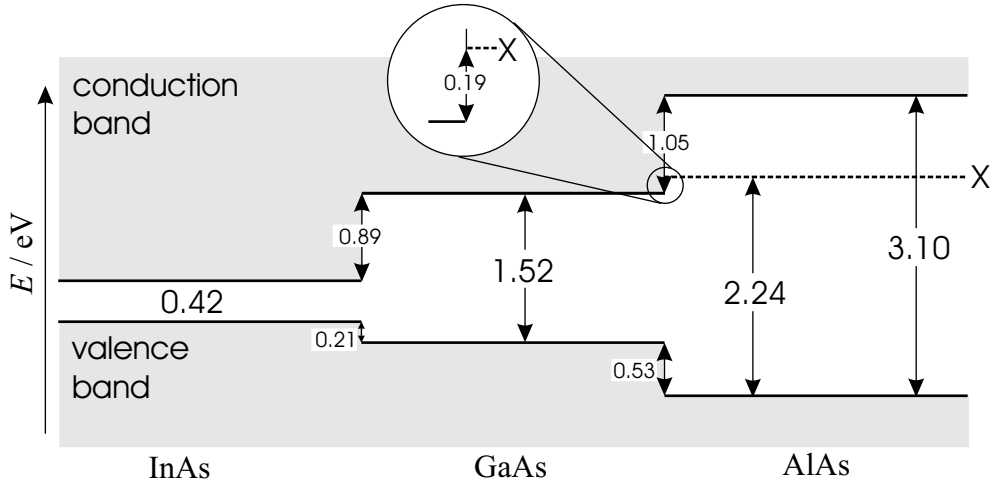


Figure 1.3: Alignment of the  $\Gamma$  conduction bands and valence bands of GaAs, AlAs and InAs at  $T = 0$  K. The  $X$  conduction band of AlAs is also shown as a dotted line. Data from Vurgaftman *et al.* (2001).

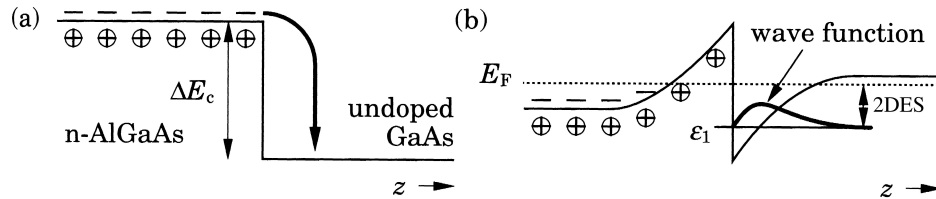


Figure 1.4: Schematic of the conduction band at a GaAs/(AlGa)As heterojunction, (a) before, and (b) after equilibrium has been achieved. From Davies (1998).

the subject of chapters 3, 4 and 5. However, in this case, the well is formed as a consequence of an externally applied voltage, though the profile of the well is fundamentally the same in both cases.

Electrons trapped in the well are free to move in the  $xy$  plane but motion in the  $z$  direction becomes restricted. Quantum mechanically, this means that the  $z$ -component of the kinetic energy is quantised so that it may only take values of  $E_j$  ( $j = 0, 1, 2, \dots$ ), whereas the  $x$  and  $y$  components can vary continuously. Within the effective mass approximation, the energy,  $E$ , of a bound electron relative to the bottom of the conduction band is thus given by

$$E = E_j + \frac{\hbar^2(k_x^2 + k_y^2)}{2m^*}. \quad (1.15)$$

Note that this equation assumes that there are no random potential fluctua-

tions in the well, which are invariably present in any real device. The effects of disorder are covered briefly in section 1.4.2.

A set of states that all have the same  $z$ -component of kinetic energy,  $E_j$ , is known as a *sub-band*. If the temperature is low enough and if the energy separation between  $E_1$  and  $E_0$  can be made larger than the Fermi energy,  $E_{F0} = E_F - E_0$ , then the electrons become trapped in the lowest ( $j = 0$ ) sub-band. Motion in the  $z$  direction now becomes impossible, since this requires an electron to enter a superposition with states of higher  $j$ . Thus the electrons are said to form a *two-dimensional electron system* (2DES).

The energy density of states (DOS) in a given 2D sub-band is a constant, (Davies 1998)

$$D(\epsilon) = \frac{m^*}{\pi\hbar^2}. \quad (1.16)$$

The number of electrons per unit area,  $n_s$ , is obtained by integrating the DOS between  $E_0$  and the Fermi energy,  $E_F$ . This gives

$$\begin{aligned} n_s &= \int_{E_0}^{E_F} D(\epsilon) d\epsilon \\ &= (E_F - E_0) \frac{m^*}{\pi\hbar^2}. \end{aligned} \quad (1.17)$$

### 1.4.1 Two dimensional system in a magnetic field

When a magnetic field,  $B$ , is applied along the  $z$  direction perpendicular to the plane of a 2DES, and an electric field is applied in the plane of the 2DES, say parallel to the  $x$  direction, then a Hall voltage,  $V_y$ , is developed in the  $y$  direction perpendicular to the applied electric field (Kittel 1996). Classically, the Hall voltage is simply proportional to the magnitude of  $B$  and the current flow,  $I_x$ . At sufficiently low temperatures however, the Hall voltage and the longitudinal resistivity,  $\rho_{xx}$ , show structure periodic in  $1/B$  known as *Shubnikov-de Haas* oscillations (von Klitzing 1986). Wherever there is a minima in  $\rho_{xx}$ , there is a corresponding plateau in  $\rho_{xy} = V_y/I_x$ ; this is known as the *Quantum Hall Effect*. Both effects are the product of the quantisation of the orbital motion of the electrons in the magnetic field. This gives rise to a drastic modification of the spectrum of single particle energy

levels in the 2DES. The (quasi) continuous spectrum of energy levels in each sub-band is replaced by a set of discrete, highly degenerate levels known as Landau levels. The energy separation between the levels is proportional to the magnetic field,  $B$ , so that as the magnitude of  $B$  is increased, the Landau levels pass through the Fermi level consecutively. This is the origin of the periodicity in  $\rho_{xx}$  and  $\rho_{xy}$  with  $B$ . In the next section, expressions are obtained for the one-electron energy levels and wave functions of the 2DES in a magnetic field  $B \parallel z$ .

### Landau levels

In a magnetic field, the total momentum of a particle is the sum of its kinetic momentum,  $\mathbf{p}_{\text{kin}}$  (its mass multiplied by its velocity), plus a potential momentum  $q\mathbf{A}$ , where  $q$  is the charge on the particle. The total momentum of an electron in a magnetic field is thus (McMurry 1993)

$$\mathbf{p} = \mathbf{p}_{\text{kin}} - e\mathbf{A}. \quad (1.18)$$

The corresponding quantum mechanical operator for the total momentum is  $\hat{\mathbf{p}} = -i\hbar\nabla$ . The one-electron Hamiltonian is therefore (McMurry 1993)

$$\hat{\mathcal{H}} = \frac{1}{2m^*}(-i\hbar\nabla + e\mathbf{A})^2 + U. \quad (1.19)$$

The eigenfunctions of this Hamiltonian are simplest in a Landau gauge. Choosing  $\mathbf{A} = (0, Bx, 0)$ , the Schrödinger equation is (McMurry 1993)

$$\frac{-\hbar^2}{2m^*} \left[ \frac{\partial^2}{\partial z^2} + \frac{\partial^2}{\partial x^2} + \left( \frac{\partial}{\partial y} + \frac{ieB}{\hbar}x \right)^2 + U(\mathbf{r}) \right] \psi(\mathbf{r}) = \epsilon\psi(\mathbf{r}) \quad (1.20)$$

For the moment the effect of the intrinsic spin of the electron will be ignored, except for the fact that it doubles the number of electron states. However, in a magnetic field there is a difference in energy between spin states parallel and anti-parallel to the field. This will be covered in section 1.6.

In a two-dimensional electron system, assuming there is no disorder, the confinement potential,  $U$ , is a function of  $z$  only and therefore  $\psi(x, y, z)$  can

be factored as  $\psi(x, y, z) = \phi(x, y)\chi(z)$ . The stationary solutions for  $\phi$  are (McMurry 1993)

$$\phi_{nk}(x, y) = AH_n\left(\frac{x - x_0}{l_B}\right) \exp\left[-(x - x_0)^2/2l_B^2\right] \exp(iky), \quad (1.21)$$

where  $n = 0, 1, 2, \dots$ ,  $\omega_c = |eB/m^*|$  is the cyclotron frequency and  $H_n(\dots)$  is the Hermite polynomial function.  $A$  is a normalisation factor and  $x_0 = -l_B^2 k$ .  $l_B = \sqrt{\hbar/m\omega_c} = \sqrt{\hbar/e|B|}$  is the magnetic length.  $l_B(B = 1 \text{ T}) \approx 26 \text{ nm}$ . The corresponding energy eigenvalues form a set of discrete energy levels,  $\{E_n\}$ , known as *Landau levels*, (McMurry 1993)

$$E_n = E_j + (n + \frac{1}{2})\hbar\omega_c, \quad (1.22)$$

where  $E_j$  is the energy of the  $j$ th sub-band (section 1.4). In a 2DES only the  $j = 0$  state is occupied. Note that the energy depends only on the quantum number  $n$  and not on  $k$ , so the energy levels are highly degenerate.

The number of electrons that can populate each Landau level is determined by the number of  $k$ -states available per Landau level. Approximating the 2DES by a rectangle of size  $L_x \times L_y$  and using periodic boundary conditions in the  $y$  direction, we find that the allowed values of  $k$  form a set of discrete values, spaced  $\Delta k = 2\pi/L_y$  apart. The wave functions,  $\phi_{nk}$ , take the form of stripes running parallel to the  $y$  direction. Each stripe is centred on  $x = x_0 = -l_B^2 k$ . Since the size of the sample,  $L_x$ , restricts the range of  $x_0$ , this limits the number of  $k$ -states available per Landau level. This results in  $L_x/\Delta x_0 = (e/h)BL_xL_y$  allowed  $k$ -states per Landau level. The number of electron states per Landau level is a factor of 2 larger due to spin. However, it is usual to count the two spin states as different levels, so the number of electron states per spin-split Landau level, per unit area is (McMurry 1993)

$$n_{\text{LL}} = \frac{e}{h}B. \quad (1.23)$$

The *filling factor*,  $\nu$ , is defined as the number of occupied Landau levels, counting the two spins as separate levels,

$$\nu = \frac{n_s}{n_{\text{LL}}}. \quad (1.24)$$

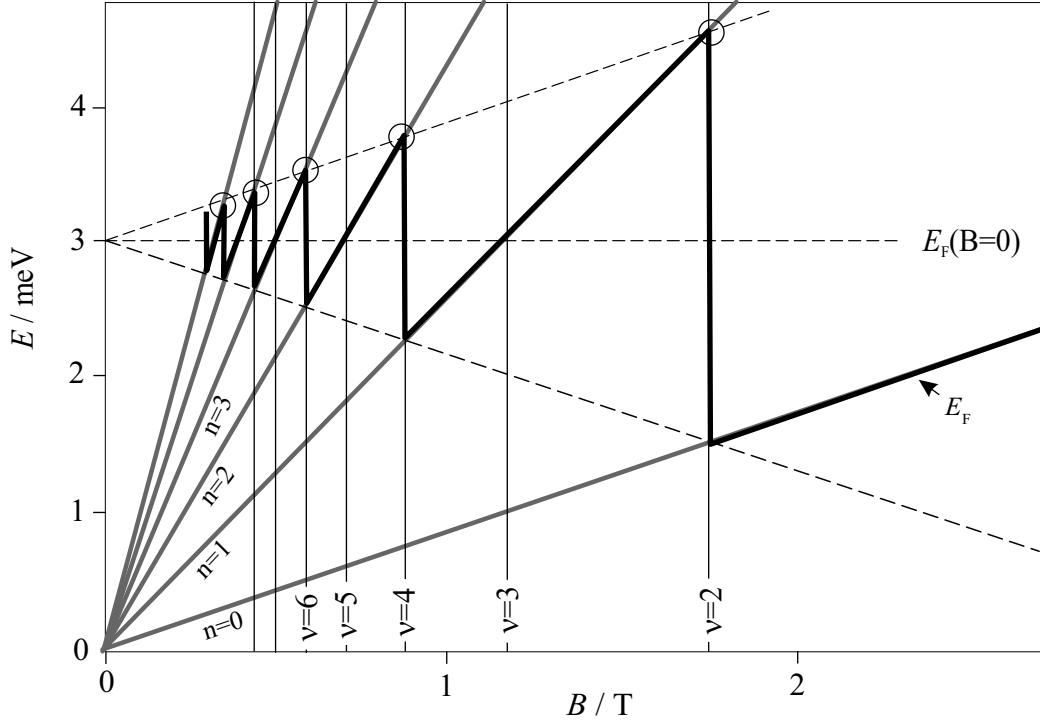


Figure 1.5: Graph of the Landau level energy  $\epsilon = (n + \frac{1}{2})\hbar\omega_c$  versus  $B$  (ignoring spin-splitting) for a 2DES in GaAs, with a Fermi energy at  $B = 0$  of 3 meV. The thin vertical lines show the magnetic field positions of integer filling factor, calculated according to equation 1.24, using an electron density of  $n_s = 8.4 \times 10^{14} \text{ m}^{-2}$  calculated from the Fermi energy at  $B = 0$  (equation 1.17). The thick black line shows how the position of the Fermi level varies with  $B$ . Circles mark the points where each Landau level depopulates.

Whereas the density of states is a constant at  $B = 0$  (equation 1.16), for  $B > 0$  equation 1.22 shows that it takes the form of a series of delta functions, (McMurry 1993)

$$D(\epsilon) = \sum_n \delta(\epsilon - E_n), \quad (1.25)$$

where the delta-functions are separated in energy by the *cyclotron energy*,  $\hbar\omega_c$ . As  $B$  increases, the cyclotron energy increases. Since the Fermi level must lie within occupied states, it is ‘pinned’ to the energy of the highest occupied Landau level. Therefore, as  $B$  increases, so  $E_F$  must increase along with it, tracking with the energy of the highest occupied Landau level. However, because the degeneracy,  $n_{LL}$ , of each Landau level also increases with  $B$ , and since the total number of electrons in the 2DES is conserved,

the occupancy of the Landau level at the Fermi level must *decrease* with increasing  $B$ . As  $B$  is increased further, eventually the occupancy reaches zero and the Fermi level then moves down to the next lowest lying Landau level. In other words, there is a step change in the Fermi energy whenever

$$\frac{1}{B} = \frac{e}{h} \frac{1}{n_s} \nu, \quad (1.26)$$

where  $\nu = 2, 4, 6, \dots$ . The result is that, as  $B$  is increased, the Fermi energy oscillates about its value at  $B = 0$ , with a period that is constant in  $1/B$ .

Figure 1.5 shows a graph of the Landau level energy,  $\epsilon = (n + \frac{1}{2})\hbar\omega_c$ , versus  $B$  (ignoring spin-splitting) for a 2DES in GaAs, with a Fermi energy at  $B = 0$  of 3 meV. The thin vertical lines show the magnetic field positions of integer filling factor, calculated according to equation 1.24, using an electron density of  $n_s = 8.4 \times 10^{14} \text{ m}^{-2}$  calculated from the Fermi energy at  $B = 0$  (equation 1.17). The thick black line shows how the position of the Fermi level varies with  $B$ . Circles mark the points where each Landau level depopulates.

### 1.4.2 Scattering effects

In any real device the potential well forming the 2DES is not perfect. There is an additional random ‘disorder’ potential due to surface roughness at the heterojunction, impurities and lattice strain effects. In most devices, efforts are made to keep this disorder potential small enough so that it can be treated as a small perturbation. This requires that the materials on either side of the junction are grown carefully to avoid lattice defects and unwanted impurities. Donor impurities are spatially separated from their liberated electrons (‘modulation doping’).

With the addition of the disorder potential a 2DES no longer has a uniform sheet density. The electron waves are scattered and interference between the scattered waves produces localised areas of higher than average and lower than average probability as a function of both spatial distance and energy.

Since the electron density is no longer constant over the area of the 2DES, it is more useful to use a *local* energy density of states (LDOS) to describe

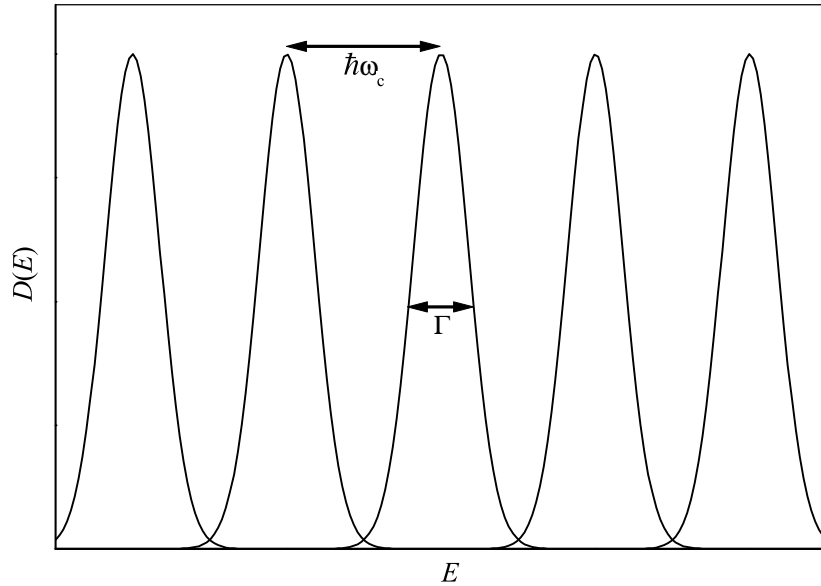


Figure 1.6: The Landau level energy density of states in a disordered 2DES. States near the extremities of each peak are *localised* states while states forming the core of each peak are *extended* states.

the system. The LDOS is defined as (Davies 1998)

$$D(\epsilon, \mathbf{r}) = \sum_n |\psi_n(\mathbf{r})|^2 \delta(\epsilon - E_n), \quad (1.27)$$

where  $\psi_n$  are the stationary solutions of a Hamiltonian that includes the disorder potential. The local charge density in the 2DES can then be obtained by integrating the LDOS from the bottom of the sub-band to the Fermi energy.

In addition, the Coulomb interaction between individual electrons means that the one-electron levels discussed in the previous section are not strictly stationary states. Instead, electrons scatter from one such state to another (limited by the exclusion principle). Assuming that the scattering rate is small enough so that we can still retain an independent particle picture,\* the effect is to introduce an uncertainty (or ‘broadening’) into the energy of

---

\*This is the subject of Fermi-liquid theory. For a discussion about why an independent particle picture remains a valid approximation in the presence of electron-electron scattering see Ashcroft and Mermin (1976) or Pines and Nozières (1989).

the one-electron levels.

### Landau levels in the presence of scattering

The effect of scattering (by defects, impurities, electron-electron interaction et cetera) is to break the degeneracy of the states within each Landau level. As shown in figure 1.6, the delta function peaks in the DOS are broadened into peaks with finite energy width,  $\Gamma$ . States near the extremities of each peak are *localised* states in which the amplitude of the wave function falls off exponentially away from a localisation site. The core of each peak consists of *extended* states whose wave functions spread over the whole region of the 2DES (von Klitzing 1986). When the Fermi level lies within extended states, the 2DES can conduct an electric current. If the Fermi level lies within localised states however, the conductivity is zero. For this reason, the parts of the energy level spectrum between the extended states are known as *mobility gaps*.

## 1.5 Zero dimensional electron system

In a zero-dimensional system, the electrons are confined in all three dimensions. The one-electron energy level spectrum of such a system takes the form of a set of truly discrete energy levels, like that of an atom.

### 1.5.1 InAs quantum dot

The lattice constant of InAs is approximately 7% greater than the lattice constants of GaAs and AlAs. When InAs is deposited on GaAs or AlAs, therefore, (by MBE or MOCVD) the InAs is bi-axially compressed and a significant strain develops at the interface. Beyond a critical thickness of InAs, the growth mode switches from layer-by-layer growth to the formation of three-dimensional islands. When such InAs islands are covered by GaAs or AlAs they act as three-dimensional potential wells, known as (self-assembled) quantum dots (QDs), within the GaAs or AlAs matrix. The

growth of InAs QDs will be covered in more detail in chapter 2.

Calculating the energy levels of such InAs QDs is complicated primarily by the presence of the significant inhomogeneous strain in the crystal lattice, but also by the possibility of Al and Ga atoms from the surrounding matrix migrating into the QDs during and after the growth process (section 2.4.2), and because it is difficult to determine the precise size and shape of the QDs once they have been buried within the surrounding matrix.

The electron ground state energy of such QDs is usually several hundred meV above the conduction band edge, so the effective mass may be significantly larger than the band-edge InAs effective mass of  $m^* = 0.026m_e$ . Capacitance spectroscopy experiments on InAs QDs embedded in a GaAs matrix suggest an electron effective mass of  $m^* \approx 0.057m_e$  (Miller *et al.* 1997). This result is consistent with an estimate of  $m^*$  made from photoluminescence measurements (Itskevich *et al.* 1997),  $m^* \approx 0.055m_e$ .

Kim *et al.* (1998) and Stier *et al.* (1999) have independently calculated the one-electron energy levels in a strained InAs QD grown on (100) GaAs, using two different techniques. For a pyramidal QD of base size 9 nm and height 4.5 nm they independently obtained a one-electron ground state that is approximately 180 meV below the GaAs conduction band edge ( $\sim 700$  meV above the InAs conduction band edge), with the next two excited states approximately 110 meV higher in energy.

## 1.6 Electron $g$ factor

The spin of the electron gives it an intrinsic magnetic moment. The operator for this moment is (McMurry 1993)

$$\hat{\boldsymbol{\mu}}_S = -g\mu_B\hat{\boldsymbol{\sigma}}, \quad (1.28)$$

where  $\hbar\hat{\boldsymbol{\sigma}}$  is the intrinsic angular momentum of the electron and  $g$  is a constant known as the  $g$ -factor.

For a free electron in a magnetic field,  $\mathbf{B}$ , the interaction of the electron's

intrinsic magnetic moment with the field adds the potential energy,

$$\hat{V}_{\text{spin}} = -\mathbf{B} \cdot \hat{\boldsymbol{\mu}}_S. \quad (1.29)$$

If  $\mathbf{B}$  lies along a (arbitrarily defined) axis,  $z$ , then  $\hat{V}_{\text{spin}}$  can be written as

$$\hat{V}_{\text{spin}} = g\mu_B B \hat{\sigma}_z, \quad (1.30)$$

where  $\hat{\sigma}_z$  is the  $z$ -component of the electron spin. There are two eigenvalues of  $\hat{\sigma}_z$  for the electron,  $m_s = \pm\frac{1}{2}$ , so that the energy *difference* between the two spin states is

$$\epsilon_{\text{spin}} = g\mu_B B. \quad (1.31)$$

For *free* electrons, the  $g$  factor is (Ashcroft and Mermin 1976)

$$\begin{aligned} g_0 &= 2[1 + \alpha/2\pi + O(\alpha^2) + \dots] \\ &\approx +2.00232 \\ &(\alpha = e^2/\hbar c). \end{aligned} \quad (1.32)$$

### 1.6.1 Effective $g$ factor in a crystal

An electron moving through an environment containing other charges—a crystal lattice, for example—experiences an additional force that is equivalent to a magnetic field in the reference frame of the moving electron. This magnetic field interacts with the magnetic moment due to the electron's intrinsic spin, giving rise to an additional *spin-orbit* coupling potential (Schiff 1949),

$$\hat{\mathcal{H}}_{\text{SO}} = \frac{\hbar}{4m^2} \nabla U(\mathbf{r}) \times \hat{\mathbf{p}} \cdot \hat{\boldsymbol{\sigma}}. \quad (1.33)$$

The addition to the one-electron energy resulting from the spin-orbit interaction is found to be directly proportional to the externally applied magnetic field and the spin of the electron,  $m_s$ .<sup>†</sup> This is the same behaviour as equa-

---

<sup>†</sup>See the appendix to Yu and Cardona's book (2001). In the present edition, the appendix is only available on the World Wide Web; link from <http://physics.berkeley.edu>.

tion 1.30, enabling the energy splitting between the two spin states in a magnetic field to be written as

$$\epsilon_{\text{spin}} = g^* \mu_B B, \quad (1.34)$$

where  $g^*$  is known as the *effective g-factor*, and may be quite different from the free-electron  $g$ -factor. For example, in bulk GaAs the value of  $g^*$  is measured to be  $g^* = -0.44$ , while for bulk  $\text{Al}_{0.2}\text{Ga}_{0.8}\text{As}$  it is estimated to be  $g^* \approx +0.2$  (Weisbuch and Hermann 1977). In addition, the apparent value of  $g$  can be further altered by the effect of the electron-electron interaction. This effect will be discussed in chapter 5.

The motion of an electron through a crystal lattice, and therefore the  $g$ -factor, can be obtained from the band structure of the crystal. Using  $\mathbf{k} \cdot \mathbf{p}$  theory, the  $g$ -factor can be related to the energy gaps and wave functions at band extrema. A simple three-band  $\mathbf{k} \cdot \mathbf{p}$  approximation gives the  $g$ -factor at the  $\Gamma$  point as (Hermann and Weisbuch 1977)

$$g^* = g_0 \left[ 1 + \frac{P^2}{3} \left( \frac{1}{E_g} - \frac{1}{E_g + \Delta} \right) \right], \quad (1.35)$$

where  $E_g$  is the energy gap at the  $\Gamma$  point,  $\Delta$  is the spin-orbit splitting of the valence band and  $P$  represents the coupling between the conduction and valence bands. This model is used in chapter 5 to estimate the electron  $g$ -factor in an InAs quantum dot.

## 1.7 Tunnelling

At an interface between GaAs and (AlGa)As there is a step change in the energy of the  $\Gamma$  conduction band,  $E_\Gamma$ . This presents a potential barrier to an electron incident from the GaAs conduction band  $\Gamma$  valley. In this way, a potential *tunnelling barrier* can be created by growing a layer of (AlGa)As within GaAs.

In the effective mass approximation, an electron incident from the left of

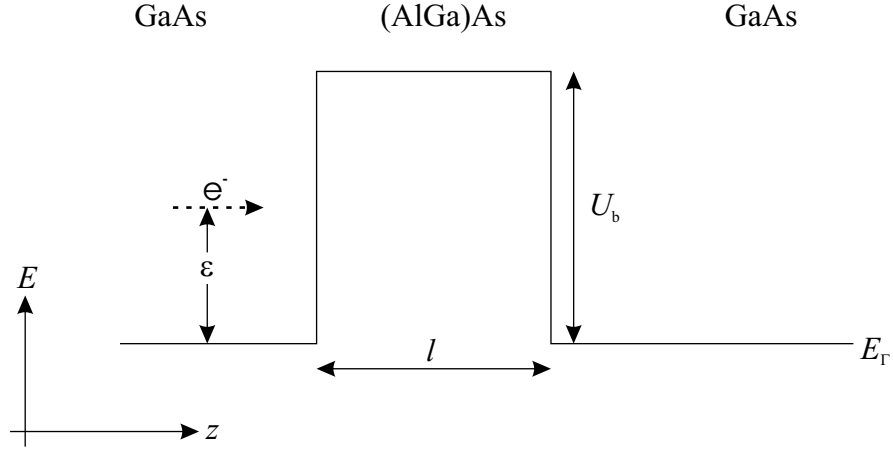


Figure 1.7: Diagram showing an electron incident on a potential barrier formed by sandwiching a layer of (AlGa)As between two layers of GaAs.  $E_\Gamma$  is the energy of the conduction band at the  $\Gamma$  point,  $l$  is the width of the barrier,  $U_b$  is the potential height of the barrier and  $\epsilon$  is the energy of the incident electron.

the (AlGa)As potential barrier can be described by the wave function,

$$\psi(z) = \begin{cases} A_L e^{ikz} + B_L e^{-ikz} & (z < -l/2) \\ \alpha e^{ik'z} + \beta e^{-ik'z} & (-l/2 < z < l/2) \\ A_R e^{ikz} & (z > l/2) \end{cases}, \quad (1.36)$$

where the GaAs/(AlGa)As interfaces are at  $z = -l/2$  and  $z = l/2$ , as shown in figure 1.7. The wave numbers  $k$  and  $k'$  are related to the energy,  $E$ , of the incident particle,

$$\begin{aligned} E &= E_\Gamma^{\text{GaAs}} + \frac{\hbar^2 k^2}{2m^*} \\ &= E_\Gamma^{(\text{AlGa})\text{As}} + \frac{\hbar^2 k'^2}{2m^*}. \end{aligned} \quad (1.37)$$

The ratio  $|A_L/A_R|^2$  is the *transmission probability*,  $T$ . This is the probability that an electron, incident on the barrier, will pass through it rather than be reflected from it. If we make the crude approximation that  $m^*$  is the same for (AlGa)As and GaAs, we obtain the result (Davies 1998)

$$T(\epsilon) = \left[ 1 + \frac{U_b^2}{4\epsilon(\epsilon - U_b)} \sin^2(k'l) \right]^{-1}, \quad (1.38)$$

where  $U_b$  is the potential height of the barrier, equal to  $E_\Gamma^{(\text{AlGa})\text{As}} - E_\Gamma^{\text{GaAs}}$ ,

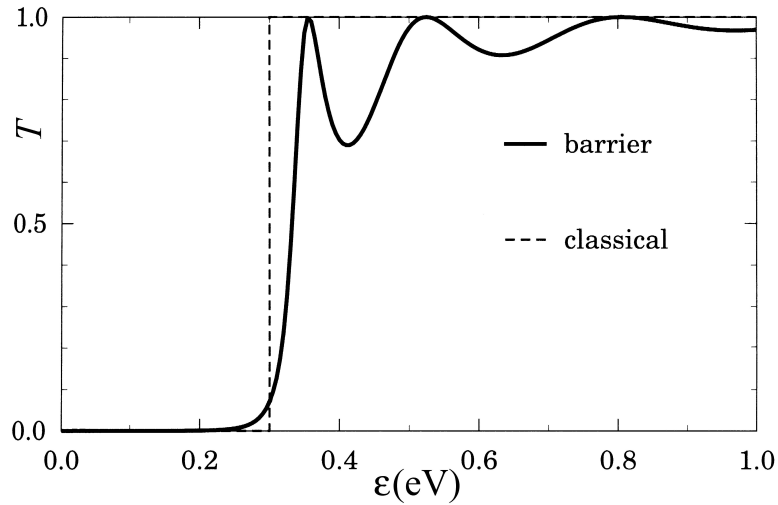


Figure 1.8: Transmission probability,  $T$ , as a function of energy,  $\epsilon$  for a rectangular potential barrier of width  $b = 10$  nm and height  $U_b = 300$  meV. The dashed line shows the classical transmission. From Davies (1998).

and  $\epsilon$  is the energy of the incident electron, equal to  $E - E_{\Gamma}^{\text{GaAs}}$  as shown in figure 1.7. Note that  $k'$  is *real* when  $\epsilon > U_b$  and *imaginary* when  $\epsilon < U_b$ .

Figure 1.8 shows a plot of the transmission probability for a barrier of width  $l = 100$  nm and height  $U_b = 300$  meV. For energies  $\epsilon > U_b$  *resonances* in the transmission probability occur whenever  $k'l$  is a multiple of  $\pi$ . For energies  $\epsilon < U_b$  there are no such resonances and the transmission probability decays rapidly to zero with decreasing energy. We define  $i\kappa = k'$  so that  $\kappa$  is a real number for  $\epsilon < U_b$ . Then, for  $\kappa l \gg 1$ , i.e. for low tunnelling probabilities,  $T$  depends approximately exponentially on the tunnel height and width,

$$T(\epsilon) \approx \frac{16\epsilon(U_b - \epsilon)}{U_b^2} e^{-2\kappa l}. \quad (1.39)$$

To obtain a net current across the barrier there must be a difference in the chemical potentials on either side of the barrier. This means that an electric field must be applied and this distorts the square shape of the barrier so that the above equation for the transmission probability is no longer strictly applicable. However, for small electric fields, it is still a useful approximation.

### 1.7.1 Resonant tunnelling

As discussed in the introduction, the transmission probability of a double barrier structure can exhibit resonances at energies  $\epsilon < U_b$ . This is known as *resonant tunnelling* and is directly analogous to the resonant transmission of light waves through the Fabry-Pérot étalon in classical optics.

The transmission probability for these structures can, in principle, be calculated in the same way as for the single tunnel barrier, i.e., by finding solutions to a Schrödinger equation that includes the potential landscape of the whole structure. In practice, analytical solutions are difficult to obtain for all but the simplest cases so solutions must be sought using numerical methods.

An alternative approach is to use the *transfer Hamiltonian* approach invented by Oppenheimer (1928) and Bardeen (1961), and developed as a description of resonant tunnelling by Luryi (1985), Payne (1986) and Weil and Vinter (1987) [see also Duke (1969)].

In this approach, the system is imagined as being split up into three individual ‘sub-systems’: an emitter (e), a collector (c) and a quantum well (w). Three sub-systems that, combined, form a double barrier structure are shown in figure 1.9. The stationary states of the three sub-systems are defined by three independent Hamiltonians,

$$\begin{aligned}\hat{\mathcal{H}}_e\psi_e &= E_e\psi_e, \\ \hat{\mathcal{H}}_c\psi_c &= E_c\psi_c, \\ \hat{\mathcal{H}}_w\psi_w &= E_w\psi_w,\end{aligned}\tag{1.40}$$

where  $\hat{\mathcal{H}}_e$ ,  $\hat{\mathcal{H}}_c$  and  $\hat{\mathcal{H}}_w$  are the Hamiltonians for each sub-system in isolation. Since the stationary states of each sub-system form a complete set, a stationary state of the double barrier system can be expressed as a superposition of the stationary states of any of the sub-systems. If an electron is placed in a stationary state of one of the sub-systems, it will not remain in that state since it is not in a stationary state of the Hamiltonian  $\hat{\mathcal{H}}$  of the double barrier system. Instead, the electron tunnels from one sub-system to another.

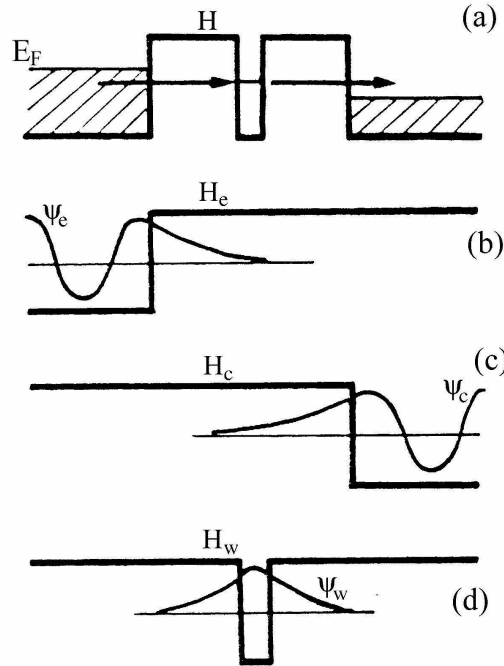


Figure 1.9: (a) Conduction band of the double barrier structure. The chemical potentials on either side of the structure are different so as to allow a net current to flow. (b), (c) and (d) The Hamiltonians of the three individual sub-systems. Eigenfunctions of each of the sub-systems are shown. From M. C. Payne (1986).

The rate of probability transfer between an initial state  $|i\rangle$  in one sub-system and a final state  $|f\rangle$  in a *different* sub-system is given by Fermi's Golden Rule,

$$\mathcal{W}_{fi} = \frac{2\pi}{\hbar} |\mathcal{V}_{fi}|^2 \delta(E_f - E_i), \quad (1.41)$$

where  $E_f$  and  $E_i$  are the energies of the final and initial states respectively. If the electron does not live long in the final state before it tunnels out again, the delta function in equation 1.41 should be replaced by another function (usually a Lorentzian), also of unit area but with a finite width  $\hbar/\tau$ , where  $\tau$  is the characteristic lifetime of the electron in the final state (Davies 1998). For example, in tunnelling from the emitter to a quasi-bound state in the well,  $\tau$  would represent the lifetime of the electron in the well.  $\mathcal{V}_{fi}$  is the *Bardeen transfer matrix* element given by (Duke 1969, Fromhold 1990)

$$\mathcal{V}_{fi} = i\hbar \int_S \mathbf{J}_{fi} \cdot d\mathbf{S}, \quad (1.42)$$

where the integral is taken over any surface,  $S$ , within the barrier region common to both sub-systems.  $\mathbf{J}_{fi}$  is the current density between states  $|f\rangle$  and  $|i\rangle$ , given by (Duke 1969)

$$\mathbf{J}_{fi} = \frac{i\hbar}{2m^*} (\psi_f^* \nabla \psi_i - \psi_i \nabla \psi_f^*). \quad (1.43)$$

In fact, in the presence of a magnetic field, an additional term proportional to the vector potential must be added to the above expression, giving  $\mathbf{J}_{fi} = (\frac{1}{2}i\hbar/m^*) (\psi_f^* \nabla \psi_i - \psi_i \nabla \psi_f^*) - (q/m^*) \psi_f^* \psi_i \mathbf{A}$ . However, the Landau gauge is used throughout this thesis so it is always possible to choose the direction of the vector potential to be parallel to the surface  $S$ . Therefore the term containing the vector potential disappears when the dot product with  $d\mathbf{S}$  is taken in equation 1.42.

Summing over all initial states in a sub-system ( $a$ ) and all final states in a sub-system ( $b$ ) gives the tunnel current between the two sub-systems ( $a$ ) and ( $b$ ), (Demmerle *et al.* 1993)

$$I_{a \rightarrow b} = e \sum_{f,i} \mathcal{W}_{fi} [\rho_a(i) - \rho_b(f)], \quad (1.44)$$

where the notation  $\rho_x(j)$  represents the occupancy (the probability of occupation) of the  $j$ th state in sub-system  $x$ .

Resonant tunnelling via a state in the quantum well ( $w$ ) can now be imagined as a two-stage *sequential* process: (1) electron tunnels from a state in the emitter to one of the quasi-bound states in the potential well, and then (2) electron tunnels from the well state to a state in the collector.

Electrons tunnelling directly from the emitter to the collector give rise to a non-resonant current,  $I_{e \rightarrow c}$ . Alternatively, an electron in the emitter with energy within  $\hbar/\tau$  of a quasi-bound state in the well can tunnel into the well state, where it dwells for some time before tunnelling out into the collector. This gives rise to an additional *resonant* tunnel current. In equilibrium, the current flow from the emitter to the quasi-bound state in the well,  $I_{e \rightarrow w}$ , must equal that of the bound state to the collector,  $I_{w \rightarrow c}$ . Therefore, the equilibrium resonant current through the quasi-bound state is found by equating  $I_{e \rightarrow w}$  with  $I_{w \rightarrow c}$  (Payne 1986). We define  $\gamma_e$  and  $\gamma_c$  as the tunnelling rates

across the emitter-side and collector-side tunnel barriers, such that

$$I_{e \rightarrow w} = e [\rho_e(E_w) - \rho_w] \gamma_e, \quad (1.45)$$

and

$$I_{w \rightarrow c} = e [\rho_w - \rho_c(E_w)] \gamma_c, \quad (1.46)$$

where  $E_w$  is the energy of the quasi-bound state in the well,  $\rho_w$  is the occupancy of the bound-state, (i.e. the probability that there is an electron occupying the bound state) and  $\rho_e(E_w)$  and  $\rho_c(E_w)$  are the occupancies of states in the emitter and collector respectively with energy  $E_w$ . In the experiments in this thesis, sufficient voltage is applied across the device so that the chemical potential on the collector side is well below that of the bound state. In this case we can assume that  $\rho_c(E_w) = 0$ . Equating  $I_{e \rightarrow w}$  with  $I_{w \rightarrow c}$  we therefore obtain (Deshpande *et al.* 2000),

$$I = e \rho_e(E_w) \frac{\gamma_e \gamma_c}{\gamma_e + \gamma_c}. \quad (1.47)$$

Furthermore, in the experiments in this thesis, the tunnelling rate across the collector barrier is usually much greater than that across the emitter barrier. In this case, the resonant current through the quasi-bound state is

$$I \approx e \rho_e(E_w) \gamma_e. \quad (1.48)$$

In this sequential model of resonant tunnelling, no attempt is made to take into account the phase coherence between the tunnelling-in step and the tunnelling-out step. Nevertheless, it has been shown (Payne 1986, Weil and Vinter 1987) that the resonant tunnel current calculated in this way is equal to that calculated using a coherent tunnelling model, provided that the range of electron energies in the emitter is larger than that of the energy width of the bound state in the well. Note that, simply because the sequential tunnelling model does not include the phase coherence between the two tunnelling steps, this does *not* imply that some (undefined) scattering processes are occurring in order to randomise the phase of the electron whilst it is in the well. As Liu and Aers (1989) explain, the model should be viewed as a ‘mathematical trick’ to derive a coherent result from a sequential pic-

ture of resonant tunnelling. Physically, if there are indeed some scattering processes taking place in the well, the energetic width of the quasi-bound states in the well are broadened, and coherent and incoherent tunnelling processes are distinguishable (Büttiker 1988).

In chapters 3 and 6, the sequential tunnelling picture is used to model the resonant tunnel current through a zero-dimensional state of a quantum dot.

### 1.7.2 Analytic expressions for the Bardeen transfer matrix

In order to obtain an analytic expression for the transfer probability between a state  $|i\rangle$  in sub-system ( $a$ ) and a state  $|f\rangle$  in sub-system ( $b$ ) it is convenient to separate the electron wave functions into the product of  $xy$  (parallel to growth-plane) and  $z$  (perpendicular to growth-plane) components,

$$\begin{aligned}\psi_a(x, y, z) &= \phi_a(x, y)\chi_a(z) \\ \psi_b(x, y, z) &= \phi_b(x, y)\chi_b(z).\end{aligned}\tag{1.49}$$

The transfer matrix element between the two states  $|i\rangle$  and  $|f\rangle$  may then be written in the form (Mori 2000)

$$\mathcal{V} = \frac{-\hbar^2}{2m^*} \times \mathcal{M} \times \mathcal{T},\tag{1.50}$$

where

$$\mathcal{M} = \int_{xy} \phi_a^*(x, y)\phi_b(x, y) dx dy,\tag{1.51}$$

and

$$\mathcal{T} = \left[ \chi_a^*(z) \frac{d}{dz} \chi_b(z) - \chi_b(z) \frac{d}{dz} \chi_a^*(z) \right]_z,\tag{1.52}$$

where the derivatives between the square brackets are evaluated at any value of  $z$  within the barrier region common to both sub-systems.

The separation of the wave functions into  $xy$  and  $z$  components is trivial to do in the case of planar structures but is not possible in tunnelling through zero-dimensional structures such as quantum dots. In such cases further

approximations must be used in order to obtain analytic expressions for the tunnelling probability. This will be discussed below.

### Tunnelling between a 3D and a 2D system

In a planar double barrier structure electrons resonantly tunnel from a three-dimensional emitter into a two-dimensional quantum well and out into a three-dimensional collector. In an ideal structure containing no impurities or disorder in the crystal lattice, the eigenfunctions of the 3D emitter (or collector) sub-system (e) and the 2D well sub-system (w) take the form,

$$\begin{aligned}\psi_e(\mathbf{r}, z) &= \exp(i\mathbf{k}_e \cdot \mathbf{r})\chi_e(z) \\ \psi_w(\mathbf{r}, z) &= \exp(i\mathbf{k}_w \cdot \mathbf{r})\chi_w(z),\end{aligned}\tag{1.53}$$

where the vectors  $\mathbf{r}$  and  $\mathbf{k}$  lie in the  $xy$  plane. Substituting the above forms for the wave functions into equations 1.51 and 1.52 we obtain the transfer matrix element between an initial state  $|i\rangle$  in sub-system (e) and a final state  $|f\rangle$  in sub-system (w),

$$\mathcal{V} = \frac{-\hbar^2}{2m^*} \times \delta(\mathbf{k}_w - \mathbf{k}_e) \times \left[ \chi_w^* \frac{d}{dz} \chi_e - \chi_e \frac{d}{dz} \chi_w^* \right]_{z_e < z < z_w},\tag{1.54}$$

where  $z_e < z < z_w$  is any point in the barrier region common to both emitter and well sub-systems. The important thing to note is the delta function, which indicates that tunnelling is only possible between two states that have the same in-plane crystal momentum,  $\mathbf{k}$ . In other words  $\mathbf{k}$  is *conserved* in tunnelling between 3D and 2D systems.

### Tunnelling between a 2D and a 0D system

In chapters 3, 4 and 5 we consider resonant tunnelling via the zero-dimensional state of a quantum dot.

It is not possible to write the electron wave function of a QD in the form of equation 1.49 since the confinement potential of the QD,  $U(x, y, z)$ , is not separable into a simple sum of  $xy$  and  $z$  components. Liu and Aers

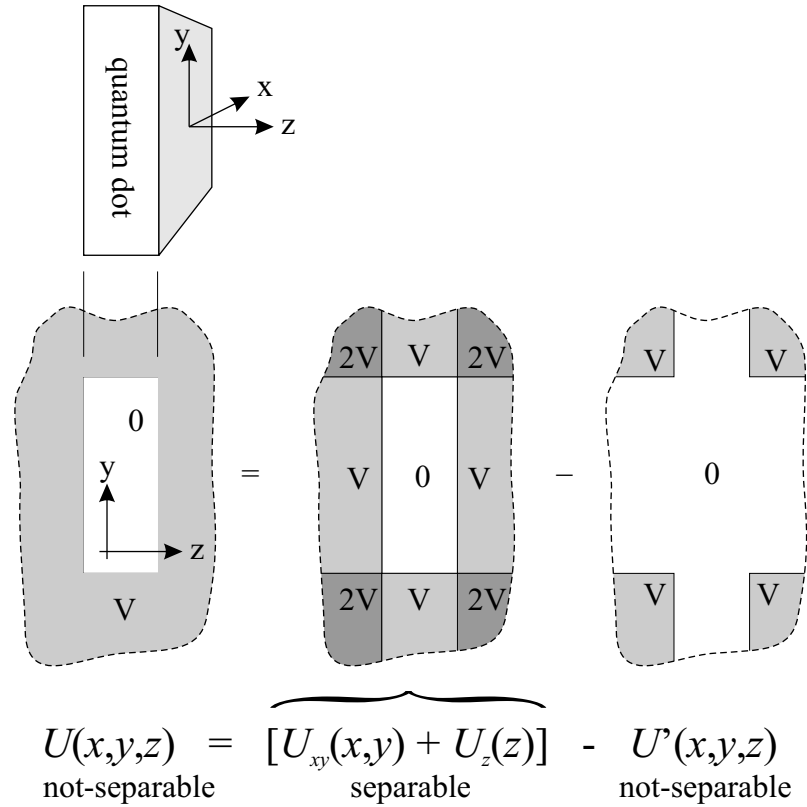


Figure 1.10: The confinement potential  $U(x, y, z)$  of a quantum dot expressed as the sum of separable parts  $U_{xy}(x, y) + U_z(z)$  plus a non-separable part  $U'(x, y, z)$ . The non-separable part of the potential  $U'$  is then treated as a perturbation. After Liu and Aers (1989).

(1989) suggest that one way around this problem is to write the confinement potential of the QD as the sum of separable parts  $U_{xy}(x, y) + U_z(z)$  plus a non-separable part  $U'(x, y, z)$  (see figure 1.10). The non-separable part of the potential  $U'$  is then treated as a perturbation. The solutions to the unperturbed Hamiltonian may be written as in the form  $\psi_{\text{qd}}(x, y, z) = \phi_{\text{qd}}(x, y)\chi_{\text{qd}}(z)$ .

For the self-assembled quantum dots considered in this thesis, the confinement length in the  $z$  direction is generally significantly smaller than that in the  $xy$  direction. This means that, for the lowest energy states in the QD, there is little coupling between the states when the perturbation is 'switched on' so the functions  $\psi_{\text{qd}}(x, y, z)$  remain good first approximations for the wave function.

Assuming that there is no disorder in the two dimensional emitter sub-

system, the electron wave function in this sub-system can be written as

$$\psi_e(\mathbf{r}, z) = \exp(i\mathbf{k}_e \cdot \mathbf{r})\chi_a(z), \quad (1.55)$$

where the vectors  $\mathbf{r}$  and  $\mathbf{k}$  lie in the  $xy$  plane.

The transfer probability between an initial state  $|i\rangle$  in the two-dimensional emitter sub-system (e) and a final state  $|f\rangle$  in the quantum dot sub-system (qd) is then approximated by,

$$\mathcal{V} = \frac{-\hbar^2}{2m^*} \times \tilde{\phi}_{\text{qd}}(\mathbf{k}_e) \times \left[ \chi_{\text{qd}}^* \frac{d}{dz} \chi_e - \chi_e \frac{d}{dz} \chi_{\text{qd}}^* \right]_{z_e < z < z_{\text{qd}}}, \quad (1.56)$$

where  $z_e < z < z_{\text{qd}}$  is any point in the barrier region common to both the emitter and QD sub-systems and  $\tilde{\phi}_{\text{qd}}(\mathbf{k})$  is the 2D Fourier transform of  $\phi_{\text{qd}}(\mathbf{r})$ . The important point is that, in this case, unlike in the 3D-2D tunnelling case, strict conservation of the in-plane crystal momentum,  $\mathbf{k}$ , in tunnelling is relaxed, although energy is still required to be conserved. Note also that, although  $\mathcal{V}$  depends upon  $\tilde{\phi}_{\text{qd}}(\mathbf{k}_e)$ , the range of  $\mathbf{k}_e$  representing *occupied* states in the emitter is often small compared to the extent of the QD wave function in  $k$ -space,  $\tilde{\phi}_{\text{qd}}$ . If this is the case, then the resonant current through a particular QD state, obtained by summing  $|\mathcal{V}_{fi}|^2$  over all occupied states in the emitter (equation 1.44), will depend only weakly on  $\mathbf{k}_e$ .

# Chapter 2

## Apparatus, experimental techniques and samples

This chapter discusses the apparatus and methodology used in the experiments presented in this thesis. The structure of the samples is explained, including the details of their fabrication. A brief description of the molecular beam epitaxy process is included with emphasis on the Stranski-Krastanow process that leads to self-assembled QD formation. All electrical measurement on the samples were performed at temperatures of 4 K or less, requiring the use of cryostats.

### 2.1 Oxford Instruments 0.3 K $\text{He}^3$ cryostat

This cryostat consists of a main bath that contains liquid  $\text{He}^4$  at 4 K. The bath is surrounded by a vacuum chamber containing superinsulation and metal radiation shields. The latter are cooled by the low temperature vapour escaping from the bath.

A low temperature insert is suspended within the bath. The insert comprises a sample space, a charcoal adsorption pump (SORB) and a 1 K pot. The sample space is connected to an external dump vessel containing a charge of  $\text{He}^3$ . The insert is insulated from the main bath by a second ‘inner’ vacuum chamber. The sample is mounted to a sample stage at the end

of a telescopic probe. The probe is then inserted into the sample space via a set of sliding seals. The probe is also equipped with a temperature sensor and a small heater. Cooling below 4 K is achieved by reducing the pressure inside the 1K-pot by means of an external gas pump. This condenses the He<sup>3</sup> gas in contact with the outside of the pot, which then runs down into the bottom of the sample space, where it pools. Once the He<sup>3</sup> has been condensed the process of cooling the He<sup>3</sup> to 300 mK can commence. This is achieved by cooling the charcoal SORB to below  $T \sim 10$  K. At such temperatures, the remaining He<sup>3</sup> vapour adsorbs onto the charcoal surface, thus reducing the pressure inside the sample space and therefore reducing the boiling point of the liquid He<sup>3</sup>. During the period that these experiments were conducted, the temperature could be held at a constant 300 mK for lengths of time in excess of 10 hours. The temperature of the sample is measured with a calibrated Speer resistor mounted close to the sample. Stable temperatures above 300 mK, but below that of the pot temperature, can be obtained by increasing the temperature of the SORB to reduce the adsorption rate. The power output to the SORB heating element is usually governed by an electronic proportional-integral-differential controller to speed up the convergence on the required temperature. To obtain sample temperatures higher than 1 K, the sample is heated directly by using the heater on the probe. However, it is quite difficult to obtain good temperature stability by using this method.

A superconducting magnet coil occupies most of the space in the lower third of the bath and surrounds the sample space. Cooled to 4 K, the magnet can provide a uniform magnetic field of up to 16.5 T within a  $\sim 1$  cm<sup>3</sup> volume enclosing the sample. The direction of the field vector lies vertically, parallel to the probe. The current in the coil is adjusted by applying a voltage across the terminals of the coil. Once the desired field has been reached, the coil may be put into a persistent current mode by short circuiting the terminals of the coil by means of a superconducting switch.

The sample may be mounted on a rotating spindle so that it can be rotated with respect to the magnetic field direction *in situ*. The axis of rotation is perpendicular to the direction of the field, i.e. parallel to the horizontal. The sample can be fixed to the spindle in two different configurations: (1)

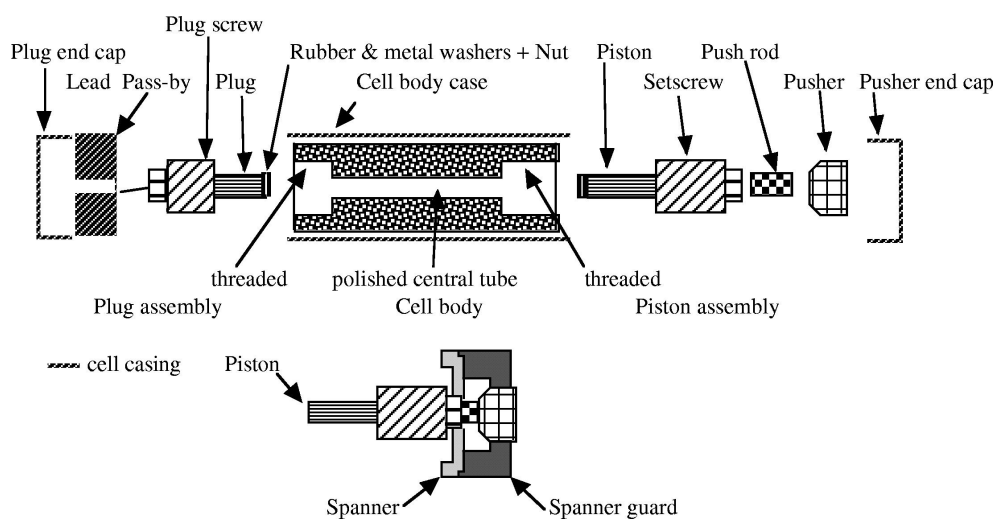


Figure 2.1: Schematic diagram of the UniPress liquid clamp cell.

rotation axis perpendicular to the plane of the sample; and (2) rotation axis in the plane of the sample.

## 2.2 High pressure apparatus

### 2.2.1 Unipress high pressure liquid clamp cell

An experiment presented in section 3.4 requires the use of a liquid clamp cell to apply pressures of up to 5 kbar (500 MPa) to the samples. The cell consists of a cylindrical cell body with a polished central tube and threaded ends (see figure 2.1). The sample is mounted onto a header which is in turn mounted onto a sample stage at the end of the *plug* (see figure). The plug is screwed into the barrel of the cell and the cell filled with an oil/petrol mixture. The oil is pressurised by applying force to the piston rod with the aid of a hydraulic press. When the desired pressure is reached, the piston rod is locked in position by screwing the *setscrew* home and the cell is then installed inside the removable vacuum chamber of the Cryogenics 4 K cryostat (see below). The pressure inside the cell is monitored with a InSb wire mounted within the sample stage. The resistivity of this wire has a calibrated pressure sensitivity, so that the pressure can be determined from a four-wire resistance measurement.

### 2.2.2 Cryogenics 4 K cryostat

This cryostat consists of a bath that is filled with liquid  $\text{He}^4$  at 4 K, surrounded by a vacuum chamber. The pressure cell is installed within a removable vacuum chamber which is immersed in the liquid  $\text{He}^4$ . On cool-down, a small quantity of  $\text{He}^4$  gas is introduced into the vacuum chamber to provide a little thermal contact between the bath and the cell. The vacuum chamber is then lowered slowly into the bath over a period of about two hours. The temperature is carefully monitored to ensure that cooling takes place at a rate which is slow enough ( $\lesssim 100 \text{ Khr}^{-1}$ ) to allow the oil/petrol mixture inside the cell to solidify homogeneously. This is necessary to maintain an even pressure over the surface of the sample inside the cell.

Such a slow cooling rate is also necessary to ensure that the majority of the excess heat in the cell is exchanged with the low temperature gas phase in the bath rather than with the liquid. This is important because the cell contains enough thermal energy at room temperature to vaporise all of the liquid in the bath.

## 2.3 $I(V)$ measurement techniques

### 2.3.1 Basic $I(V)$ measurement circuit

All of the experiments in this thesis are based upon measurement of current flow through a device as a function of some other variables. The basic measurement circuit, shown in figure 2.2, is designed to measure current flow through a device,  $I$ , as a function of a bias applied to the device,  $V$ .

A stable digital voltage source provides the bias,  $V$ , while the current is measured by using a high impedance ( $10 \text{ G}\Omega$ ) voltmeter to measure the voltage drop,  $V_{\text{shunt}}$ , across a shunt resistor,  $R_{\text{shunt}}$ , in series with the sample.  $V_{\text{shunt}}$  is related to the current flow through the sample by

$$V_{\text{shunt}} = IR_{\text{shunt}}. \quad (2.1)$$

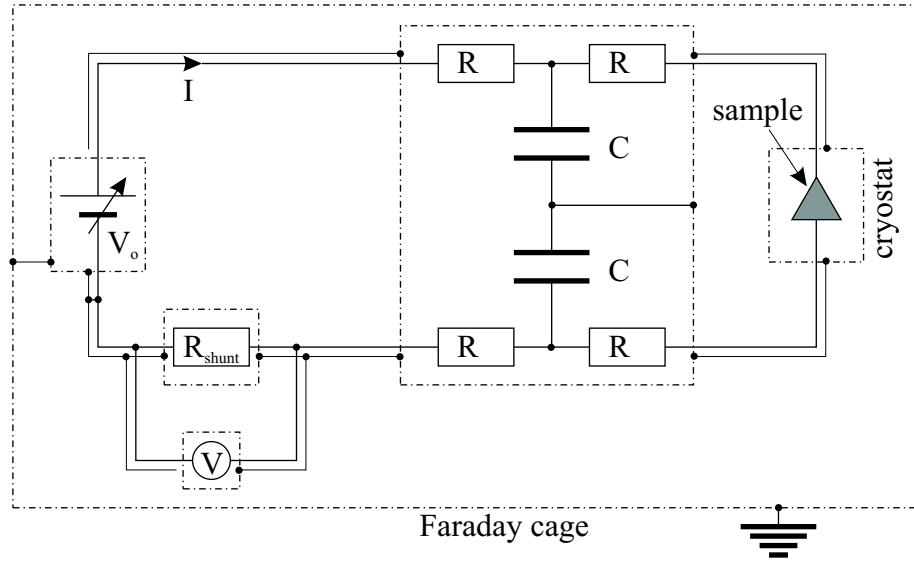


Figure 2.2: Schematic of basic  $I(V)$  measurement circuit. Broken lines indicate screened enclosures. Co-axial cable is represented by double parallel lines.

The bias applied across the sample contacts,  $V$ , is equal to the output of the voltage source,  $V_o$ , minus the voltage drop across the shunt,  $IR_{shunt}$ ,

$$V = V_o - IR_{shunt}. \quad (2.2)$$

Increasing the value of  $R_{shunt}$  increases the current sensitivity of the experiment (this is discussed in section 2.3.3). However, this also causes an increasing fraction of  $V_o$  to be dropped across the shunt. Since these samples exhibit negative differential resistance (NDR), the partitioning of the source voltage between the shunt and the sample introduces an additional complication into the measurement of the  $I(V)$ . The  $I(V_o)$  characteristic of the circuit can exhibit regions of *instability* at voltages where the sample exhibits NDR. A stylised example is shown in figure 2.3. In the instability regions there can be several possible ways to distribute the voltage  $V_o$  between the sample and the shunt. The range of  $V_o$  that shows instability becomes more extreme as the value of the shunt resistance is increased. This effect is undesirable because the  $I(V)$  characteristic of the sample cannot be determined within these unstable voltage ranges. Conversely, if the shunt resistance is small enough and the NDR is not too large, then the circuit may not show any instability at all. Therefore, a compromise must be made

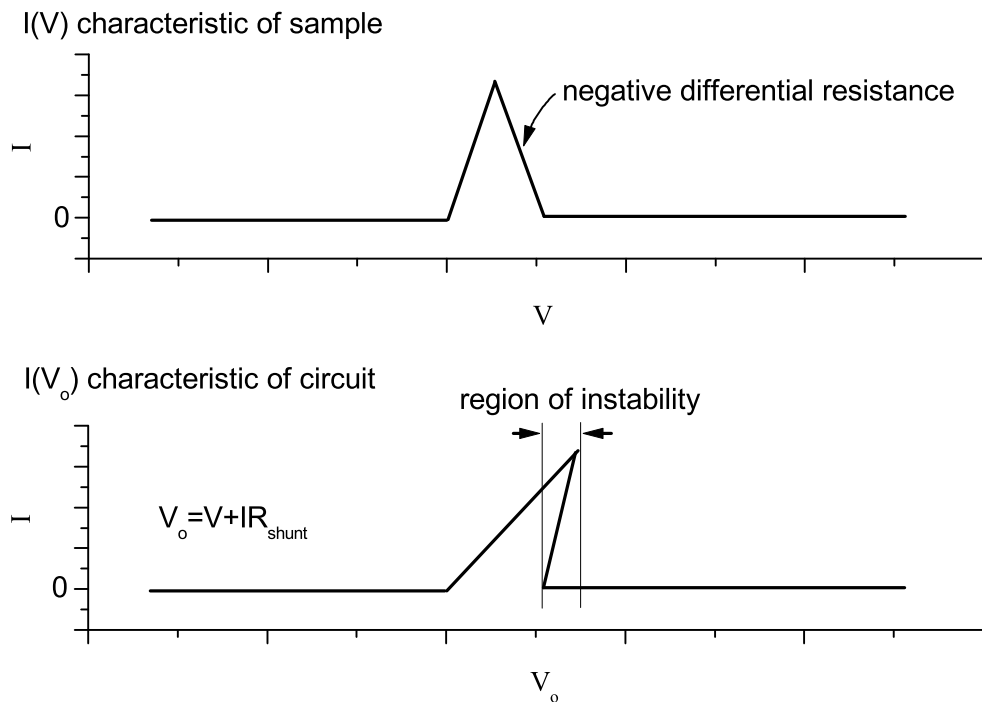


Figure 2.3: Top: A stylised  $I(V)$  characteristic of a sample that exhibits negative differential resistance. Bottom: The  $I(V_o)$  characteristic of a simple circuit consisting of the sample in series with a shunt resistance  $R_{\text{shunt}}$ , where  $V_o = V + IR_{\text{shunt}}$ . The circuit shows a region of instability corresponding to the region of negative differential resistance in the sample.

between the current sensitivity and how much instability in the circuit can be tolerated without losing too much information.

### 2.3.2 Computer assisted automation

A typical experiment in this thesis generates large quantities of data so it is necessary to introduce some degree of automation into the data acquisition process. An IBM-compatible personal computer running *Labview* by *National Instruments* is used to control the voltage output of the voltage source and record the data returned by the voltmeter. Additionally, either a magnet power supply unit, or a second voltage source could be placed under the control of the computer. Such degree of automation allows data collection to run efficiently for up to eighteen hours per day, limited only by

the hold time of the  $\text{He}^4$  in the cryostat bath.

It is also useful in some instances to use the computer to obtain some diagnostic temperature data. For instance, the cool-down rate of the pressure cell was monitored by using a Labview setup that obtained data from the temperature probe and then continuously graphed the instantaneous rate of temperature change.

Communication between the instruments and the computer is via a General Purpose Interface Bus (GPIB) or RS232 serial link.

### 2.3.3 Sources of noise and noise reduction techniques

Typically, the magnitude of the tunnel current is in the femto-amp to pico-amp range ( $10^{-15}$  to  $10^{-12}$  A). Such small currents can be easily swamped by external electrical noise, so care must be taken to properly screen and filter the sample, instruments and measurement circuit.

The cryostat, voltmeter, voltage source and measurement circuit are enclosed within an aluminium Faraday cage. This screens them from electric fields generated outside the cage, up to a maximum frequency of  $\sim 10 - 100$  GHz limited by the  $\sim 1$  cm mesh size of the cage. This is enough to screen electrical equipment and mains power supply cables (50 Hz), radio transmissions ( $\sim 100$  kHz – 2 GHz) and digital electronics ( $\sim 1$  MHz – 5 GHz).

In addition, the mains power supply inside the cage is filtered and isolated from the supply outside to prevent electrical noise entering the cage via the power supply. The cage is earthed with a metal spike driven into the ground outside the lab.

The computer is situated outside the cage and interfaces with the instruments inside the cage via an optical fibre rather than an electrical link. This prevents electrical noise from the computer entering the cage via the interface.

### Electrical equipment

Both the voltmeter and voltage source contain digital electronics and so are sources of radio frequency (RF) noise *inside* the cage. Most of the RF noise radiated through the air is screened from the sample by the metal walls of the cryostat. To reduce the noise reaching the sample via the current leads, both leads to the sample are each filtered with a simple  $RC$  low-pass filter with a time constant  $RC \sim 1$  s. The filters and shunt resistor are themselves shielded within aluminium boxes. Connections between the instruments, sample, filters and shunt resistor are made with screened leads, commonly co-axial cable with BNC connectors.

### Cables and connections

For very low level current measurements ( $I \sim 100$  fA), it was found that the co-axial cables themselves could produce enough noise to completely swamp the measurement.

One such source of noise comes from the motion of the cables in the magnetic field. Since large magnetic fields are used in most of the experiments in this thesis, even very small vibrations of the cables in the magnetic field can induce a significant voltage in a loop of cable. For this reason, it was found important to tape the leads securely to a rigid surface, such as a bench, to prevent them from moving freely. Where possible, cables carrying opposite currents were also loosely twisted together to further minimise the generation of voltages in the magnetic field. The shielding of the cables was broken in a few places (see figure 2.2) to avoid the formation of closed loops in the cable shielding.

Securing the cables also reduced the noise generated by piezo-electric and tribo-electric effects (Keithley *et al.* 1984). Current is generated by these effects when the cable is flexed. In the piezo-electric effect, a current is generated by changes in stress in the cable insulation (Feynman *et al.* 1965, Keithley *et al.* 1984, Kittel 1996). In the tribo-electric effect, currents are generated by the insulator moving against the central conductor and the shielding. Charge can be rubbed off the central conductor in this way, giving rise to

a small electric current (Keithley *et al.* 1984). Besides securing the cables, the tribo-electric effect was further reduced by using a ‘low-noise’ co-axial cable that includes a conducting low-friction sheath around the dielectric.

The lowest noise level was only obtained by leaving the cables to ‘settle’ for approximately 24 hours after setting up the circuit, before a measurement was made.

The BNC connectors could also significantly increase the noise level if the connections were weak or dirty. An intermittent bad connection was often extremely difficult to trace. Where possible therefore, for low noise measurements, BNC connections were replaced by more reliable ‘screw and clamp’ connections or by soldered joints.

A good ground connection was also found to be necessary. The measured noise level was substantially reduced if the measurement circuit was grounded at a single point. The best results were obtained by grounding the negative terminal of the voltage source. The cable shielding and aluminium boxes enclosing the shunt resistor and  $RC$  filter were also connected to cage ground.

### Fundamental noise limits

Johnson/Nyquist noise sets a fundamental limit on how far the measurement noise can be reduced. Thermal energy causes motion of the electrons within a resistor, and this motion gives rise to fluctuations in the electron density. These density fluctuations in turn produce small fluctuating electric fields (Feynman *et al.* 1965) that appear as voltage noise at the terminals of the resistor.

The power produced by this noise, in a frequency range  $\Delta f$ , is given by\* (Feynman *et al.* 1965, Keithley *et al.* 1984)

$$P = 4k_{\text{B}}T\Delta f, \quad (2.3)$$

---

\*At sufficiently low temperatures/high frequencies the  $k_{\text{B}}T$  in this equation should be replaced by  $hf/[\exp(hf/k_{\text{B}}T) - 1]$  (Feynman *et al.* 1965).

where  $T$  is the temperature of the resistor. Therefore, the RMS current noise in a resistor  $R$  is

$$I_{\text{JN}} = \sqrt{\frac{P}{R}} \quad (2.4)$$

$$= \sqrt{\frac{4k_{\text{B}}T\Delta f}{R}}. \quad (2.5)$$

Since the bandwidth of the measurement is limited by the  $RC$  time constant of the measurement circuit to  $\Delta f \sim 1/(4RC)$  (Keithley *et al.* 1984), the *measured* noise is

$$I_{\text{JN}} = \frac{1}{R} \sqrt{\frac{k_{\text{B}}T}{C}}. \quad (2.6)$$

Therefore, the larger the value of the shunt resistor used for the current measurement, the smaller is the measured current noise. However,  $R$  cannot be increased without bound as the time constant of the measurement increases as  $\tau \sim RC$ . In addition, a large series resistance can give rise to instability in the  $I(V)$  characteristic of the measurement circuit, as explained in section 2.3.1.

When sufficient care was taken in setting up the cabling and connections in the measurement circuit (see previous section), it was found that the measured noise level could be reduced to a level approaching that of the Johnson/Nyquist noise.

Another fundamental limit to the current noise is the *shot noise* level. This noise arises due to the quantisation of electric charge, i.e. into electrons. The magnitude of the measured shot noise is given by  $I_{\text{shot}} = \sqrt{2eI\Delta f}$  (Keithley *et al.* 1984), where  $\Delta f$  is the bandwidth of the measurement and  $I$  is the current flow in the circuit. However, we estimate that for the combination of current level ( $I \sim 10^{-12} - 10^{-15}$  A) and series shunt resistance ( $R \sim 10^6 - 10^8 \Omega$ ) normally used in these experiments, the magnitude of the shot noise is usually much less than that of the Johnson-Nyquist noise generated in the shunt resistor  $R$ , i.e.  $I_{\text{shot}}/I_{\text{JN}} = \sqrt{2eIR/k_{\text{B}}T} \ll 1$ .

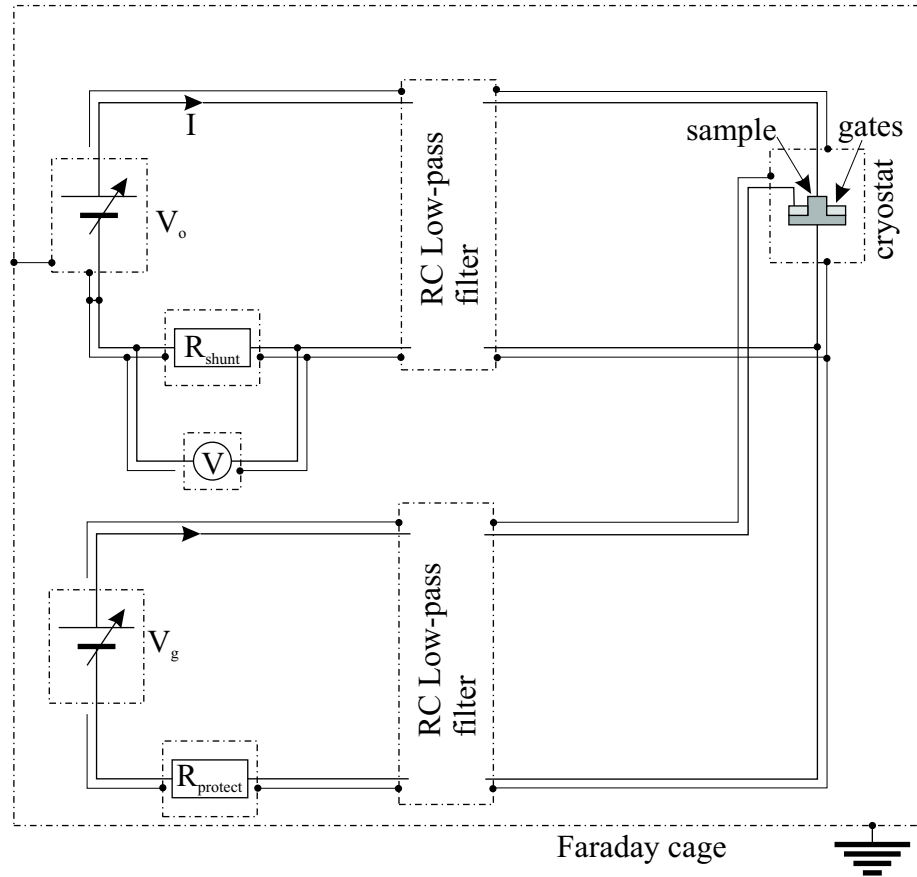


Figure 2.4: Schematic of  $I(V)$  measurement circuit including a filtered voltage source for gates. Broken lines indicate screened enclosures. Co-axial cable is represented by double parallel lines.

### 2.3.4 Applying bias to Schottky gates

One of the devices in this thesis incorporates an array of Schottky gates. Bias is applied to these gates by adding another voltage source to the measurement circuit as shown in figure 2.4. As with the original voltage source, the additional one may also be interfaced to the computer. A large resistance ( $\sim 1 \text{ M}\Omega$ ) in series with the gates limits the maximum gate leakage current flow should a large bias, accidentally applied, cause the the resistance of the Schottky barrier to collapse. In this case, the voltage source is operated in ‘floating’ mode, i.e. neither of the voltage terminals are grounded.

## 2.4 Samples

All of the samples presented in this thesis were processed from one of two wafers. Wafer *NU1403* is a GaAs/AlAs/GaAs structure grown on (100)-oriented GaAs substrate. A layer of InAs self-assembled QDs is embedded within the AlAs barrier layer. Wafer *NU1673* is a similar structure, except that the barrier layer material is  $\text{Al}_{0.2}\text{Ga}_{0.8}\text{As}$  and it was grown on a (311B)-oriented GaAs substrate. The doping profiles of the two materials are also different, so that there are important differences between the conduction band profiles of the two materials under an applied bias. More detailed information about the materials is given in sections 2.4.2 and 2.4.3.

### 2.4.1 Wafer growth

The wafers were grown by molecular beam epitaxy (MBE) (Gossard 1986) in Nottingham by Dr. M. Henini using a *Varian Gen II* reactor. This reactor is dedicated to growing GaAs/(AlGa)As-based wafers, so the concentration of unwanted impurities is minimised.

The wafers are grown on a silicon-doped GaAs substrate. This substrate is mounted on a rotating stage within the ultra-high vacuum chamber of the MBE machine. The elemental growth materials are contained within Knudson cells which, when heated to high temperature, produce a beam of atoms directed at the wafer. Computer-controlled shutters on the cells allow the beams to be turned off and on with enough precision to grow layers with atomic thicknesses. n-type doping is achieved by using a cell containing silicon. The temperature of the cells controls the beam intensity. Layer growth takes place at a typical rate of 15 nm per minute. The growth process can be followed *in situ* by using the Reflection High Energy Electron Diffraction (RHEED) technique.

For the samples in this thesis, three basic layers are grown. The first is a layer of GaAs containing graded n-type (silicon) doping. Next, a layer of nominally undoped  $\text{Al}_x\text{Ga}_{1-x}\text{As}$  is grown, to create a potential barrier layer. During the growth of this layer, the deposition of  $\text{Al}_x\text{Ga}_{1-x}\text{As}$  is interrupted

and 1.8 mono-layers (average) of InAs is deposited on the surface. Finally a second layer of graded n-type GaAs is grown on top of the  $\text{Al}_x\text{Ga}_{1-x}\text{As}$  barrier layer.

### Growth of self-assembled quantum dots

Since GaAs and (AlGa)As are almost perfectly lattice matched (see section 1.3.2), smooth, planar films of one material can be grown upon the other with minimal strain on the crystal lattice. This is not so of the (AlGa)As-InAs interface however, where the mismatch between the lattice constants is about 7%. Growth of InAs on (AlGa)As proceeds at first in a layer-by-layer mode. That is, a second mono-layer of InAs is not started until the layer below it is (almost) complete. Growth continues in this mode until the strain energy between the (AlGa)As lattice and the InAs lattice reaches a critical point. After this point, the strain energy is minimised in subsequent InAs growth by the formation of three-dimensional islands rather than planar layers (Nötzel 1992, Bimberg *et al.* 1998). The growth of the InAs islands is monitored *in situ* by using the RHEED technique. This allows InAs deposition to be halted and (AlGa)As deposition resumed before individual InAs islands can coalesce. The final result is a thin planar *wetting layer* of InAs, upon which sit individual three-dimensional InAs QDs.

Although there has been extensive research on the optical properties of such InAs QDs, much less is known about their physical size, shape and composition. This is largely because the dots are only directly accessible *before* the deposition of the final covering layer of (AlGa)As, after which the QDs are strained and some alloying with the material surrounding the QDs occurs (Siverns *et al.* 1998, Joyce *et al.* 2000, Surkova *et al.* 2001). Atomic force microscopy and scanning tunnelling microscopy measurements on uncapped InAs QDs grown on GaAs substrates have revealed a wide variety of shapes and sizes. For example, QDs grown on (100) oriented GaAs substrates yield dome-like shapes of 5 – 30 nm in diameter and 1 – 5 nm high, while QDs grown on (311B) GaAs substrates are faceted, pyramidal structures, 10 – 30 nm wide at the base and 1 – 5 nm high (Henini *et al.* 1997). InAs QDs grown on (311A) GaAs substrates have been observed to

Layer material	Thickness/nm	Doping(n-type)	Temperature/°C
GaAs	510	$4.0 \times 10^{18} \text{ cm}^{-3}$	550
GaAs	100	$2.0 \times 10^{16} \text{ cm}^{-3}$	550
GaAs	100	NID	550
AlAs	5.09	NID	550
InAs	1.8 ML	NID	520
AlAs	5.09	NID	550
GaAs	100	NID	550
GaAs	100	$2.0 \times 10^{16} \text{ cm}^{-3}$	550
GaAs	1000	$4.0 \times 10^{18} \text{ cm}^{-3}$	550
GaAs	<i>substrate</i>	$n^+$	

Table 2.1: Layer structure of wafer *NU1403*. Note that the substrate layer is at the bottom of the table. (NID - not intentionally doped.)

form  $\sim 30$  nm arrowhead-like structures (Henini *et al.* 1998). Under certain growth conditions, wire-like structures have also been observed on (100) GaAs substrates (Cirlin *et al.* 1995).

### 2.4.2 Wafer *NU1403*

The layer structure of wafer *NU1403* is shown in Table 2.1. The wafer was grown by MBE on a (100) oriented  $n^+$  doped GaAs substrate. The GaAs regions are doped with Si to produce carriers in the conduction band. The doping in these regions is graded from heavily doped, far from the AlAs barrier, to (nominally) undoped, close to the barrier. The undoped spacer layers next to the barrier reduce the diffusion of the Si dopant into the AlAs barrier. This is important, since single donors in the barrier region make additional 0D states available for resonant tunnelling, masking the resonant current due to the QDs.

To obtain an estimate of the size and shape of the QDs, a wafer identical to *NU1403* was grown, except that growth was terminated after depositing the InAs QDs. By using scanning electron microscopy and scanning tunnelling microscopy, the average size of the QDs was estimated to be approximately 10 nm in diameter and approximately 3 nm in height (Itskevich *et al.* 1996). The surface density was estimated as approximately  $2 \times 10^{15}$  QDs per square metre. Room temperature photoluminescence measurements, performed on

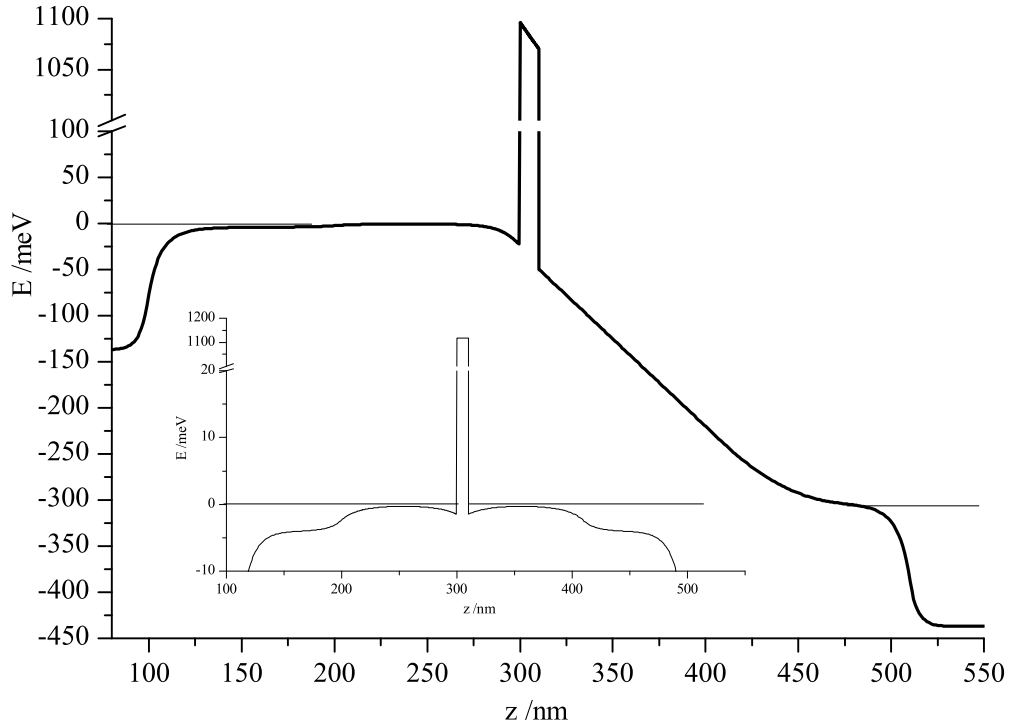


Figure 2.5: Self-consistent solution of the  $\Gamma$  conduction band of wafer *NU1403* with a bias of 300 mV applied between the contacts. The inset shows the conduction band with no applied bias. (Modelling program by Prof. G. L. Snider, University of Notre Dame.)

similar samples, show a spectrum with a strong line peaking in intensity at 1.8 eV and with a FWHM spectral line-width of approximately 0.15 eV (Leon *et al.* 1995, Polimeni *et al.* 1999a). This line is attributed to emission from the *ensemble* of QDs. Since the luminescence from the QDs is peaked at a few hundred meV above the energy of the GaAs band-gap (1.42 eV at room temperature), it is likely that the majority of QDs have electron ground states that lie of the order 100 meV *above* that of the GaAs conduction band edge (Itskevich *et al.* (1997) estimate the ratio of the hole effective mass to the electron effective mass in the QD is roughly 2:1).

Note that, although the thickness of AlAs grown before and after the InAs layer is *nominally* the same, the thickness of the AlAs layer covering a QD is reduced by the height of the QD. This implies that the thickness of AlAs covering a QD is 2 – 3 nm, compared with the 5 nm below it. This will be an important point when considering the tunnel current through the QD in

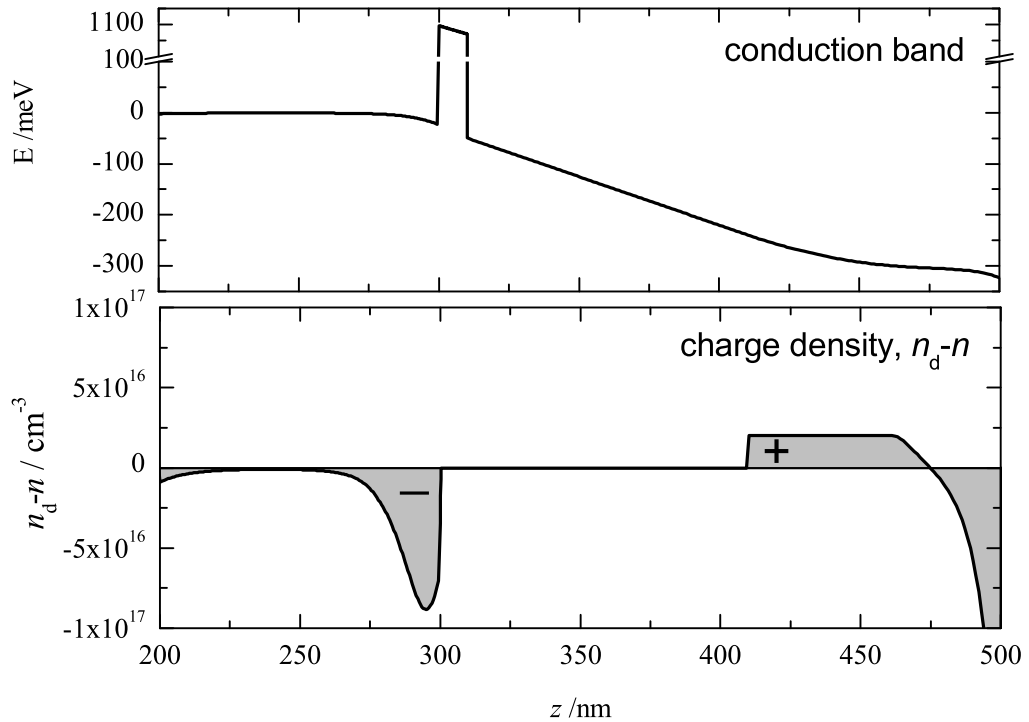


Figure 2.6: Self-consistent solution of the  $\Gamma$  conduction band of wafer *NU1403* with a bias of 300 mV applied between the contacts. The lower graph shows the net charge density, calculated by subtracting the the electron density,  $n$ , from the Si donor density,  $n_d$ . (Modelling program by Prof. G. L. Snider, University of Notre Dame.)

later chapters. Figure 2.5 shows the  $\Gamma$  conduction band of *NU1403* with a bias of 300 mV applied between the contacts. This was calculated using a computer program by Prof. G. L. Snider<sup>†</sup> that obtains a self-consistent solution to Poisson's equation by iteration. The result clearly shows the heavily doped contact regions and the undoped spacer regions next to the barrier layer. Importantly, notice that there is also a roughly triangular-shaped potential well adjacent to the barrier. Electrons accumulate in this well and, due to the strong confinement in the growth direction, the electrons form a 2DES at low temperature. Note that, as the voltage across the device is increased, the sheet density of electrons in the 2DES increases in accordance with Gauss's law. In this respect, the device is essentially a capacitor, with the 2DES acting as the 'negative plate' of the capacitor and the  $n$ -doped

<sup>†</sup>The computer program is currently available to download at [www.nd.edu/~gsnider](http://www.nd.edu/~gsnider). A description of the program is given by Tan *et al.* (1990).

region on the opposite side of the AlAs barrier acting as the ‘positive plate’ (see figure 2.6).

Recent capacitance measurements by Belyaev *et al.* (2000) have shown evidence for a small *positive* charge of  $+(1.2 \pm 0.2) \times 10^{14} e \text{ m}^{-2}$  within the AlAs barrier. It is believed that the positive charges are associated with defects in the AlAs caused by the presence of QDs. When this positive charge is taken into account in the band calculation, electron accumulation layers are formed on either side of the barrier, even at zero bias (see inset to figure 2.5).

### Device fabrication

The devices were fabricated by Mr. J. Middleton at the University of Nottingham, and Dr. A. Nogaret at the University of Glasgow.

AuGe was deposited on to the back side of the wafer and annealed to produce a common ohmic back contact. Approximately 30 circular mesas of various sizes between  $5 \mu\text{m}$  and  $400 \mu\text{m}$  in diameter, were then fabricated on small ( $10 \text{ mm} \times 10 \text{ mm}$ ) samples of wafer by standard photolithography techniques. AuGe was deposited on the surface of each mesa and annealed to produce ohmic top contacts. The sample was then fixed to the gold plated surface of a standard TO5 header by a small amount of conducting silver epoxy paste applied to the substrate. Electrical wire connections were made between the pins of the header and the top contacts of the individual mesas with the aid of a bonding machine. An additional wire was bonded to the gold plated header surface to complete the electrical path to the back side of the wafer.

#### 2.4.3 Wafer *NU1673*

The layer structure of wafer *NU1673* is shown in Table 2.2. The wafer was grown on a (311)B oriented  $n^+$  doped GaAs substrate. The GaAs regions are doped with Si to produce carriers in the conduction band. As with wafer *NU1403*, the doping in these regions is graded from heavily doped, far

Layer material	Thickness/nm	Doping (n-type)	Temperature/°C
GaAs	7	$2.0 \times 10^{18} \text{ cm}^{-3}$	450
$10 \times \delta$ doping		$1.5 \times 10^{13} \text{ cm}^{-2}$	
$10 \times$ GaAs	2.5	$2.0 \times 10^{18} \text{ cm}^{-3}$	450
GaAs	17.6	$2.0 \times 10^{18} \text{ cm}^{-3}$	450
GaAs	180	$2.0 \times 10^{17} \text{ cm}^{-3}$	550
GaAs	150	$1.4 \times 10^{17} \text{ cm}^{-3}$	550
GaAs	70.5	$1.0 \times 10^{17} \text{ cm}^{-3}$	550
GaAs	3.1	NID	550
$\text{Al}_{0.2}\text{Ga}_{0.8}\text{As}$	7.0	NID	550
InAs	1.7 ML	NID	520
$\text{Al}_{0.2}\text{Ga}_{0.8}\text{As}$	7.0	NID	550
GaAs	3.1	NID	550
GaAs	70.5	$1.0 \times 10^{17} \text{ cm}^{-3}$	550
GaAs	150	$1.4 \times 10^{17} \text{ cm}^{-3}$	550
GaAs	180	$2.0 \times 10^{17} \text{ cm}^{-3}$	550
GaAs	500	$2.0 \times 10^{18} \text{ cm}^{-3}$	550
GaAs	<i>substrate</i>	$\text{n}^+$	

Table 2.2: Layer structure of wafer *NU1673*. Note that the substrate layer is at the bottom of the table. (NID - not intentionally doped.)

from the AlGaAs barrier, to not intentionally doped, close to the barrier. However, the undoped spacer layers on either side of the barrier are much narrower than in *NU1403*, so that, in this case, a potential well does not form against the barrier under applied bias as in *NU1403*. This means that electrons tunnel through the barrier from a three-dimensional emitter.

Although we have no data on the size and density of the QDs for this particular material, we can obtain rough estimates from measurements performed on similar samples. Scanning tunnelling microscopy measurements on uncapped InAs QDs grown on a (311B) GaAs substrate show a QD density of  $\sim 0.5 - 1 \times 10^{15} \text{ m}^{-2}$  (Henini *et al.* 1997). The QDs are pyramidal in shape, with lateral sizes between 10 – 30 nm and  $\sim 5$  nm high.

Photoluminescence experiments on *NU1673* show a luminescence peak due to the QD ensemble at 1.15 eV at room temperature, with a line width of approximately 0.1 eV (Hill *et al.* 2002). This emission energy is well below the GaAs band gap (1.42 eV at room temperature). This strongly suggests that the majority of the electron ground states of the QDs lie *below* the GaAs

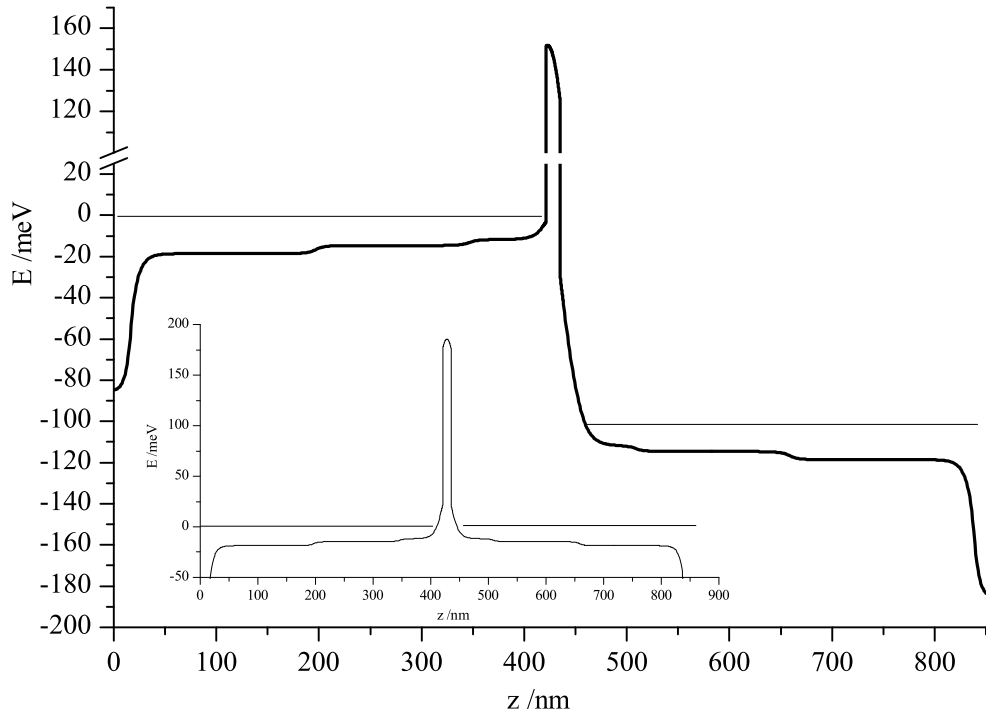


Figure 2.7: Self-consistent solution of the  $\Gamma$  conduction band of wafer *NU1673* with a bias of 100 mV applied between the contacts. The inset shows the conduction band with no applied bias. (Modelling program by Prof. G. L. Snider, University of Notre Dame.)

conduction band edge. This means that many of the QDs are occupied by electrons at zero bias, pushing up the energy of the conduction band in the vicinity of the barrier layer.

As with *NU1403*, the thickness of (AlGa)As grown before and after the InAs layer is nominally the same, but the thickness of (AlGa)As that caps each QD is reduced by the height of the QD. This means that the thickness of (AlGa)As covering a QD is 4 – 5 nm, compared with the 7 nm below it. Again, this will be an important point when considering the tunnel current through a QD.

Figure 2.7 shows the conduction band of *NU1673*, calculated using the computer program mentioned in section 2.4.2. The result shows clearly the heavily doped contact regions and the undoped spacer regions next to the barrier layer. The conduction band bending due to the negative charge in the QDs has been crudely estimated by simulating a number of acceptors in

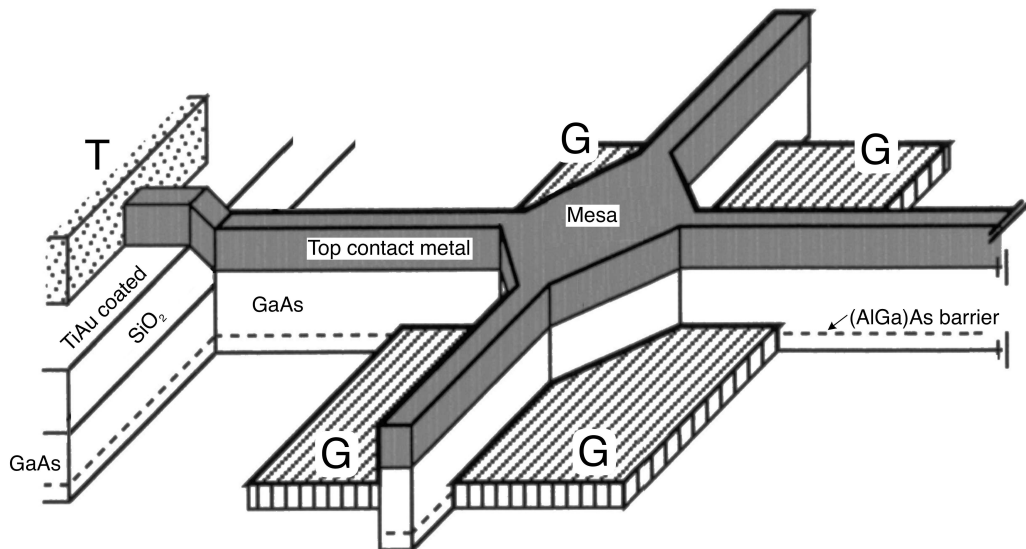


Figure 2.8: Diagram of a cross-mesa device, consisting of four narrow ( $0.2 \mu\text{m}$ ) arms which come together at a central square-shaped mesa,  $0.7 \mu\text{m}$  in diameter. The surface of the cross is metalised to provide a top contact. Four independently contacted gate electrodes, labelled G, are arranged around the central square of the cross. Wire bonds are made to either of the two top contact bond pads, labelled T (only one of which is shown in the figure). From Austing *et al.* (1999).

the barrier consistent with the number of QDs.

### Device fabrication

Several sub-micron scale ‘cross-shaped’ mesas were fabricated on small ( $10 \text{ mm} \times 10 \text{ mm}$ ) samples of wafer *NU1673* by using a combination of photolithography and electron-beam lithography techniques. The details of the fabrication are given in the following sections, and can also be found in the original paper by Austing *et al.* (1997a).

Figure 2.8 shows the structure of a single ‘cross-mesa’ device. An optical microscope image of a device, viewed from above, is shown in figure 2.9. The cross itself is defined by a combination of dry etching and wet chemical etching. The wafer is etched to a level just below the level of the (AlGa)As barrier layer (indicated in figure 2.8 by the broken line). Each cross consists of four narrow arms which come together at a central square-shaped mesa. The width of the arms are  $0.2 \mu\text{m}$  and the diameter of the central square is

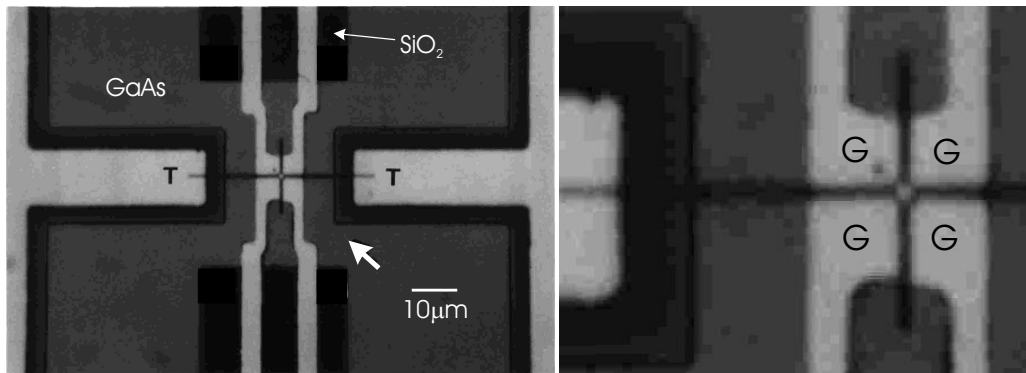


Figure 2.9: Optical microscope images of a cross-mesa device. The four gate electrodes are labelled G and the top contact bond pads are labelled T. The bond pads for each gate are not visible in these images but lie beyond the top and bottom of the picture. The white arrow indicates the view direction in figure 2.8. The right hand image is a close-up of the central area of the cross-mesa, showing the central square mesa, the four arms of the cross and the four gate electrodes (G).

0.7  $\mu\text{m}$ .

AuGeNi is deposited onto the back side of the wafer and annealed to produce a common ohmic back contact.

The surface of the cross is metalised to provide a top contact. The width of the arms are narrow enough that the surface depletion regions extend throughout the interior of each arm. Since the arms are devoid of carriers therefore, when a bias is applied between the top contact of the mesa and the common back contact, electrons flow only through the central square of the cross.

Four independently contacted gate electrodes are arranged around the central square of the cross. By applying voltage to these gates, the potential profile in the growth ( $xy$ ) plane of the barrier layer may be adjusted.

Because the mesa is too small to be able to bond a wire to it, wires are instead bonded to one of two contact pads sited at the ends of the two arms of the cross. Each pad sits on a layer of  $\text{SiO}_2$  to insulate it from the semiconductor surface underneath.

The devices were processed at the NTT Basic Research Laboratories, Atsugi, Japan, by the author under supervision from Dr. D. G. Austing. An

outline of each of the processing steps is given below and the process is also illustrated in figure 2.10.

### **Alignment marks**

The first step in the process, after the deposition and annealing of the back side contact, is to place TiAu alignment marks on the surface of the wafer, using standard photolithography techniques. These marks allow subsequent lithographies to be precisely aligned with one another.

### **Top-contact metal pads (Figure 2.10a)**

The second step in the process is to create the top contact metal pads to which the electrical wires can be bonded. (1) Photolithography is used to define two square areas per device that will become the top-contact metal pads. (2) The square areas are etched in a solution of 1 part  $\text{H}_2\text{O}_2$  to 30 parts  $\text{H}_2\text{SO}_4$  to 150 parts  $\text{H}_2\text{O}$  to a depth of approximately 80 nm. Since the etching rate is critically dependent on many factors, including the wafer composition, condition of the wafer surface, temperature of the etchant solution and exact strength of the solution, the etching process is tested first on small scrap pieces of the same wafer. (3) Between 80 nm and 150 nm of  $\text{SiO}_2$  is then sputtered into the wells left by the etching. This acts as an insulator, preventing direct conduction between the top contact pads and the substrate. (4) Approximately 30 nm of Ti followed by 20 nm of Au is evaporated on top of the  $\text{SiO}_2$  to form the contact pads. (5) Finally, the remaining photoresist and surplus  $\text{SiO}_2$  and metal is removed in acetone.

### **Electron-beam lithography (Figure 2.10b)**

The next step in the processing is to deposit the top contact metal of the cross mesa. The function of this metal is two-fold; (i) it acts as a mask for the subsequent etching processes, and (ii) the metal acts as an electrical connection between the surface of the mesa and the top contact bond pads. Because the laboratory photolithography equipment is unable to produce feature sizes as small as that of the arms of the cross ( $0.2 \mu\text{m}$ ), electron beam lithography is used instead.

Before applying the electron-beam resist to the surface, it was first cleaned by using an ozone stripper to remove any residual traces of photoresist left over from the previous photolithography.

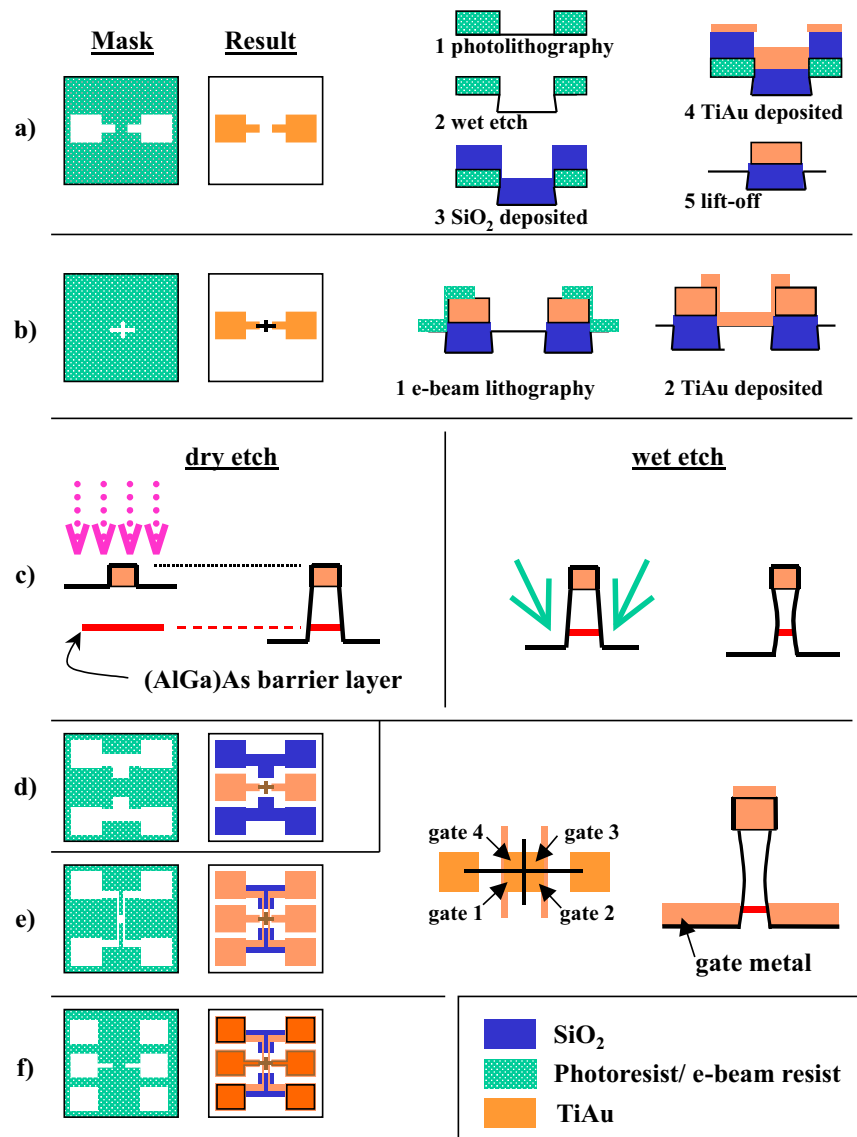


Figure 2.10: The main stages involved in fabricating a single cross-mesa device. a) Photolithography for top contacts. The diagrams numbered 1-5 show the steps involved in fabricating a single contact. b) Electron beam lithography for cross-mesa. c) Schematic diagrams illustrating the dry and wet-etching processes. The pillar represents the cross-mesa, viewed in cross-section. d) Photolithography for silicon oxide under gates. e) Photolithography for gate metal deposition. The illustrations on the right shows how the gate metal is deposited around the mesa. f) Photolithography for final contact pads.

An electron beam writer from JEOL was then used to write 136 separate cross patterns, precisely aligned to the top contact pads produced by the previous photolithography.

The electron beam resist was developed and the exposed surfaces cleaned in an argon plasma to remove all final traces of resist from the exposed surfaces.

An approximately 20 nm-thick layer of Ti followed by 150 nm of Au was then evaporated over the surface to form the surface metal layer of the cross.

Finally, the remaining electron-beam resist and surplus metal was removed in acetone.

#### **Dry and wet etch (Figure 2.10c)**

The vertical profile of the mesa is defined by a combination of dry and wet etching. A dry etch in a  $\text{BCl}_3$  plasma to a depth of  $\approx 450$  nm is performed first. This type of etch produces mesas with almost vertical side walls.

Next, the sample is etched in a solution of 1 part  $\text{H}_2\text{O}_2$  to 30 parts  $\text{H}_2\text{SO}_4$  to 150 parts  $\text{H}_2\text{O}$ , to give the vertical profile of the mesa a more hourglass-like shape (see figure 2.10c).

The depth of the wet etch is critical because gate metal will be deposited onto the wafer layer newly exposed by this etch. Ideally, the gate metal should be deposited onto a wafer layer that contains no doping in order that the Schottky potential barrier between the gate metal and the semiconductor be as wide as possible. However, we also require the gate metal to be deposited so that it lies in close proximity with the (AlGa)As barrier region. As a compromise, the etch was targeted to finish within the  $1 \times 10^{17} \text{ cm}^{-3}$ -doped, 70.5 nm-thick GaAs layer (see table 2.2). In order to achieve this accuracy with wet-etching, the etch was performed incrementally and the depth after each etch was checked by using an *Alpha-step* surface profiler from Tencor Instruments.

#### **Gate metal (Figure 2.10d,e)**

Before the gate metal is deposited, an additional photolithography is performed to deposit a layer of approximately 80 nm-thick  $\text{SiO}_2$  in the areas where the four gate *bond pads* will be deposited. This acts to insulate the

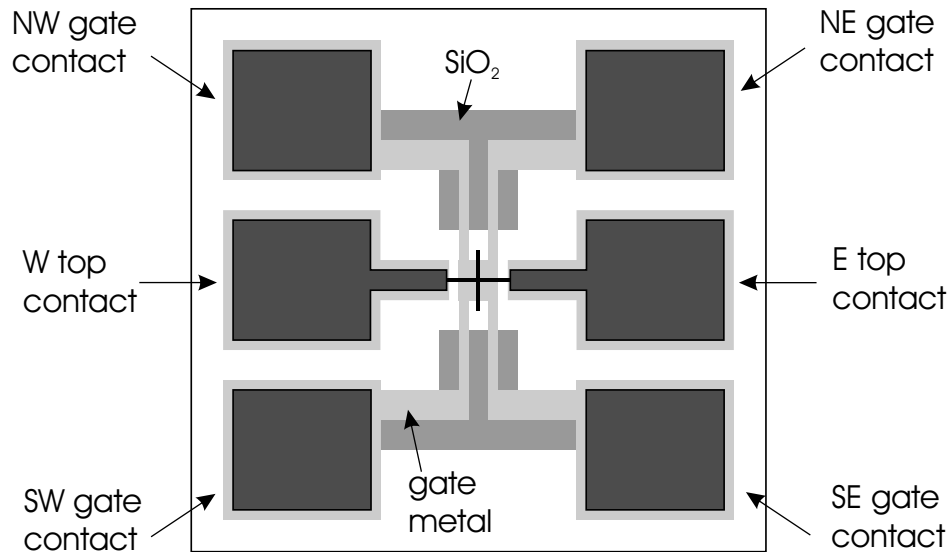


Figure 2.11: Diagram of a cross mesa device, viewed from above. The bond pads are named after points on the compass.

pads from the wafer surface underneath.

Photolithography is then used to define the areas to be covered by the gate metal (see figure 2.10e). These include four areas that will become the gate contact pads and a square region centred on the centre of the cross mesa that will form the gates proper. Approximately 45 nm of Ti followed by 45 nm of Au is then evaporated over the sample surface.

Crucially, the evaporation process is set up so that the beam of metal vapour strikes the surface at an angle perpendicular to the plane of the wafer. The hourglass-like profile of the mesa (produced by the previous wet etch) then prevents the gate metal being deposited up the side walls of the mesa (see illustration in figure 2.10e). In this way, the arms of the cross act to *split* the deposited gate metal into four *unconnected* regions to produce four independent gate electrodes.

### Contact pads (Figure 2.10f)

In the final photolithography, a thick layer of TiAu is deposited to complete the six square contact pads (figure 2.10f). The final device is shown in figure 2.11.

### Yield and post-process examination

The yield for the above fabrication process is small, often less than 5%.

Some of the most common reasons for the low yield are given below.

(i) The mesa top contact metal has to cross a slight step change in height where it runs off the bond pad and onto the semiconductor surface. This leaves the top contact metal prone to fracturing at the step and is one of the major reasons for the failure of a device.

(ii) Despite taking great care, during the lift-off process after the electron beam lithography, it frequently happened that the surplus metal would not detach from the cross metal cleanly, resulting in the cross metal being pulled from the surface.

(iii) The gate metal can fracture where the metal runs off the edge of the  $\text{SiO}_2$  insulation. In addition, for some cases, the gate metal does not stick well to the  $\text{SiO}_2$  and is removed along with the excess metal in the lift-off process.

(iv) Finally, if the vertical profile of the cross mesa does not have a sufficient undercut, or if the beam of metal vapour strikes the surface too far off perpendicular, then the gate metal can run up the sides of the mesa and make contact with the surface metal.

(v) One additional factor is that a small amount of damage occurs to the thin metal on top of the cross mesa every time a photolithography is performed.

Although the yield is quite low, the process produces a large number of devices on a single  $10 \times 10$  mm sample of wafer, so that each sample usually has around 5 workable devices. This means, however, that the devices must be examined at room temperature before testing the devices in a cryostat. All the devices are first examined under an optical microscope. Whilst the smallest ( $0.2 \mu\text{m}$ ) feature size of the device is beyond the limit of resolution of the optical (visible light) microscope, major defects such as metal missing from the mesa surface or damaged/missing gates are easily identified. Once the devices which are obviously defective have been eliminated, room temperature  $I(V)$  measurements are made on the remaining devices. This clearly identifies the other common faults: fractures of the metal on the top of the cross-mesa (little or no current flow), short circuit between one of

---

the top contacts and the substrate or between the top contact and the gate metal (current too large for a given voltage).

**Packaging**

Once a number of promising devices have been identified, the  $10 \times 10$  mm samples are scribed and cut up into smaller  $\sim 3 \times 3$  mm samples and mounted on TO5 headers, as explained in the fabrication section for *NU1403*.

# Chapter 3

## Resonant tunnelling through a single quantum dot

### 3.1 Introduction

In a tunnelling experiment electrons from below the Fermi energy can contribute to the tunnel current. For example, if a voltage is applied between two  $n$ -doped regions of GaAs, separated by an undoped potential barrier layer such as (AlGa)As, almost all of the potential drop occurs in the barrier layer. Electrons can tunnel from states *below* the Fermi level on the high potential side of the barrier into empty states above the Fermi level on the low potential side of the barrier, and a current flows. In this way, measurements of the tunnel current can provide information about electron states from below the Fermi surface.

Following work by several groups on resonant tunnelling via impurity states in GaAs/(AlGa)As/GaAs double barrier structures,\* Schmidt *et al.* (1996b, 1997) demonstrated the use of such an experiment to measure fluctuations in the local density of states (LDOS) of a three-dimensional electron system. In their experiment, electrons tunnel from a three-dimensional emit-

---

\*Resonant tunnelling via an impurity state in a GaAs/(AlGa)As system was first identified by Dellow *et al.* (1992). Also see, for example, Sakai *et al.* (1993), Geim *et al.* (1994a, 1994b), Deshpande *et al.* (1994, 1996), McDonnell *et al.* (1995), Sleight *et al.* (1996), Schmidt *et al.* (1996a)

ter, through 0D quasi-bound electron states belonging to impurities located within the central well of a double barrier structure. When a voltage is applied across the structure, the energy of the impurity states are moved to *lower* energy with respect to the Fermi level in the emitter. When a particular state of a particular impurity comes into resonance with an occupied electron state in the emitter, electrons resonantly tunnel from the emitter into the collector via the impurity, giving rise to a resonant tunnel current. Schmidt *et al.* observed oscillations in the resonant tunnel current as they increased the voltage across the device, reflecting fluctuations in the LDOS of the emitter as a function of energy. In this respect, the impurity state acts as a localised *spectrometer* of the states in the emitter adjacent to the impurity.

Shortly afterwards, Thornton *et al.* (1997)<sup>†</sup> demonstrated the use of resonant tunnelling via a single 0D state of an InAs self-assembled QD as a localised spectrometer of the LDOS in a 2DES. In this experiment, InAs QDs are embedded within the barrier layer of a GaAs/AlAs/GaAs single tunnelling barrier device. When a voltage is applied across the device, a 2DES is formed within a roughly triangular-shaped potential well adjacent to the barrier. By adjusting the voltage across the device, quasi-bound electron states belonging to different QDs can be brought into resonance with occupied states in the 2DES. In this way, the QDs in this experiment act in a similar way to the impurity states in the experiment by Schmidt *et al.*.

In both experiments, the thickness of the potential barrier through which the electrons tunnel into the impurity or QD state is thicker than that through which they tunnel out, into the collector. In the experiment by Schmidt *et al.* the barrier thicknesses are 5 nm and 8 nm. In the experiment by Thornton *et al.* the thickness of the AlAs barrier covering each QD is 2–3 nm, compared to 5 nm below it. Since the tunnelling rate decreases exponentially with tunnelling thickness, the rate with which electrons tunnel out of the impurity/QD is much larger than the rate at which they tunnel in. Consequently, the magnitude of the tunnel current is limited by the tunnelling-in rate, whilst the spectral width of the quasi-bound impurity/QD

---

<sup>†</sup>See also Itskevich *et al.* (1996)

states is governed by the tunnelling-out rate.

In this chapter it will be demonstrated how a single state of a single InAs QDs can be used as a spectroscopic probe of the LDOS in 2DES, from the Fermi level down to the 2D sub-band edge.

## 3.2 Devices

The devices used in this chapter, and in chapters 4 and 5, are circular mesas of between 5 and 100  $\mu\text{m}$  in diameter, fabricated from material *NU1403* as discussed in section 2.4.2. The QD density in this material was estimated by scanning electron and tunnelling microscopy to be of the order of  $2 \times 10^{15} \text{ m}^{-2}$  (Itskevich *et al.* 1996). This implies that we have  $\sim 40000$  QDs in a 5  $\mu\text{m}$  mesa and  $\sim 20 \times 10^6$  QDs in a 100  $\mu\text{m}$  mesa.

Figure 3.1 shows a stylised version of the  $\Gamma$  conduction band. As discussed in section 2.4.2, when a voltage is applied between the source and drain contacts of the device, an electron accumulation layer forms against the AlAs barrier; at low temperatures this forms a 2DES. As the bias on the device is increased, the sheet density,  $n_s$ , of electrons in the 2DES also increases in accordance with Gauss's law.

A resonant tunnel current flows when a QD electron state is resonant with an occupied state in the 2DES. An important feature of the experiment is that *increasing the bias across the device causes the QD states to move to lower energy with respect to the 2DES* (see figure 3.2). In this way, the energy of a particular QD state can be 'tuned' to resonate with different states in the 2DES by varying the bias. Thus, as the bias is increased, we expect peaks in the tunnel current to be observed as successive QD states become resonant with occupied states in the 2DES.

## 3.3 Low temperature $I(V)$ characteristics

Figure 3.3 shows typical low temperature  $I(V)$  traces taken from 100  $\mu\text{m}$  diameter mesas of *NU1403*. The inset to the figure shows an  $I(V)$  trace

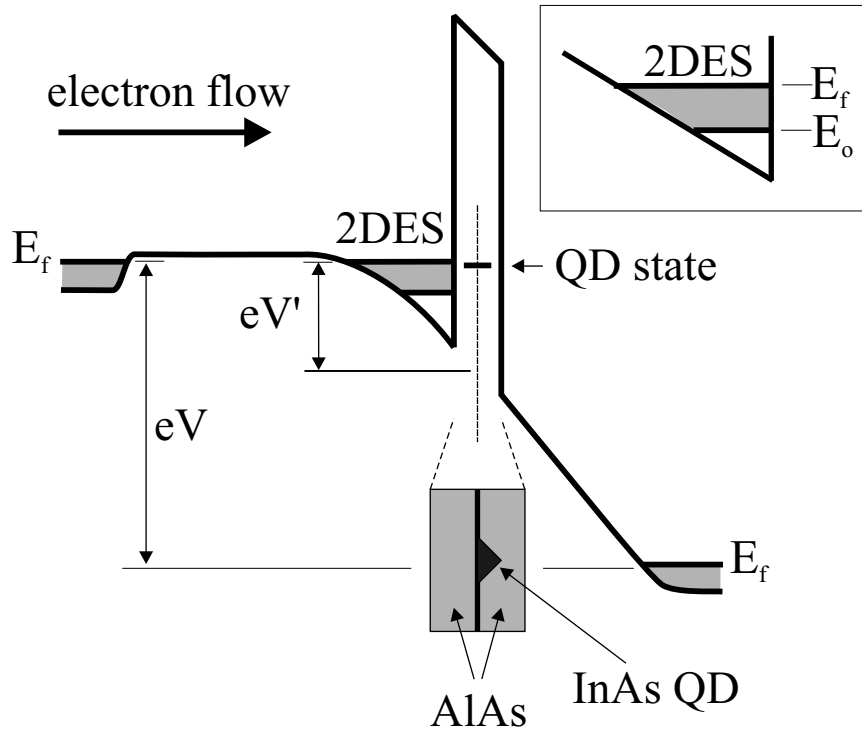


Figure 3.1: Stylised diagram of the  $\Gamma$  conduction band of *NU1403* under an applied voltage,  $V$ . The broken vertical line in the centre plane of the barrier represents the InAs layer. A single 0D state of a single QD is identified by a thick horizontal line in the barrier. The grey shading represents occupied states in the 2D emitter and the contacts. The voltage  $V'$  represents the voltage dropped between the emitter layer and the InAs layer,  $dV' = dV/\mathcal{F}$ , where  $\mathcal{F}$  is an electrostatic leverage factor, of the order  $\mathcal{F} \sim 10$  for this device. The inset at the bottom of the diagram shows the geometry of the QD within the AlAs barrier. The inset top-right shows the position of the Fermi level,  $E_F$ , and the 2D sub-band edge,  $E_0$ , in the emitter.

taken from a  $5 \mu\text{m}$  diameter mesa of *NU1403*. An  $I(V)$  trace from a  $100 \mu\text{m}$  mesa of the control material—exactly the same as *NU1403* but without the InAs layer—is included for comparison.

We define forward bias to mean the bias polarity in which the electrons tunnel into the QD through the thicker AlAs barrier, and out through the thinner layer (section 2.4.2). In this thesis, forward bias is defined as a *positive* voltage.

All traces show a very high impedance close to zero voltage ( $\sim 1 \times 10^{12} \Omega$ ) and a background current that increases exponentially with increasing voltage. Since this background current is evident in all samples—including the control sample—and scales roughly with the area of the mesa, it is attributed

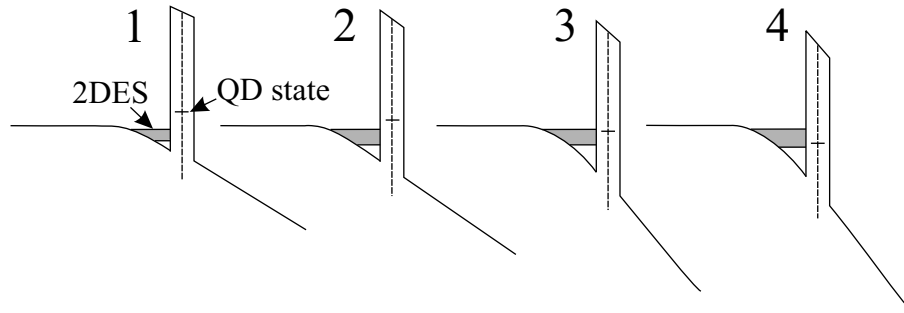


Figure 3.2: Four stylised diagrams of the  $\Gamma$  conduction band of *NU1403*. The diagrams show how the energy of a QD state changes, relative to the Fermi level in the 2DES, as the voltage between the contacts is increased. In the first, left-most diagram, a small voltage has been applied to the device and the energy of the QD state lies above the Fermi level in the 2DES. As the voltage is increased (diagrams 2 and 3) the QD state is eventually brought into resonance with the Fermi level (diagram 3). As the voltage is increased still further, the energy of the QD state moves below the Fermi level (diagram 4), and eventually moves below the 2DES sub-band edge.

to non-resonant tunnelling directly across the 10 nm AlAs layer.

The traces from the samples including the InAs layer show some additional fluctuations superimposed upon the exponentially rising background current. Since these fluctuations are not seen in the control sample, such fluctuations can only be due to the presence of the InAs layer. It can be seen that the  $I(V)$  traces show qualitatively different behaviour depending on the polarity of the bias. For positive voltages, the fluctuations are of the form of series of peak-like oscillations, while for negative voltages, the  $I(V)$  takes the form of a series of steps.

At higher bias,  $V \gtrsim 1$  V, we have observed larger, more slowly varying features, with widths of 100 – 300 mV. It is possible that these features are due to resonant tunnelling through states in the two-dimensional InAs wetting layer, or confined states in the AlAs  $X$ -band quantum well, such as has been observed in similar devices by Suzuki *et al.* (1997) and Hapke-Wurst *et al.* (1999).

Focussing more closely on the fluctuations in forward bias, it can be seen that there are a small number of single peaks at low voltage that are isolated from the others by regions of ‘quiet’ current, showing no fluctuations. In the following section it will be argued that such fluctuations can be attributed to resonant tunnelling through zero-dimensional states of the InAs

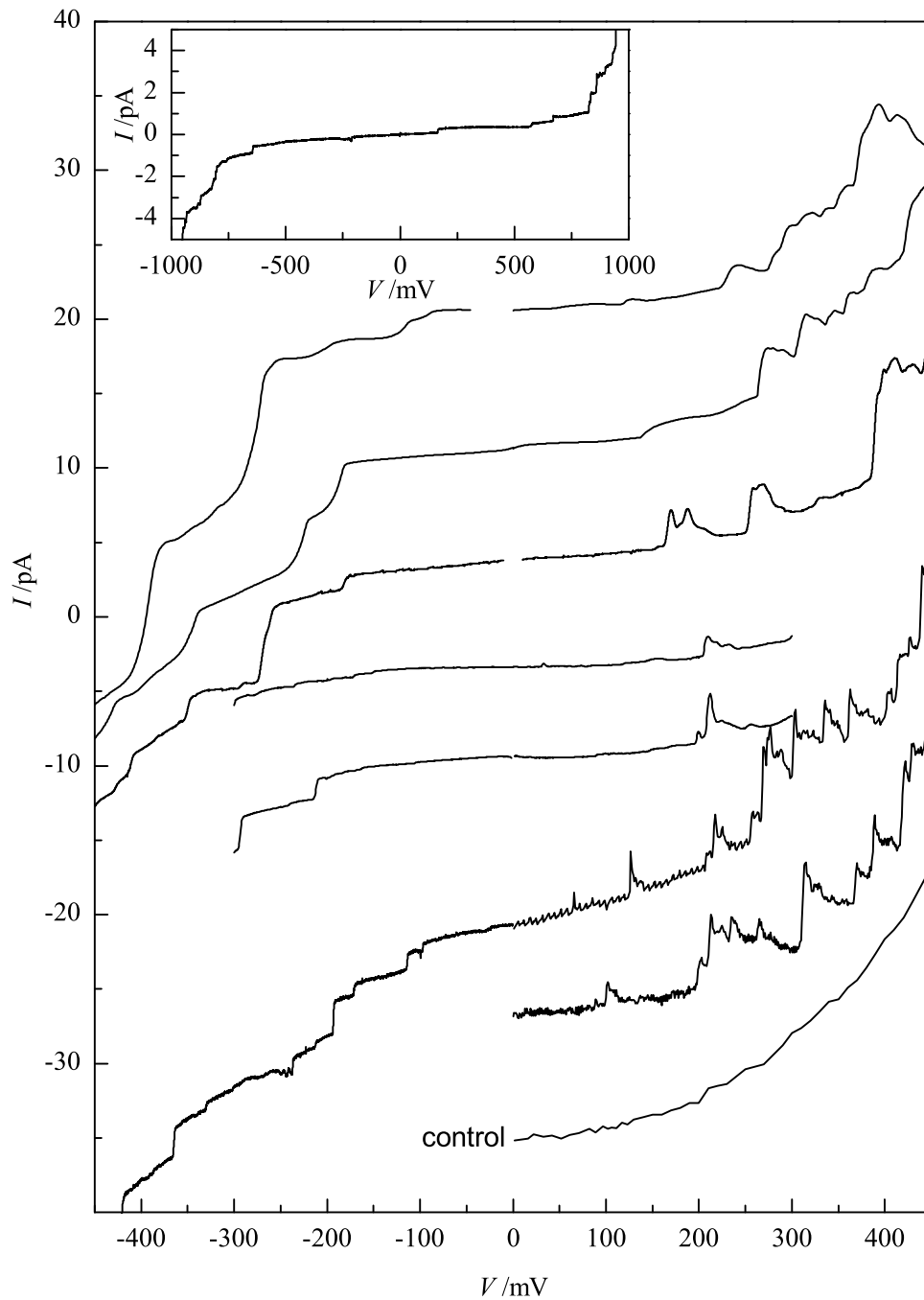


Figure 3.3: Typical  $I(V)$  traces taken from  $100\ \mu\text{m}$  diameter mesas of *NU1403*. The traces are offset for clarity. In positive ('forward') bias, the electrons tunnel into the QDs through a thicker AlAs barrier, and out through a thinner barrier (section 2.4.2). The inset shows a trace from a  $5\ \mu\text{m}$  mesa of *NU1403*. The temperature in all cases is  $0.3\ \text{K}$ . An  $I(V)$  trace taken from a  $100\ \mu\text{m}$  diameter mesa of the control material, containing no InAs layer, is included for comparison.

QDs embedded within the barrier. In section 3.6 we focus more specifically on the isolated features at low bias and argue that each individual feature corresponds to resonant tunnelling through a single state of a single QD.

### 3.4 Evidence for tunnelling via quantum dot states

In this section we argue that the observed fluctuations in  $I(V)$  below  $|V| = 0.5$  V are due to resonant tunnelling via states bound to the InAs QDs embedded within the AlAs barrier. Firstly, we note that there are no such features present in the  $I(V)$  of the control sample. This fact would appear to rule out the possibility that, at least for  $|V| \lesssim 0.5$  V, resonant tunnelling via other candidates such as defect or impurity-related states within the AlAs barrier (Itskevich *et al.* 1998, Vitusevich *et al.* 2000), or bound states in the  $X$ -valley minimum of the AlAs barrier (Finley *et al.* 1998, Hapke-Wurst *et al.* 1999) are responsible for the fluctuations in  $I(V)$ . This strongly indicates that the features must be associated with the presence of the InAs layer.

Nevertheless, whilst we do not observe such fluctuations in the  $I(V)$  of our control sample, experiments on comparable devices have found resonant features in  $I(V)$  due to tunnelling through  $X$ -valley-related impurity states (Fukuyama and Waho 1995, Khanin *et al.* 1998, Itskevich *et al.* 1998, Vitusevich *et al.* 2000). Although in our device the AlAs layer is *nominally* undoped, Si donors can migrate from the heavily doped contact regions into the undoped layers.  $\Gamma$ -related donor bound states are too high in energy to observe resonant tunnelling through these states. However, the  $X$ -valley-related donor bound states have energies low enough relative to the emitter states that resonant tunnelling might occur via the donors at reasonably low voltages (in our case  $\lesssim 1$  V). This is because the bottom of the  $X$ -valley in AlAs lies only about 100 – 200 meV above the bottom of the  $\Gamma$ -valley in GaAs, and the donor binding energy of  $X$ -valley related states in AlAs has been found to be relatively large, about 50–100 meV (Weber 1995, Itskevich *et al.* 1998, Vitusevich *et al.* 2000). Hence, by application of a small voltage to the device, such  $X$ -valley related states might be brought into resonance

with occupied states in the 2D emitter in our device.

To explore the possibility of tunnelling via  $X$ -valley related impurity states we apply high quasi-hydrostatic pressure to the device and measure the shift in the voltage positions of the resonant features with pressure. The energies of the  $\Gamma$  and  $X$  band edges change at different rates with pressure. Therefore, high pressure experiments provide a way of distinguishing between tunnelling via  $\Gamma$  related states and  $X$  related states. The details of this experiment are given in section 3.8; we indeed find evidence that some resonant features in  $I(V)$  are due to tunnelling through such  $X$ -related states. However, all such features that we observe lie above  $V \sim 300$  mV at atmospheric pressure. On the other hand, we find strong evidence that the resonances observed at lower voltage are due to tunnelling through states bound to the QDs.

It has been suggested that point *defects* in the AlAs lattice can arise as a *consequence* of QD formation (Belyaev *et al.* 2000). This opens up the possibility that we may be observing resonant tunnelling via deep-level states bound to defects in the AlAs caused by the presence of the QDs.

To investigate this possibility Itskevich *et al.* (1996) measured the shift in the voltage positions of the  $I(V)$  fluctuations with magnetic field applied parallel to the current direction ( $B \parallel z$ ). This enabled them to estimate the diamagnetic shift in energy of the candidate bound state relative to the states in the emitter, and thus obtain an estimate of the spatial extent of the bound-state wave function. Similar experiments have been performed by Hapke-Wurst *et al.* (1999). Itskevich *et al.* noted that deep level defect-related states should have wave functions that are localised on the scale of the lattice constant,  $\sim 0.6$  nm. On the other hand, the wave function of a state bound to a QD should have a much larger extent, comparable to the size of the QD, i.e. of the order of 10 nm. Therefore, it is possible to distinguish tunnelling via defect states from tunnelling via states bound to QDs.

Both groups find that their measurements of the extent of the bound state wave function are *inconsistent* with tunnelling through deep level defect states. Conversely, their results *are* consistent with the size of the InAs QDs as estimated from SEM images (in the case of Itskevich *et al.*) and

TEM/AFM images (in the case of Hapke-Wurst *et al.*).

### 3.4.1 Coulomb blockade

Compelling evidence to support the theory that resonant tunnelling is via QD states comes from the asymmetry in the  $I(V)$  between positive and negative bias. If the reverse bias current is examined, step-like features in the  $I(V)$  can be seen. Notice that these features are almost wholly absent in the forward bias current, which shows peak-like behaviour instead. This asymmetry can be explained if we assume that both the step-like features in reverse bias and the peak-like features in forward bias are due to resonant tunnelling via QD states.

In the sequential tunnelling picture (section 1.7.1) resonant tunnelling through a QD state is broken into two sequential stages: (a) electron tunnels from the 2DES, through the AlAs barrier into the QD, and (b) electron tunnels from the QD, through the AlAs barrier, into the collector. The thickness of AlAs *capping* a QD is expected to be significantly smaller than the thickness of AlAs *under* the QD (see section 2.4.2). Therefore, in forward (positive) bias, the electrons tunnel into the QD through a thicker layer of AlAs and out through a thinner layer of AlAs. In reverse (negative) bias, the opposite happens; the electron first tunnels through the thin barrier and then out through the thick barrier. Therefore, an asymmetry in the  $I(V)$  characteristic is expected for resonant tunnelling via QDs.

Since the tunnelling probability decreases exponentially with increasing barrier thickness the tunnelling rate across the thick barrier,  $\gamma_{\text{thick}}$ , is much less than the tunnelling rate across the thinner barrier,  $\gamma_{\text{thin}}$ . We can use the tunnelling rate calculated for a single one-dimensional barrier (equation 1.39) to obtain an ‘order-of-magnitude’ estimate for the ratio of  $\gamma_{\text{thick}}$  to  $\gamma_{\text{thin}}$ . Since  $\gamma$  is proportional to the tunnelling probability  $T$ ,

$$\frac{\gamma_{\text{thick}}}{\gamma_{\text{thin}}} \sim \exp[-2\kappa(l_{\text{thick}} - l_{\text{thin}})], \quad (3.1)$$

where  $\kappa \approx \hbar^{-1}\sqrt{2m^*U_b}$ ,  $U_b$  is the barrier height, and  $l_{\text{thick}}$  and  $l_{\text{thin}}$  are the thicknesses of the thick and thin barriers respectively. In this case,  $U_b \approx$

1000 meV,  $l_{\text{thick}} = 5$  nm and  $l_{\text{thin}} \approx 2 - 3$  nm, so that  $\gamma_{\text{thick}}/\gamma_{\text{thin}} \sim 1/200$ . Hence, in forward bias, electrons tunnel out of the QD almost as soon as they tunnel in.

Conversely, in reverse bias an electron that has tunnelled into the QD dwells there for some time before tunnelling out, whereupon it is replaced almost immediately by another electron tunnelling in. Therefore, when the ground state of a particular QD is brought into resonance with the 2DES—by adjusting the bias across the device—the QD becomes charged with one electron. While the ground state can accommodate two electrons (spin up and spin-down), to put the second electron into the ground state requires some extra energy to overcome the repulsive Coulomb force between the electron tunnelling in and the electron already dwelling on the QD. This extra Coulomb energy can be written as  $e^2/C$  where  $C$  is the capacitance between the QD and the ‘outside world’. Therefore, at the voltage where the ground state comes into resonance with the Fermi level of the 2DES, we see a step increase in the current, due to tunnelling through a single spin state. A second step is observed, due to tunnelling through the second spin state, only when the voltage has increased sufficiently to overcome the charging energy  $e^2/C$  (Kelly 1995).<sup>‡</sup> This is known as Coulomb blockade. In forward bias, this effect is not observed since the QD is unoccupied for most of the time. A very similar effect has been observed in resonant tunnelling diodes with asymmetric barriers (Su *et al.* 1992).

It is difficult to see how such asymmetry in the  $I(V)$  could arise if tunnelling were due to impurity or defect states in the AlAs barrier instead. Certainly, the tunnelling-in and tunnelling-out barrier thicknesses for a *particular* impurity or defect state are unlikely to be equal. However, it is reasonable to assume that the *ensemble* of impurities/defects are distributed fairly evenly throughout the AlAs barrier and thus we would not expect to see such a striking overall asymmetry in the  $I(V)$ .

---

<sup>‡</sup>In general, the extra energy required to overcome the Coulomb repulsion and place an extra electron on the QD is  $Ne^2/C$  where  $N$  is the number of electrons already dwelling on the QD. This energy is in addition to the quantum confinement energy.

### 3.4.2 Isolated resonant features at low voltage

The evidence given above points strongly to resonant tunnelling via the QDs buried with the AlAs barrier, rather than other possible candidates such as defects or impurities. However, if we are to attribute the resonant features in  $I(V)$  to resonant tunnelling through QDs, we must address the problem of why we observe only a few resonant features ( $\sim 5$ ) below 300 mV in 100  $\mu\text{m}$ -diameter mesas. In section 3.6 evidence is obtained indicating that such isolated features are due to resonant tunnelling through *individual* bound states. This is surprising, considering that a 100  $\mu\text{m}$ -diameter mesa contains of the order of  $20 \times 10^6$  QDs in the tunnel barrier.

Photoluminescence measurements on *NU1403* (section 2.4.2) suggest that the energy level distribution of QD ground electron states is peaked  $\sim 100$  meV above the GaAs conduction band edge, and therefore the Fermi level in the 2DES. Hence, it is possible that at low bias we only observe tunnelling through a small number of QDs with electron states in the lower energy ‘tail’ of the distribution. Consistent with this picture, the ‘density’ of resonant features in  $I(V)$  that we observe increases with voltage (figure 3.3). However, since the (FWHM) width of the distribution in the QD ground electron levels is measured to be around 150 meV (section 2.4.2), it is still surprising that we observe so few resonant features, even at  $V = 0$ . As yet, we do not have a satisfactory explanation for why we are able to observe tunnelling through individual QDs at low bias. We note that Narihiro *et al.* (1997) and Suzuki *et al.* (1997) have also observed such isolated resonances at low bias in similar devices, so it is not a phenomenon unique to *NU1403*.

## 3.5 A model for the resonant tunnel current

In section 1.7.1 it was shown how the resonant tunnelling of electrons through a 0D state can be described as a sequential process, in which electrons tunnel from an emitter sub-system, into a well and then out into a collector sub-system. In this section, the sequential tunnelling picture is used to model the resonant tunnel current through a single QD. The resonant tunnel current

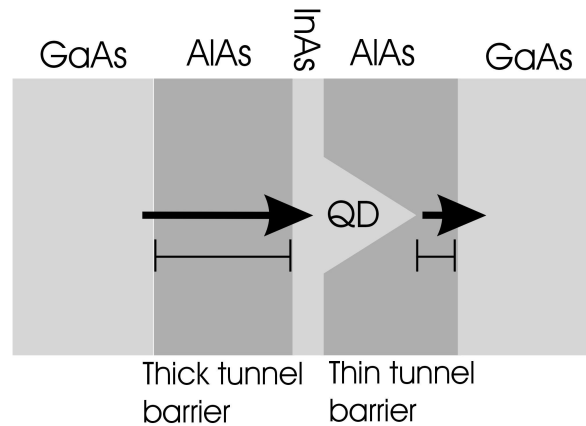


Figure 3.4: Resonant tunnelling through a QD viewed as a two stage sequential process. In forward bias the electron tunnels first through a 'thick' barrier of AlAs, into the QD and then out through a thinner AlAs barrier.

through a single QD state is found to be approximately proportional to the LDOS in the adjacent 2DES at the energy of the QD state and the location of the QD in the  $xy$  plane. By changing the bias on the device, the energy of the QD state can be tuned so that it may be brought into resonance with different states in the 2DES. In this way, the LDOS of the 2DES can be measured from the Fermi level down to its sub-band edge.

Figure 3.4 shows the geometry of a QD embedded in the AlAs barrier. In forward bias the electrons tunnel first from the emitter, through the thick barrier of AlAs, into the QD and then out through the thinner barrier of AlAs capping the QD and into the collector (section 2.4.2). In reverse bias the opposite occurs and the electrons first tunnel through the thin barrier, into the QD and out through the thick barrier. As discussed above, on the application of a voltage between the contacts of the device, a 2DES is created in the triangular potential well against the AlAs barrier. In the sequential tunnelling picture this triangular well forms the *emitter* sub-system (e). The well sub-system (w) represents the potential well formed in the AlAs layer by the presence of a QD. The collector sub-system (c) consists of the heavily doped positive contact and the undoped spacer region between the contact and the barrier. Idealised potential profiles for each sub-system are shown

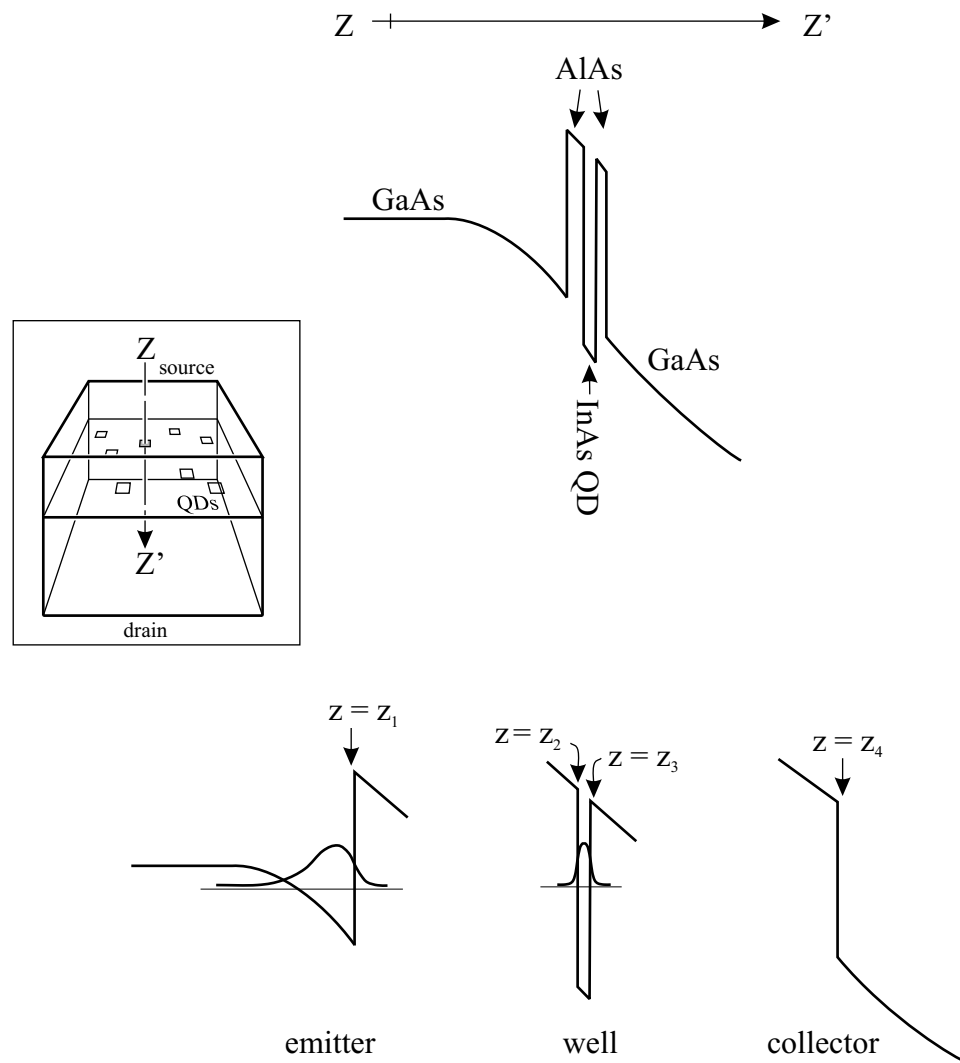


Figure 3.5: The top diagram shows the conduction band for *NU1403* under applied bias. The conduction band has been plotted for a line  $ZZ'$  which runs vertically (from source to drain) through a single InAs quantum dot, as depicted in the boxed inset. The potential well in the centre of the AlAs barrier represents the potential well due to the InAs quantum dot. In the bottom three diagrams, the conduction band has been divided into three sub-systems: an emitter which contains the 2DES, a well which represents the quantum dot, and a collector.

in figure 3.5.

### 3.5.1 Emitter state wave function

In section 1.7.2 we assumed that the wave functions of the electrons in the emitter sub-system took the form  $\psi(x, y, z) = \exp(ik_x x + ik_y y)\chi(z)$ . This assumes that the emitter potential well has translational invariance in the  $xy$  plane. In any real device, however, the emitter potential well is perturbed by the randomly distributed remote impurities (dopants) and defects in the crystal. In this section we will not assume that the potential profile of the emitter sub-system has translational invariance in the  $xy$  plane. However, we will make the assumption that the potential is still separable into  $xy$  and  $z$  components. With this assumption in mind, we write the emitter wave function in the more general form,

$$\psi_e^{(j)}(x, y, z) = \phi_e^{(j)}(x, y)\chi_e(z). \quad (3.2)$$

Since the emitter is a two-dimensional system, only the lowest sub-band in the emitter is occupied. Therefore, the  $z$  component of the wave function,  $\chi_e(z)$ , is the same for all occupied states in the emitter. To aid clarity later on, we will use the notation  $\phi_j$  to mean  $\phi_e^{(j)}$ .

### 3.5.2 Quantum dot state wave function

Following the arguments given in section 1.7.2, we make the approximation that the QD electron wave function is separable into  $xy$  and  $z$  components,

$$\psi_{\text{qd}}^{(m,n)}(x, y, z) = \phi_{\text{qd}}^{(m)}(x, y)\chi_{\text{qd}}^{(n)}(z). \quad (3.3)$$

Since we shall be calculating the current through a single QD state (rather than the sum current through all states in the QD) we shall drop the indices on the QD wave functions for clarity.

### 3.5.3 Current flow between the emitter and quantum dot state

From equation 1.41 and equation 1.44, the current flow between the emitter and a single state of a QD is

$$\begin{aligned} I &= e \frac{2\pi}{\hbar} \sum_j |\mathcal{V}_j|^2 [\rho_e(E_j) - \rho_{\text{qd}}] \delta(E_j - E_{\text{qd}}) \\ &\propto [\rho_e(E_{\text{qd}}) - \rho_{\text{qd}}] \sum_j |\mathcal{V}_j|^2 \delta(E_j - E_{\text{qd}}), \end{aligned} \quad (3.4)$$

where  $\rho_e(E)$  is the occupancy of a state in the emitter with energy  $E$ ,  $\rho_{\text{qd}}$  is the occupancy of the QD state, and  $E_j$  and  $E_{\text{qd}}$  are the energies of the  $j$ th emitter state and the QD state respectively.  $\mathcal{V}_j$  is the transfer matrix element for tunnelling between state  $|j\rangle$  in the emitter and the QD state (section 1.7.1). The sum is over all occupied states,  $|j\rangle$ , in the emitter.

#### Transfer matrix element

Since we have used wave functions that are separable into  $xy$  and  $z$  components, the transfer matrix element  $\mathcal{V}_j$  can be written as (section 1.7.2)

$$\mathcal{V}_j = \frac{-\hbar^2}{2m^*} \times \mathcal{M}_j \times \mathcal{T}, \quad (3.5)$$

where

$$\mathcal{M}_j = \int_{xy} \phi_j^*(x, y) \phi_{\text{qd}}(x, y) dx dy, \quad (3.6)$$

and

$$\mathcal{T} = \left[ \chi_e^* \frac{d}{dz} \chi_{\text{qd}} - \chi_{\text{qd}} \frac{d}{dz} \chi_e^* \right]_{z_1 < z < z_2}. \quad (3.7)$$

The derivative is performed at any value of  $z$  within the barrier region common to both the emitter and QD sub-systems.

We write the matrix element,  $\mathcal{M}_j$ , in its equivalent form in  $k$ -space,

$$\mathcal{M}_j = \int_{k_x k_y} \tilde{\phi}_j^*(k_x, k_y) \tilde{\phi}_{\text{qd}}(k_x, k_y) dk_x dk_y, \quad (3.8)$$

where  $\tilde{\phi}_j$  and  $\tilde{\phi}_{\text{qd}}$  are the Fourier transforms of  $\phi_j$  and  $\phi_{\text{qd}}$  respectively.

The Fourier transform of the QD wave function can be written as

$$\tilde{\phi}_{\text{qd}}(\mathbf{k}) = \tilde{\Phi}_{\text{qd}}(\mathbf{k}) \exp(-i\mathbf{k} \cdot \mathbf{R}), \quad (3.9)$$

where  $\mathbf{R}$  is the position of the QD in the  $xy$  plane and  $\tilde{\Phi}_{\text{qd}}(\mathbf{k})$  is the Fourier transform of  $\Phi_{\text{qd}}(\mathbf{r}) = \phi_{\text{qd}}(\mathbf{r} + \mathbf{R})$ . Note that the vectors  $\mathbf{k}$ ,  $\mathbf{r}$  and  $\mathbf{R}$  all lie in the  $xy$  plane. The matrix element  $\mathcal{M}_j$  then becomes

$$\mathcal{M}_j = \int_{k_x k_y} \tilde{\phi}_j^*(\mathbf{k}) \tilde{\Phi}_{\text{qd}}(\mathbf{k}) \exp(-i\mathbf{k} \cdot \mathbf{R}) d\mathbf{k}. \quad (3.10)$$

We now assume that the random perturbations to the emitter potential (due to the remote donors) are weak enough so that the emitter wave function  $\tilde{\phi}_j$  is a much more sharply peaked function in  $k$ -space than that of the QD wave function  $\tilde{\Phi}_{\text{qd}}$ . With this assumption, we can make the approximation

$$\begin{aligned} \mathcal{M}_j &\approx \tilde{\Phi}_{\text{qd}}(\mathbf{K}_j) \int_{k_x k_y} \tilde{\phi}_j^*(\mathbf{k}) \exp(-i\mathbf{k} \cdot \mathbf{R}) d\mathbf{k} \\ &\propto \tilde{\Phi}_{\text{qd}}(\mathbf{K}_j) \phi_j^*(\mathbf{R}), \end{aligned} \quad (3.11)$$

where  $\mathbf{K}_j$  lies in the  $xy$  plane and represents the point in  $k$ -space where the emitter wave function  $\tilde{\phi}_j$  is peaked.

### Resonant current as measure of the local density of states in the emitter

Inserting the result equation 3.11 into equation 3.4, we obtain

$$I \propto [\rho_e(E_{\text{qd}}) - \rho_{\text{qd}}] |\mathcal{T}|^2 \sum_j \left| \tilde{\Phi}_{\text{qd}}(\mathbf{K}_j) \phi_j^*(\mathbf{R}) \right|^2 \delta(E_j - E_{\text{qd}}), \quad (3.12)$$

where the sum is again over all occupied states in the emitter.

We now compare the extent (in  $k$ -space) of the wave function  $\tilde{\Phi}_{\text{qd}}(\mathbf{k})$  with the Fermi wave number in the 2DES. In order to do this, we approximate the QD confining potential in the plane by a parabolic potential,  $U_r \approx \frac{1}{2}m\omega^2 r^2$ ,

where  $\omega = \hbar/ml^2$ , and  $l$  is the in-plane radius of a typical QD,  $l \approx 5$  nm. The characteristic size of the QD wave function in  $k$ -space is then  $\sigma = 1/l \approx 0.2$  nm<sup>-1</sup>. In comparison, the Fermi wave number in the 2DES is  $k_F = \hbar^{-1}\sqrt{2mE_F}$ . In section 3.7.2, we find that the Fermi energy of the 2DES is  $E_F \sim 4$  meV; this corresponds to a Fermi wave number,  $k_F \approx 0.08$  nm<sup>-1</sup>. In other words, the range of values of  $\mathbf{K}$  that represent *occupied* states in the emitter is small in comparison to the extent of the QD wave function  $\tilde{\Phi}_{\text{qd}}$  in  $k$ -space. Therefore, we assume that the tunnel current is only weakly dependent on  $\tilde{\Phi}_{\text{qd}}(\mathbf{K})$  so that

$$I \propto [\rho_e(E_{\text{qd}}) - \rho_{\text{qd}}] |\mathcal{T}|^2 \sum_j \left| \phi_j^*(\mathbf{R}) \right|^2 \delta(E_j - E_{\text{qd}}). \quad (3.13)$$

Using the definition of the local density of states from equation 1.27, we then obtain

$$I \propto [\rho_e(E_{\text{qd}}) - \rho_{\text{qd}}] |\mathcal{T}|^2 D(E_{\text{qd}}, \mathbf{R}), \quad (3.14)$$

where  $D(E_{\text{qd}}, \mathbf{R})$  is the local density of states in the emitter at the  $xy$  position  $\mathbf{R}$  of the QD, and energy  $E_{\text{qd}}$  of the QD electron state.

The current flow between a single state of a QD and the collector is found in a similar way to that between the emitter and the QD, except that the collector is a 3D system, so we must sum over all 2D sub bands in the collector to obtain the current.

### 3.5.4 Forward bias tunnel current

In equilibrium, the current flow from the emitter to the QD,  $I_{e \rightarrow \text{qd}}$ , must equal that of the QD to the collector,  $I_{\text{qd} \rightarrow c}$ . In general, the equilibrium resonant current through the QD state is found by equating  $I_{e \rightarrow \text{qd}}$  with  $I_{\text{qd} \rightarrow c}$  to determine the occupancy of the QD in equilibrium. The resonant current can then be determined from equation 3.14. However, in section 3.4, we estimated that, in forward bias, for our device, the tunnelling rate across the emitter-side barrier is much smaller than the tunnelling rate across the collector-side barrier. Therefore we can assume that the occupancy of the QD is  $\rho_{\text{qd}} \approx 0$ . Hence, the resonant tunnel current through the QD in forward

bias is given by

$$I \propto \rho_e(E_{\text{qd}})D_e(E_{\text{qd}}, \mathbf{R})|\mathcal{T}_{e \rightarrow \text{qd}}|^2. \quad (3.15)$$

The important result is that we expect the resonant tunnel current to be proportional to the LDOS in the emitter.

### 3.5.5 Variation in the resonant current with voltage

#### Leverage factor

When the bias across the device contacts,  $V$ , is changed, there is a corresponding change in the voltage drop,  $V'$ , between the 2DES accumulation layer and the InAs layer (see figure 3.1). We define the *leverage* factor,  $\mathcal{F}$ , as the rate-of-change of  $V'$  with respect to  $V$ ,

$$\mathcal{F}^{-1} = \frac{dV'}{dV}. \quad (3.16)$$

In general, the leverage factor is not a constant, but changes with  $V$ . However, the variation in  $\mathcal{F}$  is slow enough that, over a small range of bias ( $\Delta V \sim 100$  mV), the leverage factor can be taken to be a constant. This means that, for a small change  $\Delta V$  in the applied voltage, the corresponding change in  $V'$  can be approximated by

$$\Delta V' \approx \frac{\Delta V}{\mathcal{F}}. \quad (3.17)$$

#### Change in the energy of a QD state with voltage

We assume that the energy of the quasi-bound QD states are unaffected by bias since the electric field produced by the bias is small compared to the electric field that confines the electron to the QD. Therefore, the energy of a QD state with respect to the Fermi level in the 2DES varies with  $V'$  simply as

$$E_{\text{qd}}(V') = E_{\text{qd}}(V' = 0) - eV'. \quad (3.18)$$

As a function of  $V$ , therefore,  $E_{\text{qd}}$  varies as

$$E_{\text{qd}}(V) \approx E_{\text{qd}}(V = a) - \frac{e\Delta V}{\mathcal{F}(V = a)}, \quad (3.19)$$

for small values of  $\Delta V = V - a$ .

### Occupancy of states in the emitter

The occupancy  $\rho_e(\epsilon)$  of the states in the emitter is given by the Fermi distribution function, (Ashcroft and Mermin 1976)

$$\rho_e(\epsilon) = \frac{1}{1 + \exp\left(\frac{\epsilon - E_{\text{F}}}{k_{\text{B}}T}\right)}, \quad (3.20)$$

where  $E_{\text{F}}$  is the Fermi energy in the emitter. At  $T = 0$  K, the Fermi distribution is a step function, where  $\rho_e = 0$  for  $\epsilon > E_{\text{F}}$  and  $\rho_e = 1$  for  $\epsilon < E_{\text{F}}$ . At higher temperatures, the step is ‘broadened’ so that the change in  $\rho_e$  occurs over an energy interval of  $\sim k_{\text{B}}T$ .

### 3.5.6 Result

Inserting equations 3.19 and 3.20 into equation 3.15, we obtain

$$I(V) \propto \left[1 + \exp\left(\frac{e(V_{\text{F}} - V)}{\mathcal{F}k_{\text{B}}T}\right)\right]^{-1} \times D_e\left(E_{\text{F}} - \frac{e(V - V_{\text{F}})}{\mathcal{F}}, \mathbf{R}\right) \times |\mathcal{T}_{e-\text{qd}}|^2, \quad (3.21)$$

for small voltages  $V - V_{\text{F}} \lesssim 100$  mV, where  $V_{\text{F}}$  is the voltage at which the QD state becomes resonant with the Fermi level in the emitter.

The above equation is interpreted as follows. As the voltage,  $V$ , across the device is increased the energy levels of the QD states in the AlAs barrier move to lower energy with respect to the Fermi level in the 2D emitter. When the energy of a particular QD state comes within  $\sim k_{\text{B}}T$  of the Fermi level in the emitter, we expect to see an increase in the tunnel current as electrons start to tunnel via the QD state. The onset of this current peak

should take the form of the Fermi function given in equation 3.20. As the voltage is increased further, the energy of the QD state moves below that of the Fermi energy in the emitter, to energies where  $\rho_e \approx 1$ . In this regime, the current through the QD state is proportional to the local density of states,  $D_e$ , in the emitter. As the bias is increased still further, the energy of the QD state eventually falls below the sub-band energy of the emitter 2DES and the current through the QD state falls away again. Here we have assumed that  $\mathcal{T}_{e \rightarrow \text{qd}}$  stays constant with  $V$ . This is not true in general, since the parts of the wave functions  $\chi_e$  and  $\chi_{\text{qd}}$  that penetrate the potential barrier are affected by the voltage drop across the barrier. However, for small changes in voltage  $\lesssim 100$  mV we assume  $\mathcal{T}_{e \rightarrow \text{qd}}$  to be independent of  $V$ .

### 3.6 Low temperature $I(V)$ characteristics of isolated resonant features

Figure 3.6 shows isolated features in the forward bias tunnel current  $I(V)$  of three different devices,  $a$ ,  $b$  and  $d$ . Here, ‘isolated’ means that the feature is flanked at higher and lower voltage by ‘quiet’ regions of  $I(V)$ , where the current shows no oscillations above the noise level, apart from the background non-resonant tunnel current. Device  $a$  and device  $b$  are  $100 \mu\text{m}$  diameter mesas, whilst device  $d$  is a  $5 \mu\text{m}$  diameter mesa.

Device  $a$  has an isolated features in its  $I(V)$  characteristic at  $100\text{--}116$  mV, device  $b$  has a single isolated feature at  $208\text{--}250$  mV and device  $d$  at  $212\text{--}270$  mV. These features will be referred to as features  $a$ ,  $b$  and  $d$  respectively, corresponding to the device labels. The  $I(V)$  characteristic of device  $a$  also shows an additional isolated feature at  $88\text{--}92$  mV. However, this feature is only poorly resolved so it will not be discussed here.

All the isolated features  $a$ ,  $b$  and  $d$  have a number of basic attributes in common. Firstly, there is a step increase in the current at the onset of the feature. The sharpness of the step depends on the temperature: as the temperature is increased, the rise in current occurs over a broader range of voltage. Secondly, whereas the onset shows thermal activation,

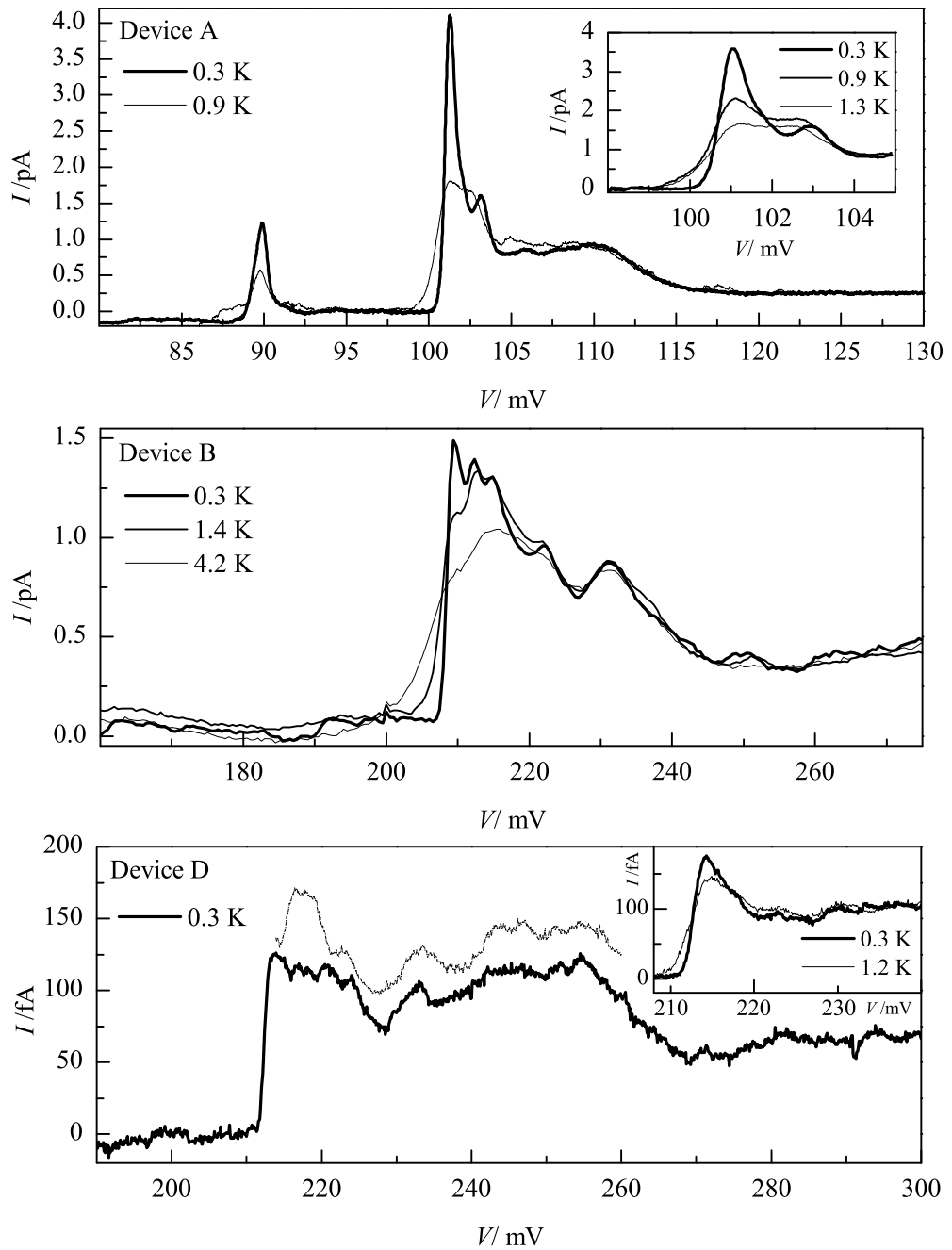


Figure 3.6: Isolated features in the forward-bias tunnel current  $I(V)$  of three different devices, at low temperature. Device *a* and device *b* are 100  $\mu\text{m}$  diameter mesas, and device *d* is a 5  $\mu\text{m}$  diameter mesa. Insets show the effect of increasing temperature (the inset for device *d* was obtained in magnetic field  $B = 300$  mT,  $\mathbf{B} \parallel \mathbf{J}$ ). The broken-line trace for device *d* was obtained two weeks after the bold trace, showing the reproducibility of the fluctuations for  $220 < V < 260$  mV (trace offset by  $\sim 25$  fA for clarity). The data for device *b* was supplied by Dr. A. S. G. Thornton.

the remainder of the feature remains largely independent of temperature. Thirdly, at the high voltage tail of each feature, the current decays smoothly back to the baseline value.

Between the onset and the tail of features  $a$  and  $d$ , there is a plateau in the current at  $I \approx 1$  pA and  $I \approx 100$  fA respectively. Feature  $a$  also shows a sharp peak in the current at the onset, rising well above the level of the plateau current. This peak can also be seen, though to a lesser extent, in feature  $d$  when the magnetic field is increased a little above zero (see inset to figure 3.6). The same peak can be seen at the onset of feature  $b$ , although in this case, it appears to dominate most of feature so that there is no discernable plateau region. The enhancement to the tunnel current at the onset is known as a *Fermi edge singularity* and is due to Coulomb interactions between the oscillating charge in the QD and the electrons in the 2DES near the Fermi level. Similar effects have been observed previously in tunnelling through 0D impurity states in the barrier (Geim *et al.* 1994b, Cobden and Muzykantskii 1995). The Fermi edge singularity in these devices has been discussed in detail elsewhere [see Thornton (1998b) and Benedict *et al.* (1998)] and will not be discussed further in this thesis.

We attribute the features  $a$ ,  $b$  and  $d$  to resonant tunnelling via the 0D states of the QDs, for the reasons given in section 3.4. In particular, we attribute these *isolated* features to resonant tunnelling through a *single* state of a *single* QD, rather than multiple states. The evidence for this is discussed below.

Firstly, the  $I(V)$  characteristics of each feature are very similar to that predicted by equation 3.21 for tunnelling from a 2DES through a single 0D state (with the exception of the current enhancement at the onset). Specifically: (i) the features show a step increase in the current, corresponding to the single QD state entering into resonance with the Fermi level in the 2DES; (ii) the onset is thermally broadened, reflecting the Fermi-Dirac occupation of the electron levels in the 2DES at low temperature; (iii) two of the features show clear plateau regions in the current, corresponding to resonant tunnelling from states in the 2DES below the Fermi energy (in feature  $b$ , the plateau is not observed due to the large current enhancement at the onset);

(iv) the current falls back (nearly) to its baseline value at the high voltage end of the features, corresponding to the energy of QD state moving below the energy of the 2DES sub-band edge.

Secondly, although not shown in the above figure, the current onset for these features has been shown to sharpen with decreasing temperature, down to at least  $T \sim 100$  mK (Thornton *et al.* 1998d). This limit indicates a maximum line width of  $k_B \times 100$  mK =  $10$   $\mu$ eV for the spectrometer state. Such a small line width makes it unlikely that such isolated features are due to resonant tunnelling through more than one state.

### 3.7 $I(V)$ characteristic of feature $d$

Feature  $d$  takes the overall form of a ‘top-hat’ function, with the onset of the feature occurring at  $V_F \approx 212$  mV and a step-down in the current, back to its baseline value at  $V \approx 265$  mV. As discussed above, the low voltage onset of the feature shows clear thermal activation whilst the remainder of the feature is independent of temperature. Between 212 mV and 265 mV the current plateaus at  $I \approx 100$  fA. This plateau region contains some fluctuations around the mean current. The fluctuations are entirely reproducible so they cannot be due to noise in the measurement circuit.

Instead, the model for the tunnel current, developed in section 3.5, indicates that the tunnel current, as a function of voltage, is proportional to the LDOS in the adjacent 2DES, as a function of energy. As the voltage is increased, the QD state is brought into resonance with successively lower energy states in the 2DES, and so the resonant tunnel current reflects the LDOS of the 2DES at successively lower energies. Therefore, we attribute such reproducible fluctuations in the plateau tunnel current to the direct observation of oscillations in the LDOS of the 2DES (section 1.4.2).

In this way, we measure the LDOS of the 2DES at the energy  $E_{qd}$  and  $xy$  position  $\mathbf{R}$  of the QD. Such fluctuations in the LDOS of a 3D emitter have also been observed in similar resonant tunnelling experiments by Schmidt *et al.* (1996b, 1997) and in a 2DES by McDonnell *et al.* (1995). In the following

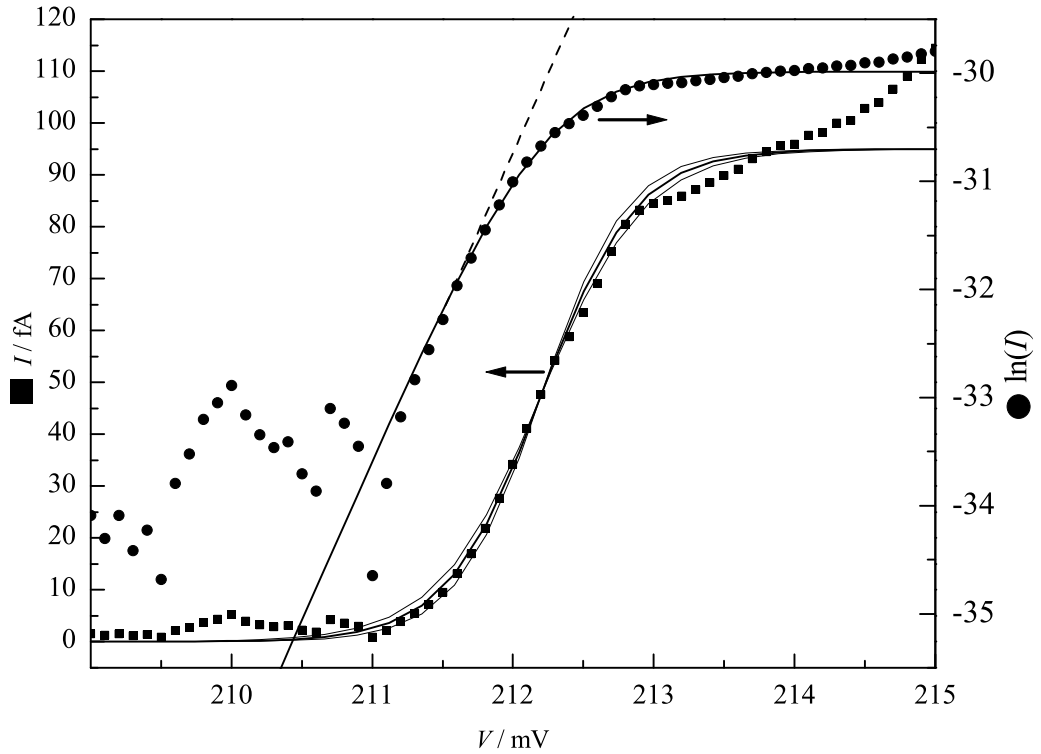


Figure 3.7: Filled squares - The current onset of feature  $d$  at  $T = 0.270$  K. The solid lines represent fits to the data by the Fermi-function, using a leverage factor of  $\mathcal{F} = 14.5 \pm 1.0$  to relate the energy scale to the voltage scale. Filled circles - Plot of  $\ln I$  versus  $V$ . The continuous line is a fit to the data by the logarithm of the Fermi-function, using  $\mathcal{F} = 14.5$ .

chapter, it will be demonstrated how such an experiment can be used to measure the LDOS in a Landau quantised 2DES.

### 3.7.1 Thermal activation of the onset and measurement of the leverage factor

At the low-voltage tail of the onset, away from the Fermi edge current enhancement, the current is expected to follow the form of the Fermi-Dirac distribution function, equation 3.20 (Cobden and Muzykantskii 1995, Thornton 1998b). Figure 3.7 shows the current onset of feature  $d$  (filled-squares) at  $T = 0.270$  K. The solid lines are fits to the data by the Fermi function,

$$I(V) = I_0 \left[ 1 + \exp \left( \frac{e(V_F - V)}{\mathcal{F}k_B T} \right) \right]^{-1}, \quad (3.22)$$

where  $V_F$  is the voltage at which the QD state becomes resonant with the Fermi level in the emitter ( $V_F \approx 212$  mV) and  $I_0$  is the plateau current ( $I_0 \approx 100$  fA). The thicker curve represents the best fit to the data, yielding a leverage factor of  $\mathcal{F} = 14.5$ . The two thinner curves represent the uncertainty in the fit, corresponding to an uncertainty of  $\pm 1.0$  in the measurement of the leverage factor.

Also shown in figure 3.7 is a plot of  $\ln I$  versus  $V$  (filled-circles). The continuous line is a fit to the data by the logarithm of equation 3.22, using  $\mathcal{F} = 14.5$ . At energies well above the Fermi energy, i.e.  $V \ll V_F$ , equation 3.22 may be approximated by

$$I(V) \approx I_0 \exp\left(\frac{-e(V_F - V)}{\mathcal{F}k_B T}\right). \quad (3.23)$$

Therefore, the logarithm of the current is linear in  $V$  for  $V \ll V_F$ , with a gradient

$$\frac{d \ln I}{dV} = \frac{e}{\mathcal{F}k_B T}. \quad (3.24)$$

This gradient has been represented on figure 3.7 as a dashed line, and is found to be a reasonable fit to the data between 211.2 mV and 211.8 mV, using  $\mathcal{F} = 14.5$ .

An estimate of the leverage factor of this feature was also made by Thornton (1998b), using a similar technique, at several different temperatures between 80 mK and 1 K; he obtained a value of  $\mathcal{F} = 14.40 \pm 0.08$  for feature  $d$ , consistent with the above analysis.

Such a value for  $\mathcal{F}$  is also consistent with estimates made by numerical calculation of the conduction band under applied bias (section 2.4.2). Figure 2.5 shows the conduction band of *NU1403* under a bias of  $V = 300$  mV, calculated by self-consistent solution of the Poisson equation. In this figure, the voltage drop between the emitter layer and the InAs layer is  $V' \approx 30$  mV. Therefore the calculated leverage factor is of the order  $\mathcal{F} \sim V/V' \approx 10$ . This value is reasonably consistent with the experimentally obtained value. However, it is not possible to make a detailed comparison between such a calculated leverage factor and the experimentally obtained value for two main reasons. Firstly, the charge in the barrier, due to charging of the QDs,

is difficult to estimate. Secondly, the experiment measures the value of  $\mathcal{F}$  *local* to the QD. This may not be the same as the areal average value of  $\mathcal{F}$ , since there can be local variations in the electron density of the 2DES, causing local variations in the electric field between the emitter and InAs layer.

### 3.7.2 Estimate of the Fermi energy of the 2DES from the voltage width of the feature

The width of the feature gives an estimate of the Fermi energy in the 2DES. From the  $I(V)$  trace shown above, it can be seen that the QD state is resonant with the Fermi level,  $E_F$ , in the 2DES at  $212 \pm 5$  mV, and the bottom of the 2DES sub-band,  $E_0$ , at  $265 \pm 5$  mV. The Fermi energy can be found by dividing the voltage width of the feature by the leverage factor,  $\mathcal{F}$ . This gives a value for the Fermi energy of  $E_{F0} = E_F - E_0 = (265 \pm 5 - 212 \pm 5) \text{ mV} \times e/\mathcal{F} = (3.7 \pm 0.7) \text{ meV}$ . Such a value of  $E_{F0}$  corresponds to an electron density of  $n_s = (1.0 \pm 0.2) \times 10^{15} \text{ m}^{-2}$  (equation 1.17). This value of  $n_s$  is the sheet density of electrons *local to the* QD; the presence of disorder in the 2DES—as suggested by the measured fluctuations in the LDOS with energy—means that this value is not necessarily the same as the areal average of the sheet density.

## 3.8 $I(V)$ characteristics at high pressure

As mentioned in section 3.4, a number of authors have observed resonant tunnelling through  $X$ -valley related donor bound states in GaAs/AlAs tunnelling structures comparable to *NU1403* (Fukuyama and Waho 1995, Khanin *et al.* 1998, Itskevich *et al.* 1998, Vitusevich *et al.* 2000).

To investigate the possibility that some of the resonant features that we observe are due to tunnelling via such  $X$ -valley related states, we applied high pressure to a number of 100–200  $\mu\text{m}$ -diameter mesas of *NU1403*, using

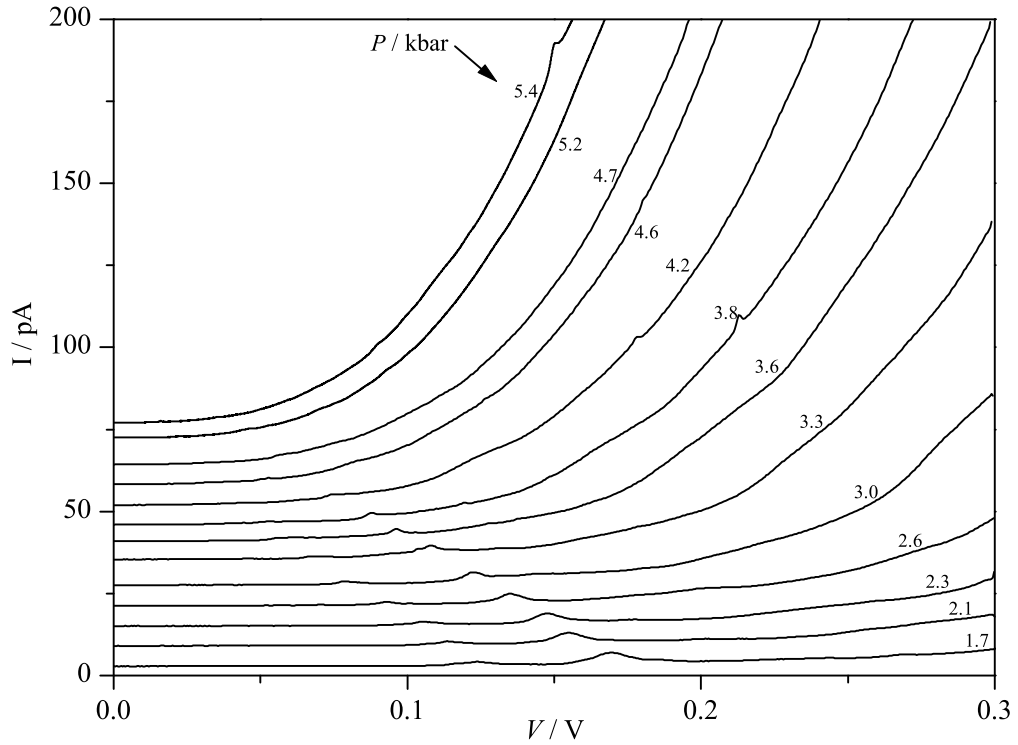


Figure 3.8:  $I(V)$  traces from a typical  $100 \mu\text{m}$  diameter mesa of *NU1403* under applied pressures between 1.7 and 5.4 kbar. The temperature is 4.2 K.

the liquid clamp cell detailed in section 2.2.1, and examined the change in the voltage positions of the resonant peaks with pressure.

Figure 3.8 shows low temperature  $I(V)$  traces from a typical  $100 \mu\text{m}$  diameter mesa under applied pressures between 1.7 and 5.4 kbar. The non-resonant component of the tunnel current increases with pressure as the energy of AlAs  $X$ -valley conduction band edge decreases with respect to the GaAs  $\Gamma$  conduction band edge. This reduces the potential barrier height for electrons tunnelling across the barrier via the  $X$ -valley in the AlAs, leading to the observed increase in the non-resonant ‘background’ tunnel current with voltage.

In order to see the positions of the resonances in  $I(V)$  more clearly, we subtract the non-resonant background current. This is done by fitting an empirical function to the background current,  $I_{\text{emp}} = aV^b$ , where  $a$  and  $b$  are fitting parameters. Figure 3.9 shows a plot of  $\Delta I(V)$ , where  $\Delta I = I - I_{\text{emp}}$ ,

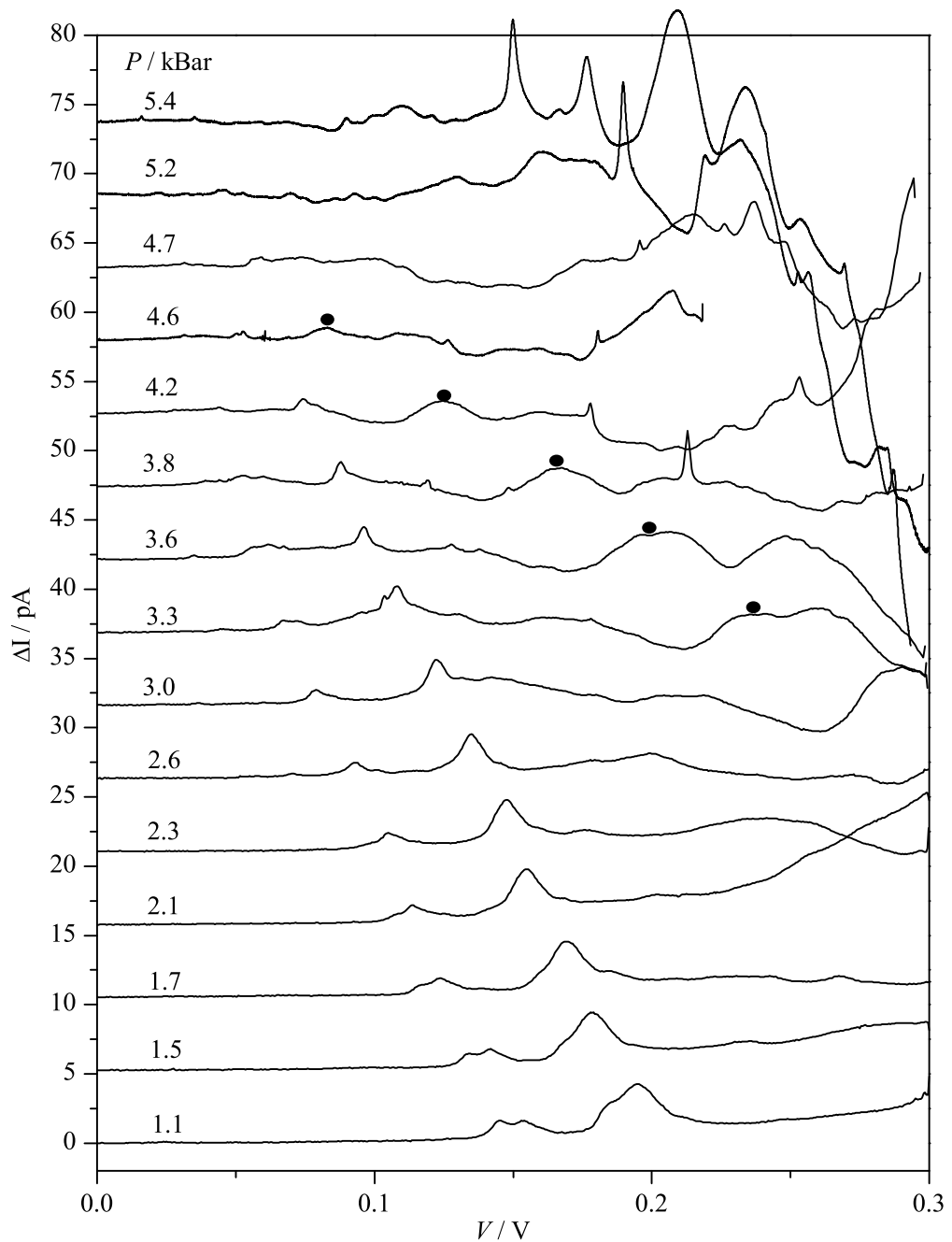


Figure 3.9:  $I(V)$  traces from a typical  $100\ \mu\text{m}$  diameter mesa of *NU1403* under applied pressures,  $P$ , between 1.1 and 5.4 kbar. In these traces, the non-resonant ‘background’ tunnel current has been subtracted according to  $\Delta I = I - aV^b$ —where  $a$  and  $b$  are fitting parameters—in order that the resonant component of the tunnel current may be seen more clearly. Two resonant features are clearly visible at  $P = 1.1$  kbar. These features move to lower voltage at a rate of approximately 40 mV per kbar. The dots highlight a feature that is moving to lower voltage at a rate of approximately 100 mV per kbar. The temperature is 4.2 K.

obtained from the data shown in figure 3.8. Two resonant features are clearly visible at  $P = 1.1$  kbar. These features move to lower voltage at a rate of approximately 40 mV per kbar. In addition, filled circles highlight a feature that is moving to lower voltage at a rate of approximately 100 mV per kbar. For the purposes of discussion, we label the 40 mV per kbar peaks as ‘slow’ moving, and the 100 mV per kbar peaks as ‘fast’ moving. Based upon measurements of the leverage factor in other *NU1403* devices, we estimate that  $\mathcal{F} \approx 10 \pm 2$  at  $V = 150$  mV (Thornton 1998b). Therefore, the energies,  $E$ , of the resonant states associated with the fast-moving peaks are moving by  $dE_{\text{fast}}/dP = -e \times 100 \text{ mV}/\mathcal{F} \approx -10 \text{ meV/kbar}$  with respect to the Fermi level in the emitter. Similarly, the energies of the resonant states associated with the slower-moving peaks are moving at  $dE_{\text{slow}}/dP \approx -4 \text{ meV/kbar}$  with respect to the Fermi level in the emitter.

Reported values for the pressure coefficient of the  $\Gamma - \Gamma$  band-gap in GaAs range from +8.5 to +12.6 meV/kbar (Wei and Zunger 1999). We assume the often reported value of +10.7 meV/kbar (Cheong *et al.* 1996). Reported values for the pressure coefficient of the  $\Gamma - X$  band-gap in AlAs range from  $-0.8$  meV/kbar (Adachi 1985) to  $-2.16$  meV/kbar (Wei and Zunger 1999). The pressure coefficient of  $X$ -valley-related donor bound excitons ( $D_X^0$ ) in GaAs, measured by photoluminescence experiments, is found to be  $(-1.34 \pm 0.04)$  meV/kbar (Wolford and Bradley 1985). Based upon these measurements, we assume that  $D_X^0$  excitons in AlAs have a pressure coefficient of  $\sim -1.5$  meV/kbar. The change in the valence band offset at the GaAs/AlAs heterointerface with pressure is  $d\Delta E_v/dP \sim +1$  meV/kbar (Lambkin *et al.* 1989). Therefore, we estimate that the energy of an  $X$ -valley-related bound electron state in AlAs should *decrease* by approximately 13 meV/kbar *relative* to the energy of the  $\Gamma$  conduction band edge in GaAs. The estimate is quite rough, due to the combined uncertainties in the pressure coefficients, nevertheless, it is reasonably consistent with our measurement of  $dE_{\text{fast}}/dP$  for the ‘fast’ moving resonances. Hence, this observation strongly suggests that such fast moving peaks in  $I(V)$  correspond to resonant tunnelling through  $X$ -related donor bound states in the AlAs layer.

On the other hand, the ‘slow’ moving peaks are reasonably consistent with tunnelling through QD states since the pressure coefficient of the pho-

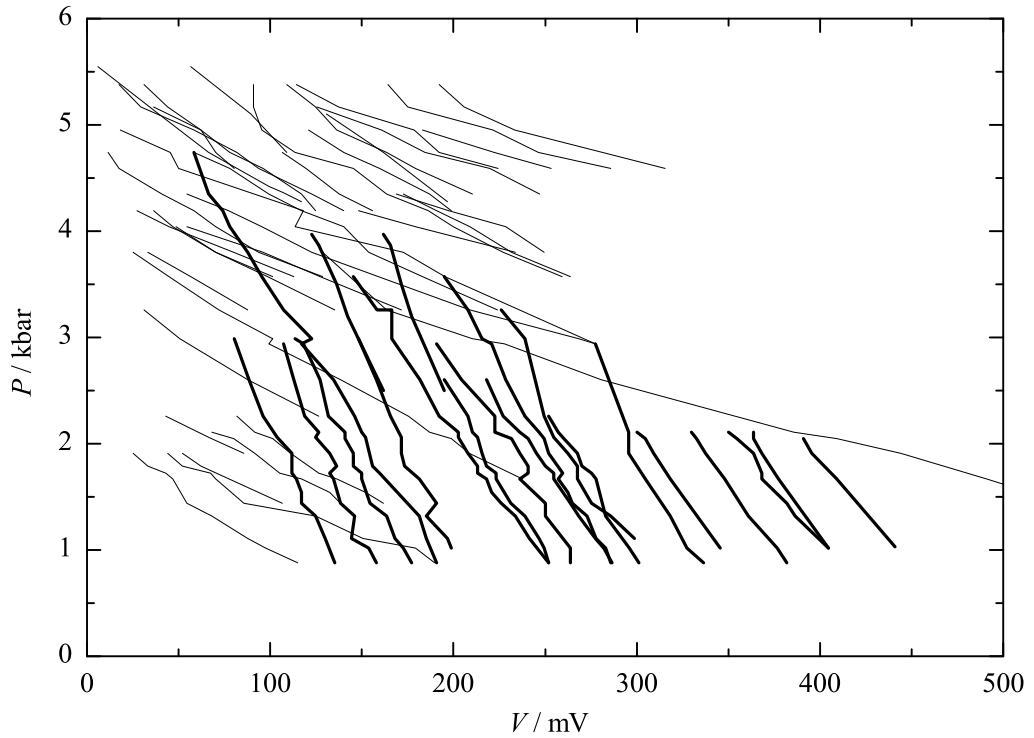


Figure 3.10: Voltage positions  $V$  of the resonant features in  $I(V)$  versus applied pressure  $P$ . The graph has been compiled from the  $I(V)$  characteristics of eight different  $100\ \mu\text{m}$ -diameter mesas of *NU1403*. The thick lines represent resonant features whose voltage positions change by approximately 40 mV per kbar. The thinner lines represent resonant features whose voltage positions change by approximately 100 – 120 mV per kbar. The temperature is 4.2 K.

toluminescence recombination line for InAs QDs buried in a GaAs matrix is measured to be  $dE_{\text{qd}}/dP = (+9.1 \pm 0.2)\ \text{meV/kbar}$  (Itskevich *et al.* 1997), compared to  $+10.7\ \text{meV/kbar}$  for the  $\Gamma - \Gamma$  band-gap in GaAs.

Figure 3.10 shows the voltage positions,  $V$ , of the resonant features in  $I(V)$  versus applied pressure,  $P$ . The graph has been compiled from the  $I(V)$  characteristics of eight different  $100\ \mu\text{m}$ -diameter mesas of *NU1403*. The thick lines represent resonant features whose voltage positions change by approximately 40 mV per kbar. The thinner lines represent resonant features whose voltage positions change by approximately 100 – 120 mV per kbar.

From this plot, we can see that all the ‘fast-moving’,  $X$ -valley related features lie above  $V \sim 300\ \text{mV}$  at atmospheric pressure. Therefore, we can

attribute all the resonant features observed at lower voltage to tunnelling via states of the QDs.

### 3.9 Summary

In summary, we have measured the tunnel current,  $I$ , through of a number of GaAs/AlAs/GaAs single tunnel barrier devices, incorporating a layer of InAs QDs within the barrier layer. When a bias,  $V$ , is applied across the device, tunnelling occurs from a 2DES that forms in a triangular potential well against the barrier. At low temperature, we observe resonant features in the  $I(V)$  characteristic. We attribute those features that occur below  $V \sim 300$  mV to resonant tunnelling via electron states in the InAs QDs buried within the AlAs layer. In some of the devices, we can observe single, isolated, resonances. We attribute these particular resonances to tunnelling via a single state of a *single* QD. Within such resonances, we observe fluctuations in the resonant current as a function of voltage. A model for the tunnel current indicates that such fluctuations are a direct observation of the LDOS fluctuations in the 2DES emitter. By adjusting the voltage across the device, we can use the QD to probe the LDOS in the 2DES from the Fermi level, down to the sub-band edge.

# Chapter 4

## Quantum dot as a spectroscopic probe of Landau levels

### 4.1 Introduction

The one-electron density of states (DOS) of a 2DES in a magnetic field  $B \parallel z$  takes the form of a series of  $\delta$ -function-like peaks known as Landau levels (section 1.4.1). Both the separation in energy between each Landau level and the degeneracy of each Landau level increase with increasing magnetic field (equation 1.22 and equation 1.23). This leads to periodic features in the transverse and longitudinal resistivities of the 2DES with changing magnetic field, each cycle corresponding to one Landau level passing through the Fermi level (section 1.4.1). This is the basis of the quantum Hall effect. Experiments that measure the conduction properties of the 2DES can provide information about states at the Fermi level. However, they are unable to probe the states at lower energies, since these electrons do not ordinarily contribute to conduction.

In the previous chapter, it was demonstrated how resonant tunnelling through a QD could be used to measure the local density of states (LDOS) of an adjacent 2DES, at energies well below the Fermi level. The experiments

presented in this chapter follow the work of Itskevich *et al.* (1996, 1997) and work presented by Thornton in his Ph.D. thesis (1998b). A single state of a single InAs QD is used as a spectroscopic probe of the LDOS in a 2DES emitter, from the Fermi level down to the 2D sub-band edge. When a magnetic field is applied in the direction perpendicular to the plane of the 2DES, the LDOS displays clearly resolved Landau levels. It is shown how these results may be used to estimate the lifetime of quasi-holes deep below the Fermi energy.

## 4.2 Spectroscopic probe of Landau levels

### 4.2.1 Low temperature $I(V)$ traces in magnetic field

Figure 4.1 shows  $I(V)$  traces from device *NU1403 d*, at various magnetic fields between 0 and 5 T, with the field applied along the  $z$ -axis. Figure 4.2 shows more traces between 0 and 1.07 T. Orientated along the  $z$ -axis, the magnetic field gives rise to Landau levels in the 2DES DOS as described in section 1.4.1. The resulting oscillations in the LDOS are clearly visible in the  $I(V)$  traces of figure 4.2. However, there is also some additional structure, which appears at  $B > 2$  T, that cannot be interpreted as Landau levels. This structure will be explored in more detail in chapter 5; this chapter will be restricted to the Landau level structure appearing in the low field data ( $B < 2$  T).

The 0.38 T trace shows two distinct peaks that can be associated with the  $n = 4$  and  $n = 5$  Landau levels, where  $n$  is the Landau level index as defined in section 1.4.1. The index number is identified by using a ‘fan-line’ diagram, which will be discussed shortly. Note that the  $n = 3$  Landau level is, however, barely visible and the  $n < 3$  Landau levels are not resolvable or are ambiguous. As the field strength is increased, the lower index Landau levels emerge successively. At 0.43 T, the Landau levels down to  $n = 2$  are resolvable. Finally, the  $n = 0$  and  $n = 1$  Landau levels are unambiguously resolved in the 1.07 T trace. We interpret the successive emergence of Landau levels with increasing  $B$  as a consequence of the quasi-particle lifetime in the 2DES. This will be discussed in section 4.3. Notice that the Landau

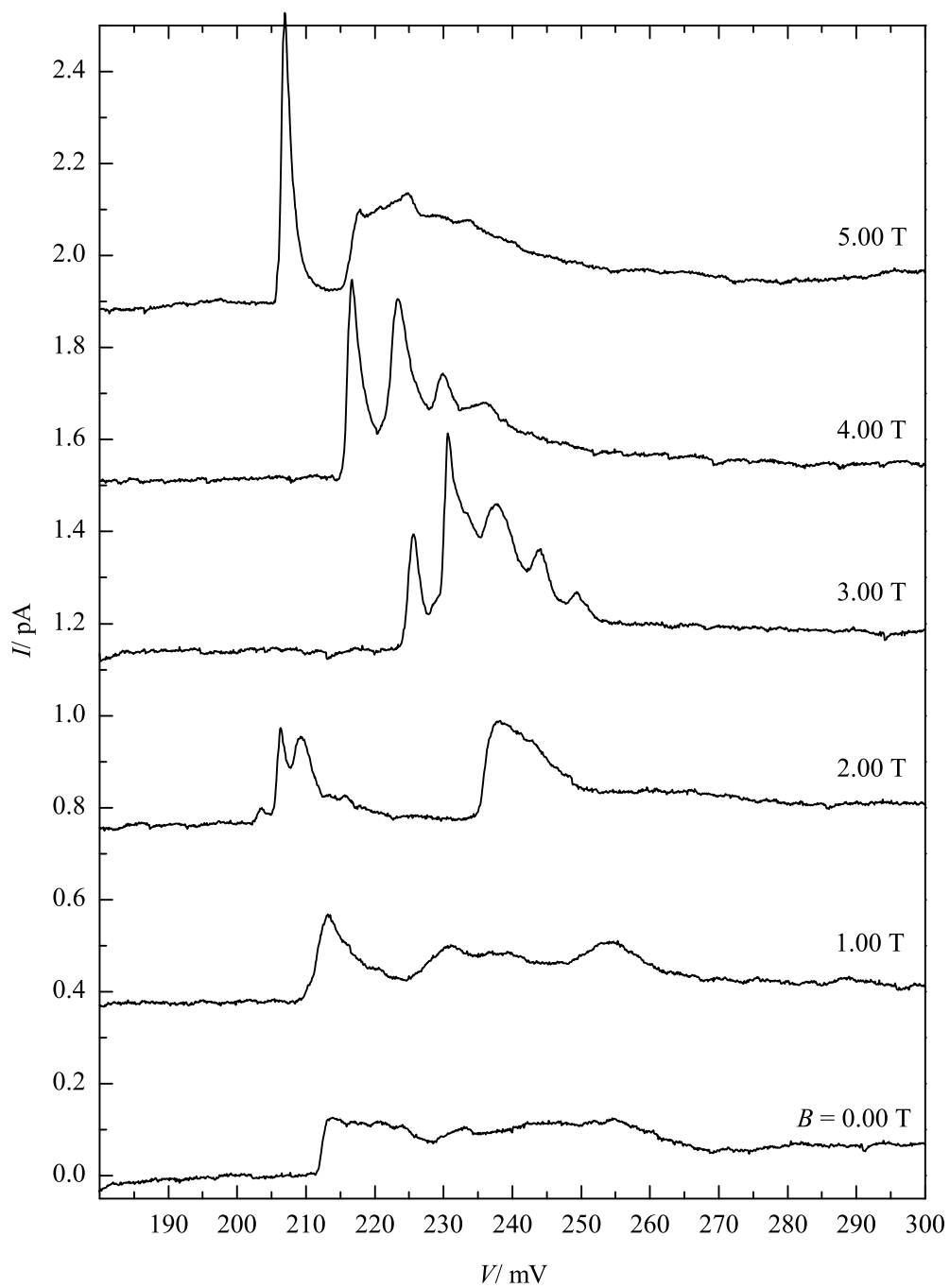


Figure 4.1:  $I(V)$  traces from device  $d$  taken at six different magnetic fields ( $B||z$ ) between 0 and 5 T. The temperature is 0.3 K. Traces are offset for clarity.

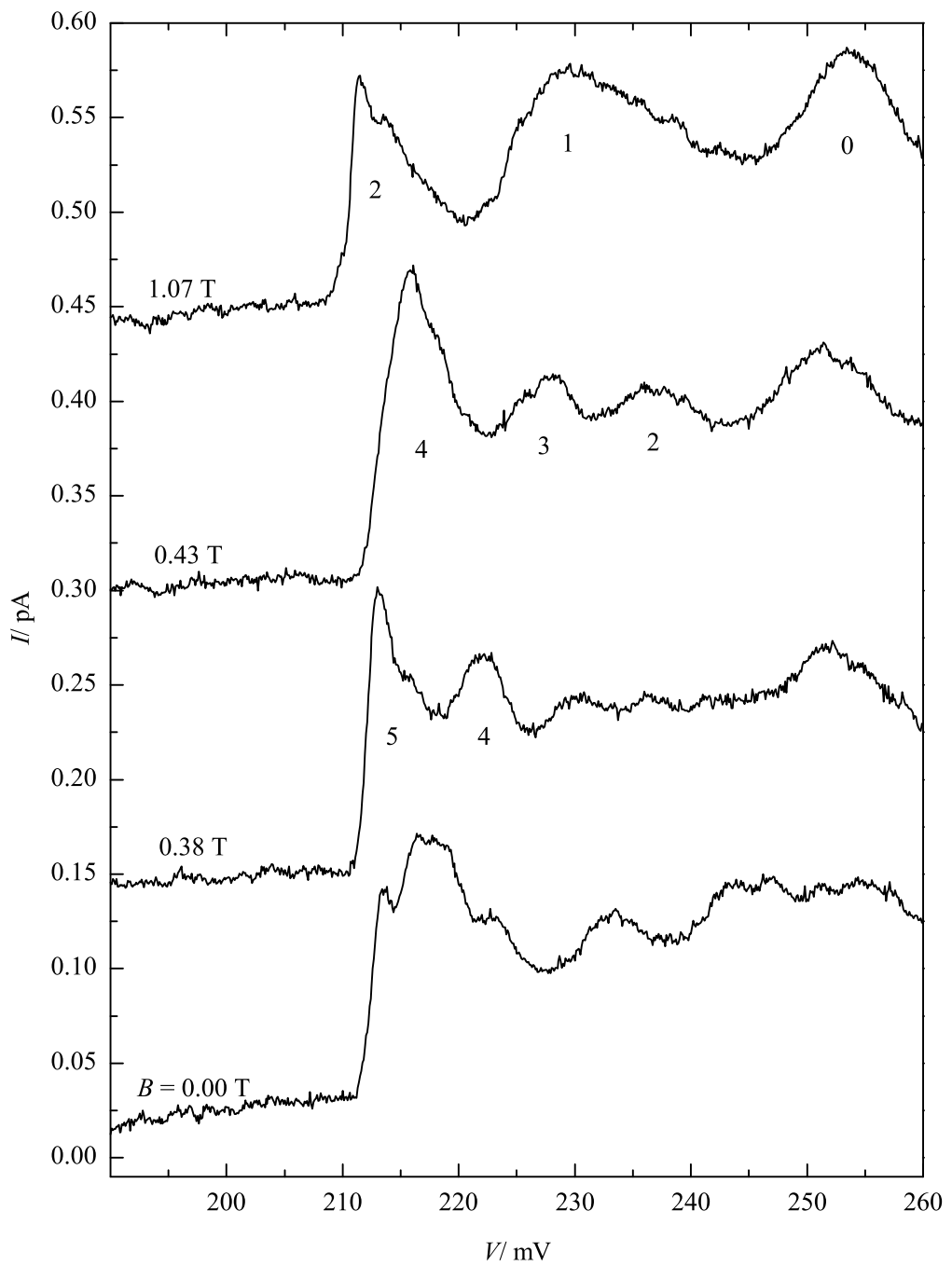


Figure 4.2:  $I(V)$  traces from device  $d$  taken at magnetic fields ( $B \parallel J$ ) between 0 and 1.07 T. The temperature is 0.3 K. Peaks are labeled according to the corresponding Landau level index,  $n$  (see main text). Traces are offset for clarity.

levels do not appear as sharp  $\delta$ -functions in the LDOS. Instead, they have a finite width as a consequence of electron scattering in the 2DES (section 1.4.2).

### 4.2.2 Colour-scale $I(B, V)$ plot of the data

Figure 4.5 (at the end of the chapter) shows the data as a colour-scale plot of the tunnel current,  $I$ , versus voltage,  $V$ , and magnetic field,  $B \parallel z$ . The colour scale has been carefully chosen to give improved contrast and to highlight the important features of the plot. In general, darker, bluer shades represent smaller currents and brighter red/yellow shades represent larger currents. A rapid change from blue to red shading occurs at  $I \sim 110$  fA. This is the mean value of the current in the plateau region of the feature at  $B = 0$ . Therefore, current values less than the mean  $B = 0$  plateau current are displayed as blue while currents greater than the plateau mean are displayed as red/yellow. In other words, this colour-scheme highlights oscillations in the current around the mean plateau value. Such oscillations include those induced by Landau level quantisation and random LDOS fluctuations.

The Landau levels are clearly visible as a ‘fan’ of diagonal red/yellow stripes on a blue background, emanating from the top left of the diagram.

There are some additional weaker features in  $I(V)$  close to  $B = 0$ . These are attributed to the random fluctuations in the LDOS as a function of energy. These occur as a consequence of disorder in the 2DES, as discussed in section 1.4.2. Similar observations have been made in experiments that can measure the LDOS in a three-dimensional emitter, by using an impurity state as a spectroscopic probe (Schmidt *et al.* 1996b). There does not appear to be any relationship between these random fluctuations and the emergence of the Landau levels, although the broad feature at  $V \sim 255$  mV does appear to emerge from the amalgamation of the  $n = 0$  and  $n = 1$  Landau levels at low  $B$ . The explanation for this behaviour is, however, not yet clear.

### 4.2.3 Expected voltage positions of the Landau levels

The solid white lines on figure 4.5 show the *expected* voltage positions,  $V_n$ , of the Landau level peaks as a function of magnetic field,  $B$ . These are determined from the Landau level energy,  $\epsilon = (n + \frac{1}{2})\hbar\omega_c$ , by using a leverage factor of  $\mathcal{F} = 14.4$  (determined in section 3.7.1) to relate the energy to the voltage scale,

$$V_n(B) = V_F(0) + \frac{\mathcal{F}}{e} [E_{F0} - (n + \frac{1}{2})\hbar\omega_c(B)], \quad (4.1)$$

where  $V_F(0)$  is the bias at which the QD state becomes resonant with the Fermi level at  $B = 0$ ;  $E_{F0}$  is the Fermi energy of the 2DES at  $B = 0$ , estimated in section 3.7.2 to be  $E_{F0} = (3.7 \pm 0.7)$  meV.

Note that this plot confirms the allocation of Landau level indices ( $n$ ) to the peaks in  $I(V)$  made in figures 4.1 and 4.2.

### 4.2.4 Fermi energy in magnetic field

The current-onset of the resonance shows up on figure 4.5 as a sharp change in colour from black to blue with increasing voltage. Notice that the voltage position of the current onset oscillates with increasing magnetic field. This reflects the variation in the Fermi energy,  $E_{F0}$ , as each Landau level depopulates in succession (see section 1.4.1).

#### Obtaining the electron density from oscillations in $E_F$

The interval in  $B$  between the depopulation of successive Landau levels depends upon the electron sheet density in the 2DES,  $n_s$ . We define  $\beta = B^{-1}$  and label the value of  $\beta$  where the  $n$ th Landau level depopulates by writing it as  $\beta_n$ . From equation 1.26, we find that  $\Delta\beta = \beta_n - \beta_{n-1}$  is a constant, independent of  $n$ ,

$$\beta_n - \beta_{n-1} = \frac{2e}{h} \times \frac{1}{n_s} [n - (n - 1)]$$

$$\Delta\beta = \frac{2e}{\hbar n_s}. \quad (4.2)$$

Therefore,  $n_s$  can be obtained by identifying the values of the magnetic field where the Landau levels depopulate.

There is a problem with the above method of determining  $n_s$ , however. Each successive Landau level depopulates at a different energy and therefore a different corresponding *voltage*. Since  $n_s$  is sensitive to changes in voltage, the value of  $n_s$  is different for each value of  $\beta_n$ . Below  $\sim 1.5$  T, though, the voltages at which each Landau level depopulates lie within  $\sim 5$  mV of each other. However, in the following chapter it is found that a 5 mV change in voltage gives rise to  $\lesssim 3\%$  change in  $n_s$ . Therefore, equation 4.2 may still be used to obtain a good approximation for the value of  $n_s$  around  $V_F(0) \approx 212$  mV. We find  $n_s(212 \text{ mV}) = (1.2 \pm 0.2) \times 10^{15} \text{ m}^{-2}$ . The error in determining  $n_s$  is primarily due to the uncertainty in pinpointing the magnetic fields where the Landau levels depopulate. The uncertainty arises due to the broadening of the Landau levels.

One final point to note about the oscillation in the Fermi energy is that, although the voltage position of the current onset,  $V_F$ , oscillates with  $B$ , the Fermi level itself must remain fixed with respect to the Fermi level in the emitter-side contact. As  $B$  increases, therefore, the depth of the triangular potential well must deepen in order to accommodate the increase in Fermi energy. This decreases the energy of the QD state in a similar way to increasing the voltage,  $V$ . In this way, the voltage position of the current onset changes with  $B$ .

### Diamagnetic shift of quantum dot state

The diamagnetic shift of the QD state with magnetic field is given by (Kittel 1996, Hapke-Wurst *et al.* 1999)

$$\Delta E(B) = \frac{e^2 B^2}{8m^*} \langle \rho^2 \rangle, \quad (4.3)$$

where  $2\sqrt{\langle\rho^2\rangle}$  is the spatial extent of the QD electron wave function in the  $xy$  plane (perpendicular to  $\mathbf{B}$ ). To obtain a rough estimate of the diamagnetic shift, we set  $2\sqrt{\langle\rho^2\rangle}$  equal to the in-plane diameter of a typical QD ( $\sim 10$  nm), and assume an effective mass of  $m^* \approx 0.06m_e$  (section 1.5.1); we obtain  $\Delta E(B) \approx 0.01B^2$  meV. This corresponds to a change in  $V_F$  of  $\Delta V_F(B) = \mathcal{F}\Delta E(B)/e \approx 0.13B^2$  mV, using a leverage factor of  $\mathcal{F} = 14.4$ . Below  $B \sim 2$  T, therefore, we expect the change in  $V_F$  due to the QD diamagnetic shift to be very much smaller than the oscillations that we observe in  $V_F$  as a consequence of Landau level depopulation. Therefore, we would not expect to observe the effects of the diamagnetic shift of the QD state below  $\sim 2$  T in this device.

### 4.3 Quasiparticle lifetime

We return now to the ability to resolve individual Landau levels, mentioned in section 4.2.1. At low magnetic field, we can observe the higher index Landau levels but the lower index Landau levels are not resolvable. For example, the  $I(V)$  trace at 0.38 T (figure 4.2) shows two distinct peaks in the tunnel current due to the  $n = 4$  and  $n = 5$  Landau levels. However, the peak corresponding to the  $n = 3$  Landau level is weak and difficult to see above the random LDOS fluctuations, whilst the  $n < 3$  Landau levels are not observed at all, or are ambiguous. As the magnetic field is increased, the lower index Landau levels emerge successively from the background noise. At 0.43 T, the Landau levels down to  $n = 2$  are resolvable, and finally the  $n = 0$  and  $n = 1$  Landau levels are unambiguously resolved in the 1.07 T trace. This effect is interpreted in terms of the quasihole lifetime in the 2DES.

A quasihole—that is, an empty state in the emitter below the Fermi energy—is left behind when an electron tunnels into the QD. The quasihole then decays due to inelastic electron-electron scattering at a rate  $\sim 1/\tau_{\text{qp}}$ . This causes the spectral width of the single particle levels in the emitter to broaden by  $\sim \hbar/\tau_{\text{qp}}$ .

The decay rate of the quasihole is limited by the ‘phase space’ available for

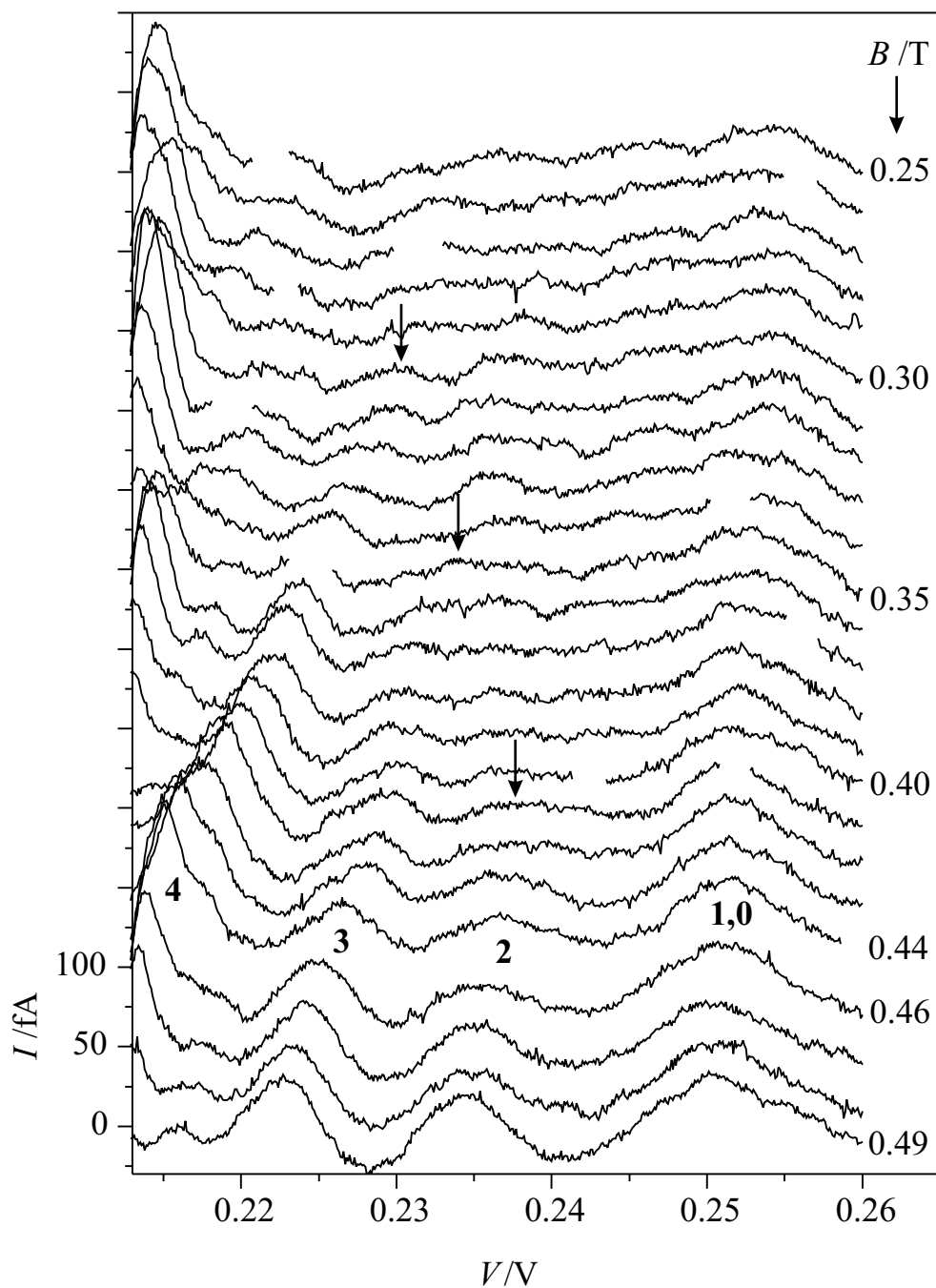


Figure 4.3:  $I(V)$  traces from device  $d$  taken at magnetic fields ( $B \parallel I$ ) between 0.24 and 0.49 T. The temperature is 0.3 K. The traces have been offset for clarity. Peaks are labelled (bold numbers) with the corresponding Landau level index,  $n$ . The arrows indicate points  $(B, V)$  where the peak due to a particular Landau level can just be resolved. These points are identified with the aid of the colour-scale plot, figure 4.5.

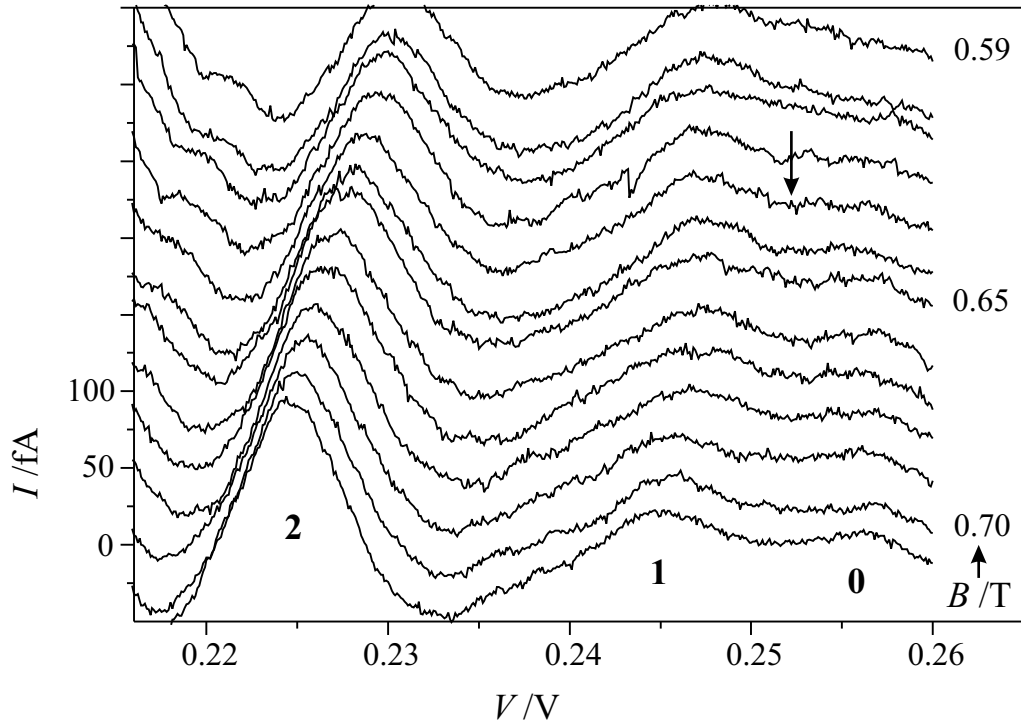


Figure 4.4:  $I(V)$  traces from device  $d$  taken at magnetic fields ( $B\parallel I$ ) between 0.59 and 0.71 T. The temperature is 0.3 K. The traces have been offset for clarity. Peaks are labeled (bold numbers) with the corresponding Landau level index,  $n$ . The arrows indicate points ( $B, V$ ) where the peak due to a particular Landau level can just be resolved. These points are identified with the aid of the colour-scale plot, figure 4.5.

inelastic scattering. Each scattering event must conserve energy and it must obey the Pauli exclusion principle. This leads to a lifetime  $\tau_{\text{qp}} \sim (E_{\text{F}} - E)^{-2}$ , where  $E$  is the energy of the quasiparticle (Ashcroft and Mermin 1976, Pines and Nozières 1989, Kittel 1996).

When  $\hbar/\tau_{\text{qp}}$  exceeds the Landau level width due to the disorder in the 2DES potential well, the width of the Landau level becomes dominated by the quasiparticle lifetime. Focusing on successively deeper lying Landau levels, the width of the Landau levels eventually approaches the cyclotron gap,  $\hbar\omega_c$ . At this point it becomes increasingly difficult to resolve an individual Landau level, due to the increasing overlap in energy between the states of adjacent Landau levels.

This information can be used to obtain an estimate of  $\tau_{\text{qp}}$ . We make the simple estimation that, in order for us to resolve a particular Landau level experimentally, the cyclotron energy,  $\hbar\omega_c$ , must be greater than the energetic

width of the Landau level due to the finite quasihole lifetime,  $\hbar/\tau_{\text{qp}}$ . Using this condition, for each Landau level we identify a value of the cyclotron energy,  $\hbar\omega_c(n)$ , at which we are only just able to resolve that Landau level in the data. These values of  $\omega_c(n)$  are indicated by the arrows on the  $I(V)$  traces shown in figures 4.3 and 4.4, and by the white circles on the  $I(B, V)$  plot (upper plot of figure 4.6). The error bars on the latter figure indicate the uncertainty in identifying the values  $\omega_c(n)$ . Note that, since both  $n = 0$  and  $n = 1$  emerge from the same broad feature at low  $B$ , we select the point at which the  $n = 0$  peak is independently resolved.

Re-arranging the above condition gives

$$\tau_{\text{qp}} \sim \frac{1}{\omega_c(n)}. \quad (4.4)$$

Then, since the energy of a particular Landau level is related to  $\omega_c(n)$  by

$$E(n) = (n + \frac{1}{2})\hbar\omega_c(n), \quad (4.5)$$

each value of  $\omega_c(n)$  yields an estimate of the quasiparticle lifetime  $\tau_{\text{qp}}$  for states with energy  $E(n)$ . The results are shown in the lower plot of figure 4.6. Note that the data points form a good straight line through the origin, of the form

$$\tau_{\text{qp}} = \beta\hbar(E_{\text{F}} - E)^{-1}, \quad (4.6)$$

where we determine  $\beta \approx 2.5$ .

Importantly, note that this result is *inconsistent* with the lifetime predicted from the exclusion principle alone [ $\tau_{\text{qp}} \sim (E_{\text{F}} - E)^{-2}$ ]. However, a number of authors have noted that the presence of disorder in the 2DES can accelerate the decay rate at energies  $E_{\text{F}} - E \lesssim \hbar/\tau$ , where  $\tau$  is the elastic mean free path time (Schmid 1974, Altshuler and Aronov 1979). For these energies, Altshuler and Aronov (1981) [see also Altshuler *et al.* (1982)] predict the alternative dependence (for a 2D system)

$$\tau_{\text{qp}} \sim (E_{\text{F}} - E)^{-1}. \quad (4.7)$$

The appearance of Landau levels close to  $E_{\text{F}}$  for  $B$  between 0.25 T and

0.3 T indicates that  $\hbar/\tau = \hbar\omega_c \approx 0.5$  meV. This is consistent with the width of the Landau levels around  $E_F$ , which is approximately  $7 \text{ mV}/\mathcal{F} \approx 0.5$  meV. Therefore, we might expect to see a crossover from  $\tau_{\text{qp}} \sim (E_F - E)^{-1}$  behaviour to  $(E_F - E)^{-2}$  behaviour around  $E_F - E \approx 0.5$  meV. That is,

$$\tau_{\text{qp}} \sim A(E_F - E)^{-1} + B(E_F - E)^{-2}. \quad (4.8)$$

That we observe linear behaviour in  $\tau_{\text{qp}}^{-1}$  up to 3 meV is not necessarily inconsistent with the above prediction. Firstly, it is not clear over what energy range the transition takes place; and secondly, there are simply not enough data points to be able to clearly identify a smooth change-over from linear to square-law behaviour. What is clear though, is that we observe *predominantly* linear behaviour in  $\tau_{\text{qp}}^{-1}$  up to 3 meV.

There are few direct measurements of  $\tau_{\text{qp}}$  with which to compare our results. Schmidt *et al.* have recently obtained a direct measurement of  $\tau_{\text{qp}}$  by measuring correlations in the fluctuations of the LDOS of a 3D emitter, using an impurity state as a localised spectrometer of the system (Schmidt *et al.* 2001). They indeed find an additional correction to the  $(E_F - E)^2$  energy dependence of  $\tau_{\text{qp}}^{-1}$  of the form  $\tau_{\text{qp}}^{-1} \propto (E_F - E)^{3/2}$  for states close to the Fermi level, as predicted by Altshuler *et al.* for a three-dimensional system. Although our results are not directly comparable to those of Schmidt *et al.*, since our results are for a two-dimensional system, their result clearly supports our observation of a correction to the  $\tau_{\text{qp}}^{-1} \sim (E_F - E)^2$  energy dependence of the form predicted by Altshuler *et al.*.

## 4.4 Data from devices *a* and *b*

In addition to feature *d* discussed above, features *a* and *b* show similar effects in a magnetic field  $B \parallel z$ . Figure 4.7 and figure 4.8 show colour-scale plots of  $I(B, V)$  for features *a* and *b*. The formation of Landau levels is clearly evident in both features, although unlike feature *d*, they can only be resolved individually for  $n = 0$  and  $n = 1$ . Interestingly, the  $n = 0$  and  $n = 1$  Landau levels again emerge from a single broad peak at the high voltage edge of the feature, so the behaviour of feature *d* in this respect is not unique.

The solid white lines on the plot of feature  $a$  show the expected voltage dependence of the Landau levels on  $B$ , using a leverage factor of  $\mathcal{F} = 8.0$ , determined from the thermal activation of the current onset at  $B = 0$  T. (Thornton *et al.* 1998c). The leverage factor for feature  $b$  could not be obtained reliably from the thermal activation of the onset. Instead, the white fan lines on the plot of feature  $b$  are simply guides to the eye, plotted using a leverage factor of  $\mathcal{F} \approx 14$ . Unfortunately, it is not possible to obtain information about  $\tau_{\text{qp}}$  from this data, since only a few Landau levels are individually resolvable.

## 4.5 Summary

In this chapter, resonant tunnelling through a single QD state has been used to measure the LDOS in a Landau quantised 2DES. At low temperature we observe clearly resolved Landau levels in the LDOS in three different devices. By varying the voltage, we can measure the LDOS from the Fermi level, down to the sub-band edge. We find that the resolution of the Landau levels decreases as we probe energies deeper below the Fermi level. We interpret this effect in terms of the dependence of the quasi-particle lifetime,  $\tau_{\text{qp}}$ , on energy, and use our results to obtain values for  $\tau_{\text{qp}}$ .

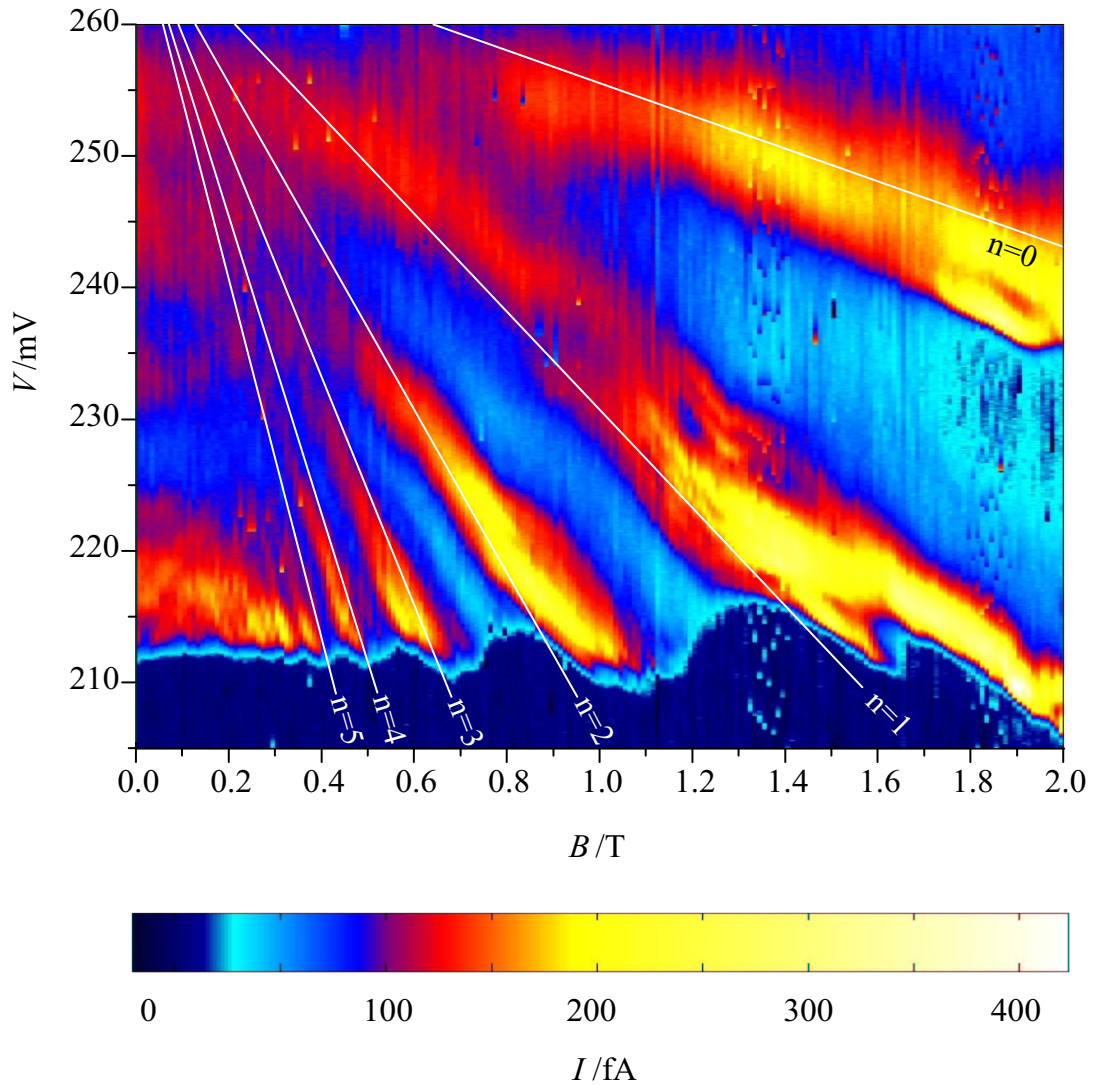


Figure 4.5: Colour-scale plot of the current,  $I$ , versus the applied bias,  $V$  and magnetic field,  $B \parallel z$  for device  $d$ . In general, darker, bluer shades represent smaller currents and brighter red/yellow shades represent larger currents. The solid white lines on show the expected voltage positions of the Landau level peaks as a function of  $B$ . These lines have been determined from the Landau level energy  $\epsilon = (n + \frac{1}{2})\hbar\omega_c$ , using a leverage factor (estimated from the thermal activation of the current onset) of  $\mathcal{F} = 14.4$  to relate the energy,  $\epsilon$  to the applied voltage,  $V$ .

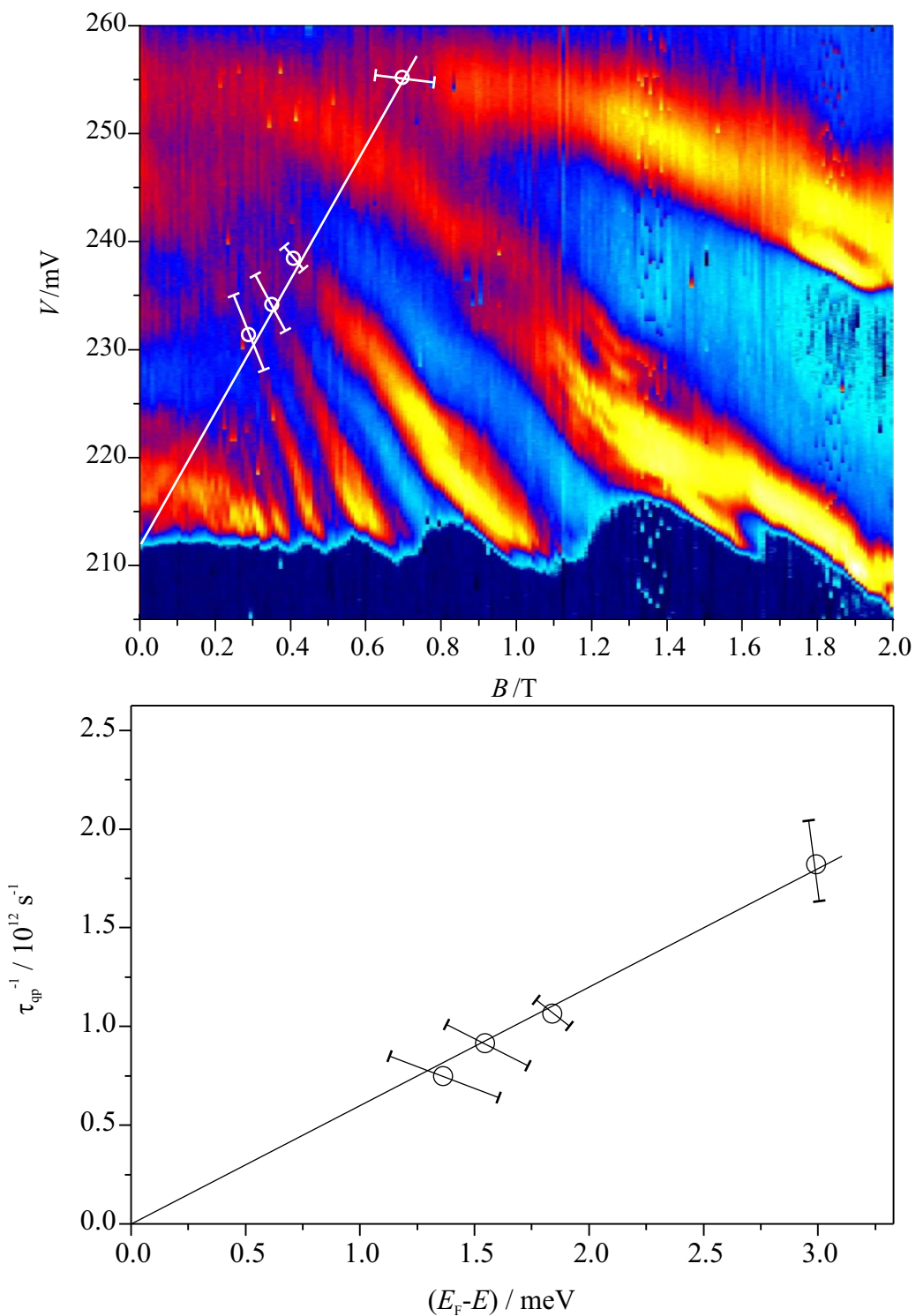


Figure 4.6: Top) Colour-scale plot of  $I(V, B)$  for device  $d$ , showing the points where the peak due to a particular Landau level can just be resolved (see main text.) Bottom) Values of  $\tau_{\text{qp}}^{-1}$  versus  $(E_{\text{F}} - E)$ . The line is  $\tau_{\text{qp}}^{-1} = (E_{\text{F}} - E)/\beta\hbar$ .

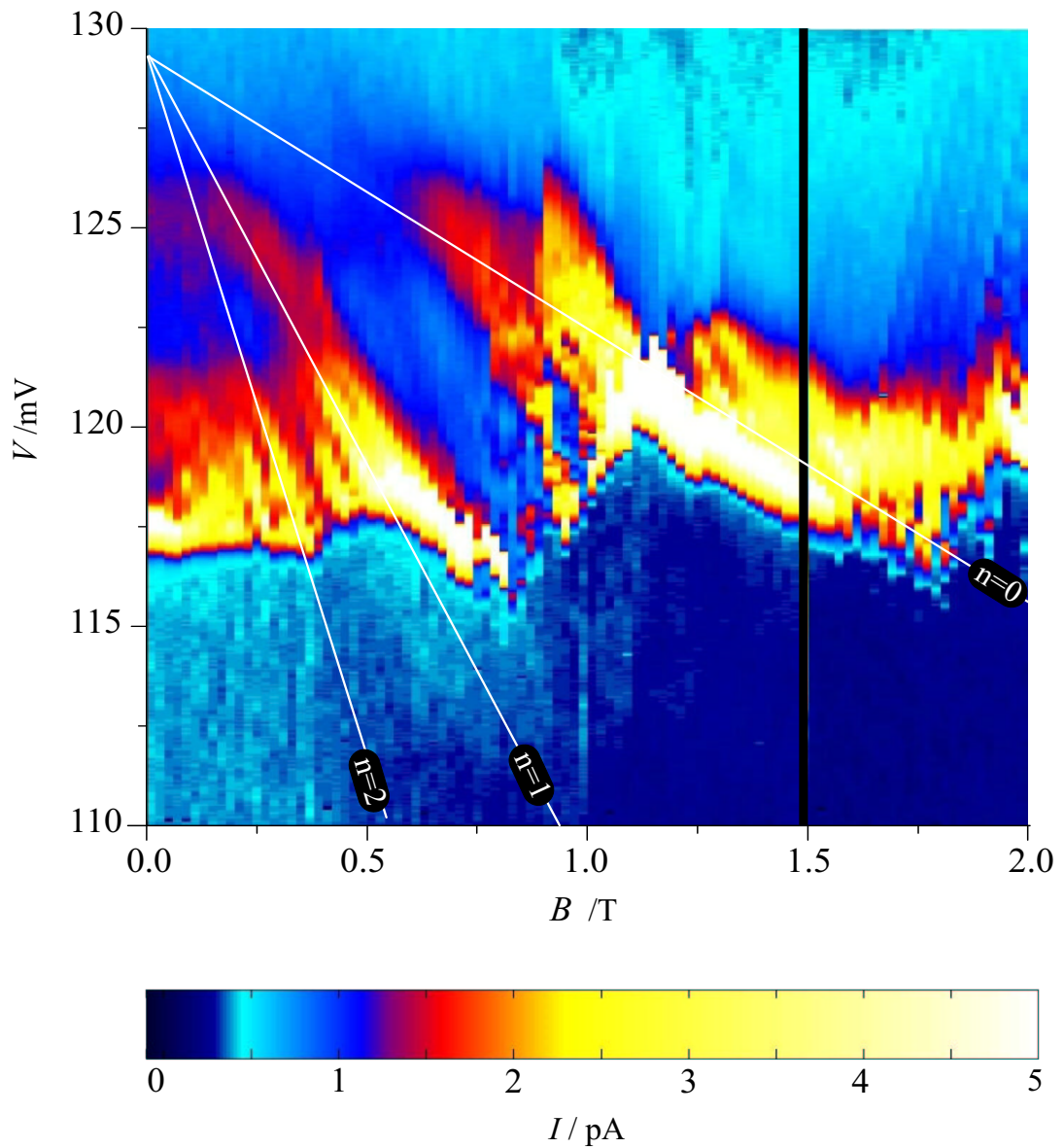


Figure 4.7: Colour-scale plot of the current,  $I$ , versus the applied bias,  $V$  and magnetic field,  $B \parallel J$  for device  $a$ . In general, darker, bluer shades represent smaller currents and brighter red/yellow shades represent larger currents. The solid white lines show the expected voltage positions of the Landau level peaks as a function of  $B$ . These lines have been determined from the Landau level energy  $\epsilon = (n + \frac{1}{2})\hbar\omega_c$  using a leverage factor (estimated from the thermal activation of the current onset) of  $\mathcal{F} = 8.0$  to relate the energy,  $\epsilon$  to the applied voltage,  $V$ . Plot constructed from data obtained by Dr. A. S. G. Thornton.

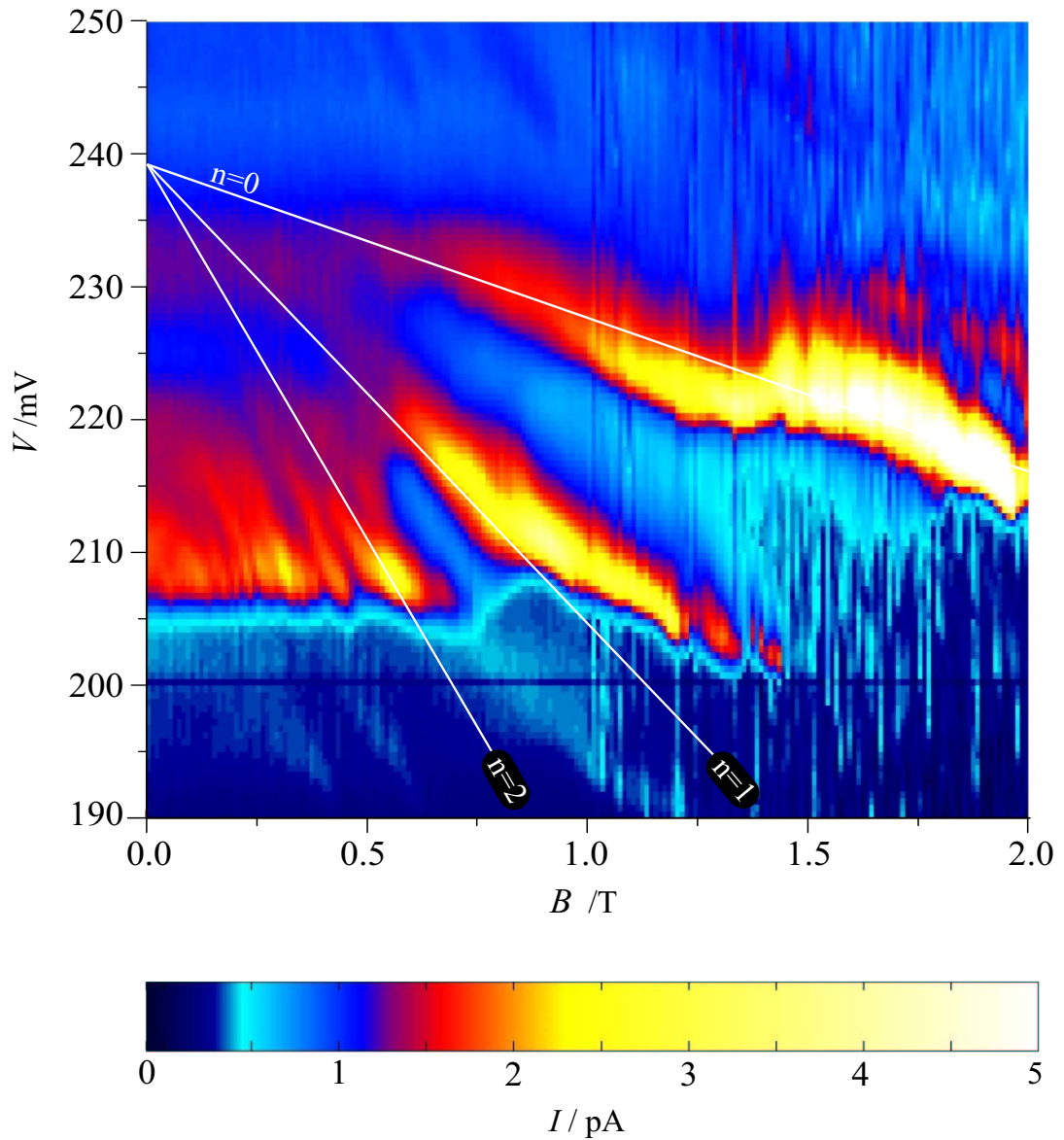


Figure 4.8: Colour-scale plot of the current,  $I$ , versus the applied bias,  $V$ , and magnetic field,  $B \parallel J$ , for device  $b$ . In general, darker, bluer shades represent smaller currents and brighter red/yellow shades represent larger currents. The solid white lines are guides to the eye. These lines have been determined from the Landau level energy  $\epsilon = (n + \frac{1}{2})\hbar\omega_c$ , using a leverage factor of  $\mathcal{F} \approx 14$  to relate the energy,  $\epsilon$ , to the applied voltage,  $V$ . Plot constructed from data obtained by Dr. A. S. G. Thornton.

# Chapter 5

## High magnetic field spectroscopy of a 2DES

### 5.1 Introduction

In the previous chapter an experiment was presented that used a single, zero-dimensional electron state of an InAs quantum dot to probe the Landau level density of states of a two dimensional electron system. In this chapter, the experiment is extended by increasing the magnitude of the magnetic field to take the 2DES into the regime of the magnetic quantum limit. In this regime, the cyclotron gap,  $\hbar\omega_c$ , is comparable to or greater than the Fermi energy of the 2DES at  $B = 0$  T so that all the electrons lie in the lowest ( $n = 0$ ) Landau level. At the highest magnetic fields, the Landau level degeneracy becomes large enough for the lowest energy spin-state to accommodate all the electrons, so that the 2DES becomes spin polarised.

In bulk GaAs, the single-electron ('bare')  $g$ -factor of states at the bottom of the conduction band has a value of  $g^* = -0.44$  (Hermann and Weisbuch 1977). The negative value of  $g$  means that electrons with spin angular-momentum vectors lying parallel to  $\mathbf{B}$  (spin 'up') have lower energy than those lying anti-parallel to  $\mathbf{B}$  (spin 'down'). However, the energy separation between the two spin-states in a system containing many electrons, such as a 2DES, can vary significantly from the single-electron spin

gap. Fang and Styles (1968) measured the  $g$  factor of a 2DES confined at a silicon surface. By analysing the oscillations in the (in-plane) magneto-conductance of the 2DES, they obtained values of  $|g|$  between 2.47 and 3.25, significantly larger than that of the bulk single-electron value for Si,  $g \approx 1.99$ . This enhancement has been attributed to electron interactions in the system (Janak 1969, Suzuki and Kamamoto 1973, Ando and Uemura 1974, Ando *et al.* 1982). In a 2DES in particular, there is also expected to be a change in the spin gap due to the effects of the 2D confinement potential (Snelling *et al.* 1991).

In the literature, enhancements to the spin gap are commonly described in terms of an ‘enhanced’  $g$ -factor. In some ways this practice is unfortunate since the contribution to the spin-gap coming from the electron-electron interactions is not necessarily directly proportional to  $B$ , so that, confusingly, the enhanced  $g$ -factor can itself be dependent on  $B$ . Since it is common to write the spin-gap in this way, however, this practice will also be adopted here in order to compare the results of this chapter with published work.

There have been a number of experiments to measure the  $g$  factor of 2DESS in GaAs/(AlGa)As heterostructures by a variety of techniques. A number of groups (Usher *et al.* 1990, Leadley *et al.* 1998, Liang *et al.* 2001) have obtained measurements of the spin gap by studying the thermal activation of the longitudinal (‘diagonal’) conductivity. If the Fermi level lies within the gap, there is no conduction at  $T = 0$  K. As the temperature is increased, however, some electrons are excited across the energy gap from filled states below the Fermi level to empty states above the Fermi level, giving rise to a conductivity which depends on the temperature and the energy gap. However, since the energy width of the delocalised (current carrying) states is finite, thermal activation techniques measure the *mobility* gap (see section 1.4.2), which can be significantly less than the spin splitting.

Dolgoplov *et al.* (1997) have measured the spin gap directly by using a magneto-capacitance technique to measure the electron density,  $n_s$ , in the 2DES as a function of gate voltage,  $V_g$ . Plateaus are observed in  $n_s(V_g)$  when the Fermi level lies in a cyclotron or spin gap; the width of the plateau reflects the width of the gap.

In both types of experiment, a  $g$ -factor is observed that is larger than the bulk one-electron value by roughly an order of magnitude. However, since both techniques require the Fermi level to be in the energy gap, the value of  $g$  can only be measured at (or very close to) odd integer filling factors. An experiment by Dobers *et al.* (1988), based on the observation of electron spin resonances in the longitudinal resistance, can access a slightly larger window of filling factors. However, the electron-spin resonance technique measures the bare  $g$ -factor (i.e. unaffected by electron-electron interactions) and is therefore not comparable with our experiment.

Conversely, the technique presented in chapters 3 and 4 allows us to probe the density of states in the 2DES well *below* the Fermi level. In principle this means that we can obtain measurements of the spin gap, and hence the  $g$  factor, at *arbitrary* filling factor. In practice, we find that it is only possible to resolve the spin gap at the larger magnetic fields, i.e. where the spin gap becomes comparable to or exceeds the spectral width of the Landau levels.

As in the previous chapter, the majority of the results come from device *d*. Results from additional devices are included for comparison.

## 5.2 Low temperature $I(V)$ in high magnetic field

Figure 5.1 shows a grey scale plot of the tunnel current through device *d* as a function of the bias across the device,  $V$ , and magnetic field  $0.0 \text{ T} < B < 7.2 \text{ T}$ . As identified in chapter 3, there is an isolated resonant feature in the tunnel current at  $V \approx 210 - 260 \text{ mV}$  due to tunnelling through a single 0D quantum dot state. As before, the magnetic field is applied perpendicular to the plane of the 2DES giving rise to Landau levels in the density of states of the 2DES. The temperature is 0.3 K. The data has been plotted in grey scale; *darker* shading indicates larger values of the current,  $I$ .\*

Figure 5.2 shows a selection of  $I(V)$  traces at different magnetic fields.

---

\*Note that this is a slightly different convention to that used in the colour plot (figure 4.5), where in general, lighter colours were used to indicate larger currents.

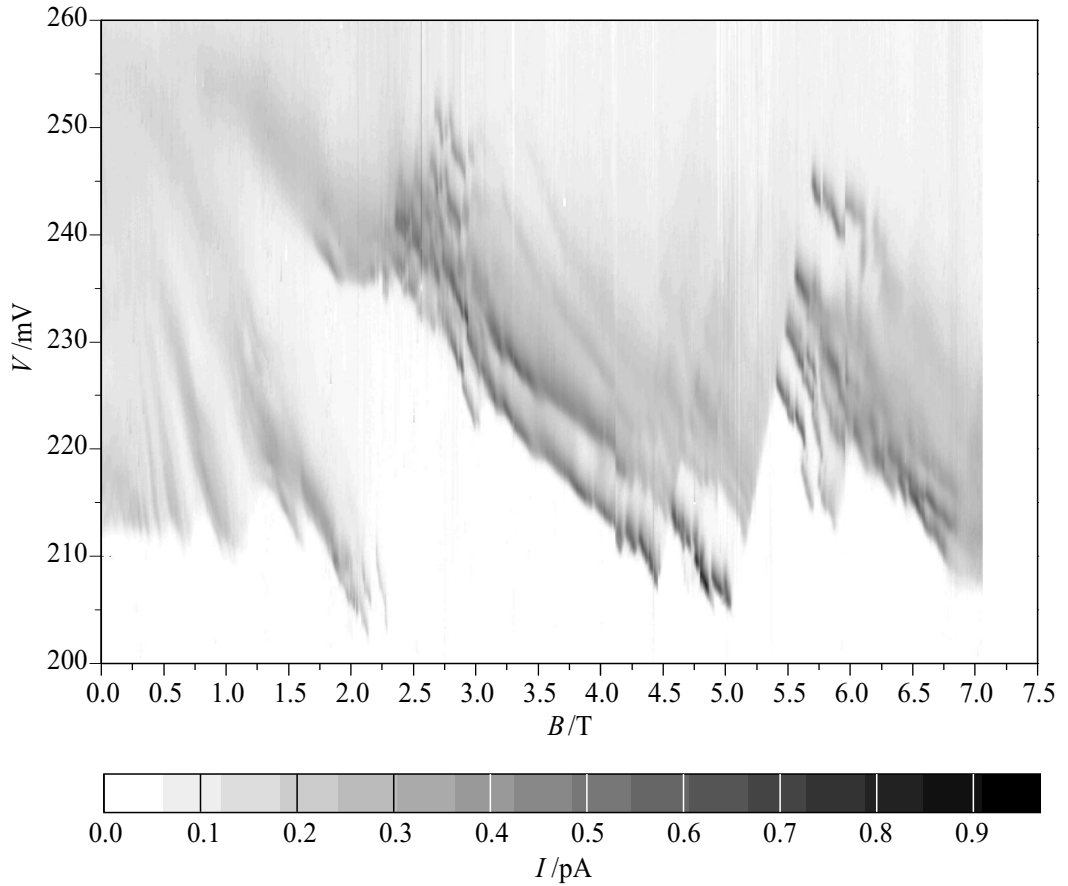


Figure 5.1: Grey-scale plot of the tunnel current  $I$  through device  $d$  versus voltage  $V$  and magnetic field  $B$ . Darker shading indicates larger current values. Note that the data in the 0 – 2 T range is the same as that shown in Figure 4.5. The temperature is 0.3 K.

### Summary of features in figure 5.1

At about 2.3 T, the peak in the tunnel current at  $V = 204 - 210$  mV, corresponding to the  $n = 1$  Landau level, disappears and there follows a marked change in the voltage position of the onset of the resonance ( $V_F$ ), indicating a sharp shift in the Fermi energy, consistent with the depopulation of the  $n = 1$  Landau level. At  $B < 2.3$  T, the  $n = 0$  Landau level gives rise to a single peak in the resonant current. However, just above 2.3 T, where the Fermi level enters the  $n = 0$  Landau level, the peak corresponding to the  $n = 0$  Landau level quickly fragments into a number of sharper peaks (also see the  $I(V)$  traces in figure 5.2). These are joined at 2.85 T by two more similar peaks at higher voltage. This structure evolves with  $B$  until, by 3.17 T, only two peaks remain. These two peaks persist, moving steadily

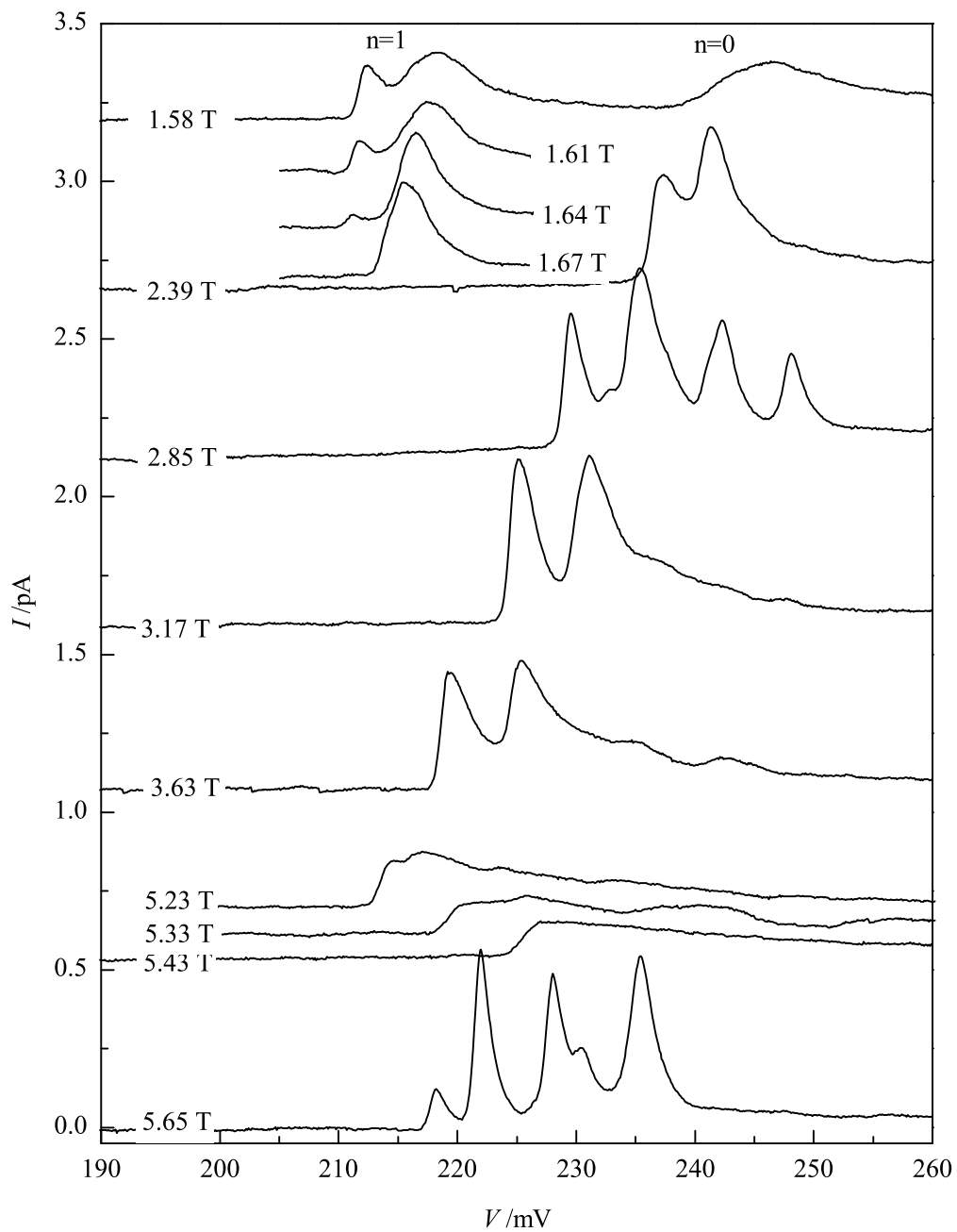


Figure 5.2:  $I(V)$  traces from device  $d$  at several different magnetic fields ( $B \parallel J$ ) between 1.58 T and 5.65 T. The temperature is 0.3 K. (Traces are offset for clarity.)

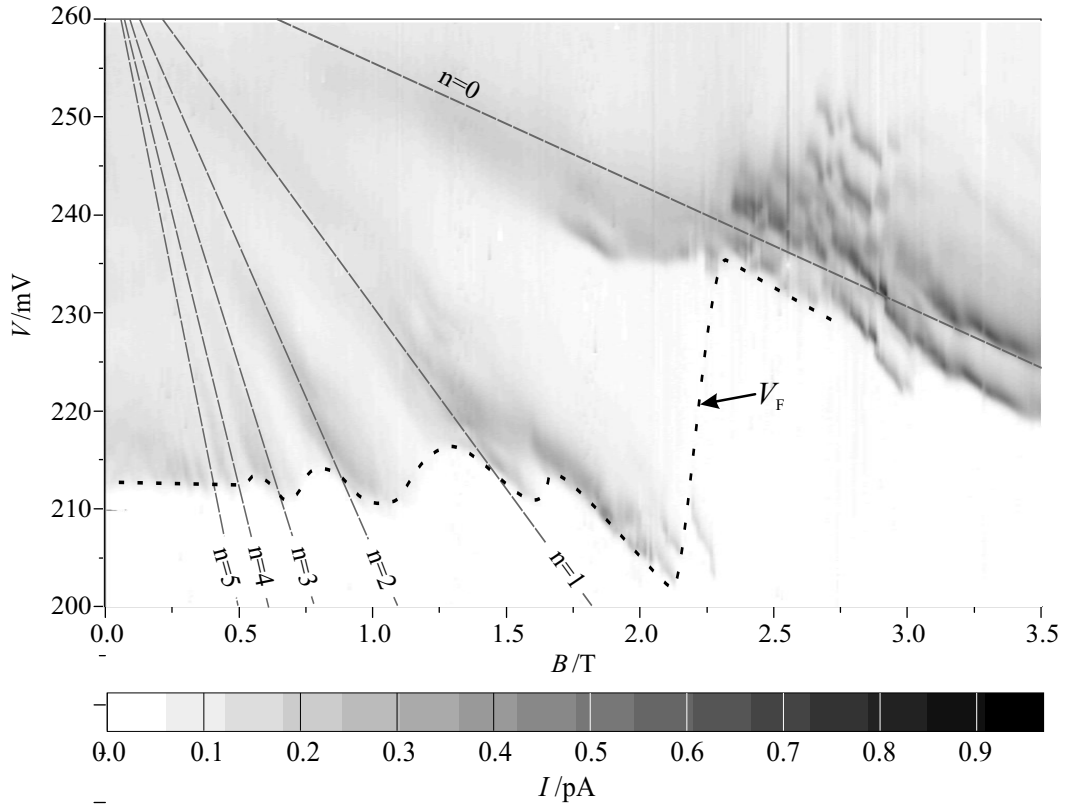


Figure 5.3: Grey-scale plot of tunnel current through device  $d$  as a function of the voltage across the device contacts,  $V$ , and magnetic field  $B$ . Darker shading indicates larger current. Note that the data in the  $0 - 2$  T range is the same as that shown in Figure 4.5. The temperature is  $0.3$  K.

to lower voltage, tracking the expected voltage position of the  $n = 0$  Landau level, until the filling factor of the 2DES approaches  $\nu = 1$  at  $\sim 5$  T. At  $4.50$  T, the movement of the onset position to lower voltage is interrupted by a sharp shift to higher voltage, and again at  $5.09$  T by a larger shift. Then, at  $B > 5.45$  T a multiple peak structure emerges which is qualitatively similar to that observed at  $\nu = 2$ .

### 5.3 Change in the Fermi energy at filling factor 2

As discussed in the previous chapter, the voltage that marks the onset of tunnelling through the QD ( $V_F$ ) oscillates with increasing  $B$  due to the successive depopulation of Landau levels in the 2DES. At about 2.3 T, the peak in the tunnel current that corresponds to the  $n = 1$  Landau level disappears reflecting the depopulation of this Landau level. There follows a marked jump in the value of  $V_F$ , which changes from  $V_F = 202$  mV at 2.17 T to 235 mV at 2.30 T as the Fermi level moves into the  $n = 0$  Landau level. However, compared with the oscillations in  $V_F$  observed at lower  $B$ , the change in  $V_F$  accompanying the depletion of  $n = 1$  is significantly larger and deserves some additional explanation.

A jump in  $V_F(B)$  is expected to occur with increasing  $B$  when the highest occupied Landau level becomes depopulated and the Fermi level moves down to the next lowest lying Landau level; i.e. whenever the filling factor  $\nu$  reaches an integer value. We ignore spin splitting for the moment and just look at the jumps in  $V_F$  that occur at even integer filling factor. In a simple picture, ignoring spin-splitting and Landau level broadening, the energy gap between each Landau level is simply the cyclotron gap,  $\hbar\omega_c$ , so the jump in  $V_F$  that occurs at even integer filling factors is given by

$$\begin{aligned} \frac{e}{\mathcal{F}}\Delta V_F(\nu) &= \hbar\omega_c \\ &= \hbar\frac{\hbar n_s}{m^*\nu}, \end{aligned} \quad (5.1)$$

where  $\nu = 2, 4, 6 \dots$ ,  $\mathcal{F}$  is the leverage factor (see previous chapter),  $\Delta V_F$  is the change in  $V_F$  that occurs at even-integer filling factor, and  $n_s$  is the sheet density of electrons in the 2DES. Therefore, in this simple picture,  $\Delta V_F(\nu = 4)$  is expected to be half that of  $\Delta V_F(\nu = 2)$ ,  $\Delta V_F(\nu = 6)$  is expected to be a third that of  $\Delta V_F(\nu = 2)$  and so on. However, the ratio of  $\Delta V_F(2)/\Delta V_F(4)$  that is observed in the data (figure 5.3) is certainly much larger than 2. The discrepancy between the observed value and the expected value can be explained by the broadening of the Landau level density of

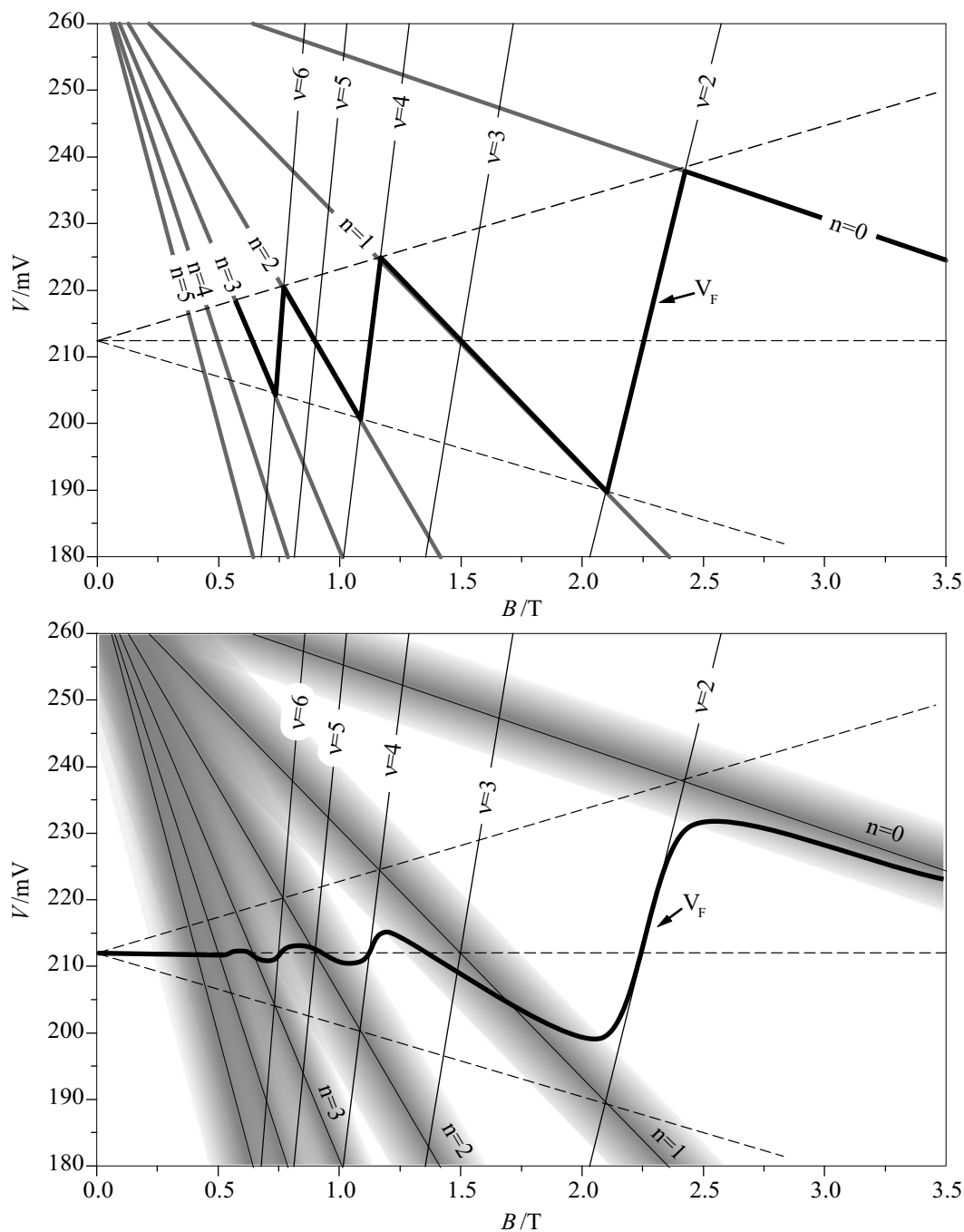


Figure 5.4: Top) The grey lines show the expected voltage positions of the Landau levels (not including spin-splitting) as a function of magnetic field, for device  $d$  (see section 4.2.3). The thin black lines show the positions of integer filling factor,  $\nu$ . (Note that  $\nu$  is also affected by  $V$  in addition to the usual dependence on  $B$ , due to the changing electron density with  $V$ . This is discussed in section 5.4). The thick black line shows the voltage position of the current onset  $V_F$ . Bottom) Broadening of the Landau levels, due to electron scattering, has the effect of dampening the oscillations in  $V_F$ . The dampening effect is greatest where there is strong overlap between the Landau levels. (Landau level broadening shown schematically only—in general, broadening is larger for Landau level energies further from the Fermi level. See section 4.3.)

states, discussed in chapter 4. The effect is shown schematically in figure 5.4. In the case of no scattering, the Landau levels are  $\delta$ -functions as shown in the top diagram. In this case,  $V_F$  exactly follows the expected voltage position of the highest occupied Landau level and  $\Delta V_F$  is proportional to  $\hbar\omega_c$  (equation 5.1). If the electrons suffer scattering, however, then the states belonging to a Landau level  $n$  are spread out in an energy interval  $\Gamma$  centred on the energy  $(n + \frac{1}{2})\hbar\omega_c$  (section 1.4.2). This broadening effectively reduces the energy gap between each Landau level. At low magnetic fields, where  $\Gamma \sim \hbar\omega_c$  there is strong overlap between the states of different Landau levels, so that there is no identifiable energy gap between each Landau level, but there remains an oscillation in the density of states. With increasing overlap between the Landau levels, the magnitude of the oscillation in  $V_F$  is reduced to an ever decreasing fraction of the amplitude expected for the no-scattering case, as can be seen in the bottom diagram of figure 5.4. At higher magnetic fields, where  $\Gamma \ll \hbar\omega_c$ , the fractional reduction in  $\Delta V_F$  is relatively minor, hence the larger than expected ratio of  $\Delta V_F(2)$  to  $\Delta V_F(4)$ .

Between  $B = 0 - 1.3$  T, the voltage position of the current peak corresponding to the  $n = 1$  Landau level agrees well with that expected from section 4.2.3. When the Fermi level enters the  $n = 1$  Landau level at  $B \approx 1.3$  T, however, the voltage position of the peak begins to deviate from the expected voltage position. The current peak still moves to lower voltage with increasing  $B$ , but at a slower rate than that expected from section 4.2.3. This discrepancy can also be accounted for by the finite energy of the Landau level. When the Fermi level enters the  $n = 1$  Landau level, the highest energy states within the Landau level begin to depopulate with increasing  $B$ . Therefore, as the Landau level energy,  $\epsilon = (n + \frac{1}{2})\hbar\omega_c$ , increases with  $B$ , the Fermi level moves through the Landau level states from high energy to low energy. Therefore, whilst there is still a net increase in the energy of the Fermi level with increasing magnetic field, it rises less quickly as the Fermi level drops through the spectrum of states *within* the Landau level. This effect is illustrated in figure 5.4.

There is a small deviation from the steady increase in  $V_F$  at  $B = 1.7$  T. Here,  $V_F$  increases from 211 mV to 213 mV over a relatively small change in  $B$  (a few tens of mT). This change occurs whilst the Fermi level is still

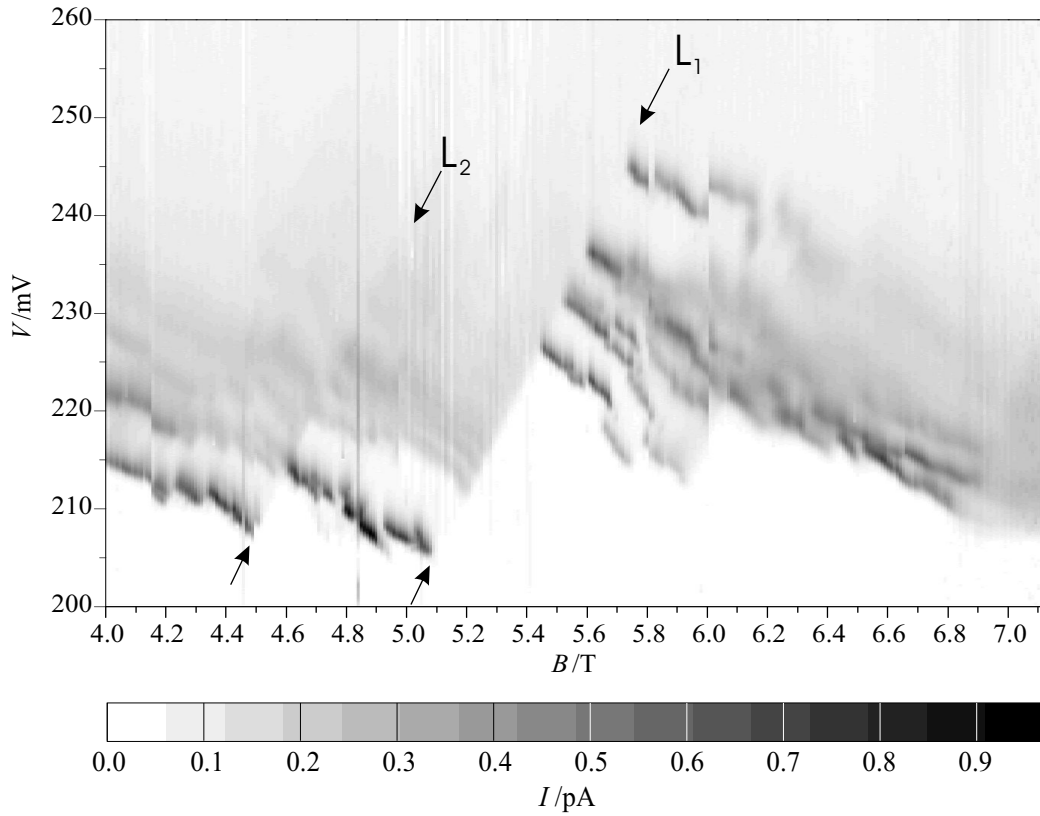


Figure 5.5: Grey-scale plot of tunnel current through device  $d$  as a function of the voltage across the device contacts,  $V$ , and magnetic field  $B$ , between 4.0 and 7.1 T. Darker shading indicates larger current. The arrows highlight the lines  $L_1$  and  $L_2$  referred to in the text. The temperature is 0.3 K.

within the  $n = 1$  Landau level so it cannot be due to depopulation of the  $n = 1$  Landau level. However, it does occur close to the magnetic field at which  $\nu = 3$  is expected to fall. Therefore, it is possible that this particular discontinuity in  $V_F$  reflects the depopulation of the higher energy *spin-split* Landau level.

## 5.4 Plot of current versus filling factor and voltage

Between  $\sim 3$  T and 4.5 T,  $V_F$  moves continuously to lower voltage with increasing  $B$ , closely following the expected voltage position of the  $n = 0$

Landau level ( $V_0$ ) (equation 4.1). At 4.48 T, however, this trend is abruptly interrupted by a relatively rapid shift of  $V_F$  to *higher* voltage—from 207 mV to 212 mV—over an interval in  $B$  of 130 mT. Then, at 4.61 T, the original trend to lower voltage is resumed again as abruptly as it was interrupted.

Beyond  $B = 4.61$  T,  $V_F$  continues to follow  $V_0(B)$  until  $B = 5.08$  T, at which point  $V_F$  abruptly begins a second rapid slide to higher voltage. This time,  $V_F$  moves from approximately 205 mV at 5.08 T to approximately 225 mV at 5.45 T, defining a sharp line across the grey scale map of  $I(B, V)$ , which, for the purposes of discussion, we label  $L_1$ . At 5.45 T,  $V_F$  again resumes tracking  $V_0$ , albeit with an offset in voltage. Then, at  $B > 5.45$  T additional peaks in  $I(V)$  begin to emerge at voltages  $V > V_F$ , from points  $(B, V)$  along the *same line*,  $L_1$ . This structure will be discussed in section 5.6; for the moment, the important point is that they define a clear straight line of finite gradient across the grey scale map  $I(B, V)$ . Notice that the rapid increase in  $V_F$  that occurs at  $B \approx 4.5$  T also defines a line of almost identical gradient to, but not quite as clear as, that of  $L_1$ . We shall call this line  $L_2$ .

Since  $L_1$  does not occur at a single value of  $B$ , but falls across a large number of successive  $I(V)$  traces, obtained at irregular intervals in time, it is difficult to explain such a linear feature in terms of a problem with the experiment. On the other hand, the gradient and the linearity of both lines  $L_1$  and  $L_2$  may be explained if we assume that they represent the loci of constant *filling factor*. This does not, however explain why the lines should be so sharply defined; this will be discussed in section 5.5. An explanation for their finite gradient is discussed in the following section.

### 5.4.1 Change in filling factor with voltage

Since the Landau level filling factor is inversely proportional to  $B$  we expect characteristics of the  $I(V)$  trace that depend on filling factor to change with  $B$ . However, as explained in chapter 3, the device is essentially a capacitor and so the electron density in the 2DES increases with the voltage applied to the device,  $V$ . The point is that a particular  $I(V)$ , obtained at a magnetic

field  $B$ , does *not* correspond to a precise value of the filling factor,  $\nu$ , since the filling factor also depends on the voltage  $V$ . In other words, in order to maintain the 2DES at a constant filling factor while increasing the voltage, there must also be a corresponding increase in the magnetic field.

To determine how the filling factor depends on  $V$ , it is necessary to know how the sheet density of the 2DES,  $n_s$ , behaves with voltage. Capacitance measurements on similar devices (Belyaev *et al.* 2000) show that as long as  $V \gtrsim 100$  mV, then for small changes in  $V$  of up to  $\sim \pm 50$  mV,  $n_s(V)$  is linear in  $V$  to a good approximation,

$$en_s(V) \approx C(V - a) + Q \quad (5.2)$$

for  $|V - a| \lesssim 50$  mV and  $|a| \gtrsim 100$  mV,

where  $C$ ,  $Q$  and  $a$  are constants.  $C$  is the differential capacitance ( $C = dQ/dV$ ) per unit area of the 2DES at  $V = a$ , and  $Q$  is the charge per unit area of the 2DES at  $V = a$ . Using this approximation, we can estimate the corresponding value of the filling factor,  $\nu$ , for any particular data point  $(B, V)$ ,

$$\begin{aligned} \nu(B, V) &= \frac{hn_s}{eB} \\ &\approx \frac{h}{B} [C(V - a) + Q]. \end{aligned} \quad (5.3)$$

Re-arranging the above equation, it can be seen that a set of points  $(B, V)$  that correspond to a particular value of  $\nu$  will form a straight line of positive gradient ( $dV/dB$ ) when plotted on a graph of  $V$  versus  $B$ ,

$$V(B) \approx a + \frac{1}{C} \left( \frac{B\nu e^2}{h} - Q \right). \quad (5.4)$$

This strongly suggests that the lines  $L_1$  and  $L_2$  represent sets of data points  $(B, V)$  that correspond to a constant filling factor.

The value of  $n_s$  determined from the oscillations in the Fermi energy at  $B < 2$  T,  $n_s(212 \text{ mV}) = (1.2 \pm 0.2) \times 10^{15} \text{ m}^{-2}$ , (section 4.2.4) places the magnetic field position of  $\nu = 1$  at  $B = 5.0 \pm 0.8$  T when the voltage is  $V \approx 212$  mV. From the plot of  $I(B, V)$ , it can be seen that this point falls

close to the line  $L_1$ . It follows that  $L_1$  must represent a filling factor close to  $\nu = 1$ , therefore suggesting that  $L_1$  might correspond to  $\nu = 1$  exactly. However, the uncertainty in the estimate of the magnetic field position of  $\nu = 1$  is too large for us to be confident of this assignment from the Fermi energy oscillations alone. In particular, the uncertainty does not rule out the assignment of  $\nu = 1$  to the line  $L_2$  instead.

Accompanying the line  $L_1$  there is the sudden emergence of a multiple peak structure at  $V > V_F$ . Similar structure can also be observed in the region around  $\nu = 2$ , and a complex structure also appears at the peak corresponding to the  $n = 1$  Landau level at  $\nu = 4$ . These structures will be commented upon in more detail in section 5.6. Regarding the identification of a filling factor with  $L_1$ , however, the important point is that the similarities between the structures observed at  $L_1$ ,  $\nu = 2$  and  $\nu = 4$  adds weight to the conjecture that  $L_1$  should be associated with integer filling factor (i.e.  $\nu = 1$ ). In particular, it does not point toward the identification of  $L_2$  with  $\nu = 1$ , since the structure observed at  $\nu = 2$  bears little resemblance to that at  $L_2$ .

### 5.4.2 Measurements of electron density

Assuming that the line  $L_1$  does represent the filling factor  $\nu = 1$ , the electron density in the 2DES as a function of voltage can now be determined. We find that the charge  $Q$  and differential capacitance of the 2DES,  $C = dQ/dV$  is

$$\begin{aligned} C/e &= (3.75 \pm 0.30) \times 10^{15} \text{ m}^{-2}\text{V}^{-1} \\ Q/e &= (1.28 \pm 0.02) \times 10^{15} \text{ m}^{-2} \end{aligned}$$

at  $V = 218$  mV. Hence the electron density for voltages close to  $V = 218$  mV is given approximately by (equation 5.3)

$$n_s(V) \approx [1.28 + 3.75(V - 0.218)] \times 10^{15} \text{ m}^{-2}. \quad (5.5)$$

This result compares well with values for the electron density obtained by magneto-capacitance measurements of *NU1403* (Belyaev *et al.* 2000), as

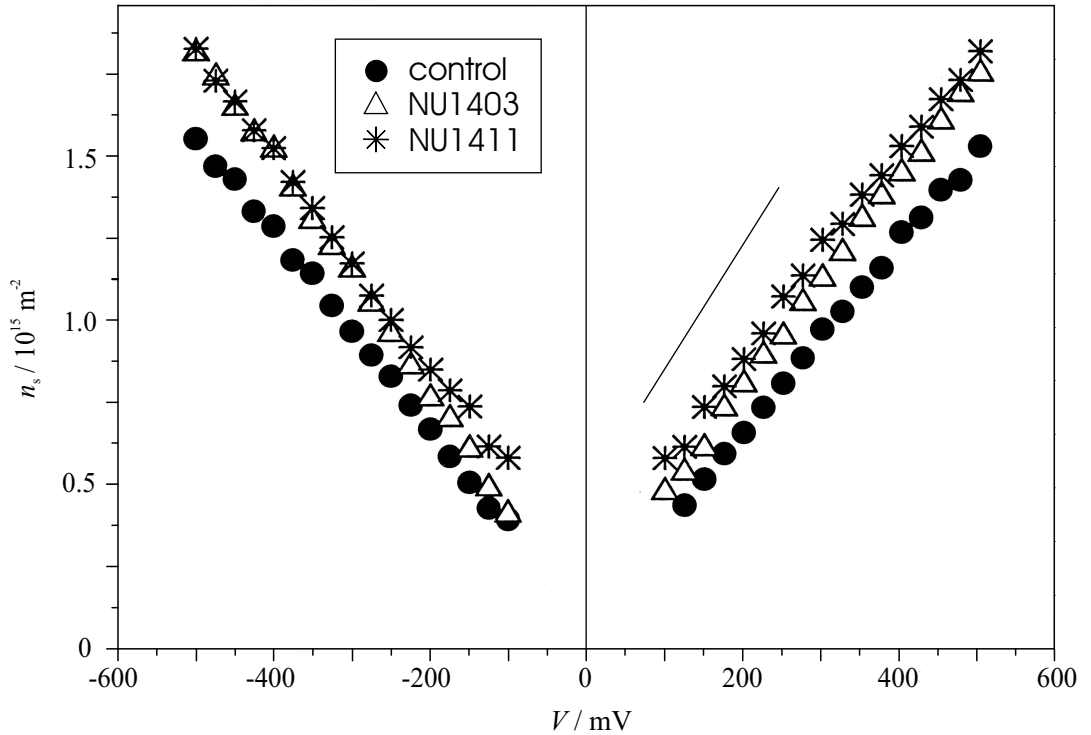


Figure 5.6: Areal average of the electron density in the 2DES versus voltage for three different devices, as determined from oscillations in the magneto-capacitance. Data from Belyaev *et al.* (2000). The solid line shows the electron density of the 2DES *local* to a QD in device NU1403 *d*, determined by a spectroscopic probe of the states in the 2DES by a bound state of the QD (see main text).

shown in figure 5.6. In particular, the differential capacitance per unit area,  $C$ , obtained from the spectroscopy measurement is identical, within error, to the measurement obtained from the capacitance results. The absolute value of  $n_s$  is slightly larger than the capacitance result, but this is not unexpected since, (i) the capacitance measures the *mean* value of  $n_s$ , averaged over the area of the 2DES, whilst the QD spectrometer state measures the value of  $n_s$  *local* to the QD; and (ii) there are expected to be fluctuations in the local value of  $n_s$  due to the presence of some disorder in the 2DES introduced by the remote donors or the strain field of the QDs. The result is also consistent with the electron density estimated from the oscillations in the Fermi level at lower magnetic fields [ $n_s = (1.2 \pm 0.2) \times 10^{15} \text{ m}^{-2}$ ], and is also reasonably consistent with the value obtained from the voltage width of the feature at  $B = 0$  (section 3.7.2).

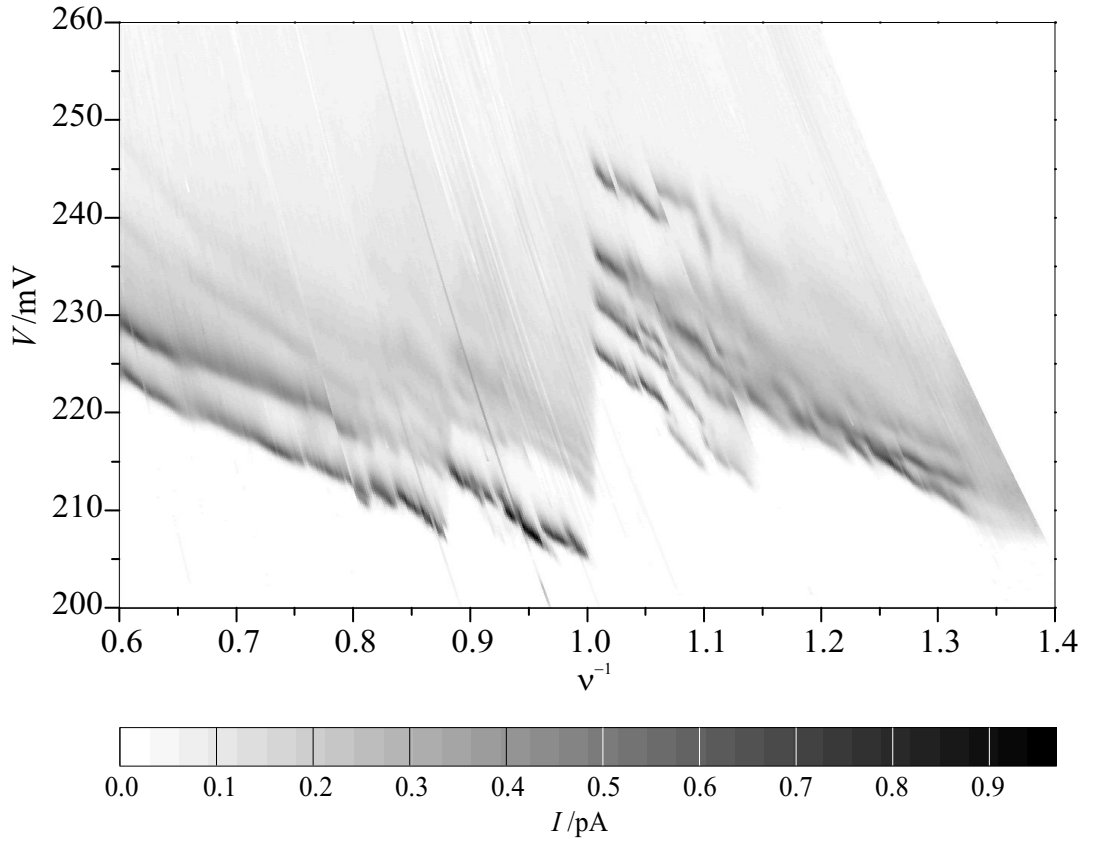


Figure 5.7: Grey-scale plot of tunnel current through device  $d$  as a function of the voltage across the device contacts,  $V$ , and Landau level filling factor  $\nu$ . Darker shading indicates larger current. The temperature is 0.3 K.

### 5.4.3 Result

A plot of  $I(\nu, V)$  can be constructed by taking each experimentally obtained data point  $(B, V)$  in turn, calculating the corresponding value of  $\nu$  using equation 5.3, and then re-plotting the value of the current  $I(B, V)$  at the coordinates  $(\nu, V)$ . In practice, we plot the data against  $1/\nu$  instead, since  $1/\nu$  is linear in  $B$  for constant  $V$  and so a plot of  $I(\nu^{-1}, V)$  more closely resembles the original  $I(B, V)$  plot. Figure 5.7 shows the result; the diagonal top-left to bottom-right streaks show the lines of constant  $B$ . These streaks are the result of obtaining the data in the form of successive  $I(V)$  traces taken at constant  $B$ . Between one  $I(V)$  trace and the succeeding trace, in practice there is always found to be a minor change in the null voltage reading of the voltmeter used to measure the current. Notice that the lines

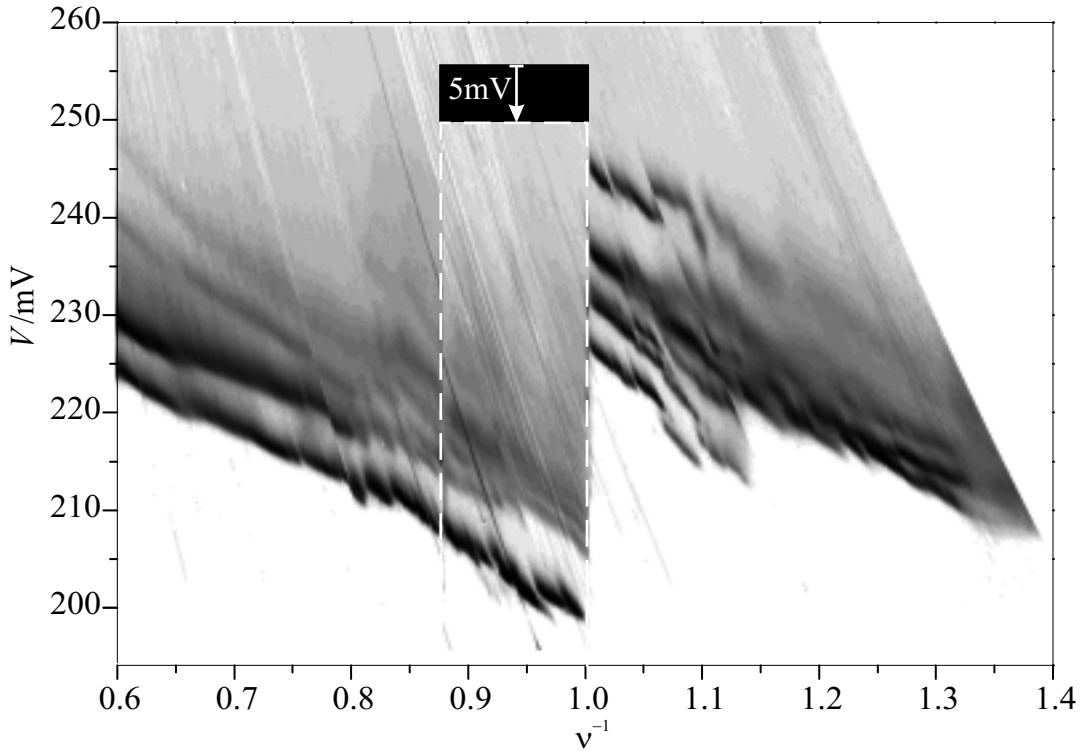


Figure 5.8: Grey-scale plot of tunnel current through device  $d$  as a function of the voltage across the device contacts,  $V$ , and Landau level filling factor  $\nu$ . Darker shading indicates larger current. The data is the same as that shown in figure 5.7, except that in this plot, the data between  $\nu = 1.13$  ( $\nu^{-1} = 0.88$ ) and  $\nu = 1$  has been shifted to lower voltage by 5 mV. The contrast has also been adjusted to enhance the visibility of some lower current features. The temperature is 0.3 K.

$L_1$  and  $L_2$  now lie along the  $y$ -axis of the plot, with  $L_1$  at  $\nu = 1$  and  $L_2$  at  $\nu = 1.13$  ( $\nu^{-1} = 0.88$ ).

## 5.5 Measuring the $g$ factor in the 2DES

Two peaks in the  $I(V)$  emerge from the multiple peak structure around  $\nu = 2$ . With increasing  $B$ , they move to lower voltage, closely following the expected voltage position of the  $n = 0$  Landau level, and the separation in voltage between them increases approximately linearly with  $B$ . This suggests that the two peaks are due to tunnelling from the one-electron spin-up and spin-down states of the  $n = 0$  Landau level in the 2DES, although how they evolve from the complex structure around  $\nu = 2$  is not clearly

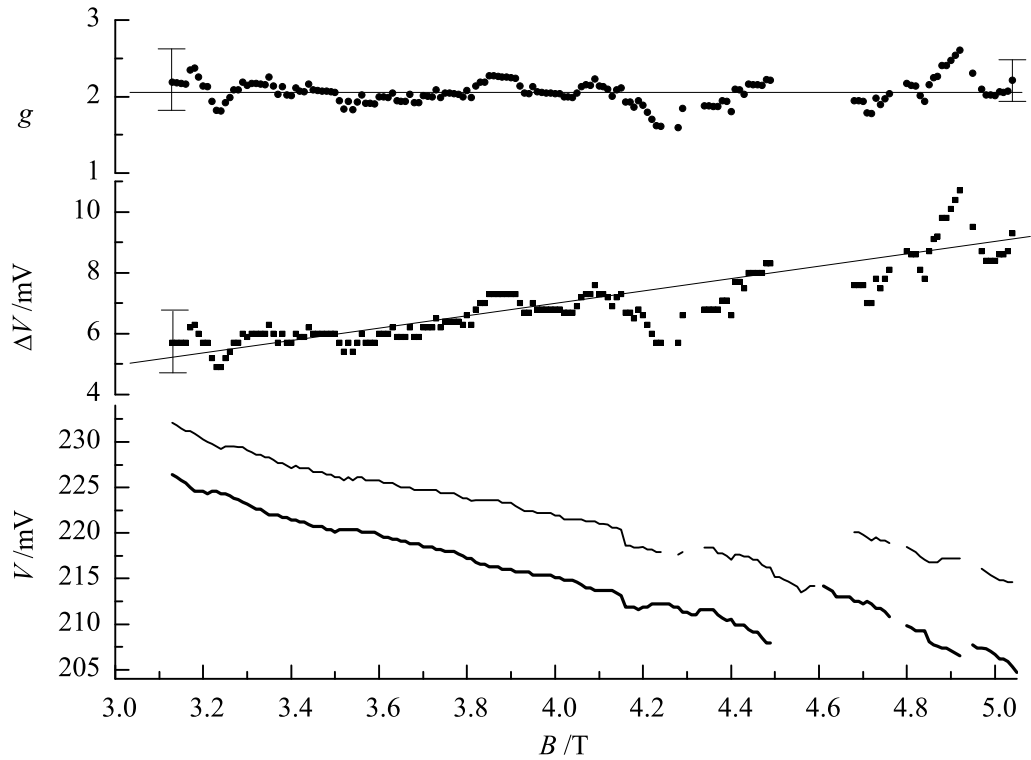


Figure 5.9: Bottom) The solid thick and thin lines show the voltage positions of the spin-up and spin-down peaks in  $I(V)$  versus magnetic field  $B \parallel z$ . Middle) Difference in voltage  $\Delta V$  between the spin-up and spin-down states. The continuous line is a guide to the eye. Top) The  $g$ -factor calculated from the voltage difference,  $g = e\Delta V/(\mathcal{F}\mu_B B)$ , using a leverage factor of  $\mathcal{F} = 14.4$ . The error in  $g$  is almost entirely due to the error in determining the voltage positions ( $\sim \pm 0.5$  mV). The continuous line is a guide to the eye.

understood. Nevertheless, since they do emerge from the structure around  $\nu = 2$ , this indicates that the two peaks must be associated with the 2DES. This rules out the possibility that the voltage splitting between the two peaks is *entirely* the result of spin-splitting in the QD state, although there is expected to be some contribution from the latter.

Assuming that the two peaks do represent the spin-up and spin-down states of the  $n = 0$  Landau level in the 2DES, then the voltage difference  $\Delta V$  between the two peaks is related to the spin gap  $\Delta E = g\mu_B B$  between the two spin states. If we ignore the spin-splitting of the QD state for the moment, then  $\Delta V$  is directly proportional to  $\Delta E$ . We will consider the contribution of the spin-splitting in the QD state to  $\Delta V$  later on in this section.

### Discontinuity at $L_2$

Before estimating the  $g$ -factor of the 2DES from the spin-splitting of the two peaks, we take a brief aside to consider the ‘discontinuity’ at  $L_2$  once more. At  $L_2$  ( $\nu = 1.13$ ) the lower voltage (higher energy) peak is abruptly quenched and the higher voltage (lower energy) peak is enhanced. Again, note that this is not an artifact; although  $L_2$  occurs at an abrupt value of  $\nu$ , the discontinuity occurs across a number of successive  $I(V)$  traces. On closer examination of the plot (figure 5.7), however, it can be seen that the lower voltage peak does *not* in fact disappear but instead, *both* peaks shift abruptly to higher voltage *together*. This gives the appearance that the lower voltage peak is enhanced when in fact it has simply been displaced by the shifted higher voltage peak. This implies that there is a change in the energy of the QD state (relative to the Fermi level in the 2DES) at  $L_2$  rather than a change in the density of states of the 2DES itself. Further evidence for this comes from the weaker ‘tail’ in the resonance current that can be seen at higher voltage  $V \sim 215 - 230$  mV at  $B \sim 5$  T. This too appears to suffer an abrupt change at  $L_2$ .

Figure 5.8 shows the same data as figure 5.7 except that the data between  $\nu = 1.13$  and  $\nu = 1$  has been shifted to lower voltage by approximately 5 mV. It can be seen that, when the data is offset in this way, the  $I(V)$  traces at  $\nu < 1.13$  align almost exactly with those at  $\nu > 1.13$ . Therefore, we will assume that the two peaks above  $\nu = 1.13$  have the same origin as those below  $\nu = 1.13$ , i.e., the high and low energy spin states of the  $n = 0$  Landau level.

It is not clear why such a shift in the energy of the QD state might occur so abruptly at the filling factor represented by  $L_2$ . One way this might occur is by a sudden change in the way that the charge is distributed between the 2DES and the emitter contact, or within the 2DES itself. The mechanism which might lead to this abrupt charge redistribution is not understood however. Note that the discontinuity at  $L_1$  is qualitatively different from that observed at  $L_2$ . Whereas a simple voltage offset can explain the change in  $I(V)$  at  $L_2$ , it is not possible to align the features in the  $I(V)$  below  $\nu = 1$  with those above  $\nu = 1$ . The similarity with  $L_2$  arises only because both the changes in the  $I(V)$  occur as a consequence of a sharp change with  $\nu$ .

### 5.5.1 The 2DES $g$ -factor between $\nu = 2$ and $\nu = 1$

Figure 5.9 shows the voltage position of the two peaks corresponding to the spin up and spin down states, the voltage separation between them and the corresponding calculation of the  $g$ -factor. The  $g$ -factor shown in the figure was calculated by assuming that the voltage gap,  $\Delta V$ , between the two peaks is directly proportional to the energy gap between the two spin states (i.e. ignoring the spin-splitting of the QD state),

$$g = \frac{\Delta E}{\mu_B B}, \quad (5.6)$$

where

$$\Delta E = e \frac{\Delta V}{\mathcal{F}}, \quad (5.7)$$

where the leverage factor is taken to be  $\mathcal{F} = 14.4$  (see section 3.7.1). This provides us with a measurement of the  $g$  factor of the electrons in the 2DES. Using this method, we find that  $|g| = 2.1 \pm 0.5$  and is independent of  $B$  within error.

#### Spin splitting of QD state

The result just obtained for the  $g$ -factor in the 2DES does not take into account the spin-splitting in the QD state. When an electron tunnels from the 2DES through the QD state we assume that the electron spin is conserved. Therefore an electron in the spin up (down) state in the 2DES will only tunnel into the spin up (down) state of the QD. Since the degeneracy of the two QD spin states is broken in a magnetic field, then the voltage separation  $\Delta V$  between the two peaks in the  $I(V)$  trace not only represents the energy difference between the two spin states in the 2DES ( $\Delta E_{2DES}$ ) but also the energy difference between the two spin states in the QD ( $\Delta E_{qd}$ ). Depending upon relative signs of the  $g$  factors of the 2DES and the QD, then  $\Delta E = e\Delta V/\mathcal{F}$  is either the sum of  $\Delta E_{2DES}$  and  $\Delta E_{qd}$  or the difference between them,

$$\Delta E = \begin{cases} \Delta E_{2DES} + \Delta E_{qd} & \text{opposite sign} \\ \Delta E_{2DES} - \Delta E_{qd} & \text{same sign} \end{cases}. \quad (5.8)$$

Thornton *et al.* (1998a) have measured the  $g$ -factors of *NU1403* QDs in a similar experiment with  $B \perp z$  ( $\mathbf{B}$  parallel to the growth plane). This is done by measuring the difference in the voltage positions of the onset to tunnelling through each spin state of the QD. For the QD associated with feature  $d$ , they obtain a value of  $|g_{\text{qd}}| = 1.6 \pm 0.1$ . Measurements on other QDs yielded values ranging from  $|g_{\text{qd}}| \approx 0.5$  to  $|g_{\text{qd}}| \approx 1.2$ . From the relative voltage widths of the two resonances (related to the Fermi energy of each spin species in the 2DES) they determined that the  $g$ -factors of the QD and the 2DES have *opposite signs*. Comparable results have been obtained recently by Hapke-Wurst *et al.* (2000, 2002). Simple three-band  $\mathbf{k} \cdot \mathbf{p}$  models for the QD yield *positive* values for the  $g$ -factor of between  $g_{\text{qd}} = +0.12$  and  $+0.34$  (Thornton *et al.* 1998a, Hapke-Wurst *et al.* 2002). Given that these models do not attempt to include effects such as the strain field of the QDs, or the shape and exact composition of the QDs, the model results agree well with the experimental results to the same order of magnitude. The point is that the models suggest that the sign of the QD  $g$ -factor is positive, and therefore that the  $g$ -factor of the 2DES is *negative*.

Since the shape, lattice strain and composition of the QD is not isotropic, the  $g$  factor of the QD in a magnetic field  $B \parallel z$  is likely to be different from that in  $B \perp z$ . Experiments by Meyer *et al.* (2001) on similar samples indicate that the QD  $g$ -factor is *reduced* by about 30% when the magnetic field is rotated from  $B \perp z$  to  $B \parallel z$ . Using their results as a guide gives the  $g$ -factor of our QD in  $B \parallel z$  as  $g_{\text{qd}} \approx +1$ . As a crude estimate therefore, we take the  $g$  factor of the QD in  $B \parallel z$  to be  $g_{\text{qd}} = +1 \pm 1$ .

## Result

Taking into account the spin-splitting of the QD state, we revise our previous estimate of the  $g$  factor of the 2DES from  $|g_{2\text{DES}}| = 2.1 \pm 0.5$  to  $g_{2\text{DES}} = -1 \pm 1$ . A comparable result was obtained by Thornton (1998b), who estimated the value of the 2DES  $g$ -factor in  $B \perp z$ .

This value of  $g$  compares well with that of the one electron  $g$ -factor determined for bulk GaAs,  $g = -0.44$  (Hermann and Weisbuch 1977). However, there are a number of factors to be aware of when making a direct compar-

ison between the  $g$ -factor measured above and the bulk GaAs value. The first is that the electron wave function of the 2DES penetrates a little into the AlAs barrier, where the  $g$ -factor has a value of  $g \sim +2$  (Kosaka *et al.* 2001). This tends to increase the  $g$ -factor in the 2DES, pushing it towards more positive values. However, work by Snelling *et al.* (1991) on electrons in GaAs/(AlGa)As/GaAs quantum wells have shown the effect of barrier penetration on the  $g$ -factor to be very small for well widths of about 5 nm and above. Since the 2DES in our device has a width of  $\sim 10$  nm and is bounded by AlAs only on one side (being formed at a heterojunction), the effect of barrier penetration on the  $g$ -factor is expected to be minimal.

Secondly, the confinement energy of the well raises the energy of the electrons above the bottom of the conduction band, effectively increasing the band-gap and therefore modifying the spin-orbit contribution to the  $g$ -factor (see section 1.6). For a well of width  $\sim 10$  nm, Snelling *et al.* estimate  $g \approx -0.35$ , a change of  $\Delta g \approx 0.1$  from the bulk value; this is a small modification compared to the uncertainty in our measured value, so we would not expect to observe this refinement.

Thirdly, as mentioned in the introduction to the chapter, there is expected to be a contribution to the  $g$ -factor due to the Coulomb repulsion between individual electrons in the 2DES. Nevertheless, from our results, it appears that, between 3 – 5 T (between  $\nu = 2$  and  $\nu = 1$ ) we are unable to detect any appreciable enhancement to the  $g$ -factor within error.

### 5.5.2 The 2DES $g$ -factor at $\nu = 1$

At  $\nu = 1$ , the peak due to the lower voltage (higher energy) spin state disappears whilst the onset to tunnelling through the lower spin state shifts abruptly from 213 mV at  $\nu$  just greater than  $\nu = 1$  to 229 mV just below  $\nu = 1$ . This represents a significant increase in the spin gap at  $\nu = 1$  which we interpret as observation of the exchange enhancement to the spin gap mentioned in the introduction to the chapter.

Since it is common practice in the literature to write the increase in the spin gap in terms of an enhanced  $g$  factor, we use our data to obtain values

of  $g$  for comparison. We find that  $|g_{2DES}|$  increases from  $1 \pm 1.5$  just above  $\nu = 1$  to  $9 \pm 1.5$  just below  $\nu = 1$ . Note that these values include a small correction for the spin-splitting of the QD state, as detailed in section 5.5.1.

This value of  $g$  is comparable with those obtained by Usher *et al.* (1990) who measure  $g = 7.3$  at  $\nu = 1$ , using a technique to measure the thermal activation of the conductivity  $\sigma_{xx}$ , and Dolgoplov *et al.* (1997) who measure  $g \approx 5.2$  at  $\nu = 1$  using a capacitance technique (section 5.1).

### 5.5.3 Discussion of results

Most experiments that investigate the  $g$ -factor in two-dimensional electron systems do so by measuring the spin-gap and cyclotron gap where it crosses the Fermi level, i.e. at integer filling factors. In such experiments it is possible to use a gate electrode to change the electron density and therefore change the filling factor independently of the magnetic field. However, they are restricted to measuring  $g$  at integer filling factors only. On the other hand, our experiment allows us to measure the variation in  $g$  at non-integer values of filling factor. However, although the electron density can be changed by varying the source-drain voltage, when investigating a particular resonance, the source drain voltage does not vary enough to change the filling factor appreciably. In our experiment, therefore, the ratio of  $\nu$  to  $B$  is effectively fixed for a particular resonance.

Ando and Uemura (1974) [see also the review article by Ando *et al.* (1982)] predict that the  $g$ -factor should oscillate with filling factor, with minima at even values of filling factor, and maxima at odd values. The oscillation is expected to arise as a consequence of electron-electron interactions, in particular the Coulomb repulsion between electrons of opposite spins. Ando and Uemura have calculated the  $g$ -factor in the ‘screened’ Hartree-Fock approximation, which attempts to extend the original Hartree-Fock approximation by taking into account the tendency of anti-parallel spins to separate due to the Coulomb repulsion between them; electrons with the same spin are kept apart by the Pauli exclusion principle, so the Coulomb repulsion between parallel spins is of less consequence (Kittel 1987). If there are equal num-

bers of spin up and spin down electrons (i.e. when  $\nu$  is an even integer), each spin species ‘feels’ equal Coulomb repulsion due to the other spin species. However, if there is an excess of one species over the other, the species in the minority experiences proportionally more repulsion than the other species. This opens up the energy gap between the two spin species. When the filling factor is odd, the difference between the number of up spins and the number of down spins goes through a local maximum giving a maximum in the energy separation of the spin levels.

The enhancement to the spin-gap is often described in the literature in terms of an ‘enhanced’  $g$ -factor,  $g^{**}$ :

$$\Delta E_{2DES} = g^{**} \mu_B B = g^* \mu_B B + \epsilon, \quad (5.9)$$

where  $g^*$  is the one-electron (or ‘bare’)  $g$ -factor and  $\epsilon$  is the enhancement to the spin-gap introduced by the correlation between anti-parallel spins. The magnitude of  $\epsilon$  is of the order of the Coulomb energy between the electrons (Usher *et al.* 1990),

$$\epsilon \sim \frac{e^2}{4\pi\epsilon_0\epsilon_r l}, \quad (5.10)$$

where  $l$  is a measure of the average separation of the electrons. Since  $\epsilon$  depends on  $B$  in general, comparisons between values of  $g^{**}$  quoted for particular filling factors should also include the value of  $B$ .<sup>†</sup>

It is not clear why the enhancement that we observe in the  $g$ -factor should occur so abruptly at  $\nu = 1$ , while we do not appear to observe any significant enhancement to the  $g$ -factor between filling factors  $\nu = 2$  and  $\nu = 1$ . It should be noted again that this is the only experiment to the author’s knowledge that has the ability to measure the  $g$ -factor at non-integer values of  $\nu$ , so the results from this experiment are still consistent with previous experiments. Having said this however, a discontinuous jump in the  $g$ -factor is inconsistent with the calculations of Ando and Uemura (1974). Their calculation does indeed predict a maximum at  $\nu = 1$  but rather than a discontinuous change at  $\nu = 1$ , the  $g$ -factor is expected to change smoothly,

---

<sup>†</sup>Having said this, several authors observe that the  $g$ -factor at a particular filling factor is *independent* of magnetic field (Usher *et al.* 1990, Dolgoplov *et al.* 1997, Leadley *et al.* 1998).

following the smooth change in the proportion of spin-up to spin-down electrons with decreasing filling factor. For certain estimates of the Landau level density of states, Ando and Uemura calculate that the  $g$ -factor should go through a sharp, ‘spike-like’ maximum at odd integer filling factor. In particular, at the small odd integer values of  $\nu$ ,  $\nu = 1$  and 3, where the changes in the proportion of spin up to spin down electrons are the most extreme, the  $g$ -factor is predicted to increase rapidly as  $|\nu|$  approaches that filling factor. However, although this might be expected to produce a sharp increase in  $g$  as  $\nu$  decreases towards  $\nu = 1$ , there would also be expected an equally sharp decrease in  $g$  as  $\nu$  falls below  $\nu = 1$ , which is not observed. Experiments by Leadley *et al.* (1998) have demonstrated a *collapse* in the exchange enhancement below a critical value of the magnetic field as a result of the presence of disorder in the 2DES. Comparing their results with a simple model, they find that the collapse occurs where the disorder potential becomes comparable to the exchange energy  $\epsilon$ . In addition, at finite temperature, electrons are excited across the spin gap effectively adding to the disorder potential. This leads them to propose that the critical condition for collapse of the exchange enhancement is given by

$$g^{**}\mu_B B = \hbar/\tau + Mk_B T, \quad (5.11)$$

where  $\tau$  is the scattering rate and  $M$  determines how the effect of thermal excitation of the electrons relates to the effective disorder. From their data, they obtain a value of  $M = 2.1$  which is independent of the sample. Applying this model to our device (using the scattering rate found in the previous chapter), we find that the collapse should occur around  $B = 1 - 2$  T, well below the magnetic field where  $L_1$  occurs.

#### 5.5.4 Conclusion

In conclusion, between  $\nu = 2$  and  $\nu = 1$  we observe a  $g$ -factor for the 2DES that is close to the bulk one-electron  $g$ -factor in GaAs. At  $\nu = 1$  we appear to observe a sharp enhancement of the  $g$ -factor. The magnitude of this enhanced  $g$ -factor compares well with experiments that measure the  $g$ -factor by thermal activation and capacitance techniques. However these

experiments are unable to measure continuously, the change in  $g$  with  $\nu$ . Sharp enhancements of the  $g$ -factor are predicted at integer filling factors but calculations are unable to explain the very rapid, step-like increase in  $g$  that we observe at  $\nu = 1$ . Disorder driven collapse of the exchange enhancement would be expected to occur in our device at a much lower value of  $B$  than the magnetic field position of  $L_1$  and, in any case, would not be expected to produce the step-like change in the  $g$ -factor that we observe.

## 5.6 Multiple peak structure at $\nu = 1, 2, 4$

Accompanying the spin gap enhancement at  $L_1$ , figure 5.7 shows the sudden emergence of a multiple peak structure when the Fermi level enters the lowest spin-polarised Landau level. Four peaks in the  $I(V)$  trace appear simultaneously at  $L_1$ : there are three peaks spaced about 5 mV apart and a fourth peak about 9 mV above the third. Similar structures also appears at  $\nu = 2$  and a complex structure appears in the peak corresponding to  $n = 1$  Landau level at  $\nu = 4$ .

Figure 5.10 shows a number of  $I(V)$  traces obtained from the regions around  $\nu = 2$  and  $\nu = 1$ . The temperature ( $T$ ) dependence of the multiple peak structures is puzzling. Whereas, at most values of  $B$ , the effect of  $T$  is limited to broadening the onset of the resonant current, according to the  $k_B T$  smearing of the density of states at the Fermi level, in this regime all four peaks are strongly affected by  $T$ . This is surprising, since the voltage positions of the peaks indicate that they are due to tunnelling from electron states up to  $100k_B T$  below the Fermi level in the 2DES.

Similar structures can also be observed at low integer filling factors in a number of other devices of *NU1403*, albeit with poorer resolution.

Figures 5.11 and 5.12 show grey scale plots of  $I(V, B)$  for resonant features  $a$  and  $b$ , taken from devices  $a$  and  $b$  respectively (section 3.6). Taking feature  $a$  first, although the Landau quantisation is not as clear as in feature  $d$ , the oscillation in the Fermi energy is still clearly visible, allowing us to identify the magnetic field positions where  $\nu = 2$  and  $\nu = 1$  fall. We estimate that

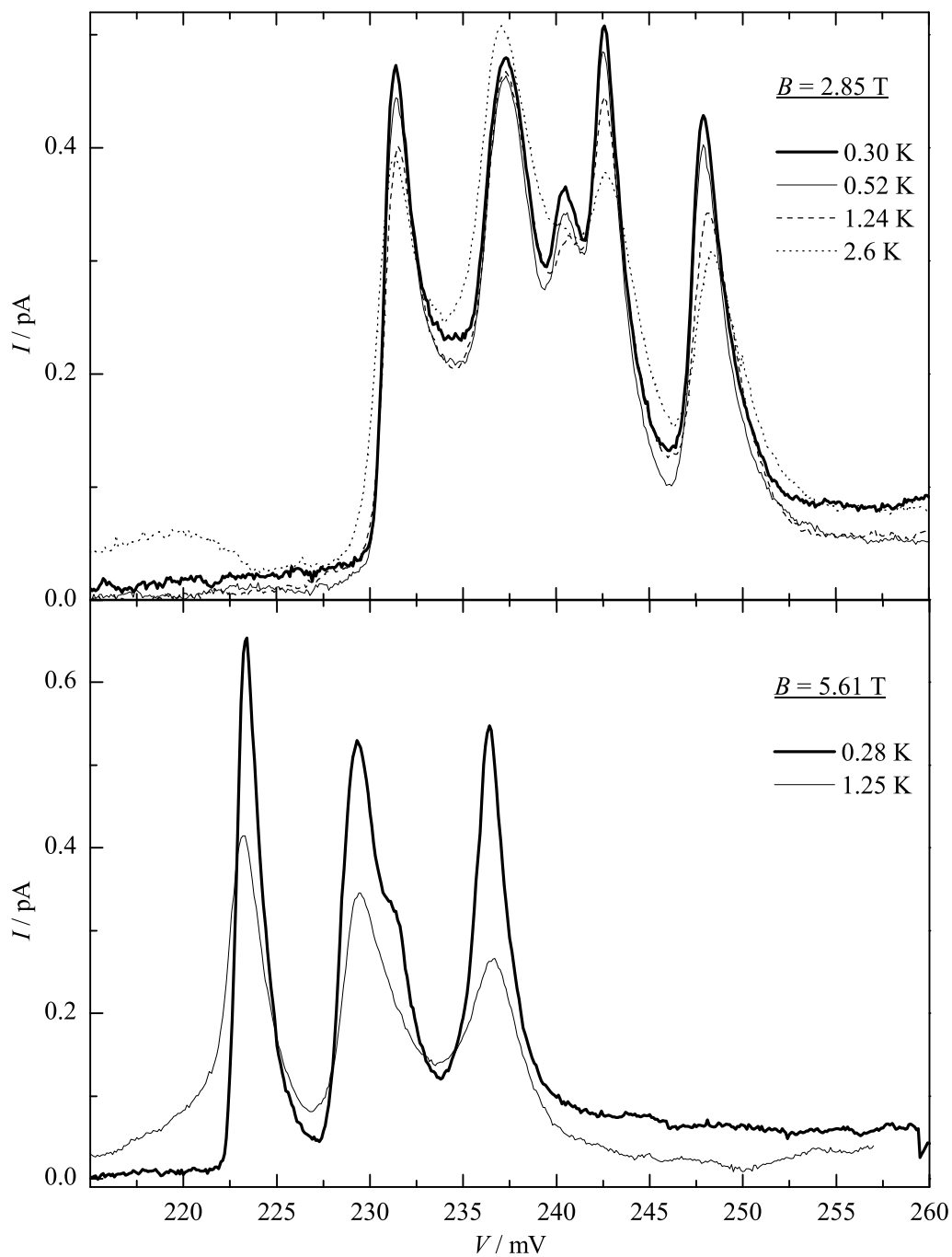


Figure 5.10: Effect of temperature on the  $I(V)$  characteristic of device  $d$  in a magnetic field  $B \parallel z$ . Top)  $I(V)$  traces from the region around  $\nu = 2$ . Bottom)  $I(V)$  traces from the region around  $\nu = 1$ .

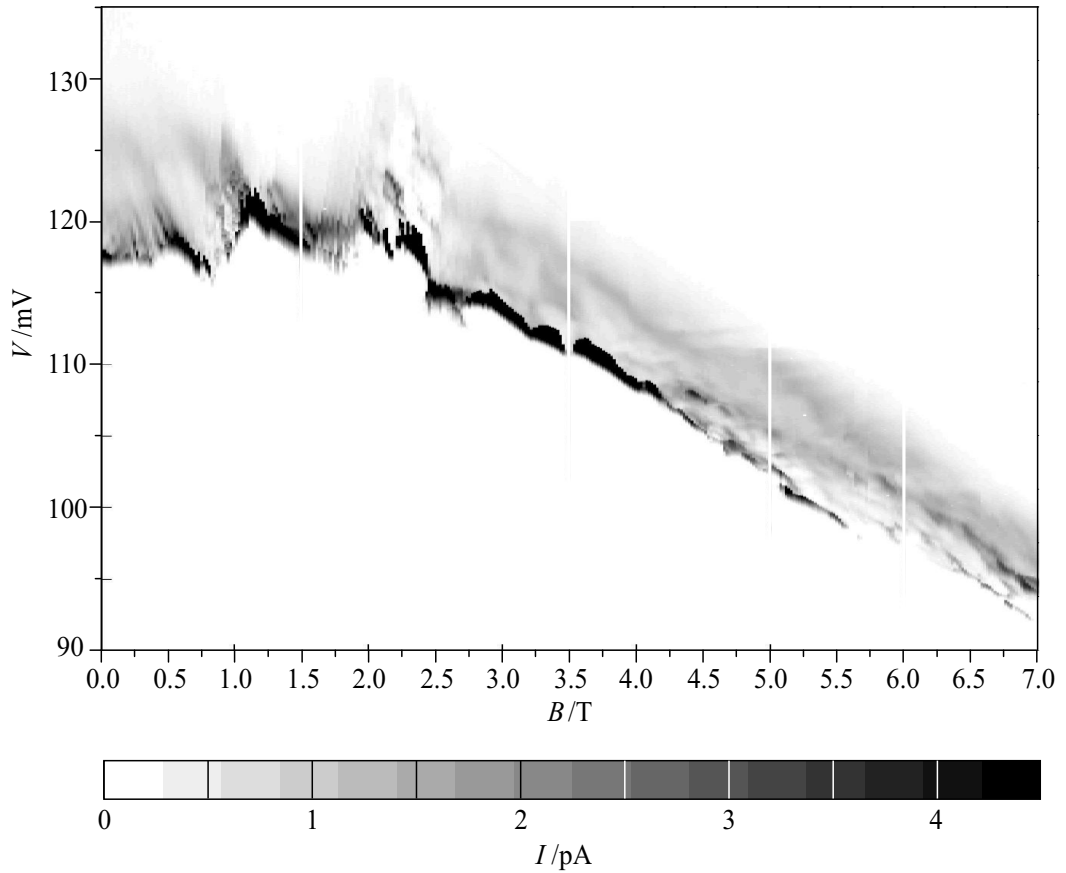


Figure 5.11: Grey-scale plot of the tunnel current  $I$  through device  $a$  versus voltage  $V$  and magnetic field  $B$ . Darker shading indicates larger current values. Plot constructed from data supplied by Dr. A. S. G. Thornton.

$\nu = 2$  falls at  $B \approx 1$  T and  $\nu = 1$  falls at  $B \approx 2$  T for this feature. The differences between the magnetic field positions of  $\nu = 1$  in feature  $d$  and feature  $a$  reflect the difference in the electron density. The QD state which gives rise to feature  $a$  becomes resonant with the 2DES at a lower voltage than in feature  $d$ , so we measure a lower electron concentration. The Fermi edge singularity is clearly visible in this plot as a sharp enhancement in the current at the low-voltage onset of the resonance.

Notwithstanding the poorer resolution with which the LDOS in feature  $a$  can be resolved, a clear step-like increase in the voltage position of the current onset can still be seen at  $\nu = 1$ , similar to that seen in feature  $d$ . This is followed by the sudden onset of a multiple peak structure as in feature  $d$ . As the field is increased further, the voltage position of the

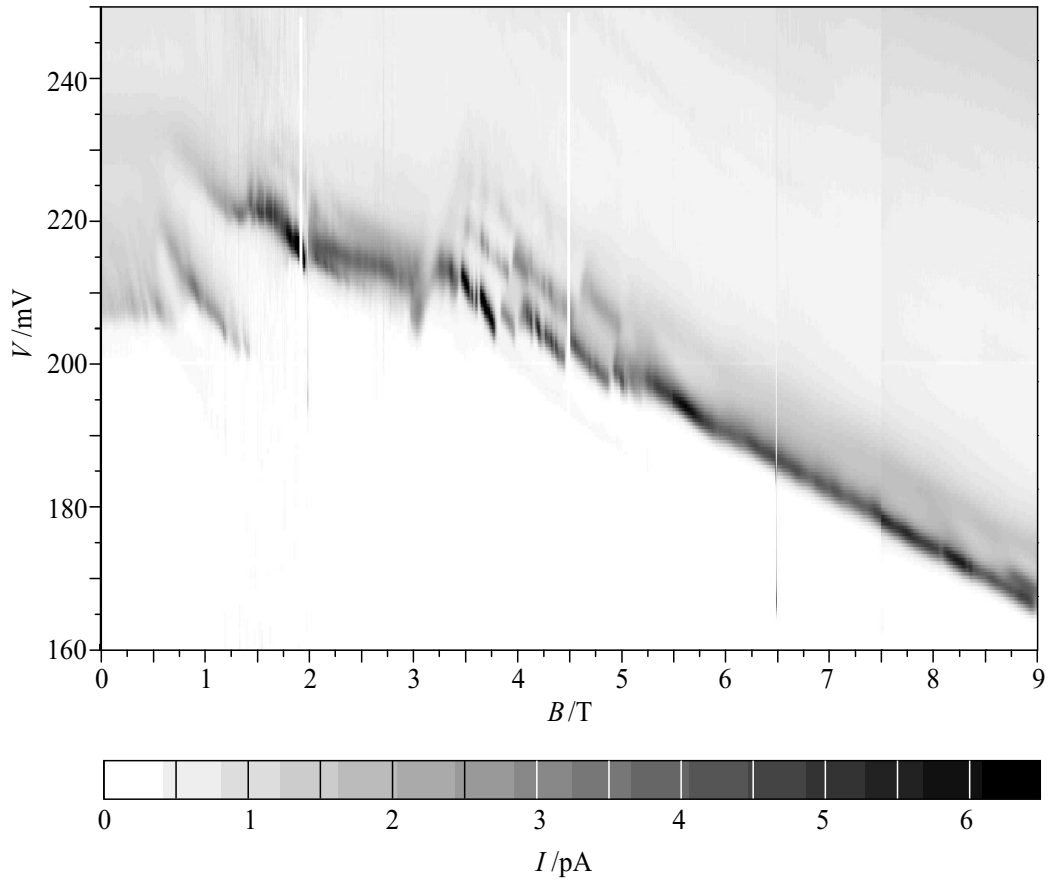


Figure 5.12: Grey-scale plot of the tunnel current  $I$  through device  $b$  versus voltage  $V$  and magnetic field  $B$ . Darker shading indicates larger current values. Plot constructed from data supplied by Dr. A. S. G. Thornton.

feature continues its slide to lower voltage, until the filling factor reaches  $\nu = 0.83$  at  $B \approx 2.4$  T, whereupon there is a sharp shift in  $V_F$  back toward lower voltage, and the multiple peak structure loses coherence. Beyond  $B = 2.5$  T,  $V_F$  continues to track the expected voltage position of the spin split  $n = 0$  Landau level.

The voltage width of the feature at  $\nu < 1$  is puzzling, because it is at least two times larger than the voltage width of the  $n = 0$  Landau level at  $\nu > 2$ . This indicates that the energy width of the  $n = 0$  Landau level is significantly larger at  $\nu < 1$  than it is at  $\nu > 2$ . A similar observation can be made of feature  $d$ . We also note that the voltage width of feature  $a$  remains almost constant with increasing  $B$  between 2.5 T and 7 T. This is also surprising, since the filling factor falls from around  $\nu \approx 0.8$  at  $B = 2.5$  T

( $V_F = 115$  mV) to around  $\nu \approx 0.2$  at  $B = 7$  T ( $V_F = 92$  mV).

Feature *b* shows similar structure to both the *a* and *d* features. We estimate the magnetic field position of  $\nu = 1$  in this feature to be at  $B \approx 3.1$  T. We again see a marked shift of the voltage position of the current onset to higher voltage at  $\nu = 1$ , followed by the sudden appearance of multiple peak structure. However, rather than the peaks losing coherence as in features *a* and *d*, a multiple peak structure persists over a relatively large range of  $B$ . There are sharp changes in the structure at  $B \approx 3.7$  T, 4.5 T and 4.7 T, qualitatively similar to the  $L_2$  discontinuity observed in feature *d*.

The origin of this multiple peak structure in  $I(V)$ , that emerges at  $\nu = 1$  and  $\nu = 2$  (and possibly also  $\nu = 4$  in feature *d*), is not clear. Since all of the peaks are thermally activated, this suggests that each peak corresponds to tunnelling through a *different* QD state. However, this explanation is inconsistent with the fact that the structure only appears around integer filling factors in the 2DES. Therefore, the appearance of such structure in the  $I(V)$  must be associated with a change in the density of states in the 2DES.

The local measurement of the electron density, obtained in section 5.4.1, suggests that tunnelling is occurring from a ‘pool’ of electrons in the 2DES, with higher-than-average electron density. Such a pool might be formed due to the local strain field introduced by the QD. The multiple peak structure, that we observe in the  $I(V)$ , might then be due to the splitting of the Landau level states in this potential. However, this interpretation does not explain why such Landau level splitting should only occur at integer filling factors and does not explain the anomalous temperature dependence.

That the structure only appears in a particular Landau level once the Fermi level has entered it, suggests that scattering events are important. Shahbazyan and Ulloa (1997) have predicted the existence of sub-Landau level structure when electrons are allowed to tunnel between a 2DES and a large number of quasi-bound QD states in resonance with the states in the 2DES. In our case, however, we have only one QD state in resonance with the 2DES during the measurement, so it is not clear whether the results of Shahbazyan and Ulloa are applicable to our experiment.

---

In conclusion, we observe the sudden appearance of a multiple-peak structure in the tunnel current,  $I(V)$ , at filling factor  $\nu = 1$  in two  $100 \mu\text{m}$  diameter mesas (devices  $a$  and  $b$ ) and at filling factors  $\nu = 1, 2$  and  $4$  in a  $5 \mu\text{m}$  diameter mesa (device  $d$ ). The peaks are thermally activated, even though their voltage positions indicate that they correspond to tunnelling from states in the 2DES up to  $100k_{\text{B}}T$  below the Fermi level. We attribute this multiple peak structure to the observation of sub-Landau level structure in the highest occupied Landau level, similar to that predicted by Shahbazyan and Ulloa. However, we have yet no satisfactory explanation for the phenomenon.

# Chapter 6

## Tunnelling through quantum dots in a gated device

### 6.1 Introduction

In a recent experiment by Vdovin *et al.* (2000)\* a magneto-tunnelling technique was used to measure the probability density of stationary electron states in InAs QDs. In their experiment the QDs are embedded within the central potential well of a double barrier resonant tunnelling diode. A magnetic field,  $\mathbf{B}$ , is applied perpendicular to the current direction. This causes the tunnelling electrons to pick up additional momentum in the barrier plane,  $\hbar\mathbf{k} = e\mathbf{B} \times \mathbf{s}$ , according to the Lorentz force, where  $\mathbf{s}$  is parallel to the current direction and represents the tunnelling distance. The tunnel current through a particular QD state is found to be proportional to the probability density of the state in  $k$ -space,  $|\phi(\mathbf{k})|^2$  (Sakai *et al.* 1993, Mori 2000, Patanè *et al.* 2002). In this way, the magneto-tunnelling technique can be regarded as a  $k$ -space analogue of scanning tunnelling microscopy; by changing the magnetic field, the ‘probe’ can be moved around the electron wave function in  $k$ -space.

However, although the tunnel current  $I(V)$  contains information about the probability density of individual QD states, it is not possible from this

---

\*See also Levin *et al.* (2001) and Patanè *et al.* (2002)

data alone to identify which states belong to which QDs.

On the other hand, recent experiments by Austing *et al.* (1999, 1997a) have demonstrated how, by using an array of in-plane gate electrodes, information about the location of QDs buried within the barrier layer can be obtained.

In this chapter, we demonstrate how this gating technique can be combined with the magneto-tunnelling technique to give a powerful method for identifying and measuring the probability density and energy levels of stationary electron states in an individual quantum dot.

## 6.2 Device

The device used in this chapter was fabricated from the material *NU1673* (see section 2.4.3). It was processed into a  $0.7\ \mu\text{m}$  diameter vertical transistor device that incorporates four independent, lateral gates in addition to source and drain contacts.

The details of the device design and the steps involved in its fabrication have been described previously in section 2.4.3. In this section, the operation of the device is explained in more detail.

Figure 6.1 shows a simple schematic diagram of the device, showing the source and drain contacts, and the arrangement of the four gate electrodes around the central  $0.7\ \mu\text{m}$  square section of the mesa. The four ‘arms’ of the mesa, which split the gate metal, and the top contact (drain) pads have been omitted from this diagram for clarity; for a more detailed diagram see figure 2.8. The active area of the mesa is reduced due to the depletion regions around the gates. This reduces the active area to a  $\sim 0.1 - 0.2\ \mu\text{m}$  wide channel within the central square, even when there is no bias applied to the gates (Austing *et al.* 1999). The depletion region is depicted in figure 6.1 as a shaded area; the active area is contained within the circle. Since the density of QDs is  $\sim 1 \times 10^{11}$  per square centimetre, this means that there are fewer than  $\sim 50$  QDs within the active region of the device.

Figure 6.2 shows a stylised diagram of the conduction band of *NU1673*

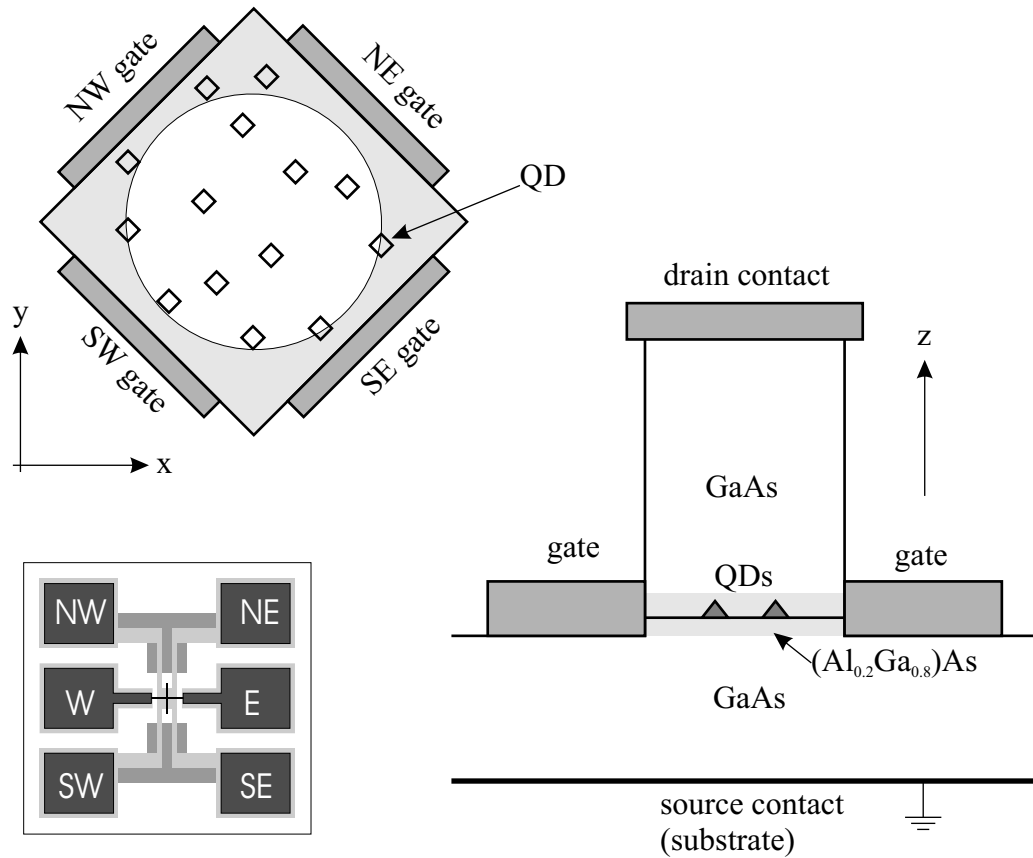


Figure 6.1: Schematic diagram of the central square mesa of the device as viewed from above and from the side. The above view shows a cross section through the  $(\text{AlGa})\text{As}$  layer, showing the arrangement of the four gate electrodes (NE,SE,SW,NW) around the central  $0.7\ \mu\text{m}$  square mesa. The small boxes represent the InAs quantum dots buried within the  $(\text{AlGa})\text{As}$  layer. The shaded area outside the circle represents the Schottky depletion region around the edges of the mesa. The side view shows the vertical positioning of the gate metal relative to the barrier layer. The inset, bottom left, shows the labelling of the gate- and top-contacts.

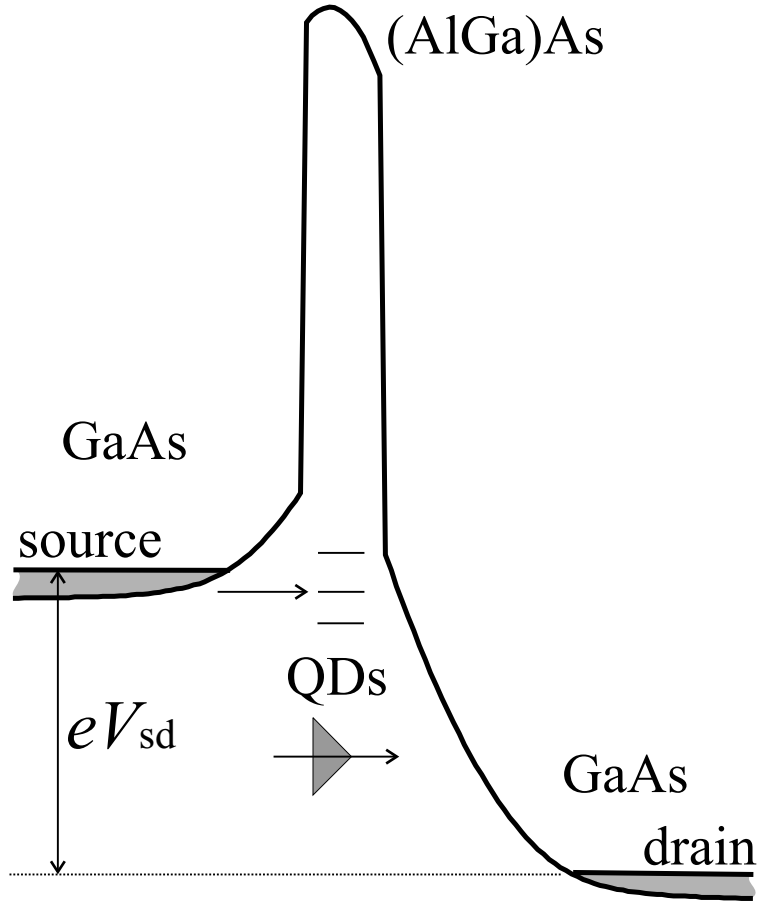


Figure 6.2: Stylised diagram of the  $\Gamma$  conduction band of *NU1673* under applied bias  $V_{sd}$ . A single 0D state of a single QD is identified by a thick horizontal line in the barrier. The triangle shows the geometry of the QD within the (AlGa)As barrier and the arrow shows the direction of electron flow in forward bias.

with a voltage  $V_{sd}$  applied between the source and drain contacts of the device. Recall that the undoped spacer layer either side of the barrier is significantly thinner in *NU1673* than in *NU1403* and there is no 2D electron accumulation layer next to the barrier. In addition a number of the QDs are charged with electrons, even at zero bias (section 2.4.3), producing depletion layers on either side of the (AlGa)As barrier. Based upon the numerical calculation of the conduction band, we estimate the leverage factor for this device—the ratio between the voltage dropped across the device to the voltage dropped between the emitter and the QD layer—to be  $\mathcal{F} \sim 2 - 3$ .

A resonant current flows when an electron state in a QD becomes resonant with an occupied electron state in the emitter layer. As with the devices

studied in the previous chapters, increasing the source-drain bias ( $V_{sd}$ ) causes the QD states to move to *lower* energy with respect to the states in the emitter. Therefore, as  $V_{sd}$  is increased, we expect to see resonant peaks in the tunnel current as the energy of successive QD states pass through the Fermi level in the emitter. The onset of a single current peak marks the voltage  $V_{sd}$  at which the corresponding QD state becomes resonant with the Fermi level.

### 6.2.1 Low temperatures $I(V)$ characteristics

Figure 6.3 shows typical low temperature  $I(V)$  traces obtained from a number of different mesas of between  $1\ \mu\text{m}$  and  $0.7\ \mu\text{m}$  in diameter, plus a trace from a  $75\ \mu\text{m}$  diameter circular mesa for comparison. As in the previous chapters, forward bias is defined as the bias in which the electrons tunnel into the QDs through a thicker potential barrier, and out through a thinner barrier (see section 2.4.3). Forward bias is defined as a positive voltage. The pair of almost identical traces were obtained from the same device; the fainter trace of the two was obtained from the ‘east’ contact, whilst the bolder trace was obtained from the ‘west’ contact. The similarity between these two traces demonstrates that we measure the tunnel current through the central mesa.

The  $I(V_{sd})$  traces from these devices have a number of similarities with the traces obtained from the *NU1403* devices:

i) The devices show very little conduction close to zero source-drain bias but with increasing voltage, the  $I(V_{sd})$  trace shows an exponentially increasing background current.

ii) The magnitude of the background current scales roughly with the size of the mesa: the current through the  $75\ \mu\text{m}$  mesa at  $V_{sd} = 0.3\ \text{V}$  is  $100\ \mu\text{A}$ , while the current at the same voltage in the  $0.7\ \mu\text{m}$  mesa is  $\sim 1 - 10\ \text{nA}$ . Therefore, as in the *NU1403* devices, we attribute the background current to non-resonant tunnelling directly across the (AlGa)As barrier layer. In comparisons between the traces from the small area ( $\sim 1\ \mu\text{m}$ ) mesas there is less correlation between the nominal mesa size and the background current.

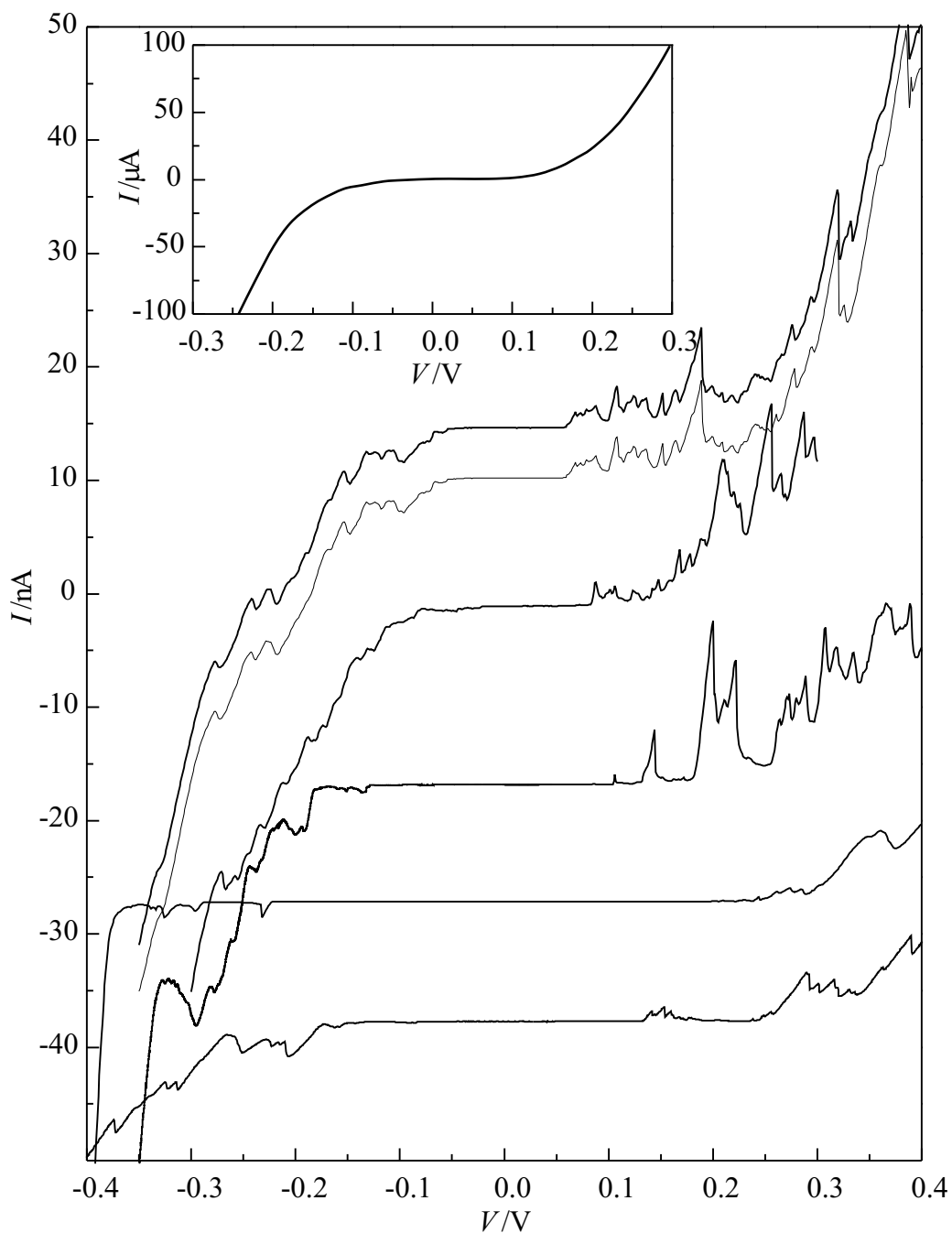


Figure 6.3: Typical low temperature (0.3 K)  $I(V)$  traces obtained from a number of different mesas of *NU1673*, of between  $1\ \mu\text{m}$  and  $0.7\ \mu\text{m}$  diameter. The pair of almost identical traces were obtained from the same device; the fainter trace of the two was obtained from the 'east' contact, whilst the bolder trace was obtained from the 'west' contact. The inset shows a trace from a  $75\ \mu\text{m}$  diameter mesa.

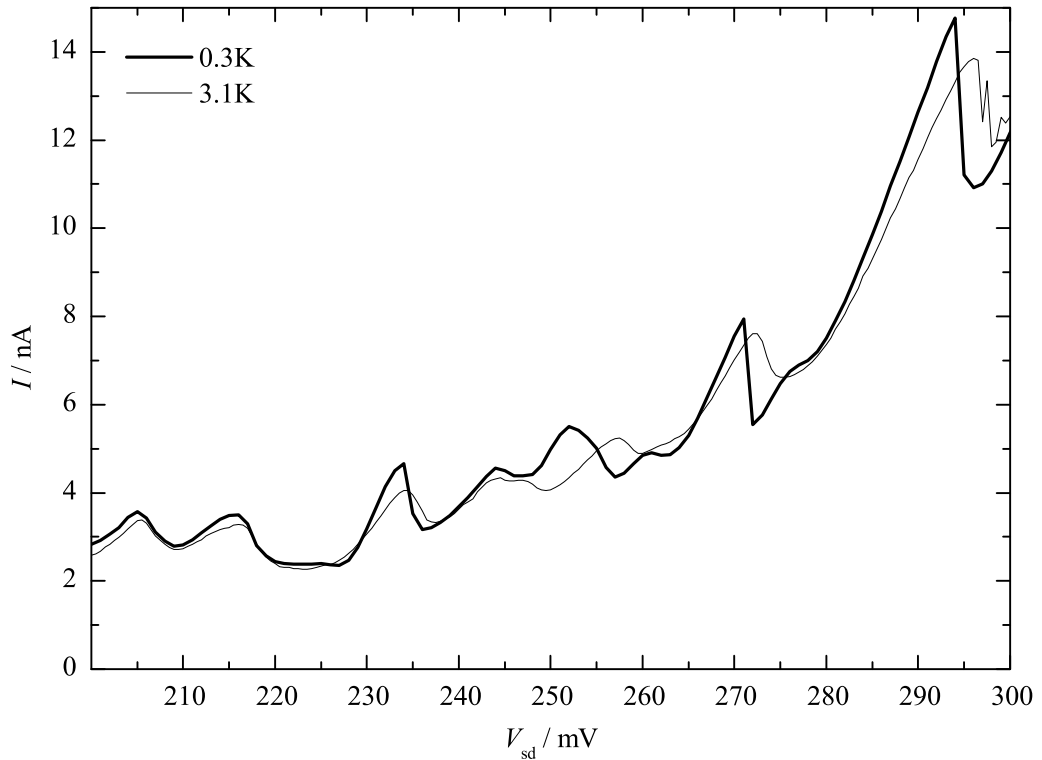


Figure 6.4:  $I(V_{sd})$  traces at 0.3 K and 3.1 K.

However, although the nominal size of the mesa is accurately set by the electron beam lithography step in the fabrication (see section 2.4.3), the variation in the actual size of the mesas can be significant due to the difficulty in controlling the amount of material removed from the circumference of the mesa during the wet etching process.

iii) The current shows additional fluctuations superimposed upon the exponentially increasing background current.

iv) The  $I(V_{sd})$  traces in forward bias are qualitatively different to those taken in reverse bias. In forward bias, the fluctuations are predominantly peak-like oscillations. On the other hand, in reverse bias, the behaviour is more step-like, although it is not as clear as in *NU1403*. As discussed in section 3.4, this points strongly towards resonant tunnelling through the QD states as the origin of the fluctuations in  $I(V)$ .

Unlike in the *NU1403* devices, however, so far we have not been able to

observe any isolated features, that is, a feature in  $I(V_{sd})$  that is isolated from the others by a region of ‘quiet’ current, showing just the background current and no other fluctuations. Therefore, it is difficult to say from the  $I(V_{sd})$  characteristic alone whether a single peak in the  $I(V_{sd})$  is due to tunnelling through a single discrete QD state or is simply the result of random ‘mesoscopic’ fluctuations resulting from tunnelling through a large number of QD states. On raising the temperature to 3.1 K, definite thermal activation can be observed in many of the larger peaks (see figure 6.4) indicating that, at most, they can only be attributed to tunnelling through a small number of QD states: were a particular peak the result of tunnelling through many QD states, we would not expect to see such a marked activation of the current onset. For the smaller fluctuations in  $I(V_{sd})$ , it is not as easy to observe their temperature dependence since they are either swamped by a larger neighbouring peak or they are difficult to resolve from neighbouring small peaks. Therefore, for these smaller fluctuations, temperature dependence alone is not able to distinguish between peaks due to tunnelling through single QD states or peaks due to the sum of the tunnel current through several QDs. One other possibility is that they are due to local density of states fluctuations in the emitter (section 1.4.2). The tunnel current from a disordered 3D emitter through a single QD state will give rise to oscillations in the  $I(V)$  just as for tunnelling from a 2D emitter (chapter 3).

### Adjustment for ‘hidden’ resistance

One last thing to note about the  $I(V_{sd})$  traces is the triangular or ‘sawtooth’ shape of some of the larger peaks. With increasing voltage, the current increases linearly and then at a critical voltage, it collapses sharply back down to its background value. A sawtooth shape is expected if we have a large resistance in series with the device, with a value comparable to, or greater than, the differential resistance of the device; this effect was discussed in section 2.3.1. An estimate of this series resistance can be obtained if we assume that, in the absence of the series resistance, the onset of the peaks should be sharp at low temperature, like the ones observed in *NU1403*. Then the series resistance is simply the minimum positive differential resistance observed in the  $I(V_{sd})$  trace. This resistance is about 1.5 M $\Omega$ . This value is

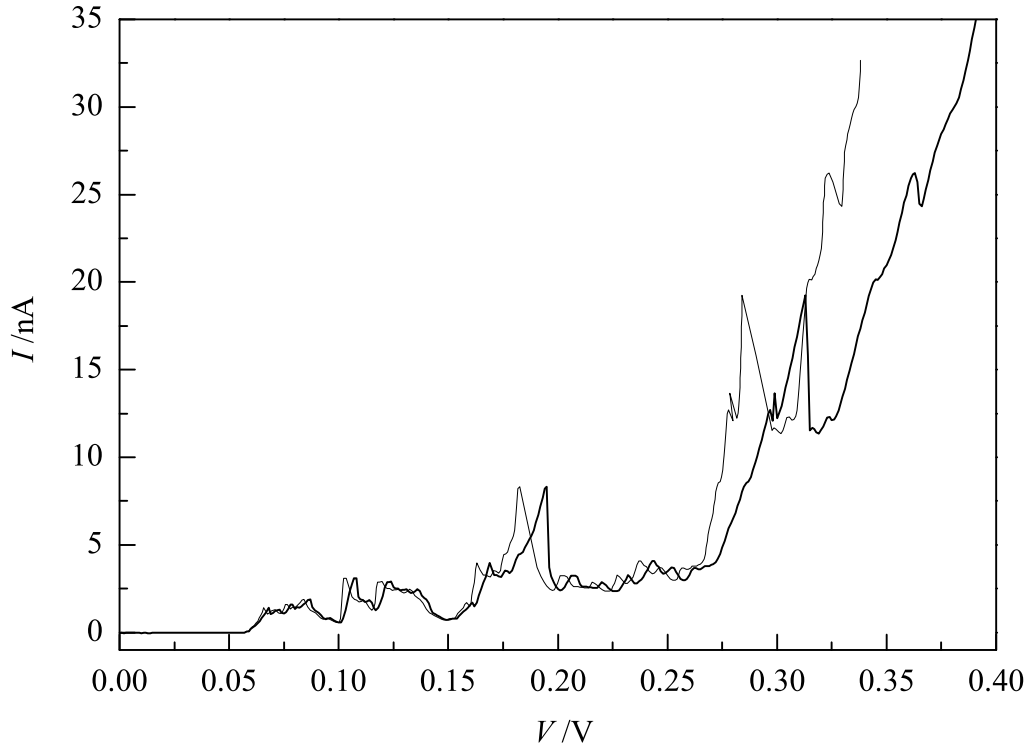


Figure 6.5:  $I(V_{sd})$  trace at 0.3 K. The bold trace shows a plot of  $I$  versus the voltage at the terminals of the voltage source. The fainter trace shows a plot of  $I$  versus the voltage across the device. The difference between the two voltages is due to a series resistance of approximately  $1.5 \text{ M}\Omega$  in the circuit. See main text.

puzzling because the measurement circuit only introduces a series resistance of around  $20 \text{ k}\Omega$  and so cannot account for the series resistance expected from the  $I(V_{sd})$  trace. Consequently, the resistance must be associated with the way in which the sample is mounted on the header or with the sample itself. Sawtooth peaks are observed in a number of samples mounted on different headers, so it is unlikely that the resistance is due to problems with bonding wires to the samples. In addition, the  $I(V_{sd})$  trace changes little when the twin top contact (section 2.4.3) is used instead (see figure 6.3). Therefore, the resistance is not likely to be associated with the top contact metal. One possible cause is the drain contact at the substrate, where the metalised layer can be polished to become quite thin prior to fabrication.

Figure 6.5 shows a ‘corrected’ plot of  $I(V_{sd})$ . In this graph, we attempt to plot the current against the actual voltage applied across the active part

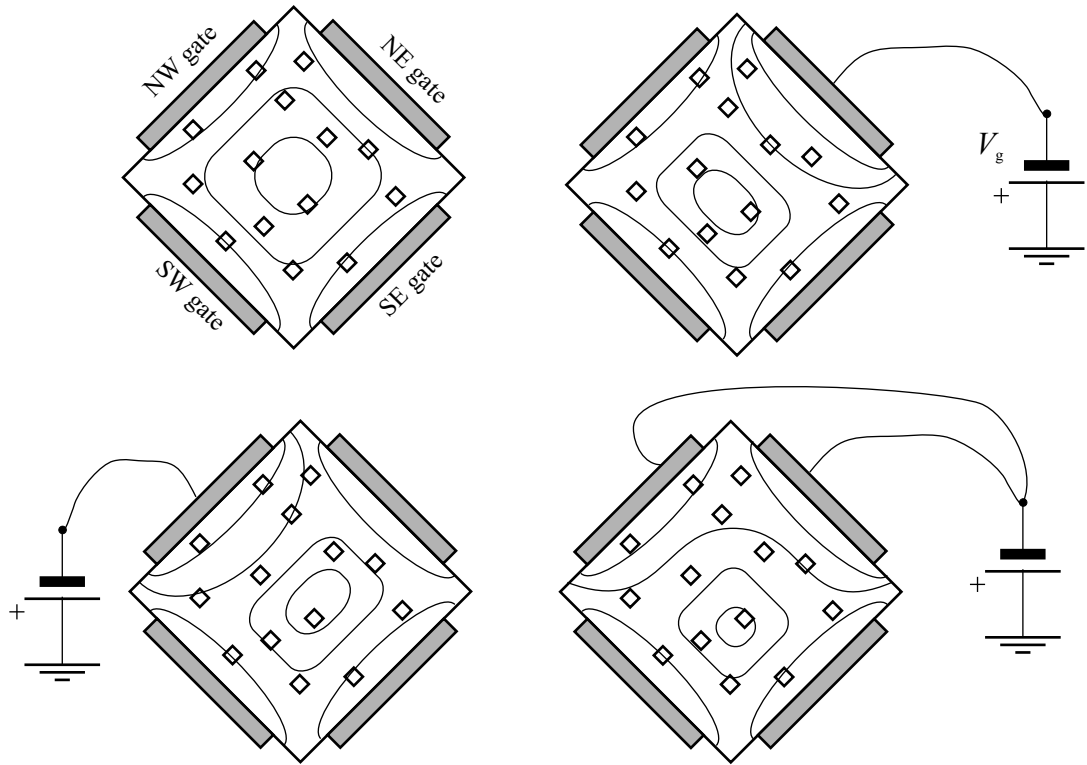


Figure 6.6: Stylised illustration of the equipotentials,  $U(x, y) = -|e|V(x, y)$ , in a cross section through the barrier layer of the device (where the electric field  $\mathbf{E} = -\nabla V$ ). As the voltage on a particular gate is made more negative with respect to the substrate, the equipotentials move toward the centre of the mesa and away from the gate.

of the device. This voltage is determined by subtracting the voltage drop,  $IR$ , across the  $R = 1.5 \text{ M}\Omega$  resistance from the voltage applied between the source and drain terminals of the device (section 2.3.1). This correction will be applied to all the remaining plots in this chapter. Further justification for this correction is obtained when gate voltage is applied in the next section.

### 6.2.2 Applying voltage to the gate electrodes

By applying voltage to the gate electrodes arranged around the central mesa, it is possible to obtain information about the location of the QDs associated with the resonant features in the  $I(V)$ . When a negative voltage is applied to one of the gates, the electric field raises the energy of the conduction band in the region close to the gate. In the  $n$ -doped areas of the device, the electric

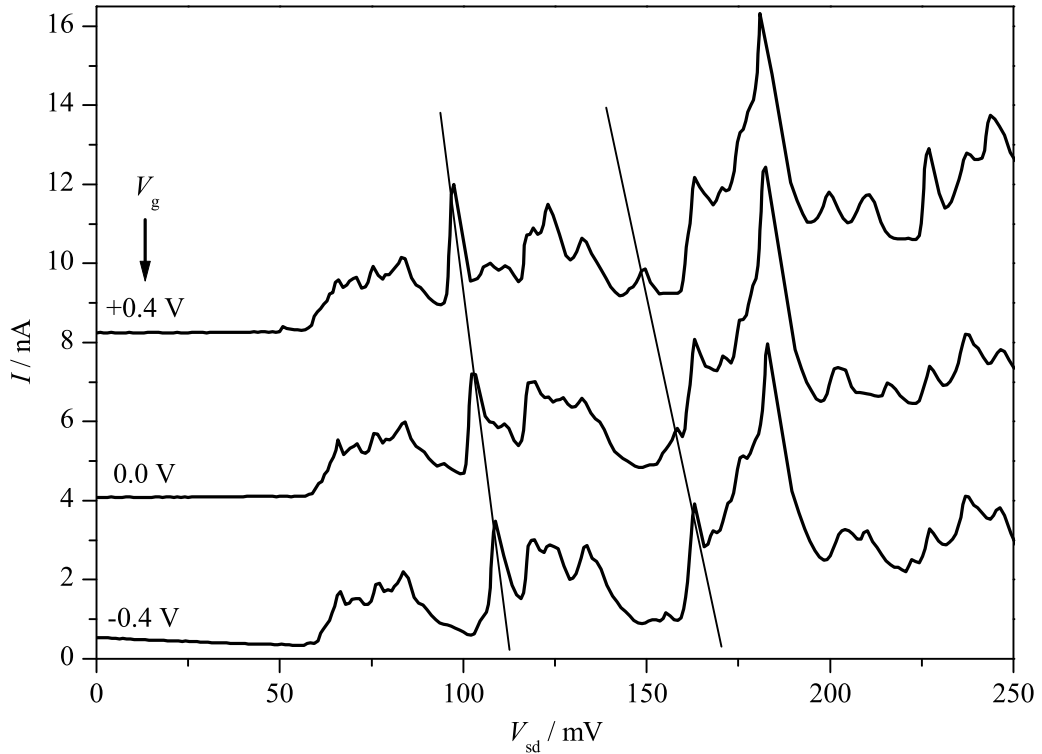


Figure 6.7: Low temperature (0.3 K)  $I(V_{sd})$  characteristic for three gate voltages ( $V_g = 0, \pm 0.4$  V). The gate voltage has been applied to the NE and NW gates. The SE and SW gates are floating. The thin lines identify two resonances whose onset positions in  $V_{sd}$  move at different rates with gate voltage  $V_g$ . The traces have been offset for clarity.

field is screened by the electrons. However, in the undoped barrier layer, the electric field penetrates further into the core of the mesa. Crucially, the effect upon a particular QD is to raise its electrostatic potential energy, relative to the emitter states, by an amount *dependent on its proximity to the gate*.

Therefore, if, for example, a particular QD state is resonant with the emitter Fermi level at a bias  $V_{sd}(1)$ , then when the gate voltage is made more negative, a larger bias  $V_{sd}(2) > V_{sd}(1)$  is required to re-establish the resonance. In other words, every feature in the  $I(V_{sd})$  trace that is associated with a particular QD will move to higher  $V_{sd}$  as the gate voltage is made more negative. The rate at which these features move,  $dV_{sd}/dV_g$ , depends on how close the QD is to the gate. Figure 6.7 shows  $I(V_{sd})$  traces at 0.3 K for three different gate voltages applied to two out of the four gate electrodes, NE

and NW (see figure 6.1).  $V_{sd}$  and  $V_g$  are measured relative to the contact at the substrate (source electrode) (section 2.4.3). Some of the features in the traces, such as the one around 0.1 V can clearly be seen to move with gate voltage. Other features, for example the feature at 0.2 V, appear to be insensitive to the two gates, implying they are due to tunnelling through QDs which are far away from the two active gates.

The effects of gate voltage on the source-drain voltage positions of the resonant features can be seen more clearly by plotting the forward bias data as a grey-scale plot of differential conductance,  $G = dI/dV_{sd}$ , versus gate voltage,  $V_g$ , and source drain voltage,  $V_{sd}$ . Plotting the conductance, rather than the current, suppresses the contribution of the slowly increasing background current from the plot, enhancing the visibility of the more rapidly varying resonant features. Also, importantly, the peaks in differential conductance highlight the positions of the *onsets* of the resonance peaks in  $I(V_{sd})$ . This allows us to determine more clearly the gate voltage dependence of the resonances. Figure 6.8 shows such a grey-scale plot, obtained at  $T = 0.3$  K. *Lighter* shading indicates more positive values of  $G$ . Again, the gate voltage was applied to the NE and the NW gates, with the SE and SW gates not connected. The most prominent features on the plot have been numbered to aid identification.

The onset positions of the resonances in forward bias show up as bright lines on the grey scale plot. It is immediately obvious that the resonances show a wide variety of sensitivity to gate voltage, reflecting the variation in the location of the QDs relative to the gates. For example, we attribute resonances whose voltage position,  $V_{sd}$ , is more sensitive to  $V_g$ , such as the ones labelled 12, 13, 16 and 35, to resonant tunnelling through QDs that are closer to the active NE and NW gates. Other resonances, for example 8, 10, 1 and 2, vary more slowly with  $V_g$  and so we attribute these resonances to QDs that lie further away from the active gates. Some resonances, for example 7,3 and 17, appear to show no dependence on gate voltage, so we attribute these features to tunnelling through QDs that are far from the active gates.

Notice that some of the more prominent resonance features, such as 3

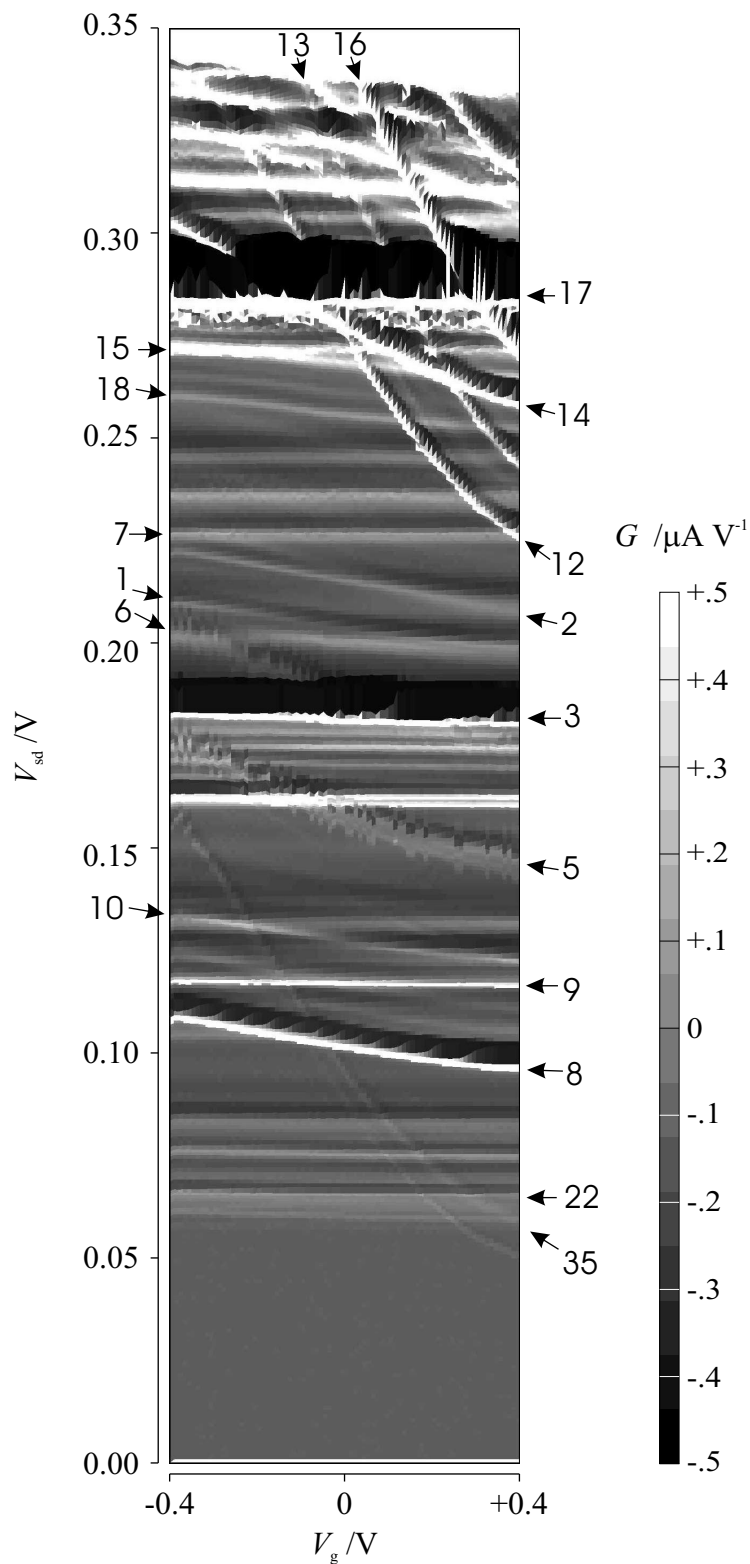


Figure 6.8: Plot of differential conductance of the device  $G = dI/dV_{sd}$  versus gate voltage  $V_g$  and source drain voltage  $V_{sd}$  in forward bias. The gate voltage has been applied to the NE and the NW gates. The SE and SW gate contacts have been left floating. Lighter shading indicates more positive values of  $G$ . The temperature is 0.3 K.

and 17 are accompanied by a ‘shadow’ region of  $V_{sd}$  on the high  $V_{sd}$  side of the resonance. Within these shadow areas, all but the largest of resonance features are strongly suppressed. These areas indicate ranges of  $V_{sd}$  where there is instability in the measurement circuit and a corresponding loss of information (see section 2.3.1).

When the NE gate is disconnected, some resonances, for example 14 and 18, now become insensitive to gate voltage as shown in figure 6.9. From this we infer that the QDs associated with these resonances must lie significantly closer to the NE gate than to the NW gate. Notice from figure 6.9 that resonances 12 and 16, which show strong dependence on  $V_g$  when both the NE and NW gates are connected, appear to be missing from the grey scale plot when the NE gate is disconnected. This is not unexpected since, if we assume that resonances 12 and 16 are *not* sensitive to the NW gate, then once the NE gate is disconnected, resonance 12 would be expected to be entirely obscured by resonance 17 and resonance 16 is expected to lie beyond  $V_{sd} = 0.35$  V, off the limits of the plot.

Equally, when the NW gate is disconnected, a different set of resonances now become insensitive to gate voltage, for example resonances 8, 10, 1, 2 and 13. Therefore, we infer that the QDs associated with these resonances must lie closer to the NW gate than the NE gate.

Interestingly, it can also be seen that resonance 35 is almost equally sensitive to both the NE *and* the NW gate, indicating that this resonance is due to a QD sited roughly equidistantly from both the NE and NW gate.

Finally, the  $V_{sd}$  position of resonance 5 seems to oscillate between two positions about 1 – 2 mV apart as the gate voltage is swept. The cause of this noise is not certain but the bistable nature of the noise is reminiscent of random ‘telegraph noise’ (Kelly 1995). This suggests that single electron charging in an impurity state (or QD) in close proximity to the QD associated with resonance 5 (Kelly 1995) may be responsible. Similar bistability can also be seen occasionally in resonance 12. This effect provides some additional clues to the origin of the features in the  $G(V_{sd})$  traces. In particular, a weaker feature, labelled 6, displays exactly the same behaviour as resonance 5, and also displays exactly the same sensitivity to gate voltage. This

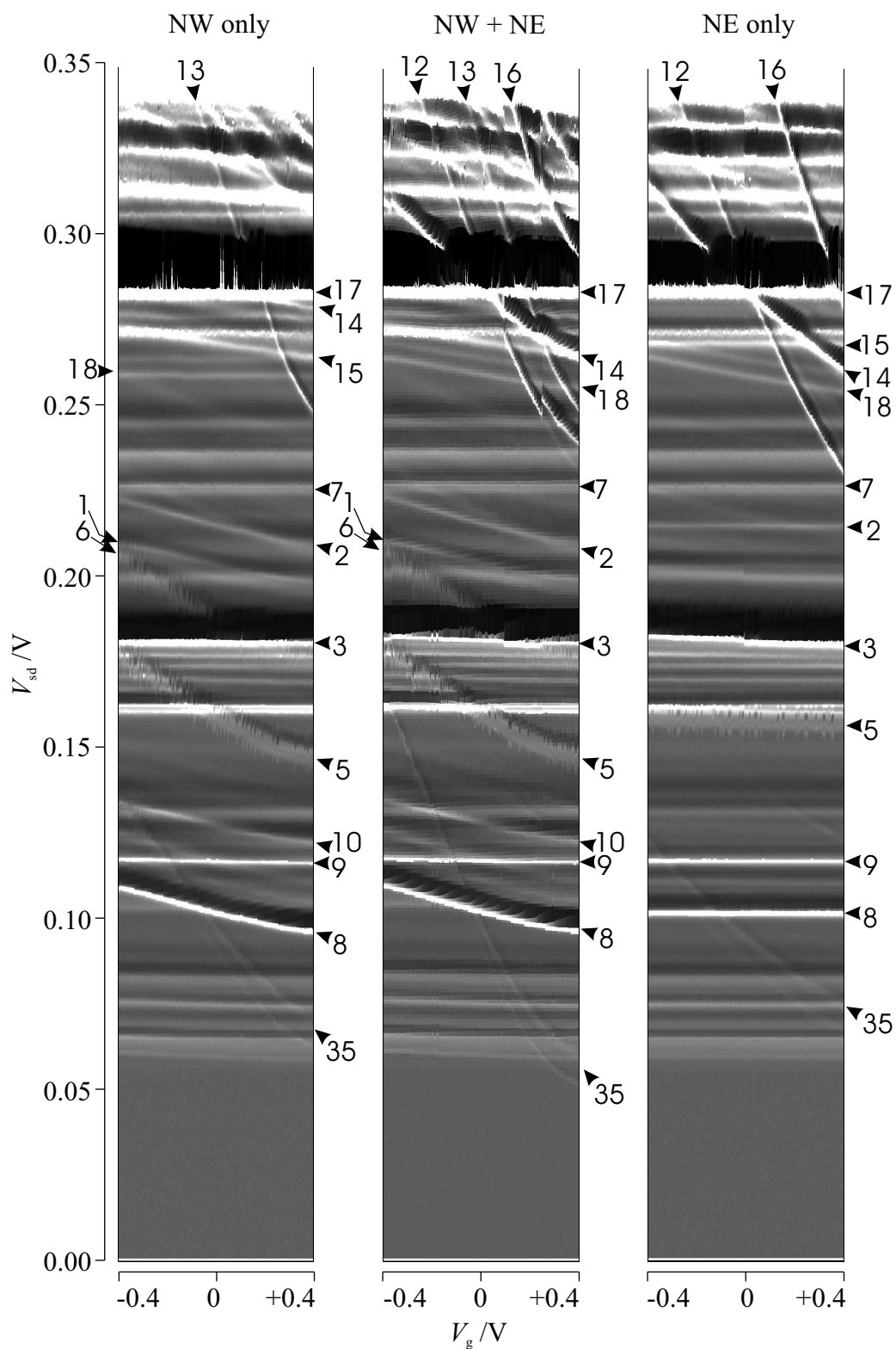


Figure 6.9: Plot of differential conductance of the device  $G = dI/dV_{sd}$  versus gate voltage  $V_g$  and source drain voltage  $V_{sd}$ . In the left-hand plot, gate voltage  $V_g$  is applied to the NW gate only. In the right-hand plot  $V_g$  is applied to the NE gate only. In the centre plot,  $V_g$  is applied to both the NE and NW gates. The SE and SW gate contacts have been left floating. Lighter shading indicates more positive values of  $G$ . The temperature is 0.3 K. The numbers refer to labels used in the text.

strongly suggests that both features 5 and 6 are due to tunnelling through the same QD. Dividing their separation in  $V_{\text{sd}}$ —about 30 mV—by the estimated leverage factor for this device— $\mathcal{F} \sim 3$ —gives a separation in energy of about 10 meV. This energy separation is comparable to the Fermi energy in the emitter so it is possible that the feature marked 5 is due to tunnelling through a QD state from states at the Fermi level in the emitter, whilst 6 is due to tunnelling through the same QD state, from states below the Fermi level in the emitter. This suggests that other features might have similar relationships, for example the stronger feature 8 and the weaker feature 10 are also separated by  $\Delta V_{\text{sd}} \approx 30$  mV and show similar sensitivity to gate voltage.

Sadly, in this particular device, the SE and SW gates are inoperative and so we cannot test the sensitivity of the resonances to these gates. If the device is examined under an optical microscope, the cause of the problem with the SE and SW gates becomes obvious. The surface metal connecting the bonding pads to these gates has pulled away from the silicon oxide insulation lying underneath, during the lift-off step in fabrication (see section 2.4.3). This is a common problem with these devices, although approximately 20 – 30% of devices come through fabrication with a full set of working gates. The complication is that only a very small fraction of devices have fully working top (drain) contacts, so the likelihood of finding a device with no defects at all is small. Nevertheless, such devices have been tested previously [see Austing *et al.* (1999)] but unfortunately they did not survive another cooling in the cryostat for this experiment.

Figure 6.10 again shows a grey scale plot of  $G = dI/dV_{\text{sd}}$  versus gate voltage  $V_{\text{g}}$  and source drain voltage  $V_{\text{sd}}$  in forward bias. The data shown in this plot is the same as that shown in figure 6.8, except that no correction has been made to the source-drain voltage  $V_{\text{sd}}$  in order to correct for the 1.5 M $\Omega$  series resistance (section 6.2.1). Without this correction, it can be seen that the  $V_{\text{sd}}$  positions of the resonances do not vary smoothly with  $V_{\text{g}}$ . This is because the voltage across the device does not vary linearly with the output of the voltage source,  $V_{\circ}$ . Instead, some fraction of  $V_{\circ}$  is dropped across the series resistance in the circuit, where the fraction depends upon the tunnel current.

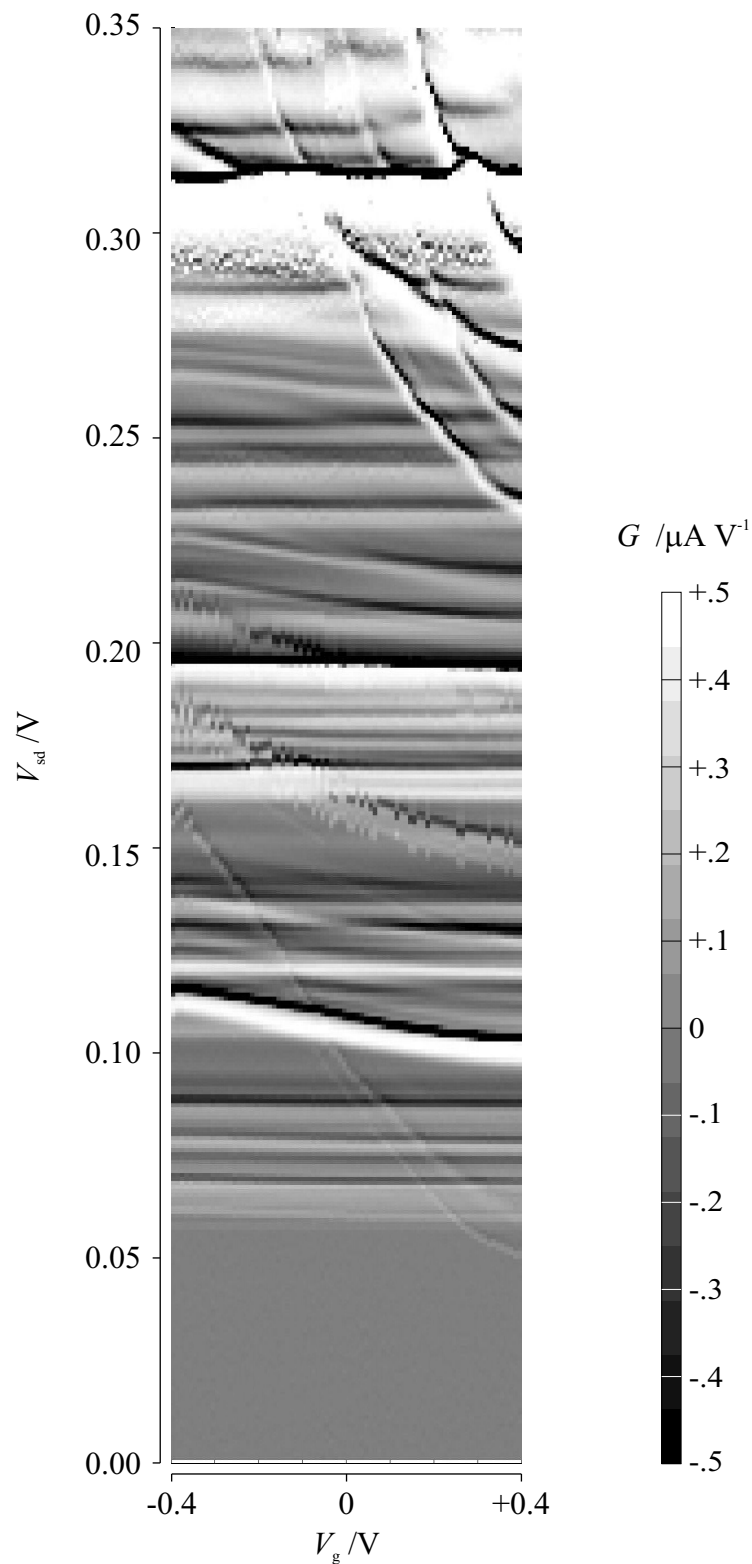


Figure 6.10: Plot of differential conductance of the device  $G = dI/dV_{sd}$  versus gate voltage  $V_g$  and source drain voltage  $V_{sd}$  in forward bias. The gate voltage has been applied to the NE and the NW gates. The SE and SW gate contacts have been left floating. Lighter shading indicates more positive values of  $G$ . The temperature is 0.3 K. In this plot, no correction has been made to the source-drain voltage,  $V_{sd}$ .

In conclusion, this section has demonstrated how the gate electrodes can be used to obtain information about the spatial location of the QDs in the  $xy$  plane.

### 6.3 Magneto-tunnelling spectroscopy

We can obtain additional information about the resonances by using the magneto-tunnelling spectroscopy (MTS) technique. This technique has been used by Sakai *et al.* (1993) to measure the electron wave function of a localised impurity state in a quantum well, and by Vdovin *et al.* (2000) [see also Patanè *et al.* (2002)] to measure the electron wave functions of an InAs quantum dot.

The MTS technique involves applying a magnetic field,  $\mathbf{B} = (B_x, B_y, 0)$  in the plane of the barrier layer of the tunnelling device. An electron tunnelling from the emitter to a QD therefore acquires an additional in-plane ( $xy$ ) momentum due to the action of the Lorentz force.

The grey-scale plots shown in figure 6.11 demonstrate the effect of changing the magnitude of the magnetic field on the amplitude of the resonance features. The direction of the magnetic field has been fixed along a direction  $y$  aligned with the  $[\bar{2}33]$  crystal axis as shown in figure 6.12. There is some experimental uncertainty in the alignment of about  $\pm 10^\circ$ . The plots show clearly that the amplitude of the resonances depend on  $B$ . In most cases, the resonances decay with magnetic field, for example, resonances, 8, 9, 3, 17. There are, however, a number of resonant features that *increase* in amplitude with  $B$ , for example, resonances 2, 7 and 15.

In addition, the voltage position of the resonances  $V_{sd}$  shows a small dependence on  $B$ . This is due to diamagnetic shift of the energies of the bound states of the QDs.

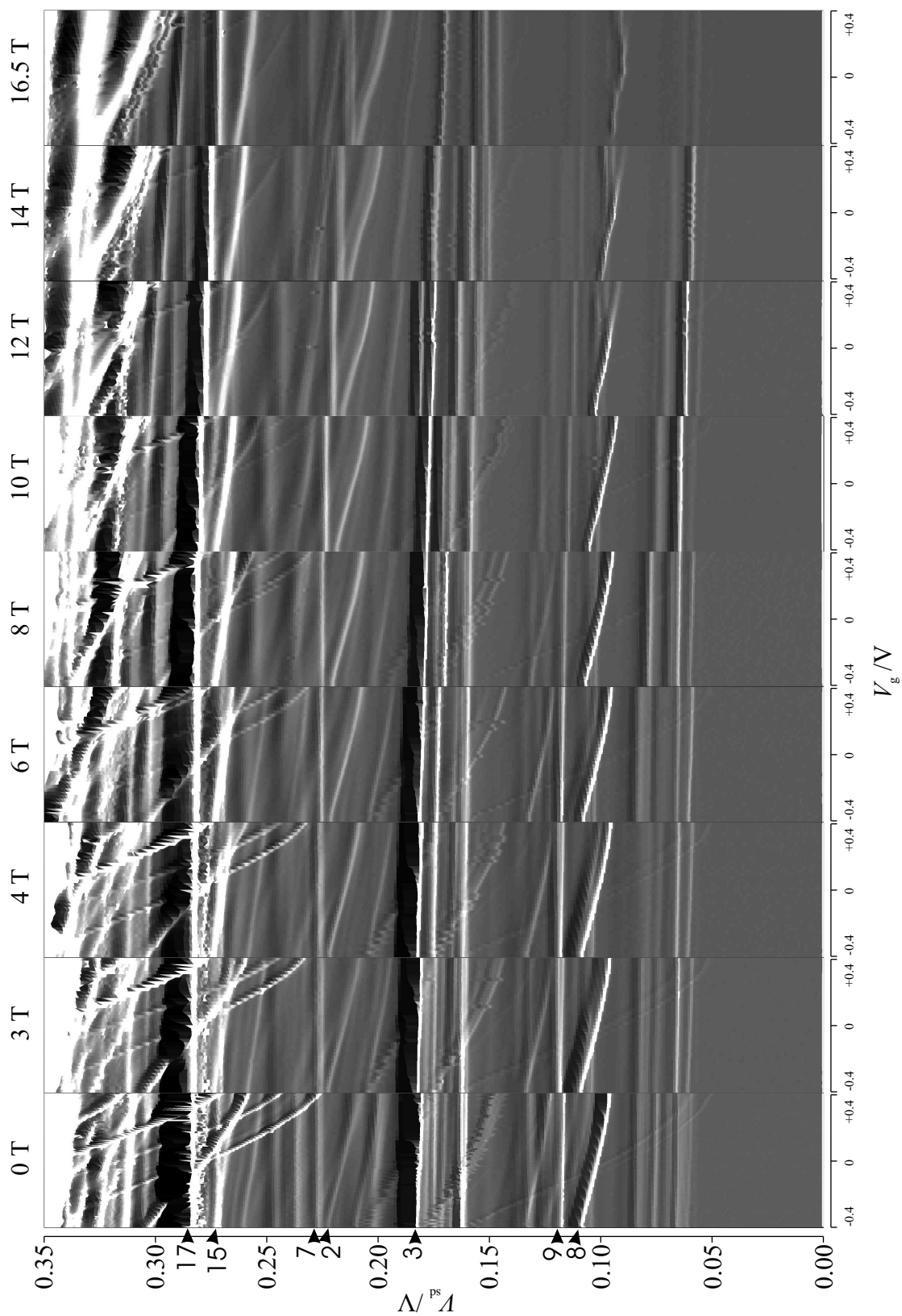


Figure 6.11: Effect of magnetic field  $B \parallel y$  on resonances at  $T = 0.3$  K. The gate voltage has been applied to the NE and NW gates in this case.

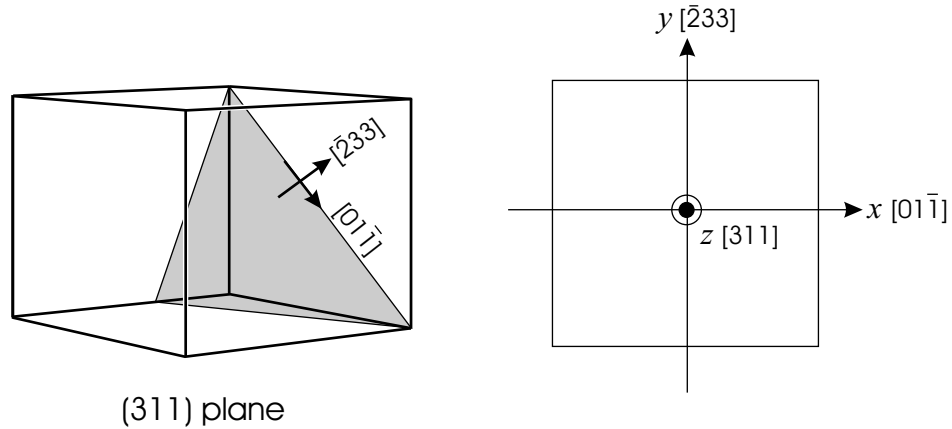


Figure 6.12: Left) (311) crystal plane. Right) The  $x$  and  $y$  axes denote the main crystallographic axes,  $[01\bar{1}]$  and  $[\bar{2}33]$ , in the (311) plane.

### 6.3.1 A model for the resonant tunnel current

The effect of  $B$  on the magnitude of the resonant current can be understood in terms of the transfer Hamiltonian approximation discussed in section 1.7.1. As before, the system is divided into three sub-systems: an emitter (e), collector (c) and well (w) formed by the quantum dot.

#### Emitter states

In chapter 3 the resonant tunnel current was modelled with the assumption that the emitter potential contained some weak random fluctuations due to disorder. To simplify the model for the tunnel current in this case, however (with  $B \perp z$ ), we assume that the potential is translationally invariant in the  $xy$  plane. Then, the emitter states, in the presence of a magnetic field, are described by the Hamiltonian

$$\hat{\mathcal{H}}_e = \frac{1}{2m^*}(\hat{\mathbf{p}} - q\mathbf{A})^2 + U_e(z), \quad (6.1)$$

where  $q = -|e|$ . In magneto-tunnelling spectroscopy, the magnetic field is applied in a direction parallel to the  $xy$  plane. For the purposes of this calculation, we apply the magnetic field along the  $x$  axis. In the experiment, the direction of the magnetic field will be rotated within the  $xy$  plane, but there is no loss of generality in choosing the  $x$  axis for the calculation. For

$\mathbf{B} = (B, 0, 0)$ , we choose the Landau gauge for the vector potential:  $\mathbf{A} = (0, -Bz, 0)$  (the other possible choice,  $\mathbf{A} = (0, 0, By)$ , is *not* chosen for the reason given in section 1.7.1). In this gauge, the Hamiltonian for the emitter becomes

$$\hat{\mathcal{H}}_e = \frac{1}{2m^*} [\hat{p}_x^2 + (\hat{p}_y + qBz)^2 + \hat{p}_z^2] + U_e(z) \quad (6.2)$$

$$= \frac{1}{2m^*} [\hat{\mathbf{p}}^2 + 2\hat{p}_y qBz + (qBz)^2] + U_e(z). \quad (6.3)$$

Since the momentum operators  $\hat{p}_x$  and  $\hat{p}_y$  commute with the Hamiltonian, the eigenstates of  $\hat{\mathcal{H}}_e$  can be written in the form (Mori 2000)

$$\psi_e(x, y, z) = e^{ik_x x} e^{ik_y y} \chi_e(z). \quad (6.4)$$

Substituting equation 6.4 into equation 6.3 gives the following eigenequation for  $\chi_e$ ,

$$\left( \frac{-\hbar^2}{2m^*} \frac{d^2}{dz^2} + U_e(z) + \frac{1}{2} m \omega_c^2 [z - z_o(k_y)]^2 \right) \chi_e(z) = \epsilon \chi_e(z). \quad (6.5)$$

If we assume that, within the emitter,  $U_e$  varies slowly compared to the magnetic potential, then the solutions are of the form

$$\chi_n \sim H_n \left( \frac{z - z_o}{l_B} \right) \exp \left[ -(z - z_o)^2 / 2l_B^2 \right], \quad (6.6)$$

where  $H_n(\dots)$  is the Hermite polynomial function. The important point is not the exact form of the wave function, but that the wave functions are centred on  $z_o$ , which, crucially, depends upon the  $y$  component of the wave vector,

$$z_o(k_y) = l_B^2 k_y. \quad (6.7)$$

### Quantum dot states

In order to obtain analytic expressions for the tunnel current, it is convenient to write the electron wave functions as a product of  $xy$  and  $z$  components, as was done for the emitter states above. Following the procedure given in section 1.7.2, we approximate the confinement potential of the QD by

$U(x, y, z) = U_{xy}(x, y) + U_z(z)$  and write the QD wave function in the form  $\psi_{\text{qd}}(x, y, z) = \phi_{\text{qd}}(x, y)\chi_{\text{qd}}(z)$ . In the presence of a magnetic field  $\mathbf{B} = (B, 0, 0)$  the Hamiltonian is then [taking  $\mathbf{A} = (0, -Bz, 0)$ ]

$$\hat{\mathcal{H}}_{\text{qd}} = \frac{1}{2m^*} (\hat{\mathbf{p}} - q\mathbf{A})^2 + U_{xy}(x, y) + U_z(z). \quad (6.8)$$

It is difficult to obtain solutions to this Hamiltonian, so we find an approximate solution using the variational method. We choose the variational wave function (Mori 2000, Patanè *et al.* 2002)

$$\psi_{\text{qd}}(x, y, z) = e^{iKy} \phi_{\text{qd}}^\circ(x, y) \chi_{\text{qd}}^\circ(z), \quad (6.9)$$

where  $K$  is the variational parameter and  $\phi_{\text{qd}}^\circ(x, y)\chi_{\text{qd}}^\circ(z)$  is the solution to the Hamiltonian at  $B = 0$ . In choosing this form for the wave function, we are expecting that the magnetic field will have little effect on the probability density of the QD state. This is a good approximation providing that the confinement length of the QD in the  $z$  direction is significantly smaller than the magnetic length; i.e., the height  $H$  of the QD ( $H \approx 3 - 5$  nm) should be small compared to  $2l_B$  where  $l_B$  is the magnetic length. The maximum magnetic field used in this experiment is 16.5 T. This corresponds to a magnetic length  $l_B(16.5 \text{ T}) = 6.3$  nm.

Calculating the expectation value of the energy  $\langle E \rangle$  gives

$$\begin{aligned} \langle E \rangle &= \langle \psi_{\text{qd}} | H | \psi_{\text{qd}} \rangle \\ &= \epsilon_\circ + \frac{1}{2} m^* \omega_c^2 \left[ \left( \frac{\hbar K}{m\omega_c} - z_{\text{qd}} \right)^2 + \langle \Delta z_{\text{qd}}^2 \rangle \right] \\ &\quad + \langle \phi_{\text{qd}}^\circ | \hat{p}_y | \phi_{\text{qd}}^\circ \rangle \omega_c \left( \frac{\hbar K}{m\omega_c} - z_{\text{qd}} \right), \end{aligned} \quad (6.10)$$

where  $\epsilon_\circ$  is the energy of the state at  $B = 0$ ,

$$z_{\text{qd}} = \langle z \rangle = \langle \chi_{\text{qd}}^\circ | z | \chi_{\text{qd}}^\circ \rangle, \quad (6.11)$$

$$\Delta z_{\text{qd}} = z - z_{\text{qd}}, \quad (6.12)$$

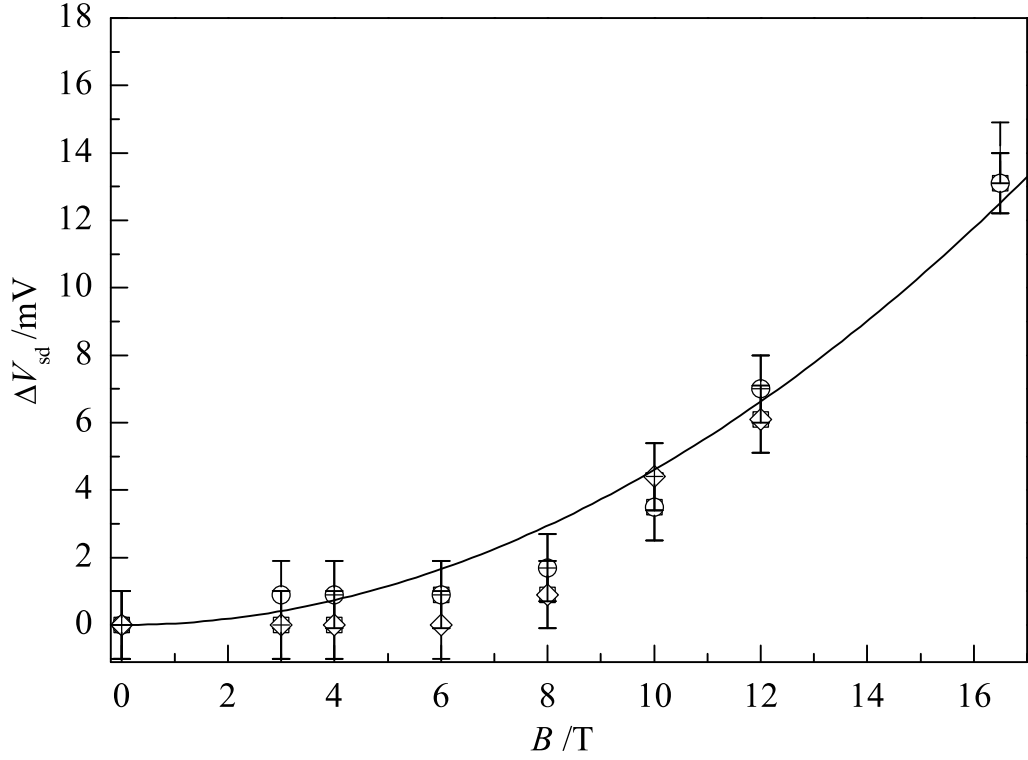


Figure 6.13: Change in the voltage positions  $V_{sd}$  of four of the clearest resonances with magnetic field  $B$ . The continuous line is a guide to the eye.

and

$$\langle \Delta z_{qd}^2 \rangle = \langle \chi_{qd}^{\circ} | \Delta z_{qd}^2 | \chi_{qd}^{\circ} \rangle. \quad (6.13)$$

Minimising  $\langle E \rangle$  with respect to  $K$  gives  $K = z_{qd}/l_B^2$  so that (Mori 2000)

$$\psi_{qd}(x, y, z) = \exp\left(i \frac{z_{qd}}{l_B^2} y\right) \phi_{qd}^{\circ}(x, y) \chi_{qd}^{\circ}(z), \quad (6.14)$$

and

$$\langle E \rangle = \epsilon_{\circ} + \frac{1}{2} m \omega_c^2 \langle \Delta z_{qd}^2 \rangle, \quad (6.15)$$

where  $\epsilon_{\circ}$  is the energy of the QD state at  $B = 0$ . The last term represents a diamagnetic shift in the energy of the state in a magnetic field. The important point is that the magnetic field introduces the phase factor  $\exp(iz_{qd}l_B^{-2}y)$  into the wave function.

We can obtain a rough estimate of the height of the QD from the diamag-

netic shift of the resonances. Figure 6.13 shows a plot of the change in the voltage position of four of the clearest resonances with magnetic field. If we use an effective mass of  $m^* \approx 0.06m_e$  (section 1.5.1) and a leverage factor of  $\mathcal{F} = 2.5 \pm 0.5$ , we obtain a measure of the spatial extent of the wave function in the  $z$  direction,  $2\sqrt{\langle \Delta z_{\text{qd}}^2 \rangle} = (7 \pm 3)$  nm. The estimate is quite rough, due to the uncertainties in the leverage factor and the effective mass. Nonetheless, the estimate is reasonably consistent with the expected height of the QDs,  $\sim 5$  nm (see section 2.4.3).

### Current flow between emitter and a single QD state

It was found in chapter 3 (section 3.5) that, in forward bias, in order to calculate the resonant current through a QD state we need only calculate the current flow between the QD state and the emitter in order to determine the equilibrium resonant current, (equation 3.4)

$$I = e [\rho_e(E_{\text{qd}}) - \rho_{\text{qd}}] \sum_j \frac{2\pi}{\hbar} |\mathcal{V}|^2 \delta(\epsilon_j - E_{\text{qd}}), \quad (6.16)$$

where  $\epsilon_j$  and  $E_{\text{qd}}$  are the energies of the  $j$ th emitter state and the QD state respectively,  $\rho_e(E_{\text{qd}})$  is the occupancy of the emitter states with energy  $\epsilon = E_{\text{qd}}$  and  $\rho_{\text{qd}}$  is the occupancy of the QD state.  $\mathcal{V}_j$  is the transfer matrix element for tunnelling between state  $|j\rangle$  in the emitter and the QD state (section 1.7.1). The sum is over all states in the emitter. In this chapter, in order to simplify the model, we assume the temperature  $T = 0$  K, so that

$$\rho_e(\epsilon) \approx \begin{cases} 0 & \epsilon > E_{\text{F}} \\ 1 & \epsilon < E_{\text{F}}. \end{cases} \quad (6.17)$$

Since we have used wave functions that are separable into  $xy$  and  $z$  components, the transfer matrix element  $\mathcal{V}$  can be written as (section 1.7.2)

$$\mathcal{V} = \frac{-\hbar^2}{2m^*} \times \mathcal{M} \times \mathcal{T}, \quad (6.18)$$

where

$$\mathcal{M} = \int_{xy} \phi_e^*(x, y) \phi_{\text{qd}}(x, y) dx dy, \quad (6.19)$$

and

$$\mathcal{T} = \left[ \chi_e^*(z) \frac{\partial}{\partial z} \chi_{\text{qd}}(z) - \chi_{\text{qd}}(z) \frac{\partial}{\partial z} \chi_e^*(z) \right]_{z_1 < z < z_2}. \quad (6.20)$$

The derivatives within the square brackets are evaluated at any value of  $z$  within the barrier region common to the emitter and QD sub-systems.

Using the wave functions given in equation 6.4 and equation 6.14, the integral  $\mathcal{M}$  becomes

$$\mathcal{M} = \int_{xy} \phi_{\text{qd}}^\circ(x, y) \exp\left(iz_{\text{qd}}y/l_B^2\right) e^{-ik_x x} e^{-ik_y y} dx dy. \quad (6.21)$$

This expression takes the form of a Fourier integral so we may write it as

$$\mathcal{M} = \sqrt{2\pi} \times \tilde{\phi}_{\text{qd}}^\circ\left(k_x, k_y - z_{\text{qd}}/l_B^2\right), \quad (6.22)$$

where  $\tilde{\phi}_{\text{qd}}^\circ(k_x, k_y)$  is the Fourier transform of  $\phi_{\text{qd}}^\circ(x, y)$ . The factor of  $\sqrt{2\pi}$  preserves the normalisation. Substituting equation 6.22 into equation 6.18, the resonant current can be written as

$$I \propto \rho_e(E_{\text{qd}}) \sum_{k_x, k_y, n} \left| \tilde{\phi}_{\text{qd}}^\circ\left(k_x, k_y - z_{\text{qd}}/l_B^2\right) \right|^2 |\mathcal{T}_n|^2 \delta(\epsilon_{k_x, k_y, n} - E_{\text{qd}}), \quad (6.23)$$

where  $\epsilon_{k_x, k_y, n}$  is the energy of the state  $\psi_e = \exp(ik_x x) \exp(ik_y y) \chi_n(z)$  in the emitter. The subscript  $n$  has been added to  $\mathcal{T}$  as a reminder that  $\mathcal{T}$  depends upon  $\chi_n$ .

We now identify the closest point of approach of the emitter electrons to the barrier and label this point  $z = z_e$ . Electron states with wave vectors  $k_y \gg z_e/l_B^2$  are empty since they are confined by the magnetic potential to a region within the depletion layer. Equally, electron states with wave vectors  $k_y \ll z_e/l_B^2$  are confined by the magnetic potential to a region deep within the emitter, far away from the  $z = z_e$  point. Such states have a low probability to tunnel into the QD, since the tunnelling distance is large and the tunnelling probability decreases exponentially with the tunnel distance. Therefore, we expect electron states with values of  $k_y$  close to  $z_e/l_B^2$  to dominate the tunnel

current. With this in mind, equation 6.23 can then be approximated as

$$I \sim \rho_e(E_{\text{qd}}) \sum_{k_x, k_y, n} \left| \tilde{\phi}_{\text{qd}}^\circ(k_x, s/l_B^2) \right|^2 |\mathcal{T}_n|^2 \delta(\epsilon_{k_x, k_y, n} - E_{\text{qd}}), \quad (6.24)$$

where  $s$  is the tunnelling distance  $s = z_{\text{qd}} - z_e$ .

Following section 3.5.3 we now assume that the range of  $k_x$  representing *occupied* states in the emitter is small compared to the extent of the QD wave function in  $k$ -space, such that the value of  $\tilde{\phi}_{\text{qd}}^\circ$  can be taken as approximately constant over this relatively small range of  $k_x$ ,

$$\tilde{\phi}_{\text{qd}}^\circ(k_x, s/l_B^2) \approx \tilde{\phi}_{\text{qd}}^\circ(0, s/l_B^2). \quad (6.25)$$

Then  $\tilde{\phi}_{\text{qd}}^\circ$  can be pulled outside the sum-over-states to give

$$I \sim \left| \tilde{\phi}_{\text{qd}}^\circ(0, -eB\hbar^{-1}s) \right|^2 \times \rho_e(E_{\text{qd}}) \sum_{k_x, k_y, n} |\mathcal{T}_n|^2 \delta(\epsilon_{k_x, k_y, n} - E_{\text{qd}}). \quad (6.26)$$

Consequently, the resonant tunnelling current through a QD state is expected to be proportional to the probability density of the QD electron state *in  $k$ -space*.

Unfortunately, justifying the assumption in equation 6.25 is difficult, primarily because there is some uncertainty in the energy of the conduction band close to the (AlGa)As layer (this will be explained in section 6.4). Instead, the assumption has to be justified a posteriori; for now we simply assume it to be true and will return to question it after discussing the results.

With the magnetic field oriented along the  $x$ -direction, as in the equations above, the tunnel current in equation 6.26 reflects the  $k$ -space probability density along the  $(-k_y)$  axis. However, since there is nothing special about the  $x$ -axis—there is nothing to distinguish it from any other direction within the  $xy$  plane—equation 6.26 can be generalised for any direction of  $\mathbf{B} = (B_x, B_y, 0)$ ,

$$I \propto \left| \tilde{\phi}_{\text{qd}}^\circ(k_x, k_y) \right|^2, \quad (6.27)$$

where

$$\begin{aligned} k_x &= +eB_y\hbar^{-1}s \\ k_y &= -eB_x\hbar^{-1}s, \end{aligned} \quad (6.28)$$

or equivalently,

$$\mathbf{k} = \frac{e}{\hbar}s \mathbf{B} \times \hat{\mathbf{z}}, \quad (6.29)$$

where  $\hat{\mathbf{z}}$  is the unit vector in the  $z$  direction.

The bottom diagram of figure 6.14 shows this idea schematically. The top diagram shows the semi-classical view of tunnelling in a magnetic field  $B \perp z$ . The trajectory of the electron is curved by the Lorentz force, so that the electron gains momentum  $\mathbf{p} = es\mathbf{B} \times \hat{\mathbf{z}}$  (i.e. parallel to the  $xy$  plane) as it travels the distance  $s$  between the emitter and the QD.

In this way, by plotting the tunnel current against the direction and magnitude of magnetic field, a map of  $|\tilde{\phi}_{\text{qd}}^{\circ}(k_x, k_y)|^2$  can be obtained.

### Dependence of $\mathcal{T}$ on $B$

One final point to note before returning to the results is that, in order to use magneto-tunnelling spectroscopy to measure probability density, it is necessary for the transmission coefficient  $|\mathcal{T}|^2$  in equation 6.24 to be independent of  $B$ . According to equation 6.5 however, the magnetic field effectively causes an increase in the height of the tunnelling barrier. This reduces the penetration of the tail of the emitter wave function into the barrier according to equation 6.5. Therefore, there is expected to be a corresponding reduction in the transmission coefficient and thus a reduction in the resonant current. If the change in  $\mathcal{T}$  with  $B$  is large, it will mask the dependence of the tunnel current on probability density. At 16.5 T, the maximum magnetic field used, an electron tunnelling from the edge of the emitter (at  $z_e$ ) experiences an additional magnetic potential of  $U_{\text{mag}} = \frac{1}{2}(e^2B^2/m^*)(z - z_e)^2 \approx 3(z - z_e)^2$  meV, where  $z$  is measured in nm. At  $z - z_e \approx 10$  nm, approximately the tunnelling distance between the emitter layer and the QD layer, the value of the magnetic potential is approximately 30 meV; between the emitter and QD, the

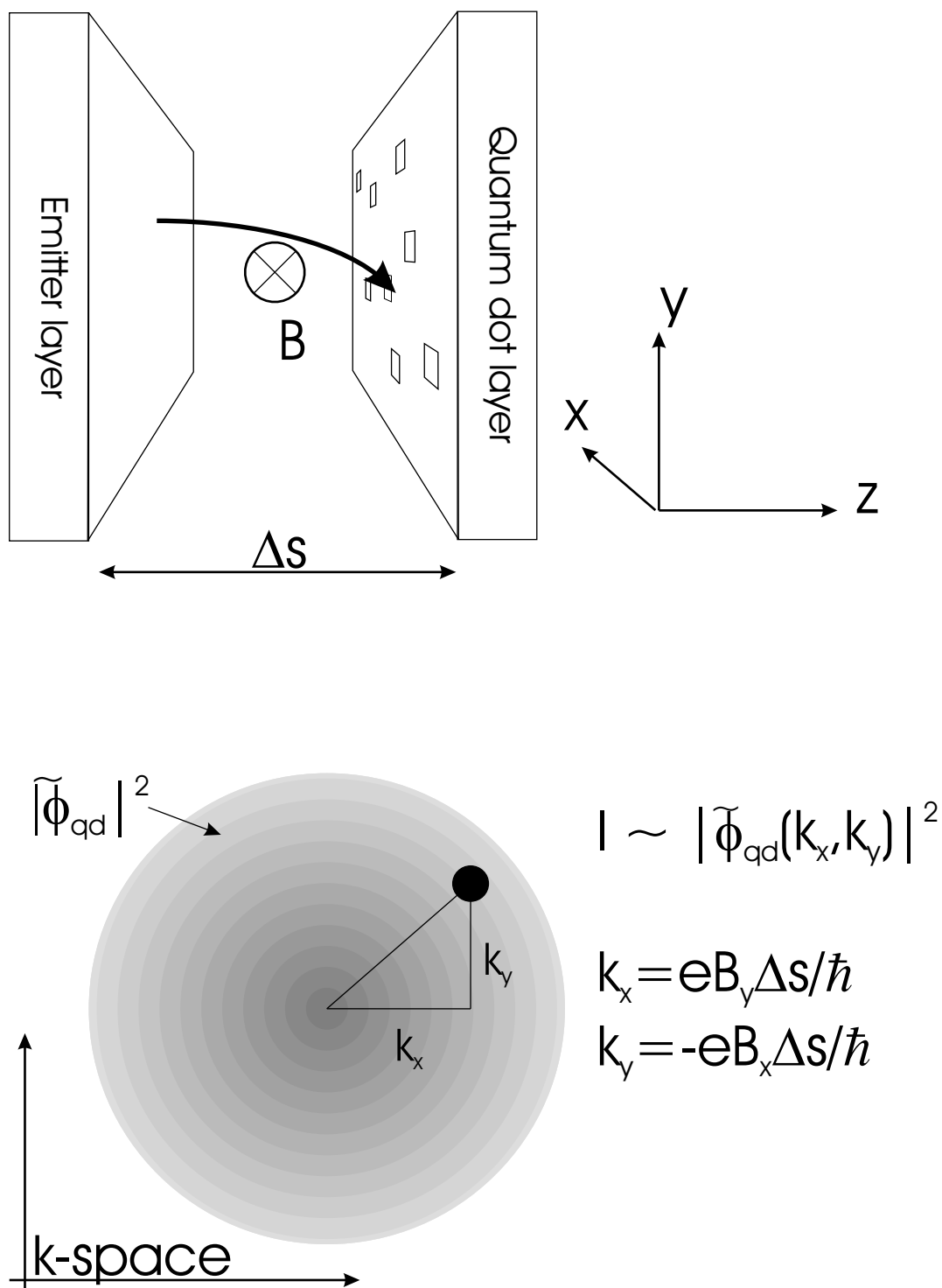


Figure 6.14: Top) Semi-classical view of tunnelling in a magnetic field: The electron trajectory is curved by the Lorentz force so that the electron gains momentum parallel to the  $xy$  plane. Bottom) The resonant current through a particular quantum dot state is proportional to the probability density of the state in  $k$ -space at a point  $(k_x, k_y)$  determined by the magnetic field  $\mathbf{B} = (B_x, B_y, 0)$ .

electron experiences a considerably smaller magnetic potential. This compares to the potential barrier height of approximately 160 meV presented by the (AlGa)As layer, so the magnetic potential adds relatively little to the barrier height. From a recent estimate of the transmission coefficient based on the WKB approximation (Patanè *et al.* 2002),  $|\mathcal{T}|^2$  is expected to decrease smoothly with increasing  $B$ . At 8 T, the value of  $|\mathcal{T}|^2$  is expected to have fallen to  $95 \pm 5\%$  of its value at  $B = 0$ ; at  $B = 16.5$  T, this fraction is  $70 \pm 5\%$ . This effect could be corrected for, but the reduction in  $|\mathcal{T}|^2$  is relatively small for all but the highest fields, so we make the approximation that  $\mathcal{T}$  is independent of  $B$  in the following results.

### 6.3.2 Results: $G(B)$ dependence

The resonances in this device are more clearly seen in the differential conductance  $G = dI/dV_{\text{sd}}$  rather than the current  $I$ , as explained above. Fortunately however, it turns out that at the onset of a resonance,  $G$  is proportional to  $I$ : From section 3.7.1, at the *onset* of a resonance in  $I(V_{\text{sd}})$ , the form of the current is dominated by the Fermi-Dirac distribution,

$$I(V_{\text{sd}}) = I_o \left[ 1 + \exp \left( \frac{e(V_{\text{F}} - V_{\text{sd}})}{\mathcal{F}k_{\text{B}}T} \right) \right]^{-1}, \quad (6.30)$$

where  $V_{\text{F}}$  is the voltage at which the QD state becomes resonant with the Fermi level in the emitter,  $\mathcal{F}$  is the leverage factor of the device,  $T$  is the temperature and  $I_o$  is the peak current. It is then straightforward to show that when the QD state crosses the Fermi level in the emitter at  $V_{\text{sd}} = V_{\text{F}}$ ,  $G = dI/dV_{\text{sd}}$  is at a maximum,

$$G_{\text{max}} = \frac{e\mathcal{F}}{4k_{\text{B}}T} I_o. \quad (6.31)$$

The important point is that  $G_{\text{max}}$  is proportional to the peak current. Therefore, the differential conductance at the onset of a resonance can also be used to obtain  $|\tilde{\phi}_{\text{qd}}^{\circ}(k_x, k_y)|^2$ .

A practical problem with this experiment is the large number of experimental variables: (i) the source drain voltage  $V_{\text{sd}}$ , (ii) the voltage applied

to the gates  $V_g$ , (iii) the combination of gates used, (iv) the magnitude of the magnetic field, and (v) the orientation of the magnetic field. It was not possible to explore all the combinations of these variables in the time available, therefore some compromises had to be made. The experiment was broken into two ‘sub-experiments’: (1) determining the dependence of  $G$  on the *magnitude* of the magnetic field, and (2) determining the dependence of  $G$  on the *orientation* of the magnetic field (with the  $xy$ -plane). In (1) the direction of  $\mathbf{B}$  was fixed along the  $y$ -axis as specified in figure 6.12, whereas in (2) the magnitude of the field was fixed at 4 T and the direction of the field rotated through  $180^\circ$ .

In both experiments, the procedure was to measure the  $I(V_{sd})$  characteristic between  $V_{sd} = 0 - 0.4$  V, incrementing the gate voltage by 10 mV between each successive  $I(V_{sd})$  trace, starting the set at  $V_g = -0.4$  V and finishing at  $V_g = +0.4$  V. Once a set of  $I(V_{sd}, V_g)$  data had been obtained, the magnetic field was adjusted and the procedure repeated.

In both experiments, the gate voltage was applied to the NE and NW gates and the temperature was  $T = 300$  mK. Although varying the gate voltage greatly increases the time taken to perform the experiments, it is useful because it helps to identify the resonances. Also, importantly, some of the resonances are only resolvable at particular  $V_g$ , they being otherwise obscured by neighbouring resonances (i.e. resonances close in  $V_{sd}$ ).

Figures 6.15-6.18 show typical  $G(V_{sd})$  traces from these experiments.

## 6.4 Magneto-tunnelling spectroscopy on an individual QD

We now focus attention on the resonant features labelled 8 and 2. Figure 6.19 shows that both features exhibit an almost identical sensitivity to gate voltage, strongly suggesting that they are due to tunnelling through the *same* QD. On the other hand, the separation in  $V_{sd}$  between the two features is much too large for them to be attributed to tunnelling through the same electron state (as was suggested for the relationship between features

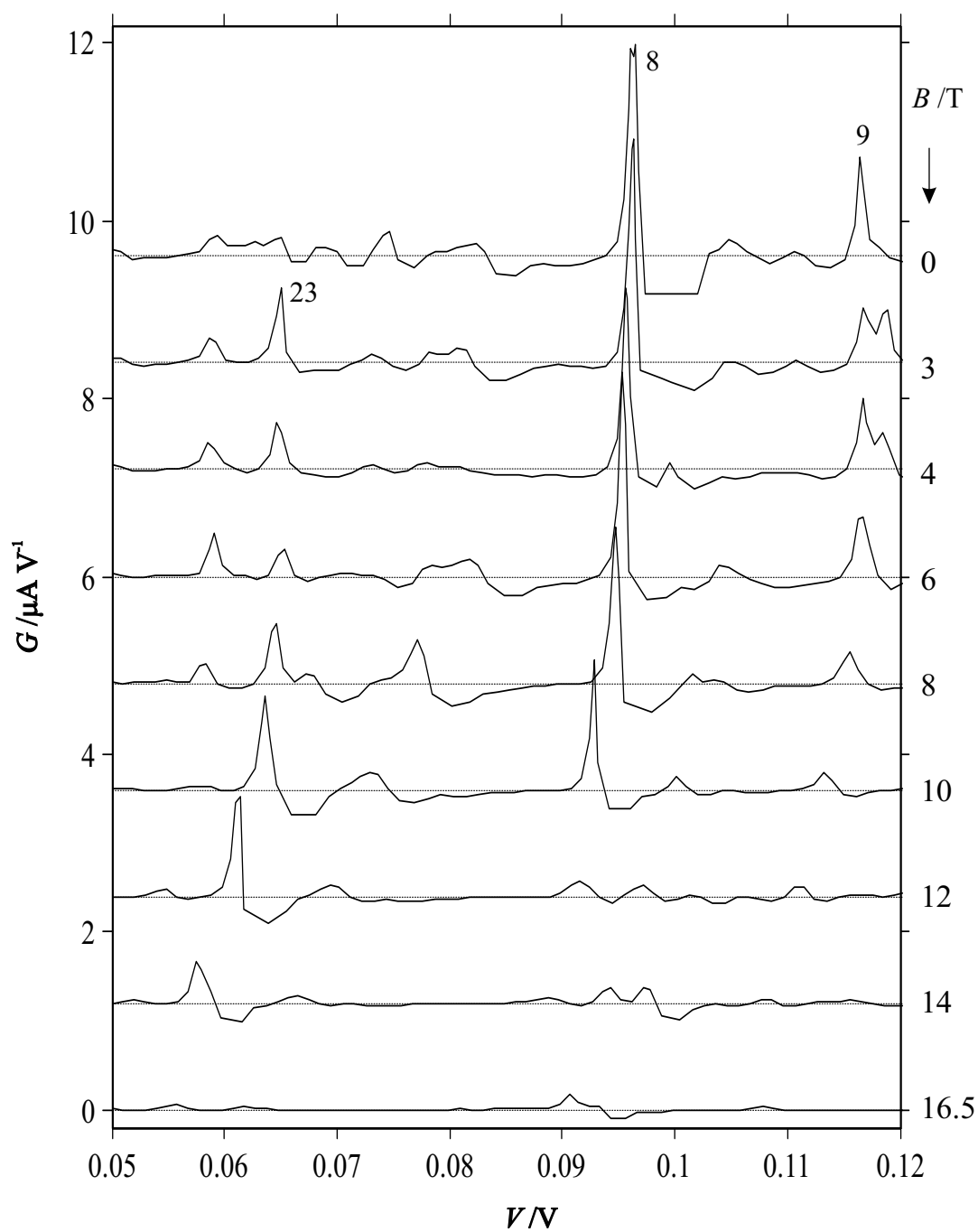


Figure 6.15: Plots of the differential conductance  $G = dI/dV_{\text{sd}}$  versus  $V_{\text{sd}}$  for magnetic fields between 0 and 16.5 T, applied parallel to the  $y$ -axis. A voltage of +400 mV has been applied to the NE and NW gates. The temperature is 0.3 K.

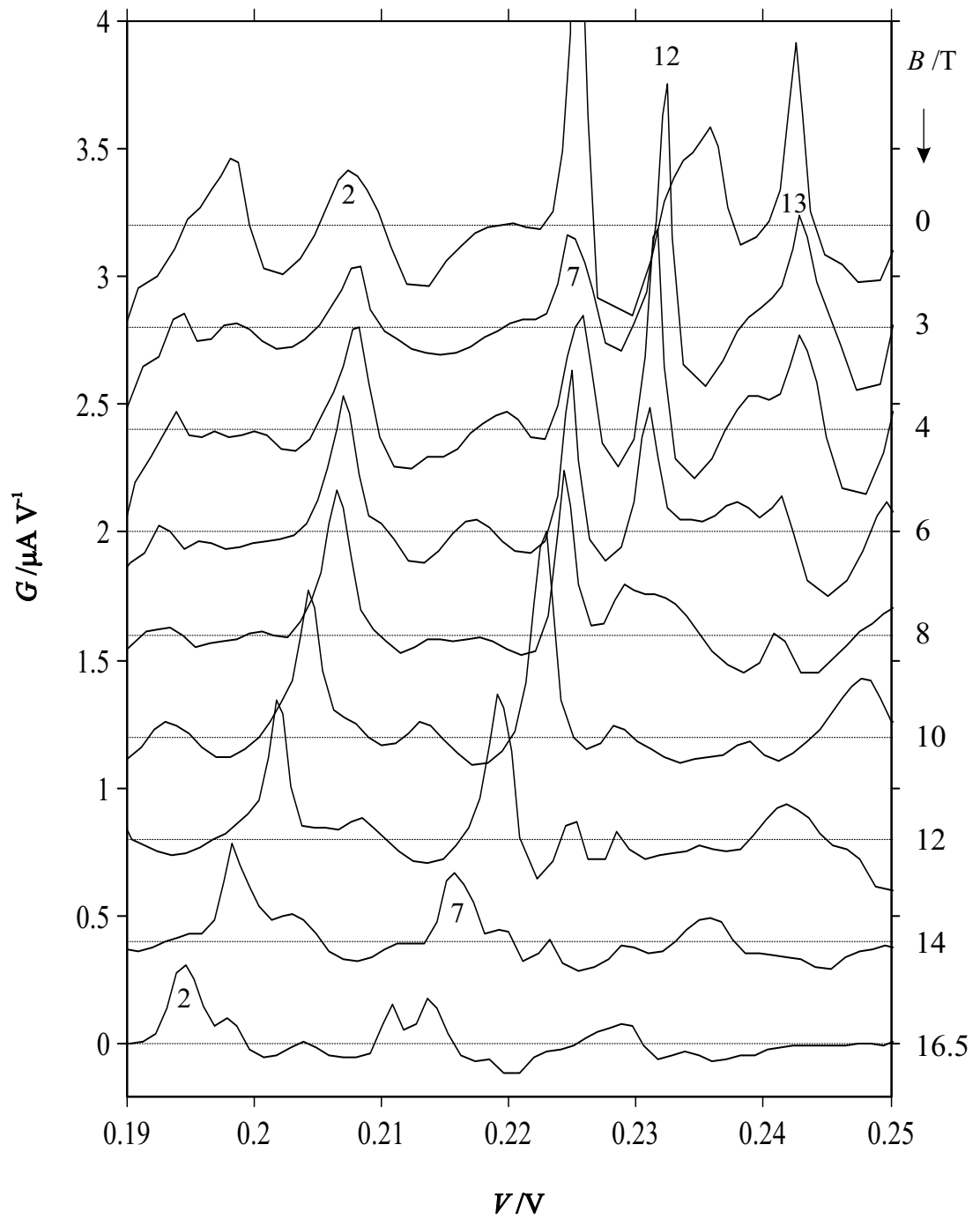


Figure 6.16: Plots of the differential conductance  $G = dI/dV_{sd}$  versus  $V_{sd}$  for magnetic fields between 0 and 16.5 T, applied parallel to the  $y$ -axis. A voltage of +400 mV has been applied to the NE and NW gates. The temperature is 0.3 K.

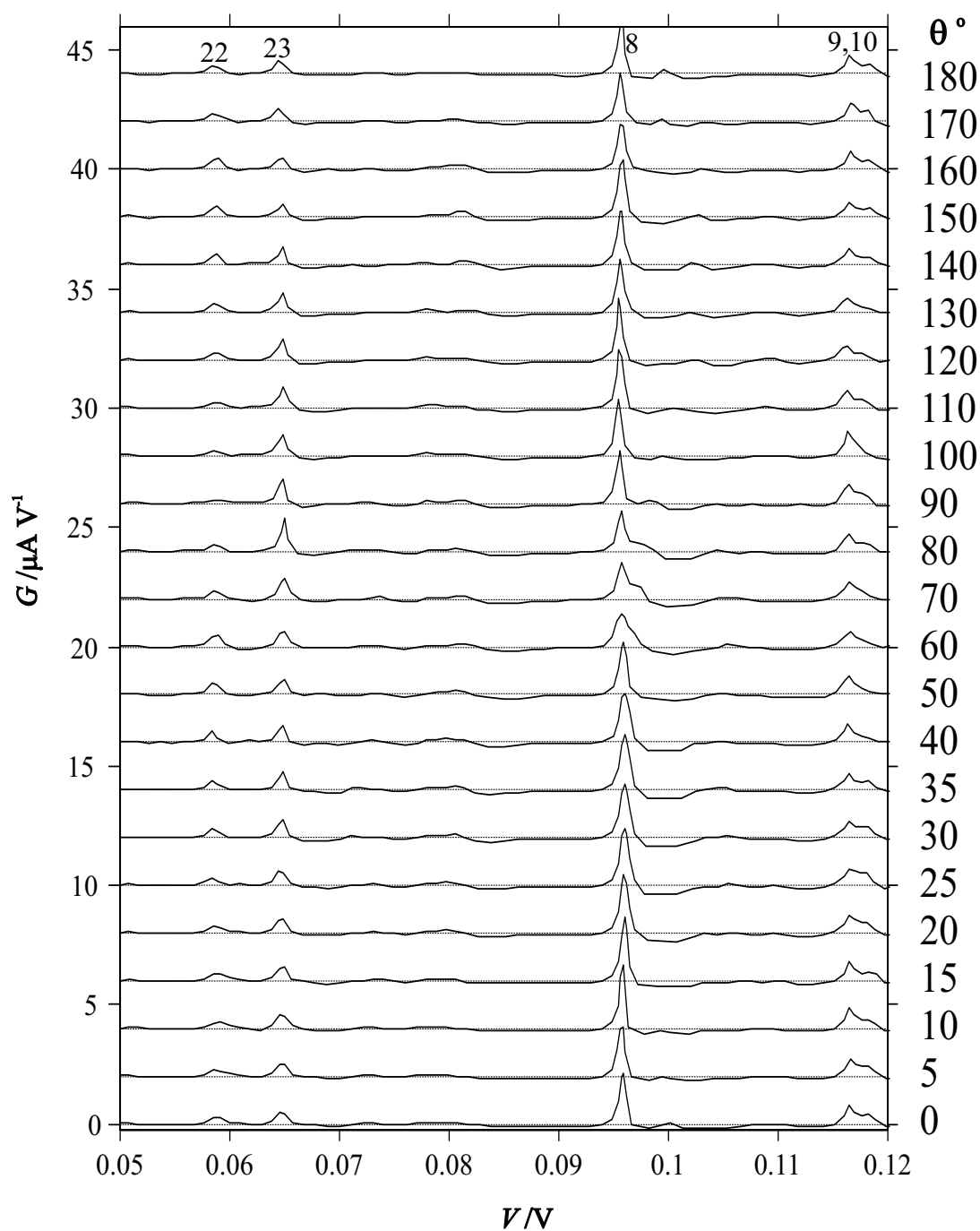


Figure 6.17: Plots of the differential conductance  $G = dI/dV_{sd}$  versus  $V_{sd}$  for a magnetic field of 4 T aligned in various directions within the  $xy$  plane: In the  $0^\circ$  position,  $\mathbf{B}$  is aligned with the  $y$ -axis; at  $90^\circ$ ,  $\mathbf{B}$  is aligned along the  $-x$ -axis; and at  $180^\circ$ ,  $\mathbf{B}$  points along the  $-y$ -axis. A voltage of +400 mV has been applied to the NE and NW gates. The temperature is 0.3 K.

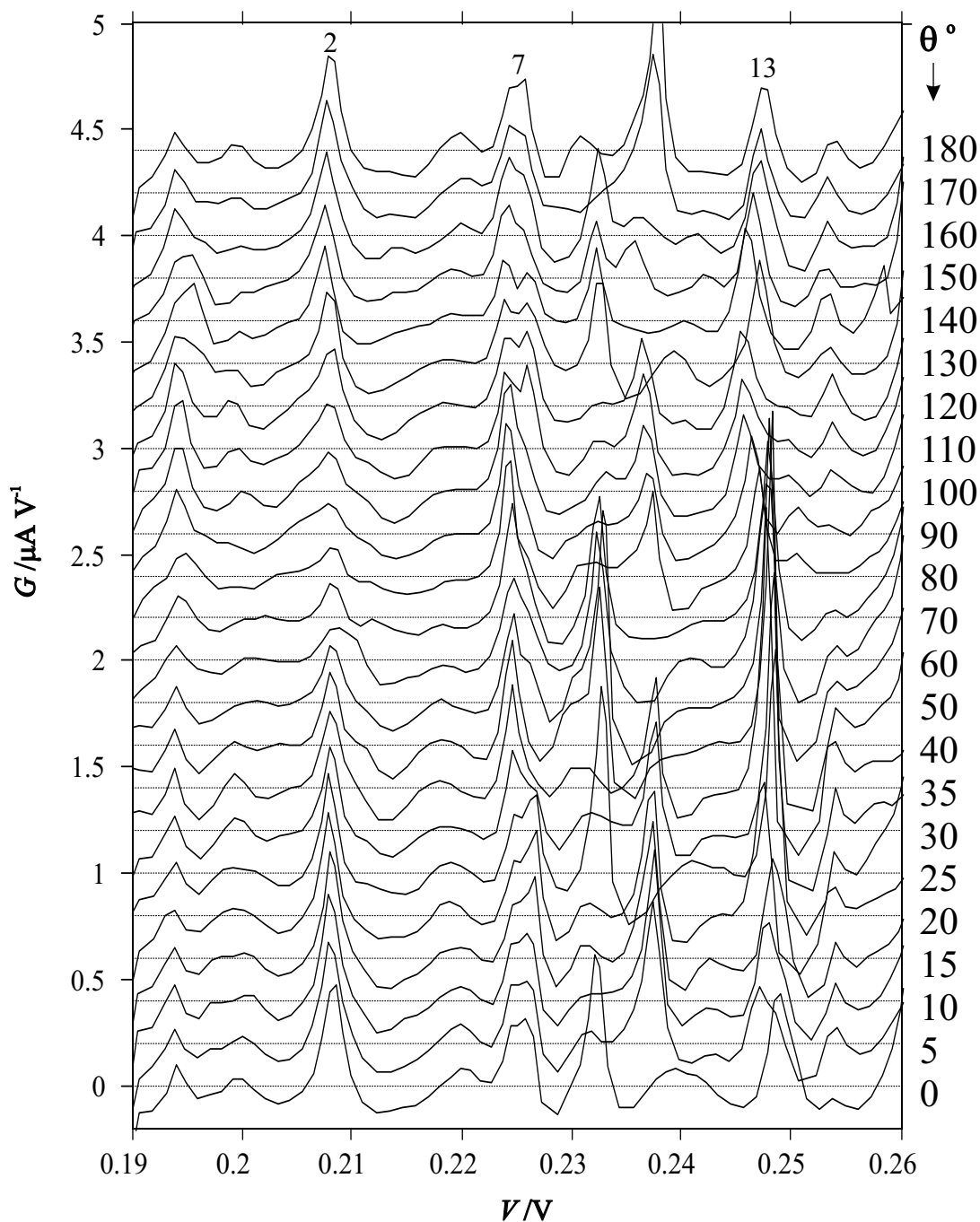


Figure 6.18: Plots of the differential conductance  $G = dI/dV_{sd}$  versus  $V_{sd}$  for a magnetic field of 4 T aligned in various directions within the  $xy$  plane: In the  $0^\circ$  position,  $\mathbf{B}$  is aligned with the  $y$ -axis; at  $90^\circ$ ,  $\mathbf{B}$  is aligned along the  $-x$ -axis; and at  $180^\circ$ ,  $\mathbf{B}$  points along the  $-y$ -axis. A voltage of +400 mV has been applied to the NE and NW gates. The temperature is 0.3 K.

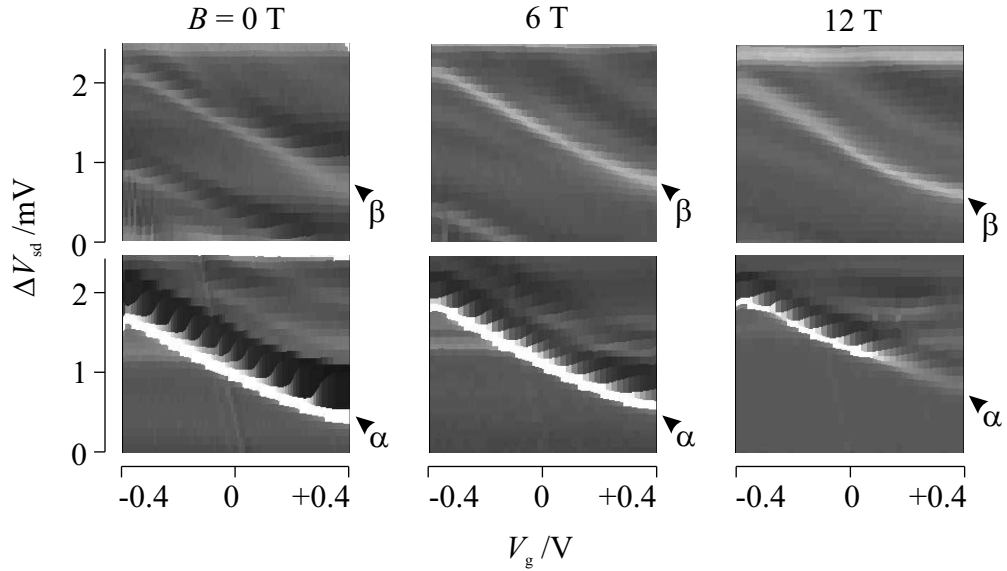


Figure 6.19: Grey-scale plots of  $G = dI/dV_{sd}$  highlighting the variation in the  $V_{sd}$  positions of resonances  $\alpha$  (8) and  $\beta$  (2) with gate voltage  $V_g$  (the gate voltage has been applied to both the NE and NW gates in this case). The plot shows that both resonances have almost identical sensitivity to  $V_g$ .

8 and 10 in section 6.2.2). This suggests that 8 and 2 are due to tunnelling through two *different* states of the *same* QD. For convenience, in this section, resonance 8 will be referred to as  $\alpha$ , and 2 will be referred to as  $\beta$ .

Figure 6.20 shows plots of  $G_{\max}(\mathbf{B})$  for resonances  $\alpha$  and  $\beta$ . In the two plots on the left, the direction of the magnetic field has been fixed along the  $y$ -axis and we plot the value of  $G_{\max}$  versus the magnitude of the field. According to equation 6.27, such a plot corresponds to a graph of the  $k$ -space probability density of the QD electron state along the  $k_x$ -axis,  $[01\bar{1}]$ .

The only variable relating the magnitude of  $B$  to the magnitude of the  $k$  vector is the tunnelling distance between the emitter and the QD state,  $s$ . Unfortunately it is rather difficult to estimate the value of  $s$ , for, although the thickness of the (AlGa)As layer is accurately known, the negative charge in this layer (see section 2.4.3) pushes the emitter electrons away from it, increasing the tunnelling distance. We can obtain a crude order of magnitude estimate of the charge in the barrier from the estimate of the QD density,  $\sim 0.5 - 1 \times 10^{15} \text{ m}^{-2}$  (Henini *et al.* 1997). Then by using this value in the numerical calculation for the conduction band (section 2.4.3), an estimate of the tunnelling distance can be obtained. At the high end of the estimate,

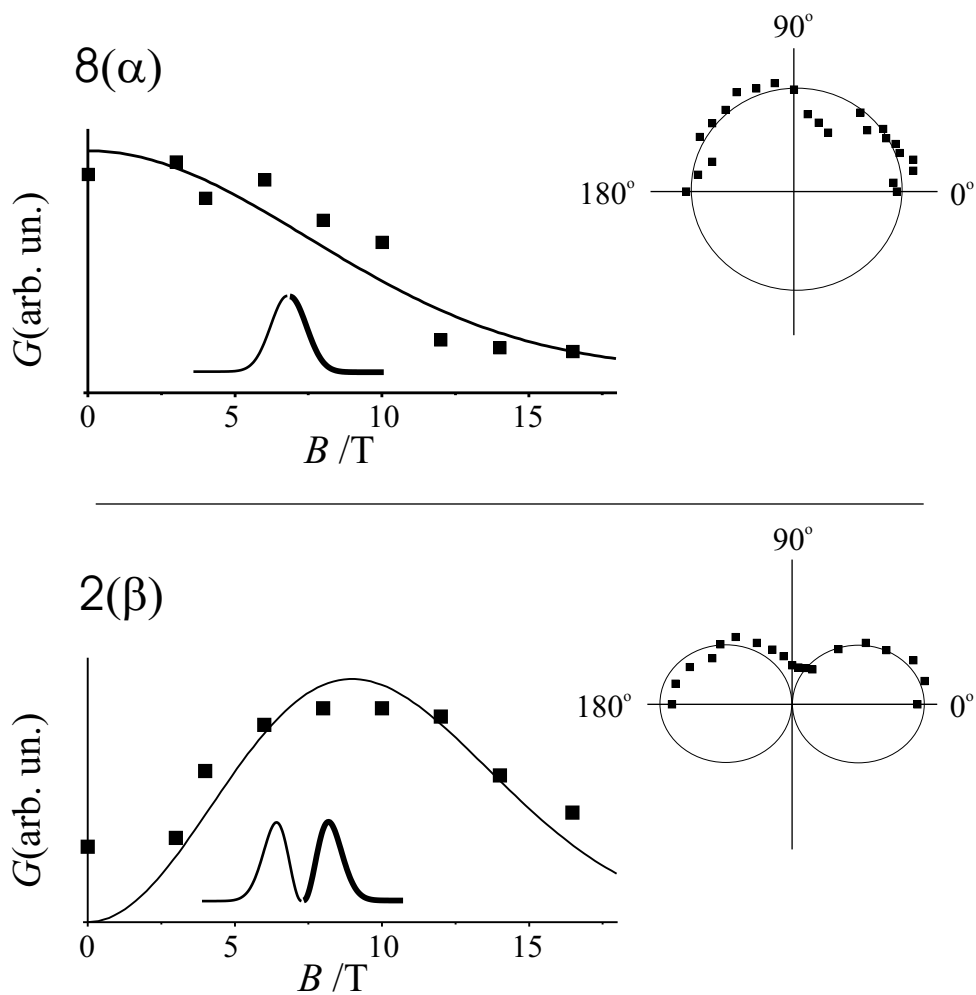


Figure 6.20: Plots of the conductance  $G = dI/dV_{sd}$  versus magnetic field  $B$  for resonances  $\alpha$  (8) and  $\beta$  (2). The graphs on the left show the dependence of  $G$  on the magnitude of a magnetic field aligned along the  $y$ -axis (see main text). The graphs on the right are polar plots showing how  $G$  varies as the direction of a 4 T magnetic field is rotated within the  $xy$  plane.

assuming that the QDs are multiply occupied by electrons ( $\sim 3 - 4$ ), the tunnelling distance is  $s \sim 10 - 20$  nm at  $V_{sd} \sim 100 - 200$  mV. However, since some disorder is present in the emitter the tunnelling distance is unlikely to be uniform at all points in the emitter. Instead some regions of the emitter will approach the (AlGa)As layer more closely, whilst others will be farther away, analogous to the variations in the shoreline on a smoothly rising beach. Since the tunnel current decreases roughly exponentially with tunnelling distance, the resonances we observe are expected to be due to tunnelling from points in the emitter closest to the QDs, so the tunnelling distance relevant to our results is likely to be significantly less than the ‘average’ tunnelling distance. However, the tunnelling distance cannot be less than 7 nm since this is the half-width of the (AlGa)As layer. Therefore, as a crude estimate, we use a value of  $7 - 15$  nm for  $s$ , so that a magnetic field of 16.5 T corresponds to  $k \sim 0.18 - 0.38$  nm $^{-1}$ . Capacitance measurements on the device [see for example Belyaev *et al.* (2000)] can provide better estimates of the average tunnelling distance, but cannot give any information on the variation in  $s$ .

Notice that the amplitude of resonance  $\alpha$  has its maximum value at 0 T. With increasing  $B$  the amplitude of the resonance decays steadily, until at about 16.5 T, the amplitude has fallen to less than 10% of its value at 0 T. Resonance  $\beta$  on the other hand shows a clearly different behaviour. The amplitude of this resonance has a *minimum* at 0 T. It then increases to a broad maximum at around 10 T beyond which it is decreasing.

The polar plots on the right hand side of figure 6.20 show how  $G$  varies as the direction of a 4 T magnetic field is *rotated* within the  $xy$  plane. The  $0^\circ$  position corresponds to alignment of  $\mathbf{B}$  along the  $+y$ -axis, the  $90^\circ$  position corresponds to the  $-x$ -axis, and the  $180^\circ$  position corresponds to the  $-y$ -axis. Therefore, according to equation 6.27, such plots reflect polar plots of the  $k$ -space probability density, with the  $0^\circ$  position marking the  $k_x$ -axis,  $[01\bar{1}]$ , and the  $90^\circ$  position marking the  $k_y$ -axis,  $[\bar{2}33]$ . Although data has only been obtained for the interval  $0 - 180^\circ$ , note that for a bound QD state, the wave function in  $k$ -space must be symmetric on rotation through  $180^\circ$ , i.e.  $|\tilde{\phi}(k_x, k_y)|^2 = |\tilde{\phi}(-k_x, -k_y)|^2$ . This must be so otherwise the expectation value of the linear momentum would be non-zero and thus the electron could

not be bound to the QD. With this symmetry in mind, the trend shown by the data points between  $0 - 180^\circ$  has also been reflected to the interval  $180 - 360^\circ$ .

Notice that the amplitude of resonance  $\alpha$  displays circular symmetry, whilst  $\beta$  displays two clear lobes aligned roughly along the  $k_x$ -axis.

The circular symmetry of the probability density of the  $\alpha$  state, with a single anti-node at  $k = 0$  ( $B = 0$ ), suggests that it represents the ground state of the QD. The form of  $\beta$  on the other hand, with two lobes lying along the  $k_x$ -axis and a single node at  $k = 0$ , suggests that it represents the first excited state of the QD.

The small deviations of the data points of  $\alpha$  from circular symmetry can be attributed to the uncertainty in obtaining the values of  $G_{\max}$  from the  $G(V_{sd})$  plots. The error results from limiting the number of data points that are obtained during each sweep of the source-drain voltage. This is a practical compromise to limit the length of the experiment to a reasonable amount of time. With more time, it should be possible to repeat the experiment, focussing on just resonances  $\alpha$  and  $\beta$  but with higher source-drain voltage resolution. On the other hand, the double-lobes seen in the polar plot of  $\beta$  are very unlikely to be due to random error since there are many data points that closely follow the expected behaviour of the first excited state.

### 6.4.1 Fits to analytic wave functions

The forms of the measured probability densities (figure 6.20) appears to be very similar to those of the two lowest energy stationary states of a 2D harmonic oscillator,

$$\begin{aligned} |\tilde{\phi}_{00}|^2 &\sim \left| \exp\left(-\frac{k_x^2}{2\sigma_x^2}\right) \exp\left(-\frac{k_y^2}{2\sigma_y^2}\right) \right|^2 \\ |\tilde{\phi}_{10}|^2 &\sim \left| \frac{k_x}{\sigma_x} \exp\left(-\frac{k_x^2}{2\sigma_x^2}\right) \exp\left(-\frac{k_y^2}{2\sigma_y^2}\right) \right|^2, \end{aligned} \quad (6.32)$$

where  $\sigma_x$  and  $\sigma_y$  are the characteristic dimensions of the harmonic potential in the  $k_x$  and  $k_y$  directions respectively.

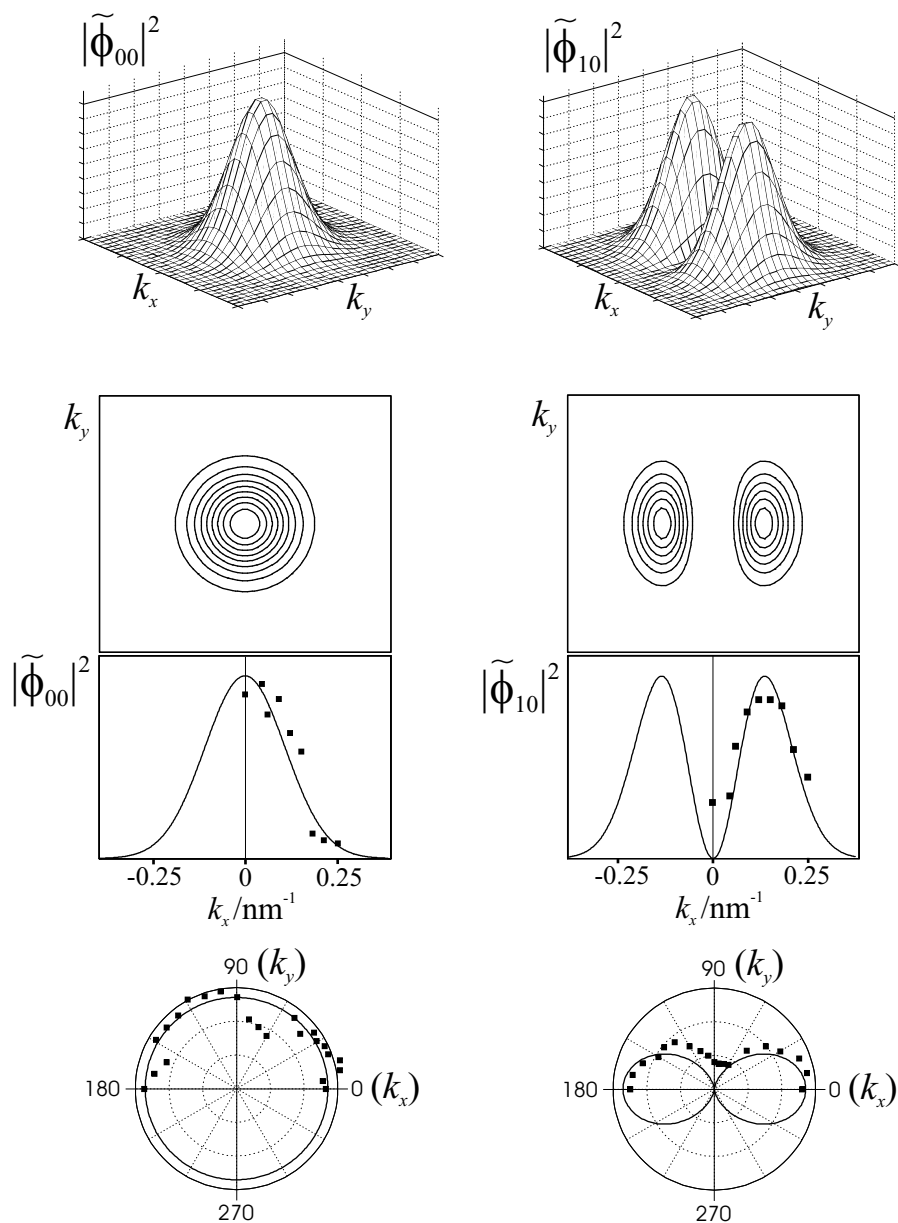


Figure 6.21: Probability densities in  $k$ -space of the two lowest energy states of a harmonic oscillator,  $|\tilde{\phi}_{00}|^2$  and  $|\tilde{\phi}_{10}|^2$ . The lower diagrams show fits to the experimentally obtained probability densities,  $\alpha$  and  $\beta$ , assuming a tunnelling distance of  $s \approx 10$  nm.

Figure 6.21 shows fits to the data by  $|\tilde{\phi}_{00}|^2$  and  $|\tilde{\phi}_{10}|^2$ , the analytic probability densities. Note that, in this fit, a tunnelling distance of  $s \approx 10$  nm has been used to relate  $B$  to  $k$ . The value of  $\sigma_x$  is varied to obtain independent fits for resonances  $\alpha$  and  $\beta$ . The fitted values are

$$\begin{aligned}\sigma_x^{-1}(\alpha) &= (7.0 \pm 1.0) \text{ nm} \\ \sigma_x^{-1}(\beta) &= (7.3 \pm 1.0) \text{ nm}.\end{aligned}$$

That the two independently obtained values of  $\sigma_x$  are in agreement supports the conjecture that  $\alpha$  and  $\beta$  are due to the same QD. Including the uncertainty in  $s$  raises the uncertainty in  $\sigma_x^{-1}$  to  $\sim \pm 3$  nm.

A problem with this analysis, however, is that the fits to the polar plots suggest that the confinement of the QD in the  $x$ -direction is similar to that in the  $y$ -direction,  $\sigma_x \approx \sigma_y$ . This means that we should observe another state with similar energy to the  $\beta$  state, corresponding to  $\tilde{\phi}_{01}$ . So far, we have not been able to identify a candidate for such a  $\tilde{\phi}_{01}$  state amongst the resonances we observe in  $I(V_{sd})$ . It is possible that this resonance is obscured by one of the more prominent resonances, such as resonance 3 or 17. However, if this is the case, this would imply that the energy of the  $\tilde{\phi}_{01}$  state is significantly different from the energy of the  $\tilde{\phi}_{10}$  state. This is inconsistent with the observation that the confinement of the QD is similar in both the  $x$  and  $y$  axes. As yet we have no satisfactory explanation for the absence of this resonance.

It is significant that we observe the lobes of  $\beta$  aligned closely with the  $[01\bar{1}]$  crystal axis as opposed to some other, arbitrary axis within the  $xy$  plane. Studies of InAs QDs grown on (100) and (311) GaAs substrates show that in many cases, the QDs have symmetrical shapes in the growth plane, for example, square, rectangular, ‘wire-like’ or arrow shapes, aligned along the main crystal axes (Cirilin *et al.* 1995, Henini *et al.* 1998, Patanè *et al.* 2002). Maps of the probability density obtained by Vdovin *et al.* for self assembled InAs QDs grown within the quantum well of an  $\text{Al}_{0.4}\text{Ga}_{0.6}\text{As}/\text{GaAs}/\text{Al}_{0.4}\text{Ga}_{0.6}\text{As}$  double barrier structure (Vdovin *et al.* 2000) also display the same alignment. However, in their case, they find that the wave functions of QDs grown on the (311) plane of the substrate display a pronounced *anisotropy*:

the wave function is elongated along the  $k_x$   $[01\bar{1}]$  direction. This is inconsistent with the results from the gated device, where the ground state  $\alpha$  does not appear to show any such anisotropy. However it is not clear whether it is valid to compare the shapes of the wave functions obtained from the double barrier experiments with those obtained in this experiment since the QDs in the double barrier experiments were grown on GaAs substrates whereas the QDs in this device were grown on an (AlGa)As substrate.

Notice that, although we observe a node in the probability density of  $\beta$  at  $B = 0$  ( $k = 0$ ), it never actually falls to zero as expected from the corresponding harmonic oscillator function. This represents a limit to the ‘resolution’ with which the MTS technique can be used to map the  $k$ -space probability density. In equation 6.24 and equation 6.25 the approximation was made that tunnelling to the QD took place from a number of states in the emitter with  $k$  values confined to a small area of  $k$ -space surrounding the point  $(k_x, k_y) = (0, z_e/l_B^2)$  (with the magnetic field aligned along the  $x$ -axis). The extent of this  $k$ -area was assumed to be small enough so that when performing the sum-over-emitter-states in equation 6.26 to find the tunnel current, the value of  $\tilde{\phi}_{\text{qd}}^\circ$  could be taken to be a constant. In this case, magneto-tunnelling spectroscopy effectively acts as a ‘point’ probe of the  $k$ -space probability density of the electron in the QD,  $|\tilde{\phi}_{\text{qd}}^\circ(k_x, k_y)|^2$ . Realistically however, the range of  $k$  values in the emitter contributing to the tunnel current covers a larger fraction of the area of the QD wave function in  $k$ -space, so that within the sum-over-states,  $\tilde{\phi}_{\text{qd}}^\circ$  cannot be taken as a constant. Then the tunnel current represents some value of  $\tilde{\phi}_{\text{qd}}^\circ(k_x, k_y)$  that has been averaged over a small range of  $k$ -space. In other words, this means that the probe of  $k$ -space has been widened from a point probe to cover a small area of  $k$ -space, limiting the resolution with which MTS can be used to map the probability density.

### 6.4.2 Estimate of the size of the QD wave functions in real space

A determination of the form of the wave function in real space requires that we also know the *phase* of the  $k$ -space wave function. However, in this

experiment, we measure the square of the wave function and are unable to obtain any phase information. Note that, although the probability density of a bound state in  $k$ -space is expected to be symmetrical, i.e.  $|\tilde{\phi}(k_x, k_y)|^2 = |\tilde{\phi}(-k_x, -k_y)|^2$ , it does not follow that the probability density in real space must also show the same symmetry, only that the real space wave function is a standing wave (possibly with an angular momentum component).

Over recent years, there has been a number of attempts to calculate the real space wave functions of stationary states of QDs from first principles, using a variety of different approaches, and assuming a range of different shapes and compositions of the QDs<sup>†</sup>. Since such calculations also include the phase of the wave function, it should be possible to Fourier transform the real space wave function into a corresponding  $k$ -space wave function for comparison with the experimentally obtained probability densities.

In the absence of this information, we can still obtain an estimate of the size of our measured wave functions in real space by Fourier transforming the fitted  $k$ -space harmonic oscillator functions. The corresponding harmonic oscillator functions in real space are

$$\begin{aligned} |\phi_{00}|^2 &\sim \left| \exp\left(-\frac{x^2}{2l_x^2}\right) \exp\left(-\frac{y^2}{2l_y^2}\right) \right|^2 \\ |\phi_{10}|^2 &\sim \left| \frac{x}{l_x} \exp\left(-\frac{x^2}{2l_x^2}\right) \exp\left(-\frac{y^2}{2l_y^2}\right) \right|^2, \end{aligned} \quad (6.33)$$

where  $l_x = 1/\sigma_x$  and  $l_y = 1/\sigma_y$ . We have already determined the value of  $\sigma_x$  in section 6.4.1. Therefore we can estimate the characteristic size,  $l_x$ , of the wave function in real space,  $l_x = \sigma_x^{-1} = (7 \pm 3)$  nm. This size is comparable to measurements of the in-plane radius of the QDs ( $\sim 7 - 9$  nm) made by atomic force microscopy (Polimeni *et al.* 1999b).

The energy separation  $\Delta E$  between the two states can be estimated by re-scaling the voltage spacing  $\Delta V_{sd}$  between them by the leverage factor for the device,  $\mathcal{F}$ . The voltage spacing is measured to be  $\Delta V_{sd} = (114 \pm 4)$  mV and the leverage factor is estimated from numerical calculation of the conduction

---

<sup>†</sup>See, for example, Grundmann *et al.* (1995), Stier *et al.* (1999), Pryor *et al.* (1997), Yang *et al.* (2000) and Wang *et al.* (1999)

band profile to be  $\mathcal{F} = 2.5 \pm 0.5$  (section 2.4.3). This gives a value for the energy separation between the two states,  $\Delta E = \Delta V_{\text{sd}}/f = 40 - 60$  meV.

A second, entirely independent estimate of the energy separation can be obtained from the data on the probability densities. To do this, we note that  $l_x$  is related to the  $x$  component of the harmonic oscillator frequency,

$$l_x = \sqrt{\frac{\hbar}{m\omega_x}}. \quad (6.34)$$

Then, since the energy level separation between the states  $\phi_{00}$  and  $\phi_{10}$  is  $\Delta E = \hbar\omega_x$ , we can obtain an estimate of the energy level separation between our measured states,

$$\Delta E = \hbar\omega = \frac{\hbar^2}{m^*l_x^2}. \quad (6.35)$$

Taking the tunnelling distance  $s = 7 - 15$  nm, the value of  $\Delta E$ , estimated from the size of the wave function, becomes equal to the estimate made from the voltage separation ( $\Delta E = \Delta V_{\text{sd}}/\mathcal{F}$ ) when the effective mass is  $m^* = 0.013 - 0.12m_e$ . The uncertainty is rather large because the measurement of the effective mass depends on the tunnelling distance as  $m^* \sim s^2$ . Nevertheless, this crude estimate suggests a value of  $m^*$  significantly larger than that of bulk InAs. Such an effective mass would not be unexpected for a number of reasons: (i) the indium content of the QD is typically less than 100% due to alloying with aluminium in the barrier layers (Surkova *et al.* 2001); (ii) the electron wave function in the QD penetrates into the (AlGa)As barrier layer where the effective mass is  $\sim 0.07m_e$ ; (iii) the QD introduces a strain into the lattice which can affect the effective mass (Aspnes and Cardona 1978); (iv) the electron bound state energies of the QD lie well above the bottom of the conduction band so there is likely to be an adjustment to the effective mass due to non-parabolicity (section 1.5.1).

### 6.4.3 Comparisons with results from other QDs

In addition to resonances  $\alpha$  and  $\beta$  we can also identify some other possible groupings from the grey-scale plots of figures 6.8 and 6.9.

The resonances labelled 9 and 7, for example, are clearly resolved and

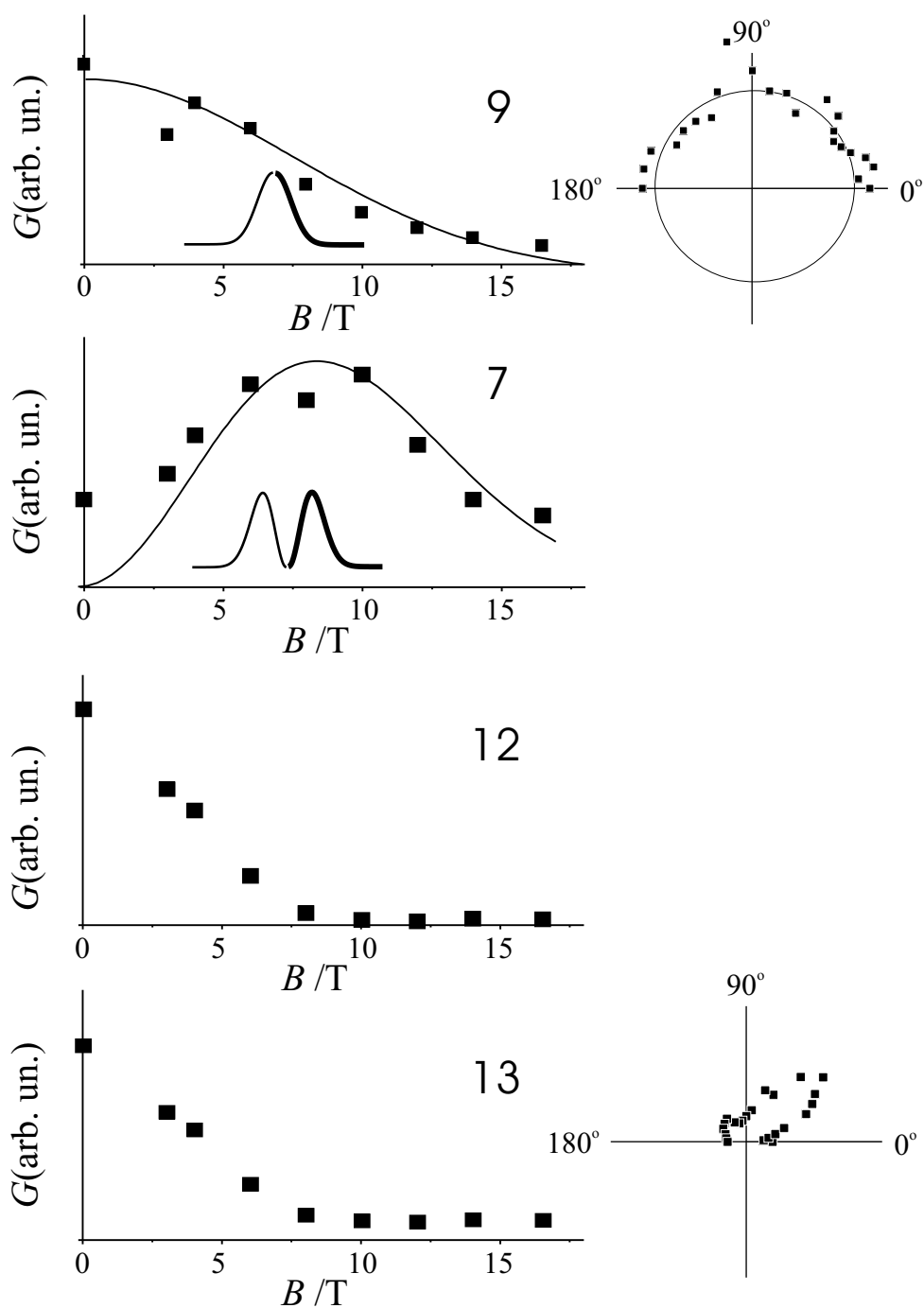


Figure 6.22: Plots of the conductance  $G = dI/dV_{sd}$  versus magnetic field  $B$  for resonances 9, 7, 12 and 13. The graphs on the left show the dependence of  $G$  on the magnitude of a magnetic field aligned along the  $y$ -axis (see main text). The graphs on the right are polar plots showing how  $G$  varies as the direction of a 4 T magnetic field is rotated within the  $xy$  plane.

appear to show ground-state and first-excited state behaviour respectively (figure 6.22). They also have a similar energy spacing to that of  $\alpha$  and  $\beta$ . In this case however, the resonances do not respond to either the NE or NW gates and so we cannot verify their assignment to a single QD. On the other hand, the features labelled 1 and 15 show very similar sensitivity to the same gate, but it is difficult to extract the dependence of  $G(B)$  for these features due to difficulties in resolving them from other nearby features.

We also observe a number of features, 35, 12, 13 and 16, that shift relatively rapidly with gate voltage, implying that they originate from QDs in close proximity to a gate. Despite the fact that this group of resonances all appear to show very similar sensitivities to gate voltage when applied equally to both the NE and NW gate, the features must in fact be due to different quantum dots since: features 12 and 16 respond only to the NE gate, 13 responds only to the NW gate and feature 35 responds roughly equally to both gates.

Examining the  $G(B)$  dependence of features 12 and 13 (it is not possible to resolve resonances 35 and 16 clearly enough to extract their  $G(B)$  dependence) we find strikingly different behaviour from resonances 2, 8, 9 and 7. The conductance of 12 and 13 fall sharply with  $B$  aligned along the  $x$ -axis but are enhanced when we rotate the field toward the  $y$ -axis by about  $40^\circ$  (figure 6.22). A possible explanation for this might be that the close proximity to the gate gives rise to a significant potential drop across the diameter of the QD, which is enough to deform the wave function observably.

## 6.5 Conclusions and future prospects

The experiments presented in this chapter have demonstrated how a multiple-gating technology may be used to address individual QDs from an ensemble. Combined with the magneto-tunnelling spectroscopy technique, it has been demonstrated how the probability density and energy levels of the electron states of a single QD can be measured.

Although the particular device featured in this chapter had two defective

---

gate electrodes, devices with four working electrodes have been tested previously (Austing *et al.* 1999). Unfortunately, these devices did not survive another cool-down in the cryostat for the magneto-tunnelling experiment. With four working gates, it becomes possible individually to address a larger number of QDs and to pinpoint better their location in the  $xy$  plane. Combined with the magneto-tunnelling spectroscopy technique, this presents the opportunity to observe the ensemble distribution of the QD energy levels and wave functions and thus to obtain information about the variation in the size, shape and compositions of the QDs, complementing surface techniques such as atomic force microscopy and scanning tunnelling microscopy.

Finally, the data obtained from resonant features 12 and 13 suggests that it may be possible to use the gate electrodes to deform the QD electron wave functions. Combined with the MTS technique, this opens up the possibility of being able to measure such deformation as a function of gate voltage.

# Bibliography

- Adachi S (1985). *GaAs, AlAs and (AlGa)As: material parameters for use in research and device applications*. J. Appl. Phys. **58**, R1.
- Altshuler B L and Aronov A G (1979). *Damping of one-electron excitations in metals*. JETP Lett. **30**, 482.
- Altshuler B L and Aronov A G (1981). *Electron density of states and energy relaxation time in magnetic field*. Solid State Commun. **38**, 11.
- Altshuler B L, Aronov A G and Khmel'nitsky D E (1982). *Effects of electron-electron collisions with small energy transfers on quantum localisation*. J. Phys. C **15**, 7367.
- Ando T, Fowler A B and Stern F (1982). *Electronic properties of two-dimensional systems*. Rev. Mod. Phys. **54**, 437.
- Ando T and Uemura Y (1974). *Theory of oscillatory g factor in an MOS inversion layer under strong magnetic fields*. J. Phys. Soc. Japan **37**, 1044.
- Ashcroft N W and Mermin N D (1976). *Solid State Physics*. Saunders College Publishing.
- Aspnes D E and Cardona M (1978). *Strain dependence of effective masses in tetrahedral semiconductors*. Phys. Rev. B **17**, 726.
- Austing D G, Honda T and Tarucha S (1997a). *Multiple-gated submicron vertical tunnelling structures*. Semicond. Sci. Technol. **12**, 631.
- Austing D G, Honda T and Tarucha S (1997b). *Vertical single electron transistors with separate gates*. Jpn. J. Appl. Phys. **36**, 4151.
- Austing D G, Honda T, Tokura Y and Tarucha S (1995). *Sub-micron vertical AlGaAs/GaAs resonant tunnelling single electron transistor*. Jpn. J. Appl. Phys. **34**, 1320.
- Austing D G, Tarucha S, Main P C, Henini M, Stoddart S T and Eaves L (1999). *Multiple gated InAs dot ensembles*. Appl. Phys. Lett. **75**, 671.

- Bardeen J (1961). *Tunnelling from a many particle point of view*. Phys. Rev. Lett. **6**, 57.
- Belyaev A E, Stoddart S T, Martin P M, Main P C, Eaves L and Henini M (2000). *Positively charged defects associated with self-assembled quantum dot formation*. Appl. Phys. Lett. **76**, 3570.
- Bending S J and Beasley M R (1985). *Transport processes via localised states in thin a-Si tunnel barriers*. Phys. Rev. Lett. **55**, 324.
- Benedict K A, Thornton A S G, Ihn T, Main P C, Eaves L and Henini M (1998). *Fermi edge singularities in high magnetic fields*. Physica B **256-258**, 519.
- Bimberg D, Grundman M and Ledentsov N N (1998). *Growth, spectroscopy and laser application of self-ordered III-V quantum dots*. MRS Bulletin February 1998 p. 31.
- Büttiker M (1988). *Coherent and sequential tunnelling in series barriers*. IBM J. Res. Develop. **32**, 63.
- Chelikowsky J R and Cohen M L (1976). *Nonlocal pseudopotential calculations for the electronic structure of eleven diamond and zinc-blende semiconductors*. Phys. Rev. B **14**, 556.
- Cheong H M, Burnett J H, Paul W, Hopkins P F, Campman K and Gosard A C (1996). *Hydrostatic-pressure coefficient of the direct band-gap energy of Al(x)Ga(1-x)As for x=0 to 0.35*. Phys. Rev. B **53**, 10916.
- Cirlin G E, Guryanov G M, Golubok A O, Tipsishev S Y, Ledentsov N N, Kop'ev P S, Grundmann M and Bimberg D (1995). *Ordering phenomena in InAs strained layer morphological transformation on GaAs (100) surface*. Appl. Phys. Lett. **67**, 97.
- Cobden D H and Muzykantskii B A (1995). *Finite-temperature Fermi-edge singularity in tunneling studied using random telegraph signals*. Phys. Rev. Lett. **75**, 4274.
- Davies J H (1998). *The Physics of Low-dimensional Semiconductors*. Cambridge University Press.
- Dellow M W, Beton P H, Langerak C J G M, Foster T J, Main P C, Eaves L, Henini M, Beaumont S P and Wilkinson C D W (1992). *Resonant tunnelling through the bound states of a single donor atom in a quantum well*. Phys. Rev. Lett. **68**, 1754.

- Demmerle W, Smoliner J, Gornik E, Boöm G and Weiman G (1993). *Tunnelling studies of energy levels and selection rules in low-dimensional structures*. Phys. Rev. B **47**, 13574.
- Deshpande M R, Hornbeck E S, Kozodoy P, Dekker N R, Sleight J W, Reed M A, Fernando C L and Frensley W R (1994). *Low-dimensional resonant tunnelling and coulomb blockade: a comparison of fabricated versus impurity confinement*. Semicond. Sci. Technol. **9**, 1919.
- Deshpande M R, Sleight J W, Reed M A and Wheeler R G (2000). *Sequential tunnelling and spin degeneracy of zero-dimensional states*. Phys. Rev. B **62**, 8240.
- Deshpande M R, Sleight J W, Reed M A, Wheeler R G and Matyi R J (1996). *Spin splitting of single 0D impurity states in semiconductor heterostructure quantum wells*. Phys. Rev. Lett. **76**, 1328.
- Dobers M, von Klitzing K and Weimann G (1988). *Electron-spin resonance in the two-dimensional electron gas of GaAs-Al(x)Ga(1-x) heterostructures*. Phys. Rev. B **38**, 5453.
- Dolgoplov V T, Shashkin A A, Aristov A V, Schmerek D, Hansen W, Kotthaus J P and Holland M (1997). *Direct measurements of the spin gap in the two-dimensional electron gas of AlGaAs-GaAs heterojunctions*. Phys. Rev. Lett. **79**, 729.
- Duke C B (1969). *Solid State Phys. Suppl. 10*. Academic Press.
- Fang F F and Stiles P J (1968). *Effects of a tilted magnetic field on a two-dimensional electron gas*. Phys. Rev. **174**, 823.
- Feynman R, Leighton R B and Sands M L (1965). *The Feynman lectures on physics*. Addison-Wesley.
- Finley J J, Teissier R J, Skolnick M S, Cockburn J W, Roberts G A, Grey R, Hill G, Pate M A and Planel R (1998). *Role of the X minimum on transport through AlAs single-barrier structures*. Phys. Rev. B **58**, 10619.
- Fromhold T M (1990). *Magnetotunnelling in semiconductor heterostructures*. PhD thesis. University of Nottingham, United Kingdom.
- Fukuyama H and Waho T (1995). *Excess current through single-barrier structures with Si-planar-doped AlAs layer*. Jpn. J. Appl. Phys. **34**, L342.
- Geim A K, Foster T J, Nogaret A, Mori N, McDonnell P J, La Scala Jr. N, Main P C and Eaves L (1994a). *Resonant tunnelling through donor molecules*. Phys. Rev. B **50**, 8074.

- Geim A K, Main P C, La Scala Jr. N, Eaves L, Foster T J, Beton P H, Sakai J W, Sheard F W and Henini M (1994b). *Fermi-edge singularity in resonant tunneling*. Phys. Rev. Lett. **72**, 2061.
- Gossard A C (1986). *Growth of microstructures by molecular beam epitaxy*. IEEE J. Quantum Electronics **QE-22**, 1649.
- Grundmann M, Stier O and Bimberg D (1995). *InAs/GaAs pyramidal quantum dots: Strain distribution, optical phonons and electronic structure*. Phys. Rev. B **52**, 11969.
- Hapke-Wurst I, Zeitler U, Frahm H, Jansen A G M, Haug R J and Pierz K (2000). *Magnetic-field-induced singularities in spin-dependent tunnelling through InAs quantum dots*. Phys. Rev. B **62**, 12621.
- Hapke-Wurst I, Zeitler U, Haug R J and Pierz K (2002). *Mapping the g factor anisotropy of InAs self-assembled quantum dots*. Physica E **12**, 802.
- Hapke-Wurst I, Zeitler U, Schumacher H W, Haug R J, Pierz K and Ahlers F J (1999). *Size determination of InAs quantum dots using magnetotunnelling experiments*. Semicond. Sci. Technol. **14**, L41.
- Henini M, Sanguinetti S, Brusaferrri L, Grilli E, Guzzi M, Upward M D, Moriarty P and Beton P H (1997). *Structural and optical characterization of self-assembled InAs-GaAs quantum dots grown on high index surfaces*. Microelectron. J. **28**, 933.
- Henini M, Sanguinetti S, Fortina S C, Grilli E, Guzzi M, Panzarini G, Andreani L C, Upward M D, Moriarty P, Beton P H and Eaves L (1998). *Optical anisotropy in arrow-shaped InAs quantum dots*. Phys. Rev. B **57**, R6815.
- Hermann C and Weisbuch C (1977). *k.p perturbation theory in III-V compounds and alloys: a reexamination*. Phys. Rev. B **15**, 823.
- Hill R J A, Patanè A, Main P C, Henini M, Eaves L, Austing D G and Tarucha S (2002). *Controlling the electron tunneling through InAs self-assembled dots*. J. Appl. Phys. **91**, 3474.
- Holder J P, Savchenko A K, Fal'ko V I, Jouault B, Faini G, Laruelle F and Bedel E (2000). *Enhanced fluctuations of the tunnelling density of states near the bottom of a Landau band measured by a local spectrometer*. Phys. Rev. Lett. **84**, 1563.
- Itskevich I E, Eaves L, Main P C and Henini M (1998). *X-valley-related donor states and resonant tunnelling in a single-barrier diode*. Phys. Rev. B **57**, 7214.

- Itskevich I E, Henini M, Carmona H A, Eaves L and Main P C (1997). *Photoluminescence spectroscopy of self-assembled InAs quantum dots in strong magnetic field and under high pressure*. Appl. Phys. Lett. **70**, 505.
- Itskevich I E, Ihn T, Thornton A S G, Henini M, Foster T J, Moriarty P, Nogaret A, Beton P H, Eaves L and Main P C (1996). *Resonant magnetotunnelling through individual self-assembled InAs quantum dots*. Phys. Rev. B **54**, 16401.
- Janak J F (1969). *g factor of the two-dimensional interacting electron gas*. Phys. Rev. **178**, 1416.
- Joyce P B, Krzyzewski T J, Bell G R, Jones T S, Malik S, Childs D and Murray R (2000). *Effect of growth rate on the size, composition, and optical properties of InAs/GaAs quantum dots grown by molecular-beam epitaxy*. Phys. Rev. B **62**, 10891.
- Keithley J F, Yeager J R and Erdman R J (1984). *Low level measurements, 3rd Ed.* Keithley Instruments, Inc.
- Kelly M J (1995). *Low-dimensional semiconductors*. Oxford University Press.
- Khanin Y, Vdovin E, Novoselov K, Dubrovskii Y, Omling P and Carlsson S B (1998).  *$\Gamma$ -X tunnelling in GaAs/AlAs/GaAs heterostructure*. Jpn. J. Appl. Phys. **37**, 3245.
- Kim J, Wang L W and Zunger A (1998). *Comparison of the electronic structure of InAs/GaAs pyramidal quantum dots with different facet orientations*. Phys. Rev. B **57**, R9408.
- Kittel C (1987). *Quantum Theory of Solids, 2nd Ed.* Wiley.
- Kittel C (1996). *Introduction to Solid State Physics, 7th Ed.* Wiley.
- Koch R H and Hartstein A (1985). *Evidence for resonant tunnelling of electrons via sodium ions in silicon dioxide*. Phys. Rev. Lett. **54**, 1848.
- Kosaka H, Kislev A, Baron F A, Kim K W and Yablonovitch E (2001). *Electron g factor engineering in III-V semiconductors for quantum communications*. arxiv:quant-ph/0102056 .
- Lambe J and Jaklevic R C (1968). *Molecular vibration spectra by inelastic electron tunnelling*. Phys. Rev. **165**, 821.

- Lambkin J D, Adams A R, Dunstan D J, Dawson P and Foxon C T (1989). *Pressure dependence of the valence-band discontinuity in GaAs/AlAs and GaAs/Al(x)Ga(1-x)As quantum-well structures*. Phys. Rev. B **39**, 5546.
- Leadley D R, Nicholas R J, Harris J J and Foxon C T (1998). *Critical collapse of the exchange-enhanced spin splitting in two dimensional systems*. Phys. Rev. B **58**, 13036.
- Leon R, Fafard S, Leonard D, Merz J L and Petroff P M (1995). *Visible luminescence from semiconductor quantum dots in large ensembles*. Appl. Phys. Lett. **67**, 521.
- Levin A, Vdovin E E, Patanè A, Eaves L, Main P C, Khanin Y N, Dubrovskii Y V, Henini M and Hill G (2001). *Magneto-tunnelling spectroscopy for spatial mapping of orbital wavefunctions of the ground and excited states in self-assembled quantum dots*. Phys. Stat. Sol. (b) **224**, 715.
- Liang C T, Cheng Y M, Huang T Y, Huang C F, Simmons M Y, Ritchie D A, Kim G H, Leem J Y, Chang Y H and Chen Y F (2001). *Quantum magneto-transport in two-dimensional GaAs electron gases and SiGe hole gases*. J. Phys. Chem. Sol. **62**, 1789.
- Liu H C and Aers G C (1989). *Resonant tunnelling through one-, two-, and three-dimensionally confined quantum wells*. J. Appl. Phys. **65**, 4908.
- Luryi S (1985). *Frequency limit of double-barrier resonant-tunnelling oscillators*. Appl. Phys. Lett. **47**, 490.
- Main P C, Foster T J, McDonnell P, Eaves L, Gompertz M J, Mori N, Sakai J W and Henini M (2000b). *Conductance fluctuations in a double-barrier resonant tunnelling device*. Phys. Rev. B **62**, 16721.
- McDonnell P J, Geim A K, Main P C, Foster T J, Beton P H and Eaves L (1995). *Resonant tunnelling through a single impurity in high magnetic fields: Probing a two-dimensional electron gas on a nanometre scale*. Physica B **211**, 433.
- McMurry S M (1993). *Quantum mechanics*. Addison Wesley.
- Meirav U and Foxman E B (1996). *Single-electron phenomena in semiconductors*. Semicond. Sci. Technol. **11**, 255.
- Meyer J M, Hapke-Wurst I, Zeitler U, Haug R J and Pierz K (2001). *Resonant tunnelling through InAs quantum dots in tilted magnetic fields: experimental determination of the g-factor anisotropy*. Phys. Stat. Sol. (b) **224**, 685.

- Miller B T, Hansen W, Manus S, Luyken R J, Lorke A, Kotthaus J P, Huan S, Medeiros-Ribeiro G and Petroff P M (1997). *Few-electron ground states of charge-tunable self-assembled quantum dots*. Phys. Rev. B **56**, 6764.
- Mori N (2000). Private communication.
- Mori N, Beton P H, Wang J and Eaves L (1995). *Theory of resonant tunnelling through a quantum wire*. Phys. Rev. B **51**, 1735.
- Narihiro M, Yusa G, Nakamura Y, Noda T and Sakaki H (1997). *Resonant tunnelling of electrons via 20 nm scale InAs quantum dot and magnetotunnelling spectroscopy of its electronic states*. Appl. Phys. Lett. **70**, 105.
- Nötzel R (1992). *Self-organised growth of quantum-dot structures*. Semicond. Sci. Technol. **11**, 1365.
- Oppenheimer J R (1928). *Three notes on the quantum theory of aperiodic effects*. Phys. Rev. **31**, 66.
- Patanè A, Hill R J A, Eaves L, Main P C, Henini M, Zambrano M L, Levin A, Mori N, Hamaguchi C, Dubrovskii Y V, Vdovin E E, Austing D G, Tarucha S and Hill G (2002). *Probing the quantum states of self-assembled InAs dots by magneto-tunnelling spectroscopy*. Phys. Rev. B **65**, 165308.
- Payne M C (1986). *Transfer hamiltonian description of resonant tunnelling*. J. Phys. C **19**, 1145.
- Pines D and Nozières P (1989). *The theory of quantum liquids Vol. I*. Addison-Wesley.
- Polimeni A, Patanè A, Henini M, Eaves L and Main P C (1999a). *Temperature dependence of the optical properties of InAs/(AlGa)As self-organized quantum dots*. Phys. Rev. B **59**, 5064.
- Polimeni A, Patanè A, Henini M, Eaves L, Main P C, Sanguinetti S and Guzzi M (1999b). *Influence of high-index GaAs substrates on the growth of highly strained (InGa)As/GaAs heterostructures*. J. Crystal Growth **201**, 276.
- Pryor C, Pistol M E and Samuelson L (1997). *Electronic structure of strained InP/Ga(0.51)In(0.49)P quantum dots*. Phys. Rev. B **56**, 10404.
- Reed M A, Randall J N, Aggarwal R J, Matyi R J, Moore T M and Wetzel A E (1988). *Observation of discrete electronic states in a zero-dimensional semiconductor nanostructure*. Phys. Rev. Lett. **60**, 535.

- Sakai J W, Fromhold T M, Beton P H, Eaves L, Henini M, Main P C, Sheard F W and Hill G (1993). *Probing the wave function of quantum confined states by magnetotunnelling*. Phys. Rev. B **48**, 5664.
- Schiff L (1949). *Quantum mechanics*. McGraw-Hill.
- Schmid A (1974). *On the dynamics of electrons in an impure metal*. Z. Phys. **271**, 251.
- Schmidt T, Haug R J, Fal'ko V I, v. Klitzing K, Förster A and Lüth H (1996b). *Spectroscopy of local density of states fluctuations in a disordered conductor*. Europhys. Lett. **36**, 61.
- Schmidt T, Haug R J, Fal'ko V I, v. Klitzing K, Förster A and Lüth H (1997). *Observation of the local structure of landau bands in a disordered conductor*. Phys. Rev. Lett. **78**, 1540.
- Schmidt T, König P, McCann E, Fal'ko V I and Haug R J (2001). *Energy dependence of quasiparticle relaxation in a disordered Fermi liquid*. Phys. Rev. Lett. **86**, 276.
- Schmidt T, Tewordt M, Blick R H, Haug R J, Pfannkuche D, v. Klitzing K, Förster A and Lüth H (1995). *Quantum-dot ground states in a magnetic field studied by single-electron tunnelling spectroscopy on double-barrier heterostructures*. Phys. Rev. B **51**, 5570.
- Schmidt T, Tewordt M, Haug R J, von Klitzing K, Förster A and Lüth H (1996a). *Single-electron-tunnelling spectroscopy of asymmetric laterally confined double-barrier heterostructures*. Sol. State Electr. **40**, 15.
- Shahbazyan T V and Ulloa S E (1997). *Resonant scattering in a strong magnetic field: Exact density of states*. Phys. Rev. Lett. **79**, 3478.
- Sivan U, Milliken F P, Milkove K, Rishton S, Lee Y, Hong J M, Boegli V, Kern D and deFranza M (1994). *Spectroscopy, electron-electron interaction and level statistics in a disordered quantum dot*. Europhys. Lett. **25**, 605.
- Siverns P D, Malik S, McPherson G, Childs D, Roberts C, Murray R, Joyce B A and Davock H (1998). *Scanning transmission-electron microscopy study of InAs/GaAs quantum dots*. Phys. Rev. B **58**, R10127.
- Sleight J W, Hornbeck E S, Deshpande M R, Wheeler R G, Reed M A, Bowen R C, Frensley W R, Randall J N and Matyi R J (1996). *Electron-spectroscopic study of vertical In(1-x)Ga(x)As quantum dots*. Phys. Rev. B **53**, 15727.

- Smoliner J, Demmerle W, Gornik E, Böhm G and Weimann G (1994). *Tunnelling spectroscopy of 0D states*. Semicond. Sci. Technol. **9**, 1925.
- Snelling M J, Flinn G P, Plaut A S, Harley R T and Tropper A C (1991). *Magnetic g factor of electrons in GaAs/Al(x)Ga(1-x)As quantum wells*. Phys. Rev. B **44**, 11345.
- Stier O, Grundmann M and Bimberg D (1999). *Electronic and optical properties of strained quantum dots modelled by 8-band k.p theory*. Phys. Rev. B **59**, 5688.
- Su B, Goldman V J and Cunningham J E (1992). *Single-electron tunnelling in nanometer-scale double-barrier heterostructure devices*. Phys. Rev. B **46**, 7644.
- Surkova T, Patanè A, Eaves L, Main P C, Henini M, Polimeni A, Knights A P and Jaynes C (2001). *Indium interdiffusion in annealed and implanted InAs/(AlGa)As self-assembled quantum dots*. J. Appl. Phys. **89**, 6044.
- Suzuki K and Kamamoto Y (1973). *The g-factors of interacting electrons in silicon inversion layers*. J. Phys. Soc. Japan **35**, 1456.
- Suzuki T, Nomoto K, Taira K and Hase I (1997). *Tunnelling spectroscopy of InAs wetting layers and self-assembled quantum dots: resonant tunnelling through two- and zero-dimensional electronic states*. Jpn. J. Appl. Phys. **36**, 1917.
- Tan I H, Snider G L, Chang L D and Hu E L (1990). *A self-consistent solution of Schrödinger-Poisson equations using a non-uniform mesh*. J. Appl. Phys. **68**, 4071.
- Tarucha S (1998). *Transport in quantum dots: observation of atomlike properties*. MRS Bulletin February 1998 p. 49.
- Tarucha S, Austing D G, Honda T, van der Hage R J and Kouwenhoven L P (1996). *Shell filling and spin effects in a few electron quantum dot*. Phys. Rev. Lett. **77**, 3613.
- Thornton A S G (1998b). *Resonant tunnelling through zero dimensional quantum dots*. PhD thesis. University of Nottingham, United Kingdom.
- Thornton A S G, Ihn T, Main P C, Eaves L, Benedict K A and Henini M (1998d). *Many-body effects in a quantised 2DES probed by discrete-level spectroscopy*. Physica B **249-251**, 689.
- Thornton A S G, Ihn T, Main P C, Eaves L and Henini M (1998a). *Observation of spin-splitting in single InAs self-assembled quantum dots in ALAs*. Appl. Phys. Lett. **73**, 354.

- Thornton A S G, Ihn T, Main P C, Eaves L, Sheard F W and Henini M (1998c). *Magneto-tunnelling spectroscopy of single self-assembled InAs quantum dots in AlAs*. *Physica E* **2**, 657.
- Thornton A S G, Itskevich I E, Ihn T, Henini P M, Nogaret A, Beton P H, Eaves L, Main P C, Middleton J R and Heath M (1997). *Resonant magnetotunnelling through individual self-assembled InAs quantum dots*. *Superlat. & Microstruct.* **21**, 255.
- Usher A, Nicholas R J, Harris J J and Foxon C T (1990). *Observation of magnetic excitons and spin waves in activation studies of a two-dimensional electron gas*. *Phys. Rev. B* **41**, 1129.
- Vdovin E E, Levin A, Patanè A, Eaves L, Main P C, Khanin Y N, Dubrovskii Y V, Henini M and Hill G (2000). *Imaging the electron wave function in self-assembled quantum dots*. *Science* **290**, 122.
- Vitusevich S A, Förster A, Indlekofer K M, Lüth H, Belayev A E, Glavin B A and Konakova R V (2000). *Tunnelling through X-valley-related impurity states in GaAs/AlAs resonant-tunnelling diodes*. *Phys. Rev. B* **61**, 10898.
- von Klitzing K (1986). *The quantized hall effect*. *Rev. Mod. Phys.* **58**, 519.
- Vurgaftman I, Meyer J R and Ram-Mohan L R (2001). *Band parameters for III-V compound semiconductors and their alloys*. *J. Appl. Phys.* **89**, 5815.
- Wang J, Beton P H, Mori N, Eaves L, Buhmann H, Mansouri L, Main P C, Foster T J and Henini M (1994). *Resonant magnetotunnelling via one-dimensional quantum confined states*. *Phys. Rev. Lett.* **73**, 1146.
- Wang L W, Kim J and Zunger A (1999). *Electronic structures of (110)-faceted self-assembled pyramidal InAs/GaAs quantum dots*. *Phys. Rev. B* **59**, 5678.
- Weber G (1995). *Donors bound to X valleys in type II GaAs-AlAs quantum wells*. *Appl. Phys. Lett.* **67**, 1447.
- Wei S H and Zunger A (1999). *Predicted band-gap pressure coefficients of all diamond and zinc-blende semiconductors: Chemical trends*. *Phys. Rev. B* **60**, 5404.
- Weil T and Vinter B (1987). *Equivalence between resonant tunnelling and sequential tunnelling in double-barrier diodes*. *Appl. Phys. Lett.* **50**, 1281.

- Weisbuch C and Hermann C (1977). *Optical detection of conduction-electron spin resonance in GaAs, Ga(1-x)In(x)As, and Ga(1-x)Al(x)As*. Phys. Rev. B **15**, 816.
- Wolford D J and Bradley J A (1985). *Pressure dependence of shallow bound states in gallium arsenide*. Sol. State Comm. **53**, 1069.
- Yang W, Lee H, Johnson T J, Sercel P C and Norman A G (2000). *Electronic structure of self-organized InAs/GaAs quantum dots bounded by (136) facets*. Phys. Rev. B **61**, 2784.
- Yu P Y and Cardona M (2001). *Fundamentals of Semiconductors*. Springer-Verlag.